NREL/SR-520-23835 • UC Category: 1263

Processing and Modeling Issues for Thin-Film Solar Cell Devices

Final Report

R.W. Birkmire and J.E. Phillips
Institute of Energy Conversion,
University of Delaware
Newark, Delaware

NREL technical monitor: B. von Roedern

MASTER

DISTRIBUTION OF THIS DOCUMENT IS UNLIMITED

National Renewable Energy Laboratory
1617 Cole Boulevard
Golden, Colorado 80401-3393
A national laboratory of
the U.S. Department of Energy
Managed by Midwest Research Institute
for the U.S. Department of Energy
under Contract No. DE-AC36-83CH10093

Prepared under Subcontract No. XAV-3-13170-01

November 1997

This publication was reproduced from the best available camera-ready copy
submitted by the subcontractor and received no editorial review at NREL.

NOTICE

Available to DOE and DOE contractors from:
Office of Scientific and Technical Information (OSTI)
P.O. Box 62
Oak Ridge, TN 37831
Prices available by calling (423) 576-8401

Available to the public from:
National Technical Information Service (NTIS)
U.S. Department of Commerce
5285 Port Royal Road
Springfield, VA 22161
(703) 487-4650

DISCLAIMER

SUMMARY

During the third phase of the subcontract, IEC researchers have continued to provide the thin film PV community with greater depth of understanding and insight into a wide variety of issues including: the deposition and characterization of $CuIn_{1-x}Ga_xSe_2$, a-Si, CdTe, CdS, and TCO thin films; the relationships between film and device properties; and the processing and analysis of thin film PV devices. This has been achieved through the systematic investigation of all aspects of film and device production and through the analysis and quantification of the reaction chemistries involved in thin film deposition. This methodology has led to controlled fabrications of 15% efficient $CuIn_{1-x}Ga_xSe_2$ solar cells over a wide range of Ga compositions, improved process control of the fabrication of 10% efficient a-Si solar cells, and reliable and generally applicable procedures for both contacting and doping CdTe films. Additional accomplishments are listed below.

$Cu(InGa)Se_2$

Multisource Evaporation

$Cu(InGa)Se_2$ films have been deposited by elemental evaporation with Ga composition ranging from $0.25 < x < 0.80$. The films are deposited with the Ga uniformly distributed from the Mo back contact to the front surface. This allows the effects of increasing Ga to be characterized without differences in the device operation due to gradients in the electrical and optical properties of the $Cu(InGa)Se_2$.

The solar cells fabricated from these uniform films have 15% efficiency for $x < 0.5$ or $E_g < 1.3$ eV. V_{oc} increases over the entire range of Ga content, up to 820 mV, but the device efficiency declines with high Ga content due primarily to a drop in fill factor and short circuit current. Analysis of current-voltage and quantum efficiency results show that the main cause of this drop off is a voltage dependent current collection. Finally, preliminary results show that the fill factor can be improved by grading the bandgap of the $Cu(InGa)Se_2$, but there is a concurrent loss in J_{sc}.

Selenization

The selenization at temperatures up to 650°C of Cu/Ga/In results in a two phase film with $CuGaSe_2$ near the Mo back contact and $CuInSe_2$ at the top of the film. Devices made from these films have low V_{OC}, and behave similar to a $CuInSe_2$ device, consistent with the lack of Ga, and therefore low bandgap, in the front region of the absorber layer where the device behavior is controlled. However, annealing the film at $T \geq 550°C$ in an inert atmosphere results in interdiffusion of the In and Ga, converting the film to single phase $Cu(InGa)Se_2$.

The interdiffusion of Ga and In in a $CuGaSe_2$/ $CuInSe_2$ thin film diffusion couple and the diffusion of In into $CuGaSe_2$ thin films were studied by Auger depth profiling. $CuGaSe_2$ and $CuInSe_2$ were obtained via selenization by H_2Se of sequentially deposited Cu-Ga and Cu-In layers, respectively. The $CuGaSe_2/CuInSe_2$ diffusion couple was annealed at 650°C for 30 minutes in an Argon atmosphere. The thin film source of In was diffused into $CuGaSe_2$ in the temperature range of 400°C to 600°C for 30 minutes in an Argon atmosphere. Bulk interdiffusion coefficients of In and Ga in the $CuGaSe_2/CuInSe_2$ couple annealed at 650°C, and the diffusion coefficients of In in $CuGaSe_2$ films diffusion-annealed at various temperatures were determined. The interdiffusion coefficients of In and Ga at 650°C in the diffusion couple are similar ($D_{In} = 1.5 \times 10^{-11}$ cm^2/sec and

$D_{Ga} = 4.0 \times 10^{-11}$ cm^2/sec). The diffusion coefficients of In in $CuGaSe_2$ thin films varied from 2.0×10^{-13} cm^2/sec to 4.5×10^{-12} cm^2/sec in the temperature range of 400°C - 600°C.

Mo/$CuInSe_2$ Contact

A correlation was found between the relative orientation of the Mo and Cu(InGa)Se_2 films, as measured by XRD. However, unlike the compositional profile of the Cu(InGa)Se_2 films which shows a direct correlation to the device behavior, the orientation of the evaporated Cu(InGa)Se_2 shows no correlation to the device results.

Many high efficiency $CuInSe_2$ based solar cells show blocking or non-ohmic contact behavior in their current-voltage characteristic which has often been attributed to the Mo/$CuInSe_2$ back contact. A novel device configuration is presented which allows the current-voltage characteristic of the Mo/$CuInSe_2$ junction to be analyzed separately from the rest of the operating solar cell. Direct measurements of the back contact on operating $CuInSe_2$ based solar cells which demonstrate this blocking behavior show that the Mo/$CuInSe_2$ contact is ohmic with negligible contact resistance compared to the total series resistance of the device.

a-Si

Devices

The first task in improving J_{SC} and V_{OC} was to determine operational characteristics of the a-Si reactor. It was found through QE measurements and SIMS analysis that there was significant dopant carryover from one run to the next from the film deposited on the "hot" electrode. Deposition of a burying layer of a-SiC:H between device runs was found to be necessary to remedy the dopant carryover. As a result, FFs in excess of 71% were obtained reproducibly. In a second step, H_2 diluted μc n-layers, compatible with ZnO/Ag back contact as well as with tunnel junction in tandem devices, were developed. These μc n-layers with conductivities and activation energies of 1 S/cm and 0.05 eV, respectively, allowed fabrication of devices with ZnO/Ag contact with FFs as high as 72%. In the case of 25 Å Ti/5000 Å Ag contacts, the deposition rate of Ag was found to be an important parameter in that rates below 100 Å/min resulted in lower FFs.

The ungraded i-layers were about 0.5 μm thick. The buffer layer had a standard graded C profile. Devices were deposited on Asahi Type U textured SnO_2, with ZnO/Ag back contacts, and had no AR coating. All cells were scribed and surrounded by Ag paste to reduce R_S and increase FF. Pieces were sputter etched to eliminate excessive collection beyond the metal contact.

Five cells from three different pieces were tested at NREL, all having efficiencies of 10% or greater.

TCO's and Optical Enhancement

The material properties of a number of textured SnO_2 and ZnO substrates and their effect on current generation in a-Si were evaluated. Most of these TCO's have been used by others for a-Si device research or module fabrication. Bulk optoelectronic and structural properties are reported for seven TCO films with haze from 1 to 14%. Our results show that increasing haze above ~5% has limited effectiveness for increasing the generation at long wavelengths. In presently available textured ZnO, current generation is about 0.6 mA/cm^2 greater than in textured SnO_2. There may be greater advantages to using ZnO in multijunction devices since much thinner i-layers may be used to give the same J_{SC} with improved stability, shorter deposition time and less GeH_4 usage.

The effect of sputtered transparent conducting oxide (TCO) contacts on the device performance of stainless steel/n-i-p/TCO and glass/SnO_2/p-i-n/TCO/Ag solar cells were investigated. TCO materials ITO and ZnO are compared, and found to have very similar transparency at the same sheet resistance. Sputtering ZnO with O_2 in the Ar reduces FF for stainless steel /n-i-p/ZnO devices, compared to sputtering without O_2. This is attributed to an interface not bulk effect. Sputtering ITO with O_2 on the same devices increases J_{SC} due to higher ITO transparency, compared to sputtering without O_2, but has no effect on FF. Based on curvature in the J-V curve around V_{OC}, the ZnO/p layer contact appears to be non-ohmic. For p-i-n/TCO/Ag devices, µc-Si n-layers have much higher V_{OC}, J_{SC}, and FF for all variations of TCO/Ag back reflectors compared to an a-Si n-layer. Devices with ITO/Ag have lower V_{OC} and J_{SC} compared to devices with ZnO/Ag. Sputtering ZnO with O_2 has no detrimental effect on devices with µc-Si n-layers but severely reduces FF in devices with a-Si n-layers.

A novel device structure was used to study optical enhancement and back reflectors (BRs) in a-Si n-i-p solar cells by separating the effects of substrate texture, BR texture, and BR reflectivity. QE and diffuse and total reflection are compared for devices on smooth or textured substrates, with smooth or textured BRs. There is little improvement in J_{SC} for substrate haze exceeding 5%. Substrate texture is much more effective at increasing red response than the BR texture. Smooth substrates with textured BRs have comparable diffuse reflection but much higher specular reflection than textured substrates with a smooth BR. Devices on textured substrates also have lower reflection losses in the blue regions, resulting in higher QE at all wavelengths. These results apply to both superstrate and substrate device configurations.

J-V Analysis

The current-voltage data measured in light and dark from a-Si based solar cells has been analyzed to yield six parameters which completely specify the illuminated J-V curve from reverse bias to beyond open circuit voltage (V_{OC}). A simple photocurrent collection model is used which assumes drift collection in a uniform field. The method has been applied to J-V data from over twenty single junction a-Si or a-SiGe devices from five laboratories measured under standard simulated sunlight. Very good agreement results between measured and calculated J-V performance with only one adjustable parameter, the ratio of collection length to thickness $\frac{L_C}{D}$. Some of these devices have also been analyzed after extended light soaking or under filtered illumination. The effect of the voltage dependent photocurrent collection on FF and V_{OC} is considered in detail. Results under 1 sun illumination for both a-Si and a-SiGe devices are consistent with hole limited collection. Photocurrent collection in very thin devices (D~0.1 µm), or thicker devices under blue light, may be strongly influenced by interface recombination or back diffusion. The flatband voltage (V_{fb}) is dependent on the intensity and spectrum of illumination, hence is not a fundamental device property and is not equivalent to the built-in potential. V_{OC} is limited by V_{fb} not junction recombination current J_0 in typical devices. The illuminated solar cell performance is nearly independent of the forward diode current for low values of $\frac{L_C}{D}$, as occurs after light soaking or with a-SiGe. The model is also useful to investigate the intensity dependence of FF and to predict the influence of $\frac{L_C}{D}$ and V_{fb} on solar cell performance.

As part of the work associated with the device design team, this simple model was applied to a wide range of single junction devices and conditions. These included p-i-n and n-i-p cells on smooth or textured substrates, a-Si and a-SiGe cells, initial and stabilized, and under AM1.5 and red filtered light. Excellent agreement has been found between the model and the measurements. Devices analyzed covered a wide range of sources. In addition to those from IEC, cells were provided by Solarex, USSC, ECD, and APS. Analysis of triple junction cells using a parameter set based on the stabilized high, middle and low bandgap cells from USSC was also performed.

CdTe/CdS

Device Performance

In this reporting period vapor phase $CdCl_2$ treatments were developed, permitting the effects of reaction temperature and chloride concentration on materials and devices to be investigated. Vapor $CdCl_2$ treatment at 420°C was found to result in uniform modification of the film properties. Combined with the contacting process developed in the previous reporting period, the uniform and reproducible treatments have translated into greater consistency in device performance at an efficiency level of 12%. The V_{OC} is approaching state-of-the-art values, but J_{SC} and FF are low. The resistance at V_{OC} in these devices is in the range of 6 to 10 Ω-cm^2. Reducing this to 1–2 Ω-cm^2 by optimizing the CdTe doping and contact are expected to increase FF to >72% and should enhance the V_{OC}. Control over S interdiffusion with vapor treatment and use of alloyed films is described in the sections below and offers several avenues for improving J_{SC}: 1) use thick CdS (~250 nm) and high S diffusion process to thin down the CdS, boosting J_{SC} contributions from 300–550 nm and 750–900 nm; 2) use ultrathin CdS (<50 nm) and low S diffusion process to minimize loss of CdS film; and 3) deposit $CdTe_{1-x}S_x$ films with x near the solubility limit on ultrathin CdS to minimize driving force for interdiffusion.

$CdCl_2$ Treatment

All-vapor post deposition processing holds many advantages the over conventional coat-and-rinse techniques that are employed for CdTe cells. For example, the thermal separation of CdTe/CdS films from the chloride source allows independent control of both the reaction temperature and species concentration. This facilitates temperature-time configurations that: can reduce the CdS loss via interdiffusion; increase the V_{OC}; reduce the treatment time; and produce a residue-free CdTe surface.

The vapor chloride processing yields a spatially uniform grain size and a clean CdTe surface free of residual chlorides, oxides, and chlorates. This eliminates the necessity for rinsing or handling of rinsates prior to contact formation. From a device perspective, these benefits translate into spatially uniform properties and performance.

The role of $CdCl_2$ in promoting recrystallization, grain growth and interdiffusion between CdS and CdTe layers in physical vapor deposited CdS/CdTe thin film solar cells is has been examined. CdTe/CdS thin film samples prepared with different CdTe film thicknesses and treated in air at 415°C for different times with and without a surface coating of $CdCl_2$. The samples were characterized by scanning electron microscopy, transmission electron microscopy, energy dispersive x-ray spectroscopy, x-ray diffractometry, and optical absorption. The results show that $CdCl_2$ treatment enhances the recrystallization and diffusion processes, leading to a compositional variation within the CdTe layer due to diffusion of S from the CdS. The highest S concentrations observed, after 30 minute treatments with $CdCl_2$ at 415°C, are near the solubility limit for S in CdTe. The compositional distributions indicated by x-ray diffraction measurements of samples with different CdTe thickness show that the S-rich $CdTe_{1-x}S_x$ region lies near the CdTe-CdS interface. A multiple step mixing process must be inferred to account for the diffraction profiles obtained.

CdTe-CdS Alloys and Devices

The CdTe-CdS alloy system has been characterized at typical solar cell processing temperatures in order to elucidate the role of interdiffusion in CdTe/CdS-based solar cells. Predominately single phase $CdTe_{1-x}S_x$ thin films with $x\int[S]/([S]+[Te])$ ranging from 0 to 0.45, were grown by vacuum co-evaporation of CdS and CdTe. Phase segregation was promoted by heat treatment of the films at 415°C in the presence of $CdCl_2$. The solubility limits of S in CdTe and Te in CdS at 415°C were derived by measuring the compositions of the two phases in the films after the $CdCl_2$ treatment. The solubility limit of S in CdTe was determined to be 5.8%. Solar cells were fabricated with compositionally uniform absorber layers of $CdTe_{1-x}S_x$ with x near the solubility limit before heat treatment. An efficiency of 10.8% was achieved by a $CdTe_{1-x}S_x$/CdS device. The V_{oc}, J_{sc}, FF and spectral response of this device were all very similar to vacuum evaporated conventional CdTe/CdS cells where the alloy is formed by diffusion of S during cell processing.

HCl Vapor Treatment

Data on the structural and optical properties and cell performance of thermally evaporated CdTe/CdS films were determined as functions of the HCl concentration and temperature of a post-deposition heat treatment. The degree of preferred (111) orientation decreased while the grain size of the CdTe films increased with increasing HCl concentration and temperature. The sulfur content of a $CdTe_{1-x}S_x$ layer also increased with HCl concentration and temperature to a maximum value of ~2%. Cell performance improved over as-deposited values to ~8% efficiency.

Stress Testing of CdTe/CdS Devices

CdTe/CdS solar cells have been known to exhibit various combinations of reversible and irreversible degradation of conversion efficiency after being subjected to temperature, voltage and illumination at levels which equal or surpass those expected in field conditions. This section describes a series of measurements designed to quantify these phenomena. The QE and light and dark J-V characteristics of a set of CdTe devices were measured, then devices were subjected to various combinations of stresses within the parameter space of 0-70 mW/cm^2 illumination, -0.5 V to +5 mA/cm^2 electrical bias, and temperatures from 72° to 112°C. The device characteristics were measured and changes are interpreted in the context of an equivalent circuit which includes the effects of both the main junction diode, series resistor and a rectifying back contact.

LIST OF CONTRIBUTORS

PRINCIPAL INVESTIGATORS

Robert W. Birkmire

James E. Phillips

PRINCIPAL RESEARCHERS

Wayne A.Buchanan

Steven S. Hegedus

Brian E. McCandless

Peter V. Meyers

Nese Orbey

TWF Russell

William N. Shafarman

Tracey A. Yokimcus

VISITING PROFESSIONALS

Jan Egelhaaf, Visiting Scholar

Erten Eser, Visiting Scientist

Axel Hartmann, Visiting Scholar

Dirk Hofmann, Visiting Scholar

D. Garth Jensen, Visiting Scholar

Sylvain Marsillac, Visiting Scholar

Nese Orbey, Visiting Engineer

Sandeep Verma, Visiting Research Associate

Per Widenborg, Visiting Researcher

Issakha Youm, Fulbright Scholar

POST-DOCTORAL FELLOWS

Habib Hichri

Scott Jones

Reiner Klenk

Saibal Mitra

Yi Qu

Robert Wunder

Satoshi Yamanaka

TECHNICAL SUPPORT

Sarah K. Buchanan

Ronald D. Dozier

Shannon Fields

Sally I. Gordon

Kevin E. Hart

Tom Hughes-Lampros

John Laker

Yiping Li

Richard Trotman

Herbert O. Wardell

GRADUATE STUDENTS

Yibin Bai

Mike Engelmann

Greg Hanket

Matheswaran Marudachalam

Greg Norsworthy

Joseph Shan

Rajesh Venugopal

STUDENTS

Sujit Basu

Roger Clark

Mark Cress

Mike Goetz

Tony Gladwell

Eric Hall

Raymond Haraway

Jeff Janukowicz

Curtis Lawrence

Stacey Lush

Greg Meyers

Jason Quirin

Robert Raniere

Stanley Salamon

Nicole Scherneck

Richard Thompson

Tim Weddle

Lucky Withanawasam

Suzanne Woods

Johnny Yu

DOCUMENT PREPARATION

James E. Phillips

Ronald D. Dozier

Linda Granger

TABLE OF CONTENTS

LIST OF FIGURES

LIST OF TABLES

1. INTRODUCTION

The overall mission of the Institute of Energy Conversion is the development of thin film photovoltaic cells, modules, and related manufacturing technology and the education of students and professionals in photovoltaic technology. The objectives of this four-year NREL subcontract are to advance the state of the art and the acceptance of thin film PV modules in the areas of improved technology for thin film deposition, device fabrication, and material and device characterization and modeling, relating to solar cells based on $CuInSe_2$ and its alloys, on a-Si and its alloys, and on CdTe.

In the area of $CuInSe_2$ and its alloys, IEC researchers have produced $Cu(In_{1-x},Ga_x)Se_2$ films by selenization of elemental and alloyed films with H_2Se and Se vapor and by a wide variety of process variations employing co-evaporation of the elements. Careful design, execution and analysis of these experiments has led to an improved understanding of the reaction chemistry involved, including estimations of the reaction rate constants. Investigation of device fabrication has also included studies of the processing of the Mo, CdS and ZnO deposition parameters and their influence on device properties. An indication of the success of these procedures was the fabrication of a 15% efficiency $Cu(In_{1-x},Ga_x)Se_2$ solar cell with $x \leq 0.5$.

In the a-Si area, reproducibility and process control have been achieved through the optimization of processing parameters related to each of the a-Si layers: p, buffer, i, and n, as well as the TCO window and back contact. In addition, analysis and measurements of the improvement in performance of a-Si solar cells due to optical enhancements from a wide range of TCO texture substrates and back reflectors have been completed. Development of μc n-layer has allowed fabrication of a-Si devices with efficiencies over 10%.

Activities related to CdTe-based solar cells include the development of uniform and reproducible vapor phase $CdCl_2$ treatments for CdTe/CdS films which have translated into greater consistency in device performance, as well as a HCl vapor treatment that promotes changes in the structure of the films similar to those treated with $CdCl_2$. The CdTe/CdS alloy system was characterized at typical solar cell processing temperatures to evaluate the role of interdiffusion in the CdTe solar cells. In order to determine the long term stability of contacts made to CdTe, stress testing of specially prepared CdTe devices has begun.

The measurement, characterization, and modeling of thin film device operation has been specialized independently for devices produced with each class of materials. Also, data has been accumulated and analyzed to develop baseline device parameters for each type of cell.

IEC personnel are active in teamed research in all three thin film material areas, both through NREL's Thin Film PV Partnership program and on a less formal, one-on-one basis. It is partly through these interactions that IEC serves to disseminate PV expertise throughout the PV community and, thereby, achieve its larger goals.

2. Cu(In,Ga)Se_2

2.1 SUMMARY

2.1.1 Multisource Evaporation

Cu(In,Ga)Se_2 films have been deposited by elemental evaporation with Ga composition ranging from $0.25 < x < 0.80$ [201-204]. The films are deposited with the Ga uniformly distributed from the Mo back contact to the front surface. This allows the effects of increasing Ga to be characterized without differences in the device operation due to gradients in the electrical and optical properties of the Cu(In,Ga)Se_2.

The solar cells fabricated from these uniform films have 15% efficiency for $x < 0.5$ or $E_g < 1.3$ eV. V_{OC} increases over the entire range of Ga content, up to 820 mV, but the device efficiency declines with high Ga content due primarily to a drop in fill factor and short circuit current. Analysis of current-voltage and quantum efficiency results show that the main cause of this drop off is a voltage dependent current collection. Finally, preliminary results show that the fill factor can be improved by grading the bandgap of the Cu(In,Ga)Se_2, but there is a concurrent loss in J_{SC}.

2.1.2 Selenization

The selenization at temperatures up to 650°C of Cu/Ga/In results in a two phase film with $CuGaSe_2$ near the Mo back contact and $CuInSe_2$ at the top of the film [205]. Devices made from these films have low V_{OC}, and behave similar to a $CuInSe_2$ device, consistent with the lack of Ga, and therefore low bandgap, in the front region of the absorber layer where the device behavior is controlled. However, annealing the film at $T \geq 550°C$ in an inert atmosphere results in interdiffusion of the In and Ga, converting the film to single phase Cu(In,Ga)Se_2 [201].

The interdiffusion of Ga and In in a $CuGaSe_2$/$CuInSe_2$ thin film diffusion couple and the diffusion of In into $CuGaSe_2$ thin films were studied by Auger depth profiling [206]. $CuGaSe_2$ and $CuInSe_2$ were obtained via selenization by H_2Se of sequentially deposited Cu-Ga and Cu-In layers, respectively. The $CuGaSe_2$/$CuInSe_2$ diffusion couple was annealed at 650°C for 30 minutes in an Argon atmosphere. The thin film source of In was diffused into $CuGaSe_2$ in the temperature range of 400°C to 600°C for 30 minutes in an Argon atmosphere. Bulk interdiffusion coefficients of In and Ga in the $CuGaSe_2$/$CuInSe_2$ couple annealed at 650°C, and the diffusion coefficients of In in $CuGaSe_2$ films diffusion-annealed at various temperatures were determined. The interdiffusion coefficients of In and Ga at 650°C in the diffusion couple are similar ($D_{In} = 1.5 \times 10^{-11}$ cm^2/sec and $D_{Ga} = 4.0 \times 10^{-11}$ cm^2/sec). The diffusion coefficients of In in $CuGaSe_2$ thin films varied from 2.0×10^{-13} cm^2/sec to 4.5×10^{-12} cm^2/sec in the temperature range of 400°C - 600°C.

2.1.3 Mo/$CuInSe_2$ Contact

The Mo back contact has been characterized with respect to the effect of the Mo relative crystal orientation on the subsequent growth of Cu(In,Ga)Se_2 and with respect to the Mo/Cu(In,Ga)Se_2 electrical contact. A correlation was found between the relative orientation of the Mo and Cu(In,Ga)Se_2 films, as measured by XRD. However, the orientation of the evaporated Cu(In,Ga)Se_2 shows no correlation to the device results.

Many high efficiency $CuInSe_2$ based solar cells show blocking or non-ohmic contact behavior in their current-voltage characteristic which has often been attributed to the Mo/$CuInSe_2$ back contact. A novel device configuration is presented which allows the current-voltage characteristic of the Mo/$CuInSe_2$ junction to be analyzed separately from the rest of the operating solar cell [207] Direct measurements of the back contact on operating $CuInSe_2$ based solar cells which demonstrate this blocking behavior show that the Mo/$CuInSe_2$ contact is ohmic with negligible contact resistance compared to the total series resistance of the device.

2.2 MULTISOURCE EVAPORATION

2.2.1 Introduction

High efficiency solar cells have been achieved with $Cu(In,Ga)Se_2$ thin films deposited by multi-source elemental evaporation or selenization. With evaporated absorber layers the highest reported efficiencies have been achieved in cells with $x \equiv [Ga]/([In]+[Ga]) \approx 0.25$ corresponding to a bandgap (E_g) of ~1.15eV [208, 209]. These cells have $V_{OC} \approx 600$ - 650mV. The high efficiency cells have been achieved with the Ga either uniformly incorporated in the absorber layer [208] or with a gradient of the Ga decreasing from the Mo back contact to the front [209, 210]. At greater Ga content, it has been reported that the open circuit voltage did not increase proportionally to the bandgap and the efficiency decreased [202, 211-213].

The bandgap of $CuInSe_2$ thin films for solar cells has been successfully increased by the addition of Ga to form $Cu(In,Ga)Se_2$ absorber layers with increased bandgap which more closely matches the solar spectrum. This results in a tradeoff of higher open circuit voltage and lower short circuit current which should be advantageous for the manufacture of $Cu(In,Ga)Se_2$ photovoltaic modules [214]. Specifically, module performance can be improved with lower resistive losses, thinner ZnO with less optical loss and/or greater interconnect spacing with reduced associated area related losses. In addition, a higher bandgap reduces the current losses due to free carrier absorption in ZnO or other transparent conducting materials.

In this report, $Cu(In,Ga)Se_2$ films have been deposited by elemental evaporation with Ga composition ranging from $0.25 < x < 0.80$. The films are deposited with the Ga uniformly distributed from the Mo back contact to the front surface. This allows the effects of increasing Ga to be characterized without differences in the device operation due to gradients in the electrical and optical properties of the $Cu(In,Ga)Se_2$. The solar cells fabricated from these uniform films have 15% efficiency for $x < 0.5$ or $E_g < 1.3$ eV. V_{OC} increases over the entire range of Ga content, up to 820 mV, but the device efficiency declines with high Ga content due primarily to a drop in fill factor and short circuit current. Analysis of current-voltage and quantum efficiency results show that the main cause of this drop off is a voltage dependent current collection. Finally, preliminary results show that the fill factor can be improved by grading the bandgap of the $Cu(In,Ga)Se_2$, but there is a concurrent loss in J_{sc}.

2.2.2 $Cu(In,Ga)Se_2$ Deposition and Cell Fabrication

For characterization of $Cu(In,Ga)Se_2$ films and devices as a function of Ga content, the films were deposited by elemental evaporation from four Knudsen type sources to independently control the fluxes of Cu, In, Ga, and Se. The substrates were soda lime glass coated by dc sputtering with a 1 μm thick Mo layer. One bare glass substrate was included in each run to allow measurements of the sheet resistance and optical transmission. The $Cu(In,Ga)Se_2$ films were deposited using a simplified version of the bi-layer process developed for $CuInSe_2$ [211]. This began with a Cu-rich

$Cu(In,Ga)Se_2$ layer, with [Cu] > [In] + [Ga], deposited at substrate temperature T_{SS} = 450°C, followed continuously by a layer containing only In, Ga, and Se deposited at Tss = 600°C. In this process, the In, Ga, and Se source temperatures and fluxes were kept constant through both layers and the Cu source was simply turned off. A profile of the source and substrate temperatures versus time for a deposition which gave x = 0.38 is shown in Figure 2-1. The first layer had [Cu]/([In]+[Ga]) = 1.3–1.5. The final Cu content could be varied by simply changing the relative times of the two layers and the completed films in this work had [Cu]/([In]+[Ga]) ≈ 0.90 ± 0.03. The $Cu(In,Ga)Se_2$ films had thicknesses from 2.5–2.9 μm as determined by the mass gain.

With this process, $Cu(In,Ga)Se_2$ films were deposited with $0.25 \leq x \leq 0.8$, which corresponds to $1.16\ \text{eV} \leq E_g \leq 1.45\ \text{eV}$, for characterization and device fabrication. Also, $CuInSe_2$ films were deposited for comparison.

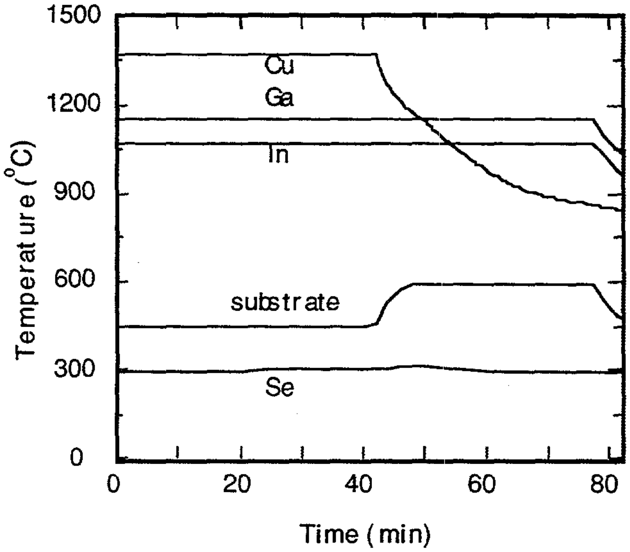

Figure 2-1 Source and substrate temperature versus time profile of a deposition to produce a $Cu(In,Ga)Se_2$ film with x = 0.38.

Solar cells were fabricated by the sequential deposition of CdS, ZnO:Al, Ni/Al grids, and MgF_2 anti-reflection layers on the glass/Mo/$Cu(In,Ga)Se_2$. The CdS was deposited with a thickness of ~30 nm by chemical bath deposition using a method similar to that described by Kessler et al. [215]. The ZnO:Al was deposited in two layers [216] by rf sputtering from a compound $ZnO{:}Al_2O_3$ target with 2% Al_2O_3 by weight. The first layer was deposited with a sputter gas composition of Ar/O_2 (2%) to give a 50 nm thick layer with resistivity $\rho \approx 50$ Ω-cm. This was followed by a layer deposited with a sputter gas composition of Ar/O_2 (0.2%) to give a 500 nm thick layer with a sheet resistance of 15 Ω/sq or $\rho \approx 8\times10^{-4}$ Ω-cm. Electron beam evaporation was used to deposit Ni/Al grids with ~ 5% shading loss and a 125 nm thick MgF_2 layer which produces a broad minimum in the reflection spectrum between 500-800 nm. Cell areas were delineated by mechanical scribing to give individual cells with area 0.4 cm^2. Characterization of the devices included the total area current-voltage (J–V) response measured at 25°C under AM1.5 illumination and quantum efficiency (QE) measured under white light bias as a function of voltage bias. J–V parameters were measured at NREL on four devices, and gave good agreement with the measurements at IEC.

2.2.3 Cu(In,Ga)Se_2 Characterization

The elemental composition of the Cu(In,Ga)Se_2 films was determined by energy dispersive X-ray spectroscopy (EDS) measurements with a 20 kV acceleration voltage and the composition was used to determine E_g according to published values [217]. The grain size and surface morphology were evaluated with a scanning electron microscope (SEM). The compositional uniformity was characterized by X-ray diffraction (XRD) and Auger electron spectroscopy (AES) depth profiles. The XRD scans were performed using Cu Kα radiation in a scanning 2θ mode with 0.01° step size. Since the Cu(In,Ga)Se_2 films are much thinner than the absorption depth of $CuInSe_2$ (13 µm) and $CuGaSe_2$ (25 µm), the entire thickness of the films was sampled. The AES measurements were done at the National Renewable Energy Laboratory (NREL). Sheet resistance was measured on the sample deposited on bare glass substrate with a four point probe.

SEM characterization of the surface and cross-section of the films showed similar surface morphology and well-defined columnar grains with 1–2 µm average grain size regardless of the Ga content. An SEM micrograph of a film with $x = 0.38$ shows this in Figure 2-2.

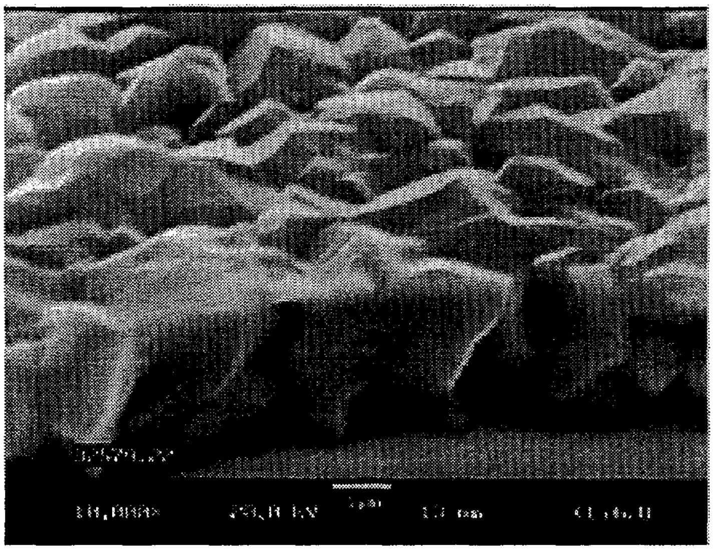

Figure 2-2 SEM micrograph of a typical film with x = 0.38.

XRD measurements were used to determine the Ga content of the films from the lattice parameter and gave good agreement with the EDS. Detailed XRD scans were made of the strongest reflections and the compositional distribution was inferred from the full width at half maximum (FWHM) and peak symmetry. This is shown by the (112) peak and the (220)/(204) peak doublet in Figure 2-3 and Figure 2-4 for four of the films spanning the compositional range. The crystal axis ratio c/a is 2.00 for $x \approx 0.25$ so there is no splitting of the (220) and (224) peaks for the film with $x = 0.27$. As x increases or decreases, c/a decreases or increases, respectively, and the doublet shows increased splitting. The peaks also show a shift in 2θ consistent with the increase in x. The (112) peaks show an instrumental asymmetry inherent to the apparatus at low 2θ. The Cu(In,Ga)Se_2 films have FWHM = 0.15–0.19° compared to the $CuInSe_2$ films with FWHM and the instrumental broadening of 0.11°. Other peaks on the Cu(In,Ga)Se_2 films which could be separated at low and high Ga concentration also had FWHM < 0.2 with no asymmetric broadening. The broadening of the $CuInSe_2$ film peaks is likely due to stress in the films because the grain size is sufficiently large to have effect on the peak shape. If the additional broadening of the Cu(In,Ga)Se_2 peaks is entirely due to compositional non-uniformity, the total variation in x would still be less than ±5% for each film corresponding to a maximum bandgap variation of ±0.03 eV. Thus the XRD spectra indicate that the films are compositionally uniform.

To characterize the relative orientation of the grains within the films the relative orientations of the (112) peak and the (220)/(204) doublet were determined by measuring the areas under the diffraction peaks. The ratios of the integrated intensity I(112) to I(220)+I(204) are compared in Table 2-1 to those of powder diffraction standards for x = 0.3 and 0.6 [218]. These relative orientations suggest that the Cu(In,Ga)Se_2 films have a nearly random crystal orientation. The Cu(In,Ga)Se_2 orientation may be related to the orientation of the substrate it is deposited on. The random orientation was obtained when the films were deposited onto (110) oriented Mo layers, but Cu(In,Ga)Se_2 deposited directly on glass had a strong (112) orientation with I(112)/[I(220)+I(204)] = 420 for the run which gave x = 0.38. We have previously shown that there is an inverse correlation between the Cu(In,Ga)Se_2 orientation and that of the Mo [219] and this will be discussed further in section 2.4.

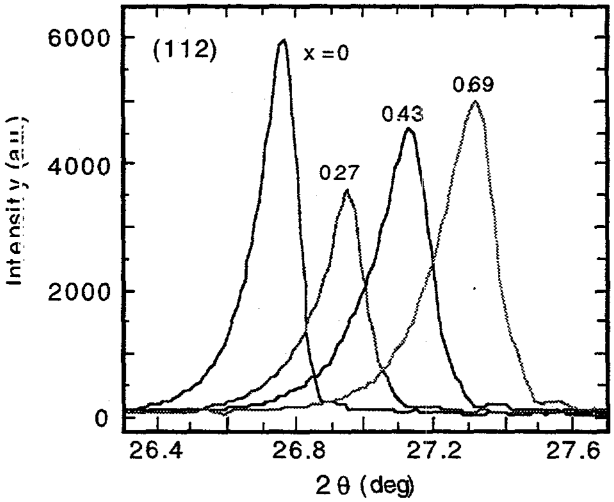

Figure 2-3 XRD scans of the (112) peak for samples with x = 0, 0.27, 0.43, and 0.69.

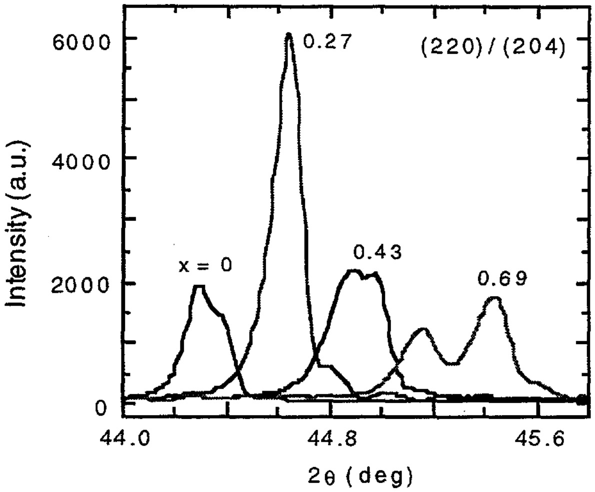

Figure 2-4 XRD scans of the (220)/(224) doublet for samples with x = 0, 0.27, 0.43, and 0.69.

Table 2-1 Relative crystallite orientation of the $Cu(In,Ga)Se_2$ measured by the ratio of the areas under the (112) and (220)/(204) peaks and intensities from powder diffraction patterns.

x	E_g (eV)	FWHM (deg)	$\frac{(112)}{(220)+(204)}$
	films		
0	1.0	0.13	2.7
0.27	1.16	0.16	0.7
0.30	1.18	0.21	1.2
0.38	1.23	0.17	0.9
0.43	1.27	0.19	1.6
0.58	1.37	0.17	1.2
0.69	1.45	0.18	1.9
	powder standards		
0	-	-	0.7
0.3	-	-	2.5
0.6	-	-	1.7

The compositional uniformity was confirmed by AES depth profiles measured on the films with x = 0.38 and 0.58. The atomic concentrations of Mo, Cu, In, Ga, and Se are shown in Figure 2-5 for the first film plotted versus sputter time. The Mo signal rises rapidly after ~130 min sputtering time indicating that the entire film was sampled in this time. The profiles show no gradient in x through the bulk of the film thickness, consistent with the XRD results, and the value of x agrees well with that determined by EDS. Thus, as the total Ga content increases there is no separation or diffusion of the In and Ga as was observed with selenized Cu(In,Ga)Se_2 films (see section 2.3.3).

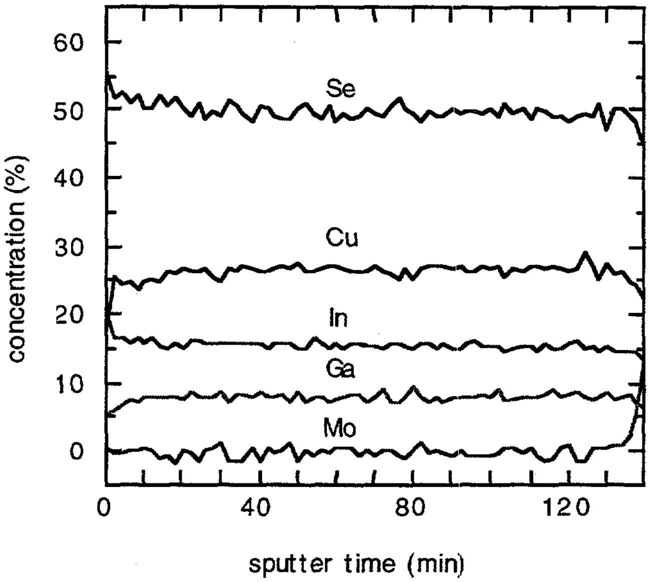

Figure 2-5 Atomic concentrations determined by AES depth profile of Mo, Cu, In, Ga, and Se for the film with x = 0.38.

The AES profiles show that the In concentration at the front surface is greater than in the bulk film while the Cu and Ga concentrations are lower near the front of the film. This is consistent with the presence of a Cu-deficient layer at the front surface of the Cu(In,Ga)Se_2 film [220]. In this case, the AES data suggests that the surface layer also has lower Ga than the bulk so the surface may prefer a Cu-In-Se phase such as $CuIn_3Se_5$ over an analogous Cu-Ga-Se_2 phase. The effect of such a layer on the device performance is unknown and no attempt is made to account for it in the device analysis below.

Finally, resistivity measurements of the films deposited simultaneously on bare glass also do not indicate any difference in the films as x increases. All films had $\rho = 25\pm15$ Ω-cm with no correlation to composition.

2.2.4 Device Results

The solar cell parameters V_{OC}, J_{SC}, fill factor (FF) and efficiency (η) determined from J-V measurements at 25°C are listed in Table 2-2 for cells with nine bandgaps from 1.16 to 1.54 eV. The same parameters are plotted versus bandgap in Figure 2-6.

Table 2-2. Cu(In,Ga)Se_2 device parameters under AM1.5 illumination at 25°C.

x	E_g (eV)	V_{oc} (mV)	J_{sc} (mA/cm^2)	FF (%)	η (%)
0.27	1.16	602	33.2	74.1	14.8
0.30	1.18	623	32.8	73.1	14.9
0.34	1.21	653	32.0	73.5	15.4
0.38	1.23	639	31.9	74.3	15.1
0.43	1.27	689	28.9	75.0	15.0
0.53	1.34	729	27.6	70.9	14.3
0.57	1.37	746	25.2	69.7	13.1
0.72	1.47	804	20.7	69.0	11.5
0.81	1.54	821	16.8	63.7	8.8

The efficiency, Figure 2-6(a), remains constant ~15% for $E_g < 1.3$ eV. V_{oc}, Figure 2-6(b), increases linearly with slope $q\Delta V_{oc}/\Delta E_g \approx 0.7$ up to $E_g = 1.4$ eV but more slowly with E_g at the highest bandgaps.. The fall-off in J_{sc} is shown in Figure 2-6(c). The dashed line is the approximate available current obtained by integrating the AM 1.5 Global spectrum and subtracting 12% to account for optical losses including reflection, grid shading, and absorption in the ZnO and CdS layers. Quantum efficiency curves for these devices show a shift in the long wavelength fall-off consistent with the shift in E_g and the decrease in J_{sc} follows the available current for low bandgap. However, there are additional losses at the highest bandgap values. Finally the fill factor is 73-75% for $E_g < 1.3$ eV but also falls off at increased bandgap. The drop in FF and J_{sc} are the main causes for the fall-off in efficiency.

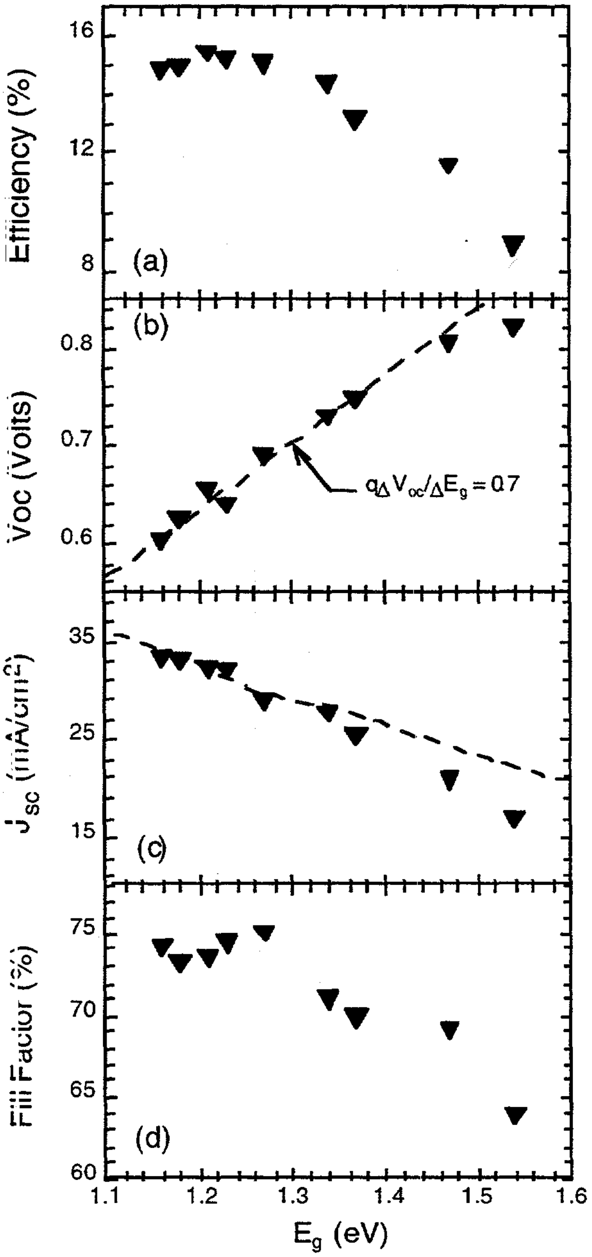

Figure 2-6 Bandgap dependence of basic J-V parameters: (a) efficiency, (b) V_{oc}, (c) J_{sc}, and (d) FF. The dashed line in (c) is the available current as described in the text.

2.2.5 Cu(In,Ga)Se$_2$ Device Analysis

The qualitative features with high Ga content in Figure 2-6 can be attributed primarily to a voltage dependent current collection . This can be shown by detailed comparison of the J-V behavior in the dark and under illumination and from the voltage bias dependence of the quantum efficiency. This analysis will be shown to elucidate the difference between the J-V behavior at low and high bandgap by comparing the cells with E_g = 1.16 and 1.47 eV. The dark and illuminated J-V curves for these two devices are shown in Figure 2-7.

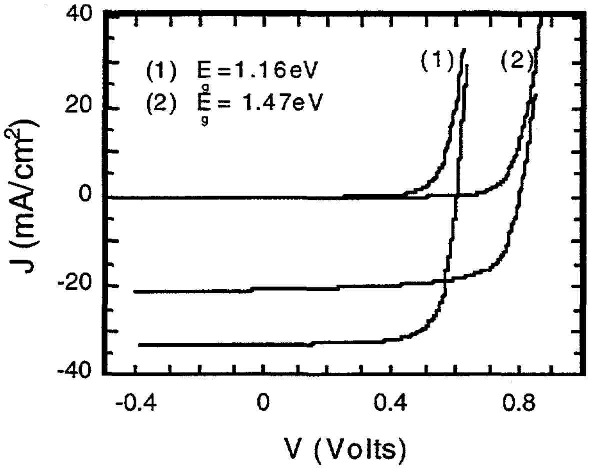

Figure 2-7 J-V curves for E_g = 1.16 and 1.47 eV.

The J-V data is described by a standard diode model which gives

$$J = J_o \exp\left[\frac{q(V - R_s J)}{AkT}\right] - J_o - J_L + GV$$

Equation 2-1

where J_o is the forward current, A the diode quality factor, J_L the light generated current, R_s the series resistance, and G the shunt conductance. With the forward diode current limited by Shockley-Read-Hall recombination through a distribution of states within the space-charge region of the $Cu(In,Ga)Se_2$ [221-223], A is between 1 and 2 and J_o is given by

$$J_o = J_{oo} \exp\left(-\frac{E_g}{2kT}\right).$$

Equation 2-2

The diode equation as written in Equation 2-1 assumes that R_s, and G, are constant, i.e. that the series and shunt terms are ohmic. In addition, J_L can be voltage dependent, but most diode analysis requires the assumption that the light generated current is constant, i.e. $J_L = J_{sc}$. These assumptions must be experimentally verified and often do not hold with thin film polycrystalline solar cells. This can be done by considering the derivatives $g(V) \equiv dJ/dV$ and $r(J) \equiv dV/dJ$. If $J_L = J_{sc}$ and the shunt term is ohmic, g(V) will be constant near V = 0 and in reverse voltage bias, where the diode contribution becomes negligible,. With R_s and J_{sc} constant and $R_sG \ll 1$, differentiating Equation 2-1 gives

$$r(J) = R_s + \frac{AkT}{q}(J + J_{sc})^{-1}.$$

Equation 2-3

In this case, a plot of r(J) vs $(J+J_{SC})^{-1}$ will be linear at large current with intercept R_s and slope AkT/q. Finally, when the assumptions of constant R_s, G, and J_L apply and Equation 2-1 is shown to be applicable, a logarithmic plot of $J+J_{SC}$ versus $V-R_sJ$ will give an intercept of J_o and slope q/AkT.

Figure 2-8 shows g(V) for the devices in Figure 2-7. With $E_g = 1.16$ eV, g(V) is constant in reverse voltage bias both in the dark and under illumination. This gives a dark shunt term G = 0.4 mS/cm^2. However, with $E_g = 1.47$ eV, g(V) is constant only in the dark, where G = 0.2 mS/cm^2. There is a clear voltage dependence under illumination. For all the devices the dark shunt term is small enough that it can be neglected in the subsequent analysis.

A similar difference is shown by r(J) in Figure 2-9. The low bandgap cell has little difference between the dark and illuminated data. The intercept gives $R_s = 0.2\ \Omega\text{-cm}^2$ and the slope gives A = 1.7. For the higher bandgap cell, the dark fit gives $R_s = 0.3\ \Omega\text{-cm}^2$ and A = 1.8. However, the illuminated data does not fit a straight line so R_s and A cannot be determined.

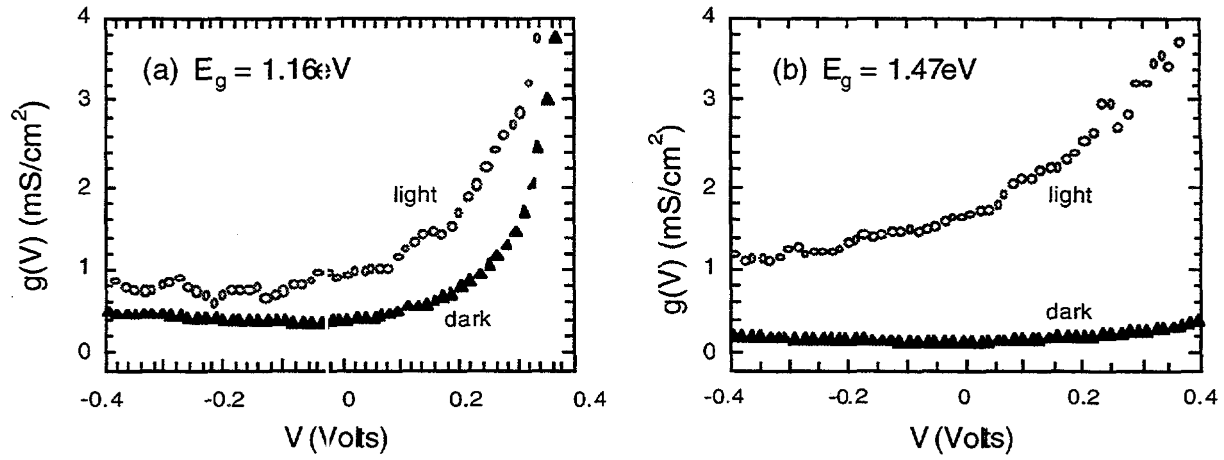

Figure 2-8 Illuminated and dark g(V) for (a) $E_g = 1.16$ eV, and (b) $E_g = 1.47$ eV.

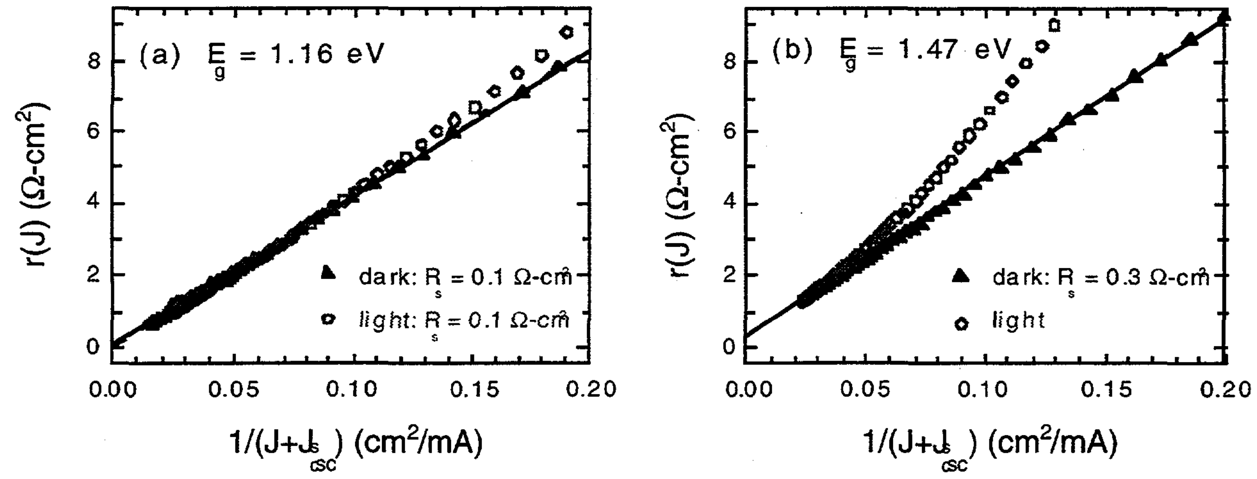

Figure 2-9 Illuminated and dark r(J) for (a) E_g = 1.16 eV, and (b) E_g = 1.47 eV. Solid lines show the fit to determine R_S.

Using the dark value of R_S, the logarithmic plot of $J+J_{SC}$ vs. $V-R_SJ$ is shown for the same two samples in Fig. 6. For E_g = 1.16 eV, the lines give A = 1.6 in the dark and 1.7 under illumination. For E_g = 1.47 eV, A = 1.8 in the dark. However, there is a large excess current under illumination and the J-V data does not fit the simple exponential form of Equation 2-1 so A and J_O cannot be determined.

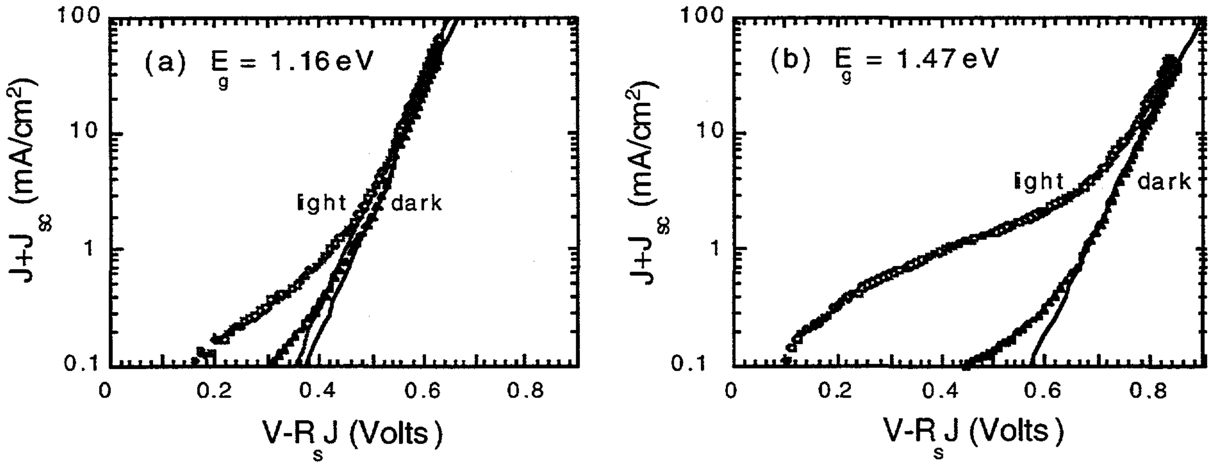

Figure 2-10 Logarithmic plot of $J+J_{SC}$ vs $V-R_SJ$ with (a) E_g = 1.16 eV, and (b) E_g = 1.47 eV. Solid lines show the fit to determine J_O and A.

The differences at high bandgap between the dark and illuminated data shown above can be attributed to a voltage dependent current collection. This is seen in the voltage dependence of the QE which is shown at 0V and -1V in Figure 2-11 for the same two devices. Increasing reverse voltage bias has little effect on the QE for the low bandgap cell. The ratio QE(-1V)/QE(0V) increases only to 1.02 at long wavelength. However, there is a much bigger difference between the two curves for the high bandgap cell and the QE(V) ratio increases to 1.10.

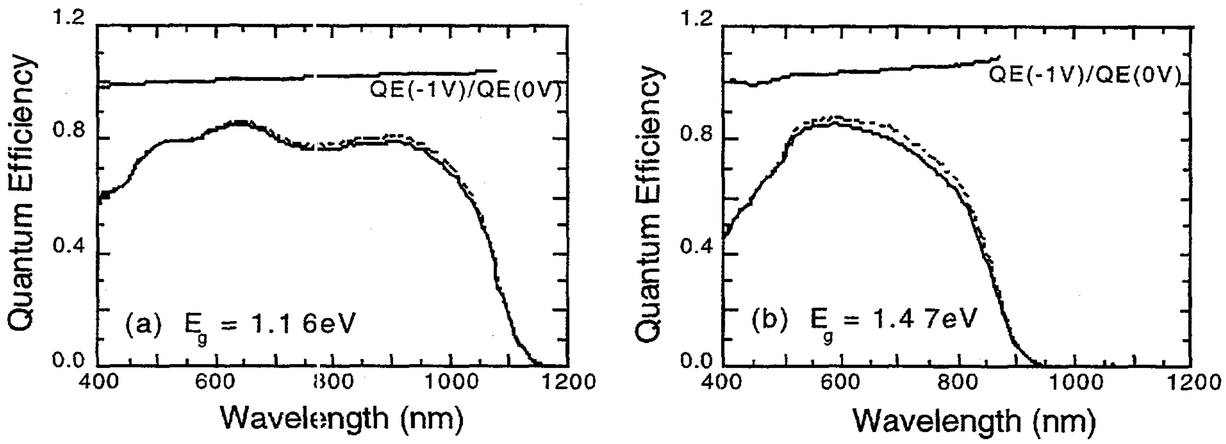

Figure 2-11 QE curves at 0 and -1V and the ratio QE(-1V)/QE(0V) for (a) E_g = 1.16 eV, and (b) E_g = 1.47 eV.

The voltage dependent current collection can also be shown by the voltage dependence of the normalized current difference $(J_{illum} - J_{dark})/J_L$ where J_{illum} and J_{dark} are the currents measured under illumination and in the dark respectively. J_L is taken as J_{illum} at V = -1 V. This is shown in Figure 2-12 for E_g increasing from 1.21 to 1.54 eV. As the bandgap increases the voltage dependence of the current clearly increases. This behavior suggests that the minority carrier diffusion length is small in these devices so that the collection of light generated current is dependent on the space charge width which varies with the applied voltage.

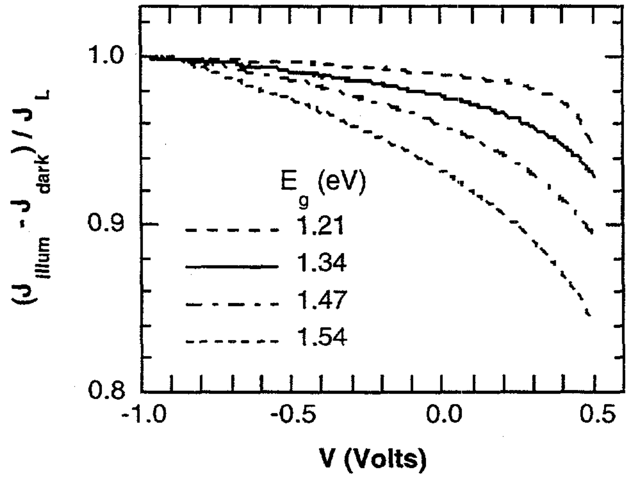

Figure 2-12. Voltage dependence of the normalized current difference $(J_{illum} - J_{dark})/J_L$ with increasing bandgap.

Results from the diode analysis for all nine devices are listed in Table 2-3. All devices could be completely characterized in the dark but the devices with $E_g > 1.3$ eV could not be analyzed under illumination due to the voltage dependent current collection. There is no increase in G or R_s as the bandgap increases and only a small increase in A, so the voltage dependent collection is apparently responsible for the drop in FF. The fall-off in J_{SC} seen at high bandgap in Fig 2 indicates that there is significant current loss even at V=0. The loss in V_{OC} at high bandgap can also be explained, at least in part, by the poor current collection.

The device parameters in Table 2-3 can be used to determine the slope of the increase in V_{OC} with E_g. Solving Equation 2-1 for J=0, with $GV_{OC} << J_{SC}$, gives:

$$qV_{OC} = \frac{A}{2}E_g + AkT\left[\ln\left(\frac{J_{SC}}{J_{OO}}\right)\right]$$

Equation 2-4

The devices with Eg < 1.3eV have $A \approx 1.7$ so the first term gives a slope $q(dV_{oc}/dE_g) = A/2 \approx 0.85$. The values of J_o under illumination in Table 2-3 with Equation 2-2 give $J_{oo} \approx 3x10^5$ mA/cm^2 so with the second term, Equation 2-4 gives a predicted slope $q(dV_{oc}/dE_g) \approx 0.75$-0.8. As shown in Figure 2-6(b), a fit to the data up to Eg = 1.4eV gives $q\Delta V_{oc}/\Delta E_g = 0.7$.

Table 2-3 Cu(In,Ga)Se$_2$ diode parameters determined by analysis of the J-V data. An asterisk indicates that the parameters could not be determined (see text).

	dark				illuminated		
E_g (eV)	G (mS/cm^2)	R_s (Ω-cm^2)	J_o (mA/cm^2)	A	R_s (Ω-cm^2)	J_o (mA/cm^2)	A
1.16	0.4	0.1	$1x10^{-5}$	1.6	0.1	$3x10^{-5}$	1.7
1.18	1.1	0.5	$2x10^{-5}$	1.7	0.3	$4x10^{-5}$	1.7
1.21	0.2	0.2	$5x10^{-6}$	1.7	0.2	$2x10^{-5}$	1.8
1.23	0.1	0.1	$2x10^{-6}$	1.6	0.1	$1x10^{-5}$	1.7
1.27	0.8	0.1	$4x10^{-6}$	1.8	0.1	$5x10^{-6}$	1.7
1.34	1.1	0.2	$2x10^{-7}$	1.6	*	*	*
1.37	0.2	0.1	$3x10^{-6}$	1.9	*	*	*
1.47	0.2	0.3	$4x10^{-7}$	1.8	*	*	*
1.54	0.1	0.2	$5x10^{-7}$	1.9	*	*	*

Analysis of the J–V and QE results show that the Cu(In,Ga)Se$_2$ solar cells are well behaved, i.e. the J-V results can be described by the standard diode equation (Equation 2-1), only for $E_g < 1.3$ eV. The dominant additional effect with higher bandgap is the voltage dependent current collection. This suggests that the minority carrier diffusion length is small in these devices so light generated carrier collection is primarily dependent on the space-charge width in the Cu(In,Ga)Se$_2$ which in turn depends on the applied voltage [224].

Other changes in the Cu(In,Ga)Se$_2$ with increasing Ga content have been suggested which might effect the cell behavior. These include a change in the forward current recombination mechanism [213] and changes in the electrical characteristics of a Cu-deficient surface layer [220, 225]. The voltage dependent collection prevents the fundamental diode parameters A and J_O from being determined by standard methods of J-V analysis for the data measured under illumination. Other methods for more complete diode characterization are needed [226].

In summary, solar cell results have been presented with Cu(In,Ga)Se_2 layers having bandgap from 1.16 to 1.54 eV with no grading of the Ga content in the absorber layers. There were no changes in the Cu(In,Ga)Se_2 deposition other than the relative amounts of In and Ga, or in any of the device fabrication steps and no change in the structure or morphology as the Ga content increased. The solar cells have ~15% efficiency with $x < 0.5$ or $E_g < 1.3$eV. V_{oc} increases over the entire bandgap range up to 821 mV but the cell efficiency falls off as E_g increases above 1.3 eV. Analysis of the J-V and QE data shows that this is attributable primarily to a voltage dependent current collection which results in a decrease in FF and J_{sc}.

2.2.6 Cell Results With Graded Cu(In,Ga)Se_2

The minority carrier current collection can occur by two different mechanisms, diffusion and field-assisted collection. Cu(In,Ga)Se_2 absorbers were fabricated to determine whether the minority carrier collection could be improved by grading the conduction band to build in additional field. This could be done with a gradient in Ga content, decreasing from the Mo contact to the Cu(In,Ga)Se_2/CdS junction [210].

To grade the Ga content, a 25 or 50 nm thick Ga layer was deposited by sputtering on the glass/Mo substrate. These were placed in the evaporator alongside the standard glass/Mo substrates for the Cu(In,Ga)Se_2 depositions that produced the films with E_g = 1.34, 1.47, and 1.54 eV. EDS measurements showed a small increase in x of ~0.02 with the 25 nm Ga layer and XRD measurements showed some asymmetrical broadening of the Cu(In,Ga)Se_2 peaks indicating that the Ga was non-uniformly incorporated through the film.

The basic device parameters are compared with and without the thin Ga layers in Table 2-4. In each case, there is an increase in FF suggesting that the current collection was improved. There is also a drop in J_{sc} and small increase in V_{oc} which may be partly due to a bandgap increase. While this Ga grading has not resulted in an increased efficiency of these high bandgap devices, the results do suggest that the loss in FF due to the voltage dependent collection can be partly recovered. More controllable methods of grading the Ga content may improve device performance.

Table 2-4 Comparison of device parameters with Cu(In,Ga)Se_2 layers deposited on Mo/Ga layers.

E_g (%)	Ga layer (nm)	V_{oc} (mV)	J_{sc} (mA/cm^2)	FF (%)	η (%)
1.34	0	729	27.6	70.9	14.3
	50	767	22.0	76.0	12.8
1.47	0	804	20.7	69.0	11.5
	25	810	15.9	71.7	9.3
1.54	0	821	16.8	63.7	8.8
	24	825	13.9	67.8	7.7

2.3 SELENIZATION OF Cu-Ga-In PRECURSORS

2.3.1 Introduction

Cu-Ga-In precursors reacted in a selenium containing atmosphere in the temperature range 400°C–500°C contain a mixture of $CuInSe_2$ and $CuGaSe_2$ phases instead of the desired single phase $Cu(GaIn)Se_2$ [227]. From X-ray diffraction and Auger analysis, the mixed phase films form a layered structure with the $CuInSe_2$ phase near the surface and the $CuGaSe_2$ phase near the Mo/film interface. Annealing of these films in the temperature range 500°C–600°C in an inert atmosphere for a duration of 60 to 90 minutes converts the multiphase structure in the film to a single phase $Cu(In,Ga)Se_2$. In this section, solar cells made with the multiphase films are shown to have properties similar to $CuInSe_2$ devices while cells made with the annealed single phase films behave like $Cu(In,Ga)Se_2$ devices with the bandgap expected for the precursor composition. Additionally, preliminary results are presented of experiments to determine the diffusion coefficient of In in $CuGaSe_2$, Ga in $CuInSe_2$ and the interdiffusion coefficients of In and Ga in a $CuGaSe_2/CuInSe_2$ diffusion couple.

2.3.2 Experimental Procedures

Metal precursor films were deposited in the sequence Cu-Ga-In at room temperature onto Mo coated soda lime glass substrates by DC magnetron sputtering 1. The Cu thickness was chosen to be 250 nm and the thicknesses of Ga and In layers were adjusted to yield a Cu/(In+Ga) ratio of approximately 0.9. Precursor films with Ga/(Ga+In) ratios of 0, 0.25, 0.5, 0.75, and 1.0 were prepared.

The films were selenized in a flowing $H_2Se/Ar/O_2$ mixture for 90 minutes after a 10 min ramp to the chosen substrate temperature [228]. A substrate temperature of 410°C was used with the Cu-In precursor while the films containing Ga were reacted at 450°C. Post-reaction heat treatments for 60–90 minutes were carried out in-situ in an Ar atmosphere at 500°C and 600°C for the films with different Ga/(Ga+In) ratios, followed by a second exposure to the gas mixture containing H_2Se to compensate a possible Se loss at the films surface. The structure of the absorber layers was examined by X-ray diffraction (XRD) and their composition was determined by energy dispersive X-ray spectroscopy (EDS) and Auger depth profiles.

$Cu(In,Ga)Se_2/CdS$ solar cells were completed on the absorber layers using the processes described in section 2.2.4. No anti-reflection coatings were used. The solar cells were characterized by current-voltage and spectral response measurements. Estimations of the parameters of minority carrier transport and the bandgap of the absorber were derived from the long wavelength cut-off of the spectral response [229]. Capacitance was measured with a 100 kHz/50 mV excitation under ambient light.

For the diffusion experiments, $CuGaSe_2$ films were coated with an In layer with thickness ~1000 Å. These films were annealed at different temperatures ranging from 400°C to 600°C for 30 minutes in an Argon atmosphere. The $CuGaSe_2/CuInSe_2$ diffusion couple was prepared by first reacting Cu-Ga films to form a $CuGaSe_2$ layer, onto which Cu and In layers, with $Cu/In \approx 0.9$, were sputter-deposited sequentially, followed by reaction in H_2Se to a form a $CuInSe_2$ layer. The desired film thicknesses of $CuInSe_2$ and $CuGaSe_2$ were approximately 2μm each. The diffusion couple was annealed at 650°C for 30 minutes in an Ar atmosphere. The concentration profiles in the above samples were determined by AES depth profiling. Depth profiles of a $CuGaSe_2/In$ sample and a $CuGaSe_2/CuInSe_2$ sample which did not undergo any annealing treatment were also measured.

2.3.3 Selenization Results

The selenization of Cu-In and Cu-Ga precursor films resulted in single phase $CuInSe_2$ and $CuGaSe_2$, respectively. However, the selenization of the Cu-Ga-In precursors resulted in a film containing $CuInSe_2$ and $CuGaSe_2$ with little intermixing. The XRD spectrum of the (220) and (204) reflections from the film with Ga/(In+Ga) ≈ 0.5 is shown in Figure 2-13. The as-selenized film showed distinct peaks corresponding to phases close to $CuInSe_2$ and $CuGaSe_2$. Even though $CuInSe_2$ and $CuGaSe_2$ are miscible at all concentrations, there is little $Cu(In,Ga)Se_2$ evident in the spectrum. The Auger depth profile of this film, shown in Figure 2-14, indicates that the film had a layered structure with $CuGaSe_2$ near the back and $CuInSe_2$ at the surface.

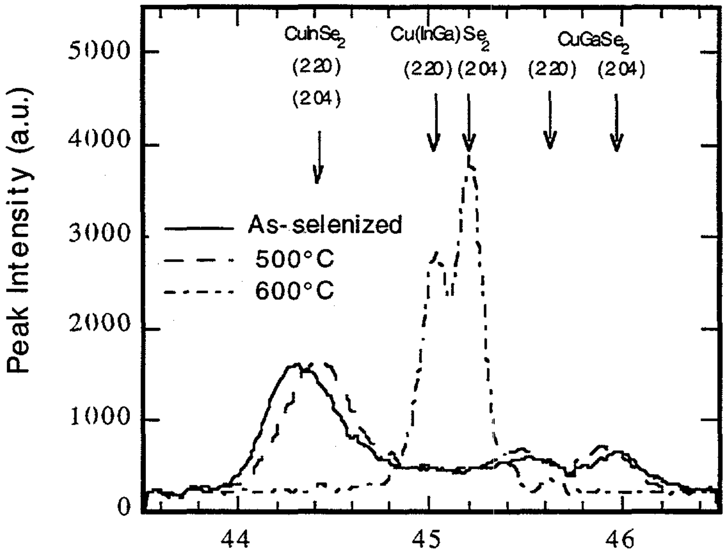

Figure 2-13 X-ray diffraction spectra of (220) and (204) reflections of as-selenized and heat treated $Cu(In,Ga)Se_2$ films with Ga/(Ga+In) ≈ 0.5.

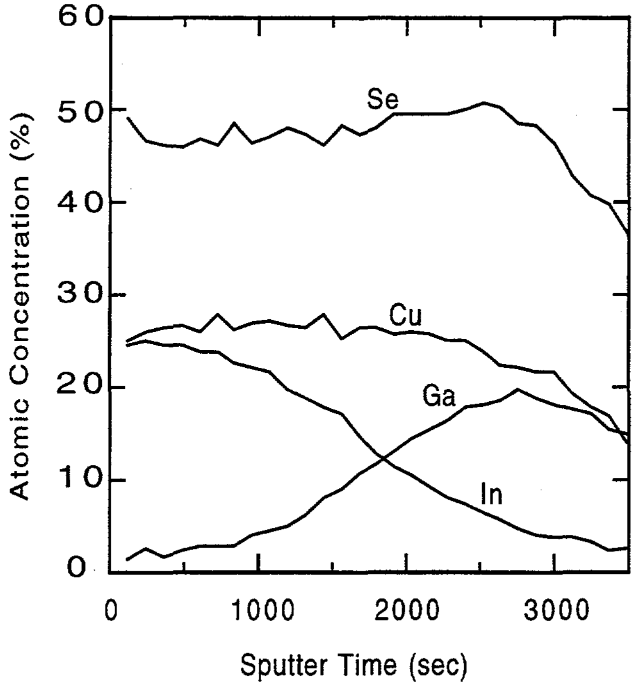

Figure 2-14 Auger depth profile of an as-selenized Cu(In,Ga)Se_2 film with a Ga/(Ga+In) ≈ 0.5.

XRD spectra after the in-situ Ar atmosphere anneals at 500°C and 600°C are also shown in Figure 2-13. After the 500°C anneal, the film still retained the two-phase structure of the as-selenized film. The 600°C anneal, however, converted the film to single phase Cu(In,Ga)Se_2. The Auger depth profile in this case is shown in Figure 2-15 and confirms that the Ga and In are more homogeneously distributed. Similar behavior was observed for the films with Ga/(In+Ga) ≈ 0.25. However, the film with Ga/(In+Ga) ≈ 0.75 was converted to single phase after the 500°C anneal. Since the homogenization occurred at a lower temperature, it is assumed that inter-diffusion of In and Ga is faster in films with greater Ga content.

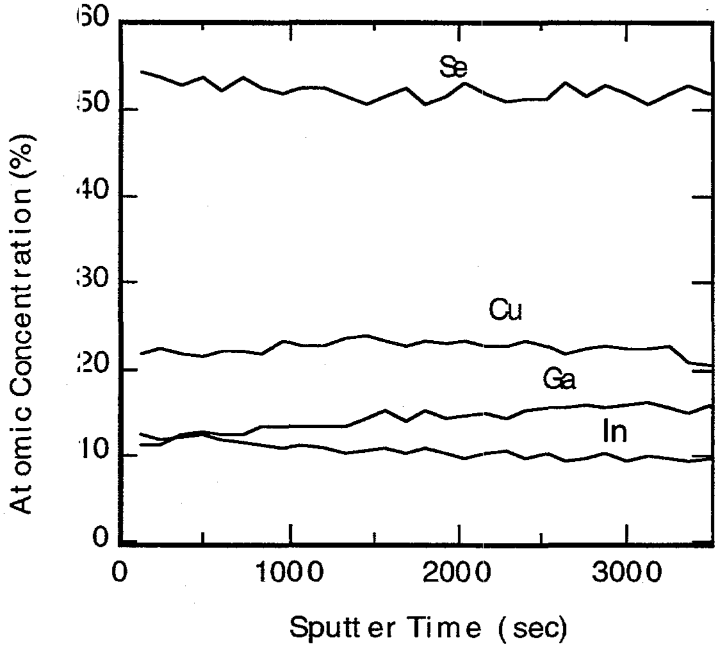

Figure 2-15. Auger depth profile of an annealed (60 minutes, 600°C in Ar) $Cu(In,Ga)Se_2$ film, with a Ga/(Ga+In) ≈ 0.5.

Device results for the solar cells made from films with the different Ga contents and anneal conditions are listed in Table 2-5. Spectral response plots for the as-selenized and annealed films with Ga/(In+Ga) ≈ 0.5 are shown in Figure 2-16. The open circuit voltage and long wavelength cut-off of the spectral response of the as-selenized multi-phase absorbers are similar to $CuInSe_2$ cells. The photovoltaic response is controlled by the more In-rich, lower bandgap phase close to the heterojunction. The second phase is separated from the active layer of the device and does not deteriorate the cell performance. Devices with the annealed single-phase films have increased V_{OC} and a shift in the spectral response cut-off consistent with the expected Ga/(In+Ga) for these films. Evaluation of the spectral response and capacitance for all cells suggests a narrow field zone and a good diffusion length of 0.6–1 μm. The long wavelength spectral response can be described with good accuracy by assuming a constant, direct bandgap, i.e., there is no indication for a graded bandgap.

Table 2-5 Cell results from selenized Cu-Ga-In precursors with different Ga content.

x	Anneal (°C)	Structure	Cu (at.%)	In (at.%)	Ga (at.%)	Se (at.%)	V_{OC} (V)	J_{SC} (mA/cm^2)	FF (%)	Eff (%)
0	-	$CuInSe_2$	23.9	25.0	-	51.1	0.44	39	66	11.2
0.25	-	multi-phase	22.3	14.0	2.9	50.8	0.46	39	58	10.4
0.25	500	multi-phase	22.7	22.5	2.6	52.2	0.45	38	68	11.5
0.25	600	single-phase	22.3	18.6	5.9	53.2	0.56	34	67	12.9
0.50	-	multi-phase	22.4	18.9	7.9	50.8	0.53	38	64	13.1
0.50	500	multi-phase	22.4	18.3	8.9	50.4	0.54	35	66	12.5
0.50	600	single-phase	22.3	12.8	13.2	51.7	0.59	30	60	10.5
0.75	600	single-phase	21.6	7.0	19.0	52.4	0.63	22	46	6.4

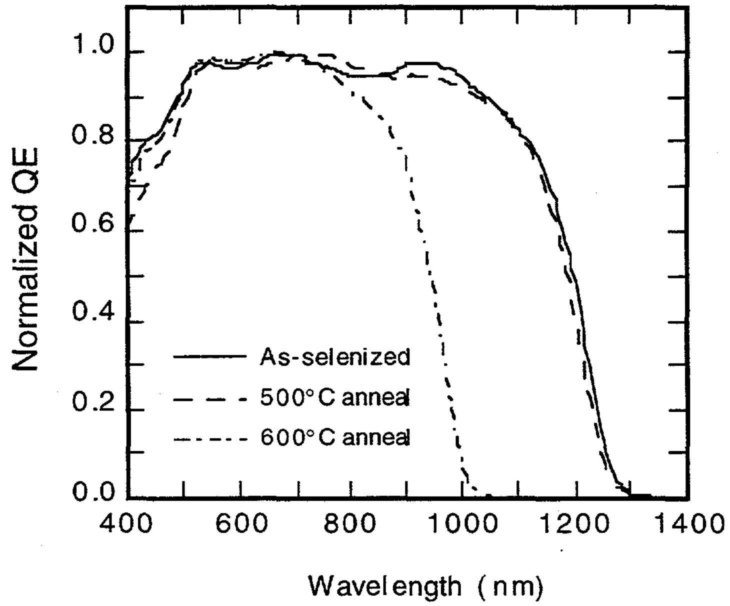

Figure 2-16 Spectral response of devices made from an as-selenized and heat treated $Cu(In,Ga)Se_2$ film with $Ga/(Ga+In) \approx 0.5$.

To summarize, absorber films prepared by selenization of Cu-Ga-In precursor layers with H_2Se are inhomogeneous with a layered structure containing two phases with compositions close to $CuInSe_2$ and $CuGaSe_2$. Cell results and spectral response measurements are consistent with the In-rich phase at the top of the film and exhibit a comparable or better performance than cells based on single phase $CuInSe_2$. An in-situ anneal in Ar, immediately after the selenization, is shown to create homogeneous, single phase films, even at high Ga-content. Material and device measurements show that these films contain the same Ga/(In+Ga) composition as the starting precursors.

2.3.4 Experimental Results

Interdiffusion of In and Ga appears to be responsible for this homogenization process of mixed-phase, as reacted $Cu(In,Ga)Se_2$ films. Walter and Schock reported that interdiffusion of In and Ga was greatly enhanced in the presence of the copper selenide phase in copper rich $CuInSe_2/CuGaSe_2$ films [230]. Thus, all the $CuGaSe_2$, $CuInSe_2$ films used for the diffusion experiments were prepared copper poor to avoid the formation of a copper selenide phase. SEM, EDS, XRD, and AES measurements have been completed on samples of In on $CuGaSe_2$, Ga on $CuInSe_2$, and $CuGaSe_2/CuInSe_2$ diffusion couples. These results are analyzed in 2.3.5 to determine the diffusion coefficients. The Auger profiles for In in $CuGaSe_2$ in the unannealed and annealed samples are shown in Figure 2-17. The concentration profiles of In and Ga for the unannealed sample and the annealed sample are shown in Figure 2-18. This data will be analyzed to determine the diffusion coefficients. The measurements made for Ga on $CuInSe_2$ gave unexpected results; after heat treatment, a multi-phase structure was formed consisting of InSe and $Cu(In,Ga)Se_2$. Additional experiments are underway to understand the results.

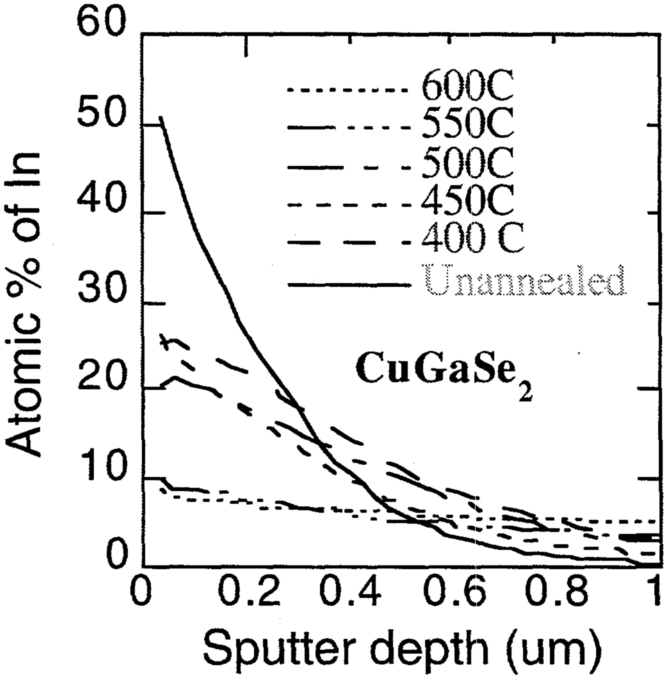

Figure 2-17 Depth profiles of In in $CuGaSe_2$

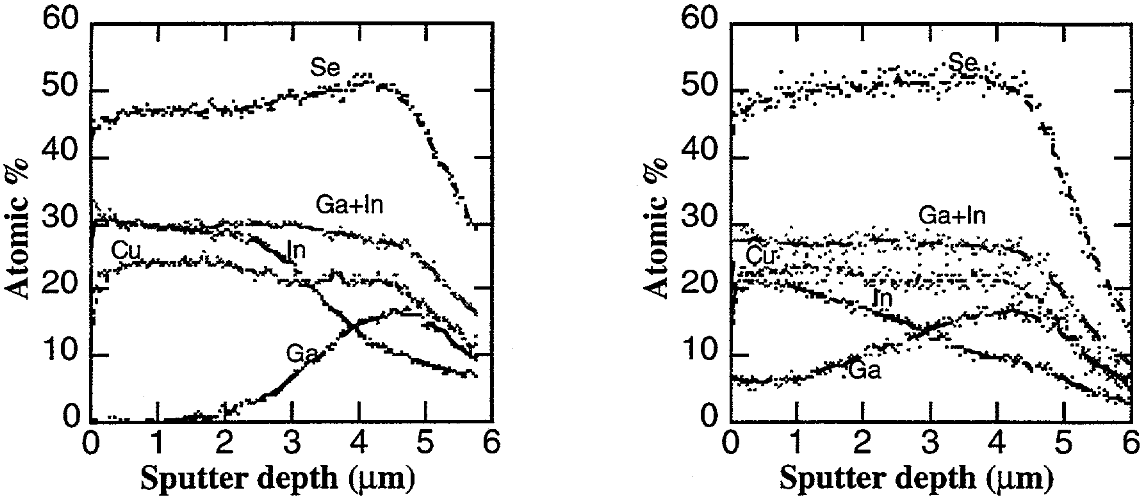

(a) (b)

Figure 2-18. Concentration profiles of Cu, In, Ga and Se in $CuGaSe_2/CuInSe_2$ diffusion couples: (a) initial distribution, (b) after annealing at 650°C for 30 min.

2.3.5 Determination of Diffusion Coefficients

The following assumptions were made in determining the diffusion coefficients (D):

1) The diffusion coefficients are independent of the concentration. However, D could depend on the extent of the deviation from the ideal stoichiometry of the $CuInSe_2$ and $CuGaSe_2$ films.

2) The diffusion of In and Ga is planar. This is a valid assumption because the concentration gradients of In and Ga are present only in one direction, i.e., in the direction of the thickness of $CuInSe_2$ and $CuGaSe_2$ films.

3) Lattice diffusion is the dominant mechanism near the In/$CuGaSe_2$ interface and the $CuInSe_2/CuGaSe_2$ interface. The grain sizes in the $CuInSe_2$ and the $CuGaSe_2$ films used in this work are in the range of 1 - 2 μm.

4) The $CuInSe_2$ and $CuGaSe_2$ films provide a semi-infinite medium for the diffusion of In and Ga.

Fick's second law of diffusion for one-dimensional, atomic diffusion is,

$$\frac{\partial C}{\partial t} = D\frac{\partial^2 C}{\partial x^2}$$

Equation 2-5

where the diffusion coefficient is assumed to be independent of concentration. The composition(C) in Equation 2-5 is a function of x and t, where x is the direction of diffusion and t is the time.

The solution to Fick's second law (Equation 2-6) for the diffusion couple, i.e., for the case of two semi-infinite layers, is an error function,

$$C(x,t) = A - B\ \mathrm{erf}\left(\frac{x}{2(Dt)^{1/2}}\right)$$

Equation 2-6

where, A and B are constants to be determined from the boundary conditions. The diffusivities, independent of concentration, are calculated from the slopes(G_t) of the

Ga(or In) profile at the $CuGaSe_2/CuInSe_2$ interface x=0, is given by: $G_t=(\pi Dt)^{-1/2}$. However, since the slope of the Ga(or In) profile in the unannealed sample is non-zero the diffusion coefficient is calculated from $D = (G_t^{-2} - G_o^{-2})/\pi t$, where G_O is the slope of the Ga(or In) profile at the interface in the unannealed sample.

For the case of thin film source diffusion into a semi-infinite slab ($In/CuGaSe_2/Mo$), the solution to Fick's second law is given by [231],

$$C(x,t) = \frac{1}{2(\pi Dt)^{1/2}} \int_0^\infty f(x')e^{-(x-x')^2/4Dt}dx'$$

Equation 2-7

where, f(x') is the initial distribution (no annealing) of the In source in $CuGaSe_2$. The initial distribution f(x') was fit to $f(x') = Ae^{-bx'^2}$. The diffusion coefficient was determined from the slope of the plot of ln(C) vs. x^2; slope = -b/(4Dtb+1). Only the concentration of In within the first 1 μm from the surface of $CuGaSe_2$ was analyzed to exclude grain boundary diffusion effects which may occur away from the surface.

2.3.6 Results and Discussion

The concentration profiles of In and Ga for the unannealed sample and the annealed sample are shown in Figure 2-18. The interdiffusion coefficients of Ga and In for the interdiffusion of In and Ga in the $CuGaSe_2/CuInSe_2$ couple were calculated as:

$D_{In} = 1.5 \times 10^{-11}$ cm^2/sec at 650°C

$D_{Ga} = 4.0 \times 10^{-11}$ cm^2/sec at 550°C

The experimental error in the interdiffusion coefficients was estimated to be within half-an-order of magnitude. Within this experimental error, the magnitude of interdiffusion coefficients of In and Ga are similar.

2.4 Mo/CuInSe$_2$ CONTACT

2.4.1 Introduction

The Mo layer in a typical $Cu(In,Ga)Se_2$ solar cell configuration can have a significant effect on the adhesion of the $Cu(In,Ga)Se_2$ film, structure of the $Cu(In,Ga)Se_2$ as it grows in the Mo layer, and on the electrical characteristics of the back contact. In this work, the glass/Mo/Cu(In,Ga)Se_2 adhesion did not present any problems, particularly with evaporated absorber films, if the stress in the Mo film was minimized by controlling the sputter pressure during deposition [219].

Many high efficiency $CuInSe_2$ based solar cells have shown blocking or non-ohmic contact behavior in their current-voltage (J-V) characteristic [221, 232, 233]. This "roll-over" of the J-V curve in forward voltage bias is seen at normal operating temperatures in some devices, but is more common and more pronounced at reduced temperatures. The shape of this roll-over behavior in the J-V curve and the temperature at which it appears depend on the processing and electronic properties of the $CuInSe_2$. In many cases this affects the J-V curve in the power quadrant, reducing the fill factor. However, it has been shown that the parasitic J-V behavior does not have any effect on the open circuit voltage of the device [233] and is therefore assumed to occur in series with the primary diode. Because of these properties, the blocking behavior has been attributed to the Mo/$CuInSe_2$ back contact. Measurements of the Mo contact to single crystal $CuInSe_2$ showed that the contact behavior depended on the defect state concentration of the $CuInSe_2$ [234]. However, there has also been evidence that the blocking behavior can be light-dependent [221] and may specifically depend on the deposition of the CdS or ZnO layers [235]. In this case, the behavior may originate at one of the interfaces between the ZnO, CdS, and $CuInSe_2$. Numerical modeling has shown that the qualitative features of the blocking behavior could be simulated by a non-ohmic Mo/$CuInSe_2$ contact or changes in the electrical properties of the $CuInSe_2$/CdS junction [236].

In this report, a novel device configuration is presented which has allowed the Mo/$CuInSe_2$ junction to be analyzed separately from the rest of the operating solar cell. Direct measurements of the contact have been completed on a device which shows a non-ohmic blocking contact in its J-V behavior. The results show that the non-ohmic behavior does not occur at the Mo/$CuInSe_2$ contact.

The effect of the Mo layer on the Cu(In,Ga)Se_2 structure has been characterized with respect to the effect of the Mo relative crystal orientation on the subsequent growth of Cu(In,Ga)Se_2. A correlation was found between the relative orientation of the Mo and Cu(In,Ga)Se_2 films, as measured by XRD. However, unlike the composition of the Cu(In,Ga)Se_2 film, the orientation of the evaporated Cu(In,Ga)Se_2 shows no correlation to the device results.

2.4.2 Mo Contact Experiment

The $CuInSe_2$ in this work was formed by the selenization of Cu/In precursor layers in a H_2Se atmosphere [228]. The Mo was deposited by sputtering, the CdS by chemical bath deposition, and the ZnO by rf sputtering as described in section 2.2.2.

The direct measure of the back contact J-V behavior requires that the $CuInSe_2$ is deposited across a gap in the Mo back contact. A schematic of the configuration is shown in Figure 2-19. The Mo has been prepared either by laser scribing the Mo or depositing the Mo through a mask. After CdS, ZnO, and Ni contacts are deposited, solar cells are defined by photolithography so the cells are isolated with the Mo gap between the cells. With the Mo deposited through a mask, the Mo gap is 1 mm wide. The cells have an 8 mm^2 area.

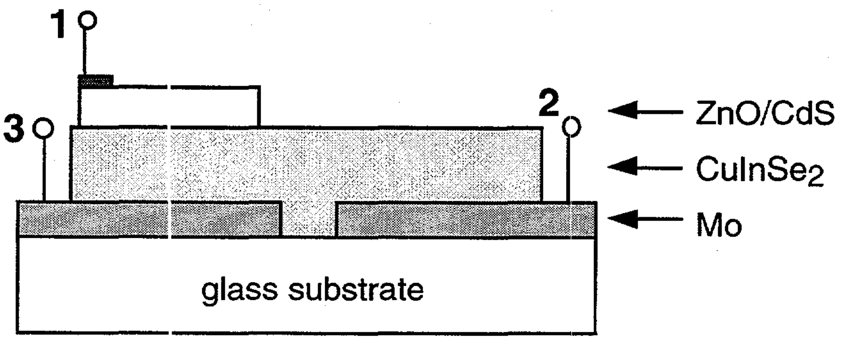

Figure 2-19. Schematic of the device structure with a gap in the Mo film.

This configuration allows a secondary Mo contact to be electrically connected to the CuInSe$_2$, but isolated from the primary Mo/CuInSe$_2$ contact. With only a high impedance voltmeter connected, there is no current flow through the secondary Mo contact.

An equivalent circuit is shown in Figure 2-20. Both the front and back contacts are shown with a resistor and blocking diode because it is not known *a priori* which is the appropriate equivalent circuit representation. The objective of this work is to determine in which case the diode occurs. A similar configuration was used to separate bulk and contact resistance in a-Si solar cells [237].

In the normal cell configuration both the current and voltage are measured between points 1 and 3, $J_{1\text{-}3}$ and $V_{1\text{-}3}$ respectively. To separate the Mo/CuInSe$_2$ back contact, the voltage drop is measured across points 2 and 3 ($V_{2\text{-}3}$), i.e. between the two adjacent Mo contacts, while the current is still measured in the normal device configuration between points 1 and 3. The only junction at which there will be any current and, therefore, a measured voltage drop will be the back contact of the operating solar cell. Similarly, with the standard current from 1 to 3 the voltage drop across the CuInSe$_2$/CdS/ZnO is isolated by measuring $V_{1\text{-}2}$. In this case, any voltage drop across the Mo/CuInSe$_2$ contact is removed from the measurement.

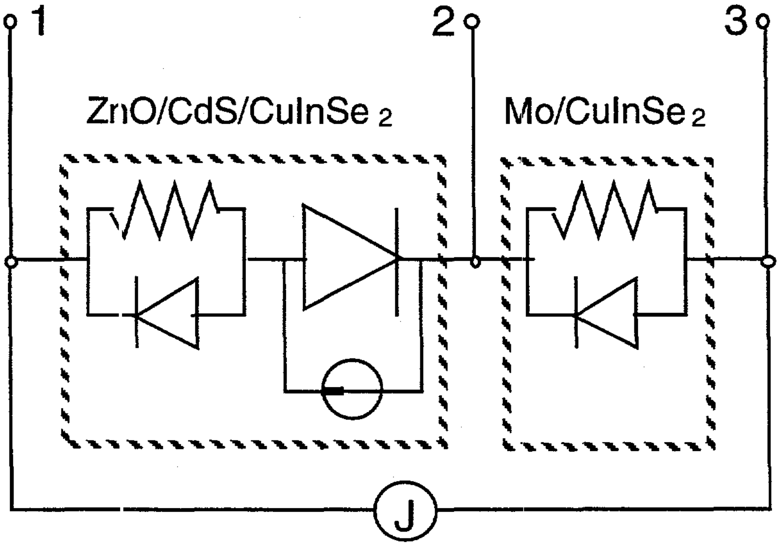

Figure 2-20 Equivalent circuit of the device configuration. Both the front and back contacts are shown with a resistor and blocking diode

2.4.3 Mo Contact Results

This method has been applied to a $CuInSe_2$ device with $V_{OC} = 0.48V$, $J_{SC} = 34\ mA/cm^2$, FF = 66%, and efficiency = 10.7% when measured at 25°C under AM1.5 illumination with the standard configuration with $V_{1\text{-}3}$. J-V curves in the standard configuration at 25°C and -70°C are shown in Figure 2-21.

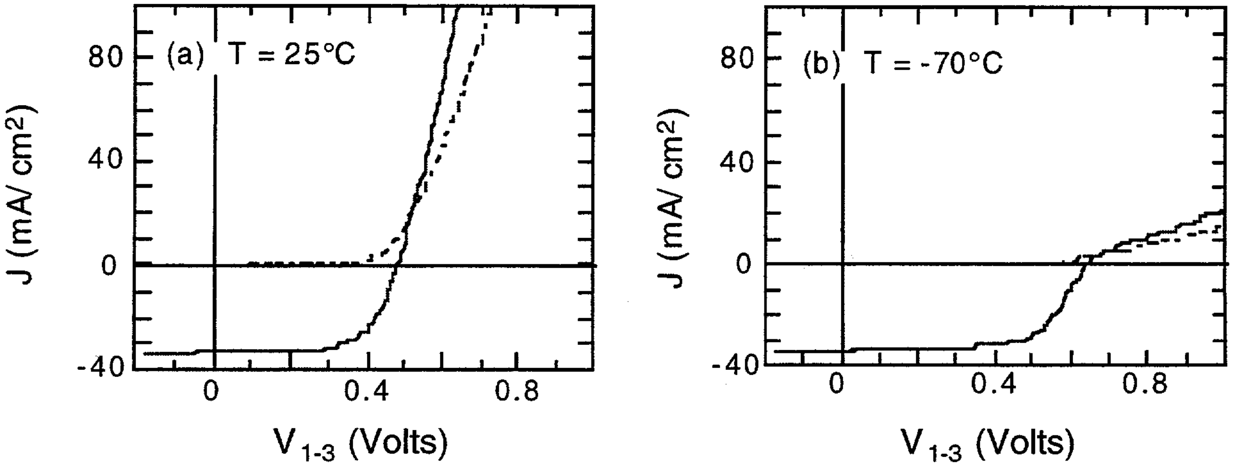

Figure 2-21 J-V characteristics with the voltage drop across the complete solar cell both in the dark and under ~100 mW/cm^2 illumination. At T = -70°C the J-V curves show strong blocking behavior for V > V_{oc}.

The voltage drop across the $CuInSe_2/CdS/ZnO$ is shown at the same temperatures in Figure 2-22. There is no significant difference between these measurements, in which the Mo contact has been electrically removed from the circuit, and the curves for the complete device in Figure 2-21.

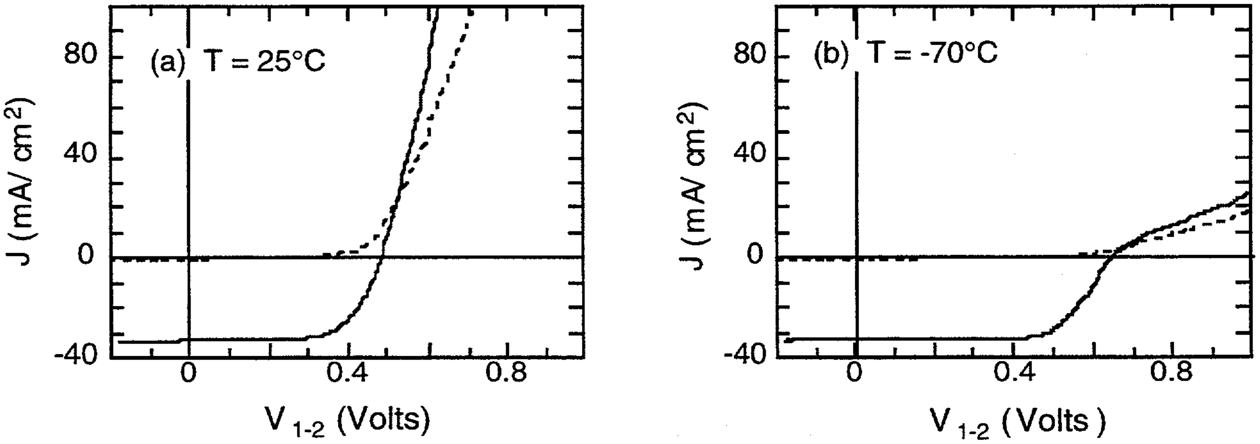

Figure 2-22 J-V characteristics with the voltage drop across the $CuInSe_2/CdS/ZnO$ for (a) T = 25°C, and (b) T = -70°C

Finally, the voltage drop across the $Mo/CuInSe_2$ is shown in Figure 2-23 on a greatly expanded voltage scale. The contact is ohmic at 25°C and remains ohmic at low temperature. The voltage offset seen at J=0 is within the instrumental limit of ± 1 mV for the zero. The resistance, 21 mΩ-cm^2 at T = 25°C and 18 mΩ-cm^2 at T = -70°C, can be taken as an upper limit to the Mo/CuInSe$_2$ contact resistance. The total series resistance, R_s, of the complete cell measurement at T = 25°C in Figure 2-21 was determined from the intercept of dV/dJ plotted versus $1/(J+J_{sc})$. This gave R_S = 1.8 Ω-cm^2 in the dark and 0.9 Ω-cm^2 under illumination. Thus, the Mo/CuInSe$_2$ resistance makes a negligible contribution to the total series resistance of the device. These results show that the parasitic blocking behavior does not occur at the Mo/CuInSe$_2$ contact.

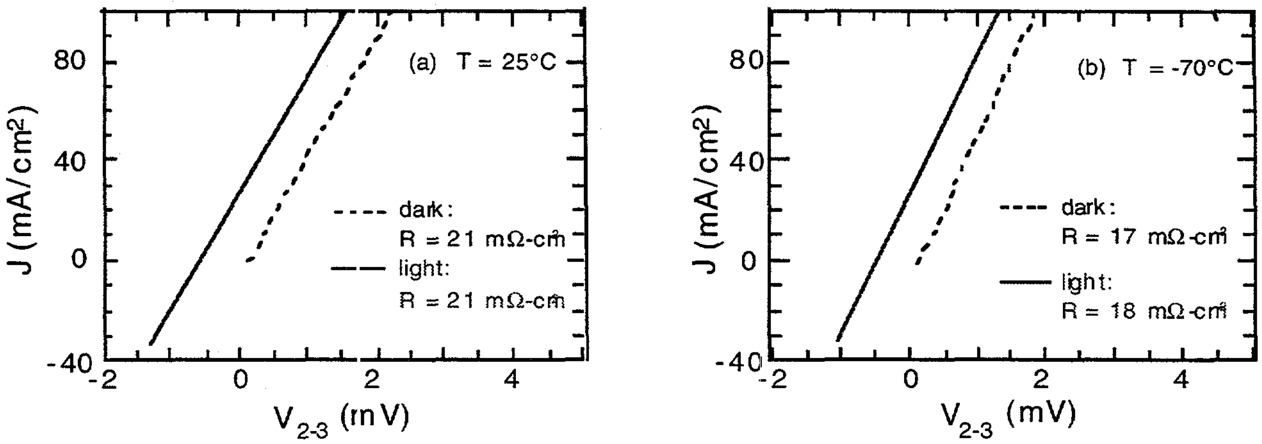

Figure 2-23. J-V characteristics with the voltage drop across the Mo/CuInSe$_2$ for (a) T = 25°C, and (b) T = -70°C

2.4.4 Discussion and Conclusions

The non-exponential or blocking I-V behavior has been shown not to occur at the Mo/CuInSe$_2$ interface, so other possibilities must be considered. Previous experimental results [221, 232, 238] show that similar non-exponential or "blocking" I-V characteristics occur on devices that were made with no ZnO layer contacting the CdS. Assuming compositionally uniform materials, this leaves the CdS/CuInSe$_2$ interface as the most likely candidate responsible for this effect. Simple numerical simulations using the ADEPT program and assuming a simple n-type CdS/p-type CuInSe$_2$ abrupt interface have been able to reproduce both the overall shape and temperature dependence of the non-exponential or "blocking" I-V behavior by making the electron affinity of the CdS about 0.4 eV less than that of the CuInSe$_2$ [236]. This would also imply changes in this type of behavior when the electron affinity of the CuInSe$_2$ is modified by alloying with either Ga or S. Now that a structure has been made to electrically separate the back contact from the junction, these changes can be verified.

In conclusion, a configuration was demonstrated which enables the front and back contacts of an operating CuInSe$_2$ solar cell to be separated. With this configuration, it was shown that the Mo/CuInSe$_2$ contact is ohmic even when the complete solar cells shows blocking behavior often seen in the J-V curves. The Mo/CuInSe$_2$ contact resistance is negligible compared to the total series resistance of the cell.

2.4.5 Mo/Cu(In,Ga)Se$_2$ Orientation

The effect of the relative orientation of the Mo and Cu(In,Ga)Se$_2$ films, as measured by XRD, and its correlation to device performance has been evaluated. Cu(In,Ga)Se$_2$ films with x = 0.3 were deposited by evaporation on two different Mo films in a single deposition. The Mo films were deposited in different sputtering systems but both were 1 μm thick with sheet resistance 0.2 Ω/sq. The primary difference in the depositions was that one film was deposited in about 60 layers on a rotating substrate while the other was deposited in a single layer on a stationary substrate.

The orientations of the Mo and Cu(In,Ga)Se_2 films are characterized by the two strongest peaks for each in Table 2-6 and compared to the JCPDS powder diffraction standards. The multi-layer Mo film is more strongly oriented than the single layer film. The Cu(In,Ga)Se_2 film deposited on the more oriented Mo film is nearly randomly oriented with I(112)/I(220) comparable to the powder standard. However, the Cu(In,Ga)Se_2 film deposited on the less oriented Mo has a strong (112) orientation with I(112)/I(220) more than 2 orders of magnitude greater. SIMS profiles of these films showed that they have comparable levels of Na impurities which had diffused from the glass.

J-V parameters for devices made from these films are listed in Table 2-7. Despite the difference in the film orientation, the device results are nearly identical. This demonstrates that the orientation of the Cu(In,Ga)Se_2 does not play a significant role in the device performance and suggests that electronic transport in the Cu(In,Ga)Se_2 layer is anisotropic.

Table 2-6. XRD peak intensities, I, for Cu(In,Ga)Se_2 and Mo films from a single evaporation run. The JCPDS powder diffraction standards are listed for comparison.

	multi-layer Mo	single layer Mo	JCPDS
	Mo peak intensities		
I(110)	100	100	100
I(211)	1.3	6.2	39
I(110)/I(211)	79	16	2.6
	Cu(In,Ga)Se_2 peak intensities		
I(112)	100	100	100
I(220)	78	0.46	40
I(112)/I(220)	1.3	217	2.5

Table 2-7 Device parameters with Cu(In,Ga)Se_2 deposited on different Mo films.

	V_{oc} (mV)	J_{sc} (mA/cm^2)	FF (%)	η (%)
multi-layer Mo	646	31	72	14.5
single layer Mo	635	32	70	14.4

3. AMORPHOUS SILICON

3.1 SUMMARY

3.1.1 Devices

Midway through this contract, it was determined that the operational characteristics of the single chamber plasma CVD reactor was limiting further improvements in device performance beyond the 8% efficiency level. It was found through QE measurements and SIMS analysis that there was significant dopant carryover from one run to the next from the film deposited on the "hot" electrode. Deposition of a burying layer of a-SiC:H between device runs was found to be necessary to remedy the dopant carryover. As a result, FFs in excess of 71% and efficiencies around 9% were obtained reproducibly. In a second step, H_2 diluted μc n-layers, compatible with ZnO/Ag back contact as well as with tunnel junction in tandem devices, were developed. These μc n-layers with conductivities and activation energies of 1 S/cm and 0.05 eV, respectively, allowed fabrication of devices with ZnO/Ag contact with FFs as high as 72% and efficiencies around 10%.

The ungraded i-layers were about 0.5 μm thick. The buffer layer had a standard graded C profile. Devices were deposited on Asahi Type U textured SnO_2, with ZnO/Ag back contacts, and had no AR coating. All cells were scribed and surrounded by Ag paste to reduce R_S and increase FF. Pieces were sputter etched to eliminate excessive collection beyond the metal contact.

Five cells from three different pieces were tested at NREL, all having efficiencies of 10% or greater. The results of these tests are shown in Table 3-1 below for one cell from each piece tested at NREL.

Table 3-1 Initial J-V parameters for three cells (areas=0.396 cm^2) measured at NREL @100 mW/cm^2 AM1.5 global illumination and 25 °C

Cell ID	V_{OC} (Volts)	J_{SC} (mA/cm^2)	FF (%)	Eff. (%)
4659-21-3	0.871	16.13	71.7	10.1
4664-21-4	0.881	15.78	72.6	10.1
4666-21-4	0.905	16.16	68.5	10.0

3.1.2 TCO's and Optical Enhancement

The material properties of a number of textured SnO_2 and ZnO substrates and their effect on current generation in a-Si were evaluated [301]. Most of these TCOs have been used by others for a-Si device research or module fabrication. Bulk optoelectronic and structural properties are reported for seven TCO films with haze from 1 to 14%. Our results show that increasing haze above ~5% has limited effectiveness for increasing the generation at long wavelengths. In presently available textured ZnO, current generation is about 0.6 mA/cm^2 greater than in textured SnO_2. There may be greater advantages to using ZnO in multijunction devices since much thinner i-layers may be used to give the same J_{SC} with improved stability, shorter deposition time and less GeH_4 usage.

The effect of sputtered transparent conducting oxide (TCO) contacts on the device performance of stainless steel/n-i-p/TCO and glass/SnO_2/p-i-n/TCO/Ag solar cells were investigated [302]. TCO materials ITO and ZnO are compared, and found to have very similar transparency at the same sheet resistance. Sputtering ZnO with O_2 in the Ar reduces FF for stainless steel /n-i-p/ZnO devices, compared to sputtering without O_2. This is attributed to an interface not bulk effect. Sputtering ITO with O_2 on the same devices increases J_{SC} due to higher ITO transparency, compared to sputtering without O_2, but has no effect on FF. Based on curvature in the J-V curve around V_{OC}, the ZnO/p layer contact appears to be non-ohmic. For p-i-n/TCO/Ag devices, μc-Si n-layers have much higher V_{OC}, J_{SC}, and FF for all variations of TCO/Ag back reflectors compared to an a-Si n-layer. Devices with ITO/Ag have lower V_{OC} and J_{SC} compared to devices with ZnO/Ag. Sputtering ZnO with O_2 has no detrimental effect on devices with μc-Si n-layers but severely reduces FF in devices with a-Si n-layers.

A novel device structure was used to study optical enhancement and back reflectors (BRs) in a-Si n-i-p solar cells by separating the effects of substrate texture, BR texture, and BR reflectivity [303]. QE and diffuse and total reflection are compared for devices on smooth or textured substrates, with smooth or textured BRs. There is little improvement in J_{SC} for substrate haze exceeding 5%. Substrate texture is much more effective at increasing red response than the BR texture. Smooth substrates with textured BRs have comparable diffuse reflection but much higher specular reflection than textured substrates with a smooth BR. Devices on textured substrates also have lower reflection losses in the blue regions, resulting in higher QE at all wavelengths. These results apply to both superstrate and substrate device configurations.

3.1.3 J-V Analysis

The current-voltage data measured in light and dark from a-Si based solar cells has been analyzed to yield six parameters which completely specify the illuminated J-V curve from reverse bias to beyond open circuit voltage (V_{OC}). A simple photocurrent collection model is used which assumes drift collection in a uniform field. The method has been applied to J-V data from over twenty single junction a-Si or a-SiGe devices from five laboratories measured under standard simulated sunlight. Very good agreement results between measured and calculated J-V performance with only one adjustable parameter, the ratio of collection length to thickness $\frac{L_C}{D}$. Some of these devices have also been analyzed after extended light soaking or under filtered illumination. The effect of the voltage dependent photocurrent collection on FF and V_{OC} is considered in detail. Results under 1 sun illumination for both a-Si and a-SiGe devices are consistent with hole limited collection. Photocurrent collection in very thin devices (D~0.1 μm), or thicker devices under blue light, may be strongly influenced by interface recombination or back diffusion. The flatband voltage (V_{fb}) is dependent on the intensity and spectrum of illumination, hence is not a fundamental device property and is not equivalent to the built-in potential. V_{OC} is limited by V_{fb} not junction recombination current J_0 in typical devices. The illuminated solar cell performance is nearly independent of the forward diode current for low values of $\frac{L_C}{D}$, as occurs after light soaking or with a-SiGe. The model is also useful to investigate the intensity dependence of FF and to predict the influence of $\frac{L_C}{D}$ and V_{fb} on solar cell performance.

As part of the work associated with the device design team, this simple model was applied to a wide range of single junction devices and conditions. These included p-i-n and n-i-p cells on smooth or textured substrates, a-Si and a-SiGe cells, initial and stabilized, and under AM1.5 and red filtered light. Excellent agreement has been found between the model and the measurements. Devices analyzed covered a wide range of sources. In addition to those from IEC, cells were provided by Solarex, USSC, ECD, and APS. Analysis of triple junction cells using a parameter set based on the stabilized high, middle and low bandgap cells from USSC was also performed.

3.2 DEVICE PROCESSING AND MEASUREMENTS

3.2.1 Device Configuration

Devices used in the present program are single junction, superstrate p-i-n a-Si:H solar cells. The device configuration is shown schematically in Figure 3.1, below.

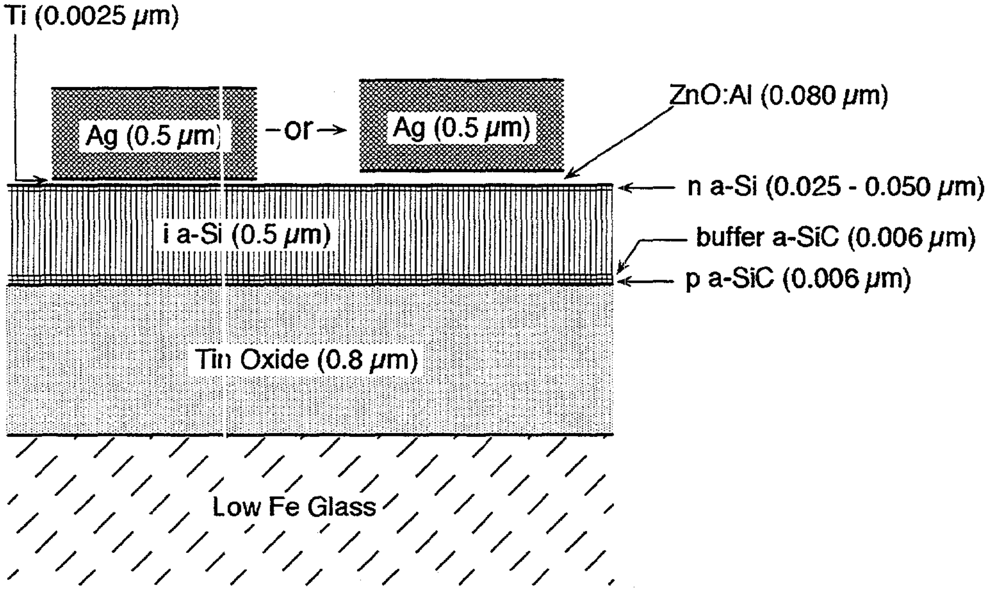

Figure 3-1 Schematic cross section of the devices used in present program.

Four circular devices of 0.28" diameter (0.4 cm^2 area) were defined on each 1" x 1" substrate by depositing back contact metallization through a 0.004" thick Mo mask. Two types of back contact metallization were used. The first is Ti (25 Å) / Ag (5000 Å) sequentially deposited by e-beam evaporation at deposition rates of 2 Å/s and 100 Å/s, respectively, with a source-to-substrate distance of 14". There was no intentional substrate cooling or heating. System base pressure was in the range of 1 to 3×10^{-6} Torr. ZnO:Al (800 Å) and Ag(5000 Å) contacts are deposited in different systems. ZnO:Al is sputtered in argon at a pressure of 3 mT and a flow rate of 100 sccm from an 8" circular target of ZnO:Al_2O_3, containing 1% by weight of Al_2O_3. Sputtering rate of 1000 Å/min was achieved at a power level of 900 W, reflected power being 25 W. Target to substrate distance was 2.5". The silver films were deposited, as before, by e-beam evaporation under the same condition.

The a-Si films were deposited in a glow discharge reactor which will be described in the next section.

Most of the devices during this contract were deposited on glass/tin oxide substrates were provided by Solarex Corporation. This glass is a low iron soda lime type of 2 mm thickness. Tin oxide films, doped with F, are made by APCVD at Solarex. The electrical and optical properties of these films are given in Table 3-2, and their surface topography is shown in Figure 3-2. However, we switched to Asahi Type U SnO_2 during the last year. There was no difference in device performance between the Solarex and Asahi SnO_2. All of the 10% devices were deposited on Asahi Type U.

Table 3-2 Typical properties of Solarex tin oxide films.

Thickness (μm)	Rsheet (Ω/sq)	ρ (mΩ·cm)	μ_H ($cm^2/V\cdot s$)	n x 10^{20} (cm^{-3})	Haze @700nm (%)	Absorp. @ 550 nm (%)
1.2	16	2.0	18	1.7	14	5.6

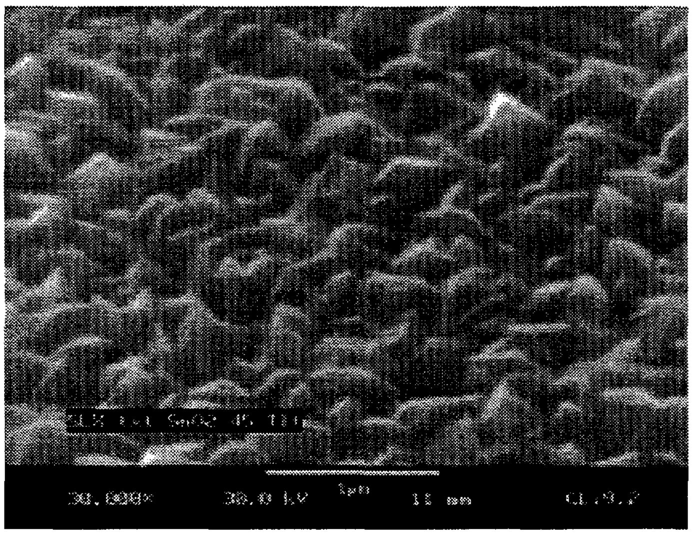

Figure 3-2 SEM micrograph showing surface topography of SnO_2 film. Magnification marker = 1 μm.

3.2.1.1 Reactor Description

The plasma-assisted CVD (PECVD) reactor used for the deposition of the a-Si:H films has been described in a previous report [304]. Therefore, only a brief description will be given here.

The reactor is of a three chambered load-locked design with a center chamber housing the deposition "can," and the two outer chambers being used for reactor loading/unloading. The reactor can accommodate substrates up to 4" x 4" in size. In the present program a standard load is four 1" x 1" SnO_2 coated glass substrates labeled -11, -12, -21, -22.

High vacuum ($\approx 10^{-7}$ Torr base pressure) pumping is achieved through the first chamber using a 170 l/s Balzers turbomolecular pumping unit. A 13 l/s Leybold D408CS corrosive series rotary vane pump is used as the process pump. Gases are delivered via mass flow controllers through a manifold into the bottom of the center chamber. Pressure is controlled by an MKS throttle valve controller and capacitance manometer. The substrates and the deposition can are heated separately, the former with quartz resistance heaters, and the latter with a single coiled resistance heating element. Temperature is controlled by Eurotherm temperature controllers. RF power is delivered by an ENI 300W power supply and matching network. The electrode is a 5 in. diameter perforated

Mo disc. The electrode-to-substrate spacing is 0.625 in. A system diagram of the reactor is shown in Figure 3-3.

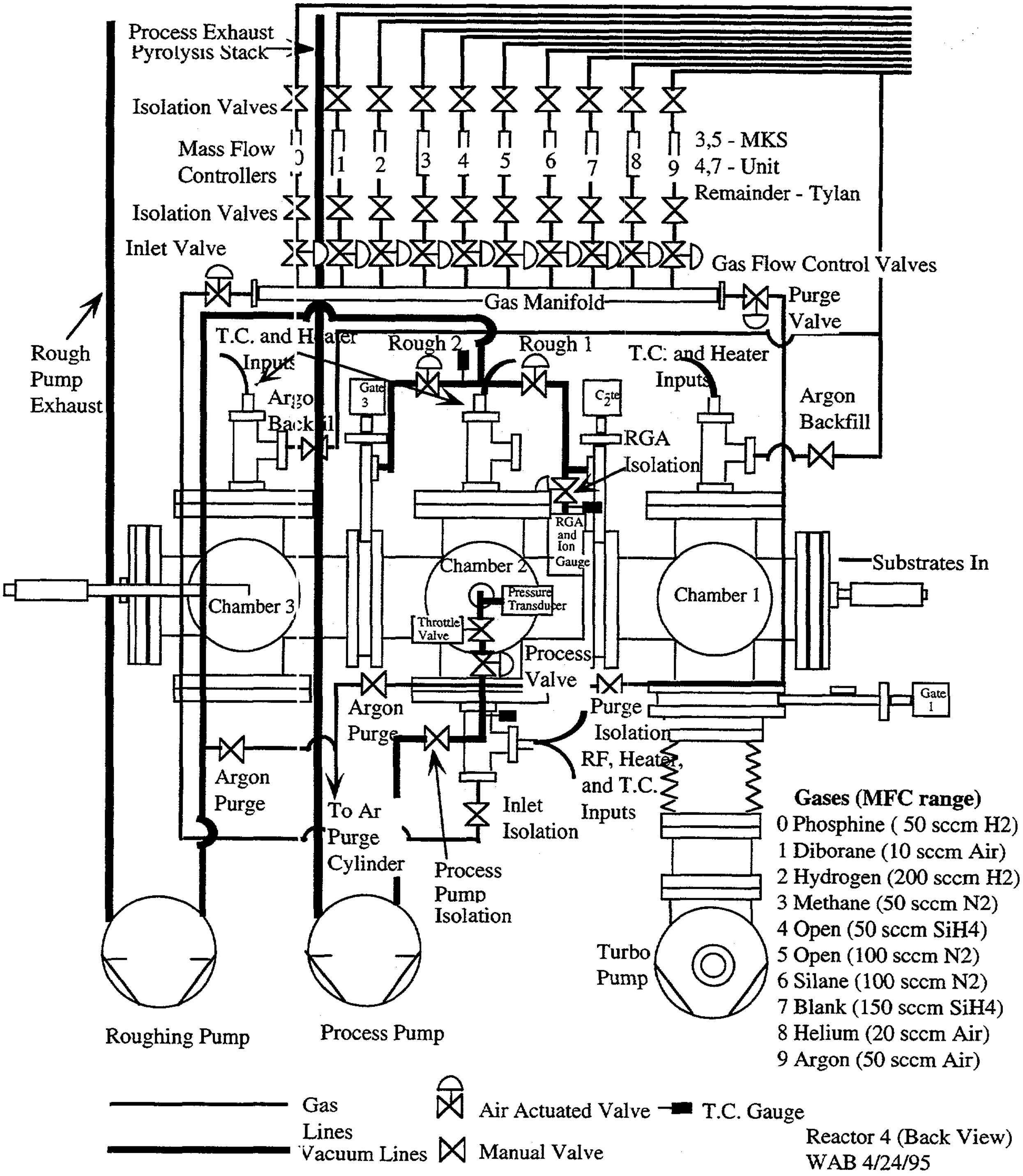

Figure 3-3 System diagram of the a-Si:H plasma-assisted CVD reactor.

3.2.2 Results And Discussion

3.2.2.1 Process Optimization and Device Results

The properties of the TCO used are given in Table 3-2 and the deposition parameters of standard devices are given in Table 3-3. Note that the only layer which has any H dilution is the µc-Si n-layer.

Table 3-3 Deposition parameters of standard devices.

Layer	p	graded-buffer	i	µc n
Time (min:sec)	0:15	0:25	30:00	8:00
Pressure (T)	0.2	0.2	0.2	1.0
Temperature (°C)	150	150	175	175
RF Power (W)	20	20	7	50
SiH_4 (sccm)	20	30	20	2
H_2 (sccm)				200
CH_4 (sccm)	30	20 -> 7.5		
2% B_2H_6 in H_2 (sccm)	1.5			
2% PH_3 in H_2 (sccm)				2

It became clear, from the SIMS (see Figure 3-4) data, that substantial amounts of phosphorous existed in the p-layer. The only possible source of this phosphorous was the phosphorous doped film deposited on the electrode of the reactor. No amount of pumping or gas flow was able to remove this film. The only possible solution is to deposit a "burying" layer before each run. Starting with run #4478, a 20 minute buffer layer was used as the burying layer between runs. After this, the FF of the devices increased to above 70% [305].

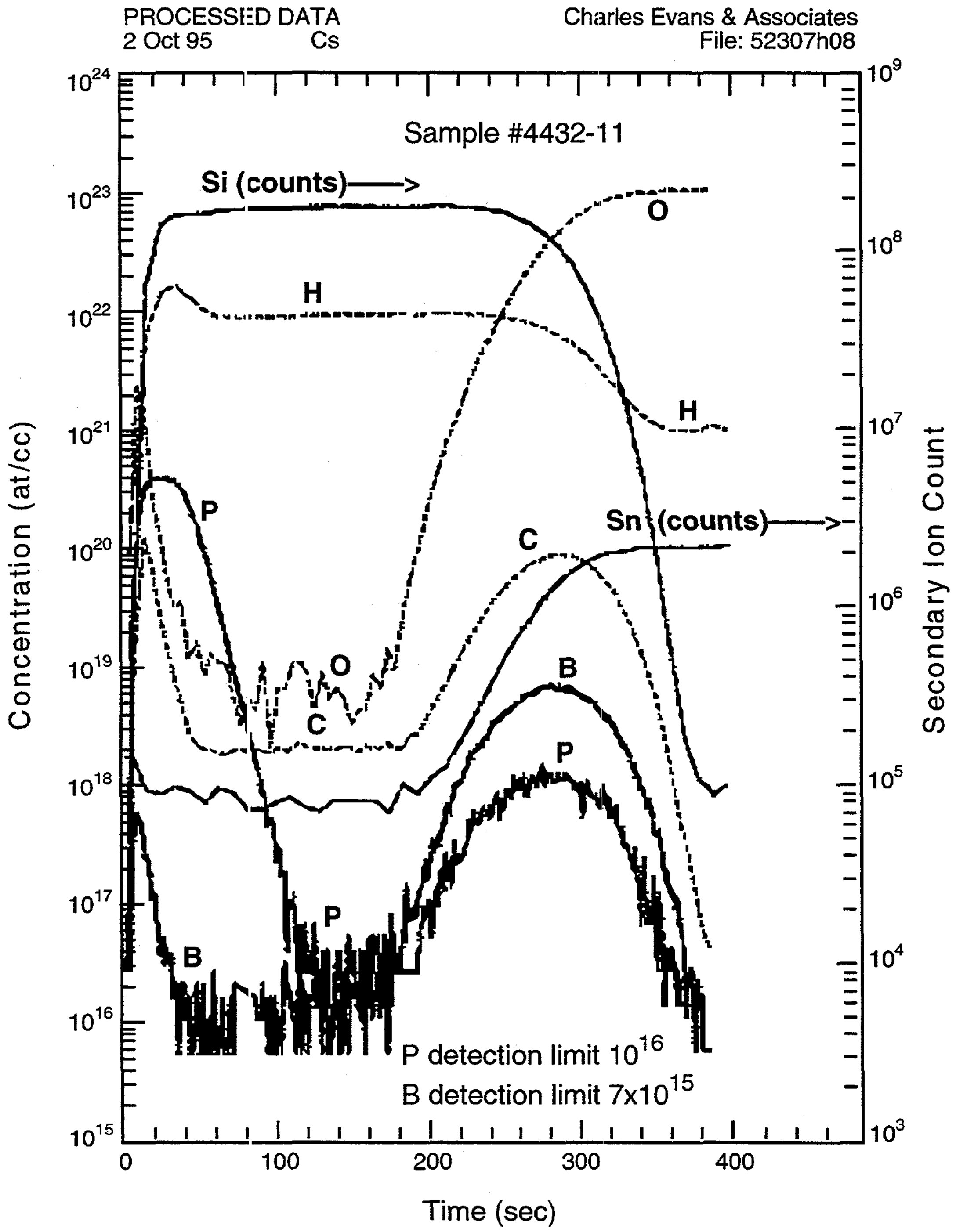

Figure 3-4 SIMS depth profiling of sample 4432-11

3.2.2.2 Development of μc n-layers

It has been reported that depositing a μc n-layer instead of an a-Si n-layer is critical for the tunnel junction of a multijunction device, and can increase V_{oc} as well due to the higher Fermi level position. Typically, μc material is obtained under conditions of high H_2 dilution and high rf power. A wide range of dilution (up to 100:1 ratio of H_2:SiH_4 flow) and rf power (10 W to 50 W) were explored.

The highest quality µc n-layers were obtained with the deposition parameters given in Table 3-3, which had the electrical properties shown in Table 3-4.

Table 3-4 Electrical and optical properties of the the standard µc n-layer.

µc n-layer Properties	Value
E_g (@ $\alpha = 2000\ cm^{-1}$)	1.9 eV
E_a	0.05 eV
σ	1 S cm^{-1}

Deposition rate of this particular type of µc n-layer was found to be ≈ 0.5 Å/s, as determined from the analysis of SEM cross section micrographs (Figure 3-5). µc n-layers had very little effect on the performance of devices having standard Ti/Ag back contacts. However, as discussed below, µc n-layers were found to be crucial when using ZnO/Ag contacts.

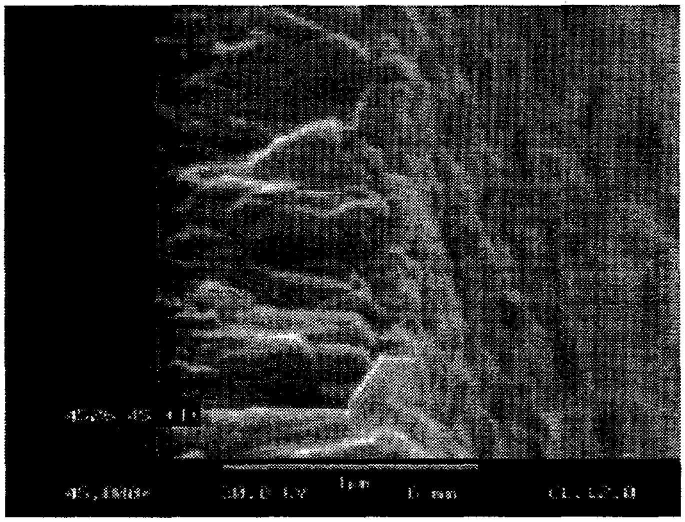

Figure 3-5 µc n-layer deposited on SnO_2; deposition time = 40 min. Magnification marker = 1 µm.

3.2.2.3 Back Contact Optimization

Three parameters of the Ti/Ag metallization were systematically varied: Ti thickness, system base pressure, and Ag deposition and rate. Post contact deposition heat treatments (HT) were also studied.

Devices were contacted without Ti, and with 25 and 50 Å Ti films (as measured by a quartz crystal monitor), followed by 5000Å Ag. Devices without Ti had much higher initial J_{SC} due to the higher red QE based on the higher reflectivity of Ag. However, the J_{SC} of devices without Ti decreased significantly after HT, primarily due to a loss in the blue QE, suggesting that Ti acts as a diffusion barrier. Devices with 25 Å Ti had higher red QE but same FF (70-71%), as were devices with 50 Å Ti interlayer. Thus, 25 Å Ti followed by 5000Å Ag became the standard back contact.

Reducing base pressure in the metallization bell jar from 1 to $3x10^{-6}$ T to $5x10^{-7}$ T before beginning the Ti deposition had no effect on initial or annealed values of FF. Since it required several hours of pumping to reach the lower pressure, metalization at low 10^{-6} base pressure range was continued.

Finally, increasing the Ag rate from 30 to 100 Å/s was found to have a beneficial effect on initial FF but made no difference after heat treatment. It is suspected that the higher electron beam power needed to achieve higher rate was heating the samples. Furthermore, devices with high rate Ag deposition showed very little improvement with HT, implying that the thermal treatment during metalization was to a certain extent equivalent to the post metal heat treatment. In any case, high rate Ag deposition was chosen as the standard process. However, it should be noted that none of the parameters which were varied during optimization (Ti thickness, system base pressure, or Ag deposition rate) had any measurable impact on final FF.

It is well known that ITO/Ag or ZnO/Ag back contact metallizations give higher J_{SC} due to higher reflectivity compared to Ti/Ag or Al. However, as was reported last year [304], although ITO/Ag or ZnO/Ag did improve J_{SC} by 1 to 2 mA/cm^2, the FF was at best 3 to 4 percentage points lower than with Ti/Ag. considerable effort was made to vary the ZnO conditions, the sputtering system vacuum cleanliness, and other process conditions. A new sputtering target was installed. However, only devices with μc n-layers, described above, gave higher FF when contacted with ZnO/Ag. This was further confirmed by sending IEC devices with amorphous and μc n-layers to Solarex for contacting with their ZnO/Ag process. In this case, as well, devices with μc n-layers had 5 to 10 percentage points higher FF than the ones with amorphous n-layers, though the highest FF in these devices was only 68%. The effort at IEC which focused on optimizing ZnO and μc n-layer deposition processes in tandem was successful in simultaneously achieving higher J_{SC} and FF. As a result, devices with ZnO/Ag contacts and μc n-layers had FF = 71 to 72% and increased J_{SC} of 15 to 16 mA/ cm^2 due to higher red response: the QE at 700 nm increased from ≈ 0.35 with Ti/Ag to ≈ 0.55 with ZnO/Ag. These results are described further in Section 3.3.2.

3.2.2.4 Conclusion

Introducing deposition of burying layers between device runs, developing high conductivity, high transparency μc n-layer, and in conjunction with the latter, optimizing ZnO deposition process allowed the increases in J_{SC} and V_{OC} shown in Table 3-1 leading to 10% efficiencies.

3.3 EFFECTS OF TRANSPARENT CONDUCTORS AND OPTICAL ENHANCEMENT SCHEMES ON SOLAR CELL PARAMETERS

3.3.1 J_{SC} Enhancement with Textured SnO_2 and ZnO

3.3.1.1 Introduction

Superstrate amorphous silicon (a-Si) solar cells or modules have a configuration of glass/transparent conducting oxide/p-i-n/rear contact. It is commonly assumed that to achieve high efficiencies, the transparent conductive oxide (TCO) must have a low sheet resistance (<15 Ω/sq.), a low absorption in the visible (< 5%), and a sufficient texture to scatter light (>5% haze). It is also required that the TCO be stable in the glow discharge environment of the a-Si deposition process. The front TCO electrode commonly used in superstrate a-Si devices is textured SnO_2F deposited by APCVD. Recently, ZnO:F deposited by APCVD and ZnO:B deposited by LPCVD have been reported to be more transparent and more stable in the glow discharge environment [306], but to have a problematic electrical contact with the p-type a-SiC:H [307, 308].

The primary purpose of the present paper is to evaluate the effect of a number of textured SnO_2 and ZnO substrates on the current generation in a-Si solar cells. This work is relevant since most of these TCOs have been used by others for a-Si device research or module fabrication.

3.3.1.2 Experimental Approach

Four SnO_2 films and three ZnO films were chosen for the present study. The TCOs are designated by the material and their haze. Samples SnO_2:14%, SnO_2:7%, SnO_2:2%, ZnO:5%a and ZnO:5%b were obtained from commercial vendors or a-Si industrial sources and have been used for a-Si module fabrication. Note that there are 2 ZnO:B samples with 5% haze. Sample SnO_2:1% was included in this study since it was nearly specular to obtain a lower limit to the generation without optical enhancement. Sample ZnO:6% was deposited at Harvard University [309]. All films were fully characterized as to their physical, electrical and optical properties. Surface topographies and thicknesses were determined by Scanning Electron Microscopy. Film thicknesses obtained by profilometric methods were in good agreement. Resistivities, carrier densities and mobilities were measured by four point probe and Hall effect methods. Optical absorption was measured by the index matching liquid [301] method in a spectrophotometer fitted with an integrating sphere. The haze was calculated from the ratio of diffuse to total transmission at 700 nm.

a-Si p-i-n devices were deposited in a standard PECVD system keeping all deposition parameters constant. Prior to each deposition, TCO substrates were cleaned in methanol and baked under vacuum for 1 hour at 225°C since exposure to T>225°C increases the resistivity of LPCVD ZnO [306]. Standard cleaning in ultrasonic water bath was found to damage the LPCVD ZnO films. The device structure chosen for the present study was: 200 Å a-SiC:H(B) p-layer /150Å a-SiC:H buffer/ 3500 Å a-Si:H i-layer / 500 Å a-Si:H(P) n-layer. The p-layer bandgap was about 1.96 eV. These conditions do not give the highest efficiencies but permit more reliable device comparison and analysis. For example, the present p-layer thickness of 200Å results in low J_{SC} but minimizes problems associated with incomplete p-layer coverage, shunting and low V_{OC} in the highly textured TCOs [310]. Four devices were made on each substrate by the e-beam deposition of four 0.4 cm^2 Ti (25Å) / Ag (5000 Å) contacts. All the devices were characterized by J-V measurements under an AM1.5 Oriel simulator calibrated to 100 mW/cm^2, and by quantum efficiency measurements at -1 V bias.

3.3.1.3 Results

Table 3-5 lists of the TCOs used in the present study along with their respective deposition methods and physical characteristics and their SEM micrographs are shown in Figure 3-6. The two SnO_2:F samples shown have large well-formed grains with angular facets. Grain sizes are similar. Compared to SnO_2:14%, SnO_2:7% had half the haze but greater variation in surface topology, with occasional spikes protuding from the surface. SnO_2:2% has two sizes of grains, but lower haze due to the lower average grain size. ZnO:5%a and ZnO:5%b were deposited by a low temperature (<250°C) LPCVD process while ZnO:6% was deposited by a high temperature (>400°C) APCVD process. Note the significant difference in grain shape and size. The LPCVD ZnO has faceted pyramidal grains while the APCVD ZnO had small blunt rounded grains, yet all three ZnO had similar haze values.

Table 3-5 List of TCOs and their physical characteristics

Label TCO (matl:haze)	Material	Depo. process	Thickness (µm)	Surface Topography from SEM	
				Feature Size (µm)	Feature Shape
SnO_2:14%	SnO_2:F	APCVD	1.0	0.6	Angular grains
SnO_2:7%	SnO_2:F	APCVD	0.8	0.6	Well formed faceted angular grains
SnO_2:2%	SnO_2:F	APCVD	0.7	0.3	Bi-modal size, some well formed grains
SnO_2:1%	SnO_2:F	APCVD	0.4	0.2	Small grains, some rounded, some well formed
ZnO:5%a	ZnO:B	LPCVD	1.5	0.4	Angular grains
ZnO:5%b	ZnO:B	LPCVD	1.6	0.5	Well formed faceted angular grains
ZnO:6%	ZnO:F	APCVD	1.2	0.3	Small rounded grains

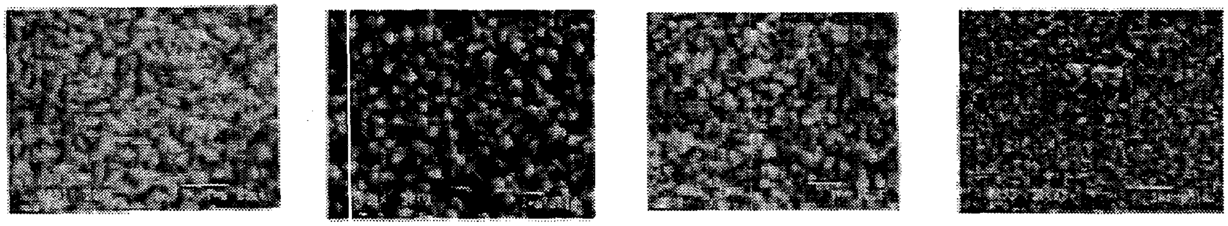

SnO_2:14% SnO_2:7% SnO_2:2% SnO_2:1%

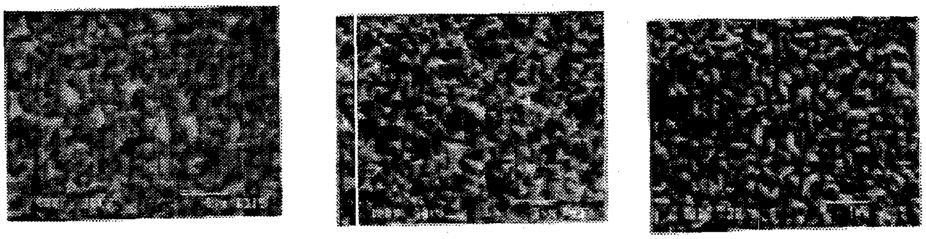

ZnO:5%a ZnO:5%b ZnO:6%

Figure 3-6 SEM micrographs of 7 TCO samples designated by (TCO material: haze)

Table 3-6 gives the electrical and optical characteristics. With the exception of SnO_2:2%, all the TCO's have electrical properties which are similar within a factor of 2: resistivities between 1-2x10^{-3} Ω-cm, electron concentrations between 1-2x10^{20} cm^{-3}, and Hall mobilities from 18 to 38 cm^2/Vs. The absorption at 550 nm for the 3 ZnO films is lower than for the 3 SnO_2 films of comparable resistivity. This confirms the higher transmission for ZnO over SnO_2 is achieved regardless of the source of the ZnO, despite the fact that the 3 ZnO films are thicker than the 3 SnO_2. The figure of merit [3-11] is the inverse of the product of the absorption at 550 nm and R_{SH}, or $1/(R_{SH}*A)$. This is an approximately thickness independent indication of the quality of the TCO for a-Si solar cell applications: higher values refer to higher film quality. Based on this evaluation all the ZnO films would make better front TCOs for a-Si devices because they have lower absorption at the same sheet resistance.

Table 3-6 Electrical and optical characteristics of the TCOs.

TCO Label (matl:haze)	R_{SH} (Ω/sq)	ρ x 10^{-3} (Ω-cm)	μ_H (cm^2/V s)	n x 10^{20} (cm^{-3})	Haze @ 700nm (%)	Absorp @ 550 nm (%)	Figure of Merit @ 550 nm (Ω/sq)$^{-1}$
SnO_2:14%	16	1.6	18	1.7	14	5.6	1.1
SnO_2:7%	10	1.0	38	1.6	7	4.8	2.1
SnO_2:2%	10	0.6	32	3.0	2	5.4	1.8
SnO_2:1%	30	1.3	20	2.4	1	2.2	1.5
ZnO:5%a	11	2.0	19	1.7	5	3.3	2.8
ZnO:5%b	10	1.6	25	1.6	5	3.8	2.6
ZnO:6%	13	1.6	20	1.2	6	3.3	2.3

Table 3-7 J-V performance results, QE(-1V) and ∫QE(-1V) over the AM1.5 global spectrum

TCO Label (matl:haze)	V_{OC} (V)	J_{SC} (mA/cm^2)	FF (%)	Eff. (%)	QE (-1V) @			∫QE(-1V)
					450 nm	550 nm	700 nm	(mA/cm^2)
SnO_2:14%	0.813	13.1	72.5	7.7	0.68	0.82	0.29	13.6
SnO_2:7%	0.787	13.2	73.4	7.6	0.69	0.81	0.29	13.6
SnO_2:2%	0.810	12.3	72.6	7.3	0.65	0.79	0.27	12.8
SnO_2:1%	0.804	12.6	68.4	7.0	0.65	0.80	0.25	13.0
ZnO:5%a	0.746	13.5	67.0	6.7	0.73	0.86	0.30	14.1
ZnO:5%b	0.803	13.4	54.8	5.9	0.73	0.86	0.30	14.2
ZnO:6%	0.718	11.5	62.7	5.2	0.62	0.80	0.29	13.2

Table 3-7 gives the cell J-V performance and the QE data for devices made with TCOs analyzed above. Results shown in this table are for comparison only and do not correspond, as stated earlier, to results which might be expected by optimizing for each TCO. In general, the high FF (at least on the SnO_2 devices) indicates a high quality a-Si i-layer and interfaces. Trends in these results are representative of other device runs we have made on these TCOs with varying i-layer thickness. First, comparing the SnO_2 pieces, note that increasing haze from 1 to 7% increased J_{SC} by 0.6 mA/cm^2 but increasing haze from 7 to 14% had no effect on J_{SC}. The QE at 700 nm, which is strongly influenced by increased scattering, increases from 0.25 to 0.29 with haze increasing from 1 to 7% but does not increase further with a haze of 14%. The effect of haze on the short wavelength QE is related to the front surface reflection (R) which decreases as haze increases due to increased light scattering [303, 312]. The device on low haze SnO_2:1%, had higher reflection losses at 450 nm consistent with its lower QE. Second, SnO_2:2% has a lower J_{SC} and QE at all wavelengths because it is the only TCO on standard soda-lime glass. All other TCO's are on less absorbing low iron soda-lime glass. Finally, SnO_2:7% always has significantly lower V_{OC} but slightly higher FF than the other SnO_2 pieces. As mentioned above, SnO_2:7% had surface features with greater peak-to-valley heights than the other TCOs.I It also exhibited unstable J-V behavior in reverse bias, consistent with a texture-related shunting mechanism [310]. Comparing the ZnO results, it is interesting that ZnO:5%a and ZnO:5%b, both LPCVD ZnO, give very different V_{OC} and FF, yet had nearly identical surface structure and optoelectronic properties (Table 3-5 andTable 3-6). ZnO:5%a always gives much lower V_{OC} and only moderately lower FF, while ZnO:5%b gives typical V_{OC} but much poorer FF. The lower FF for ZnO:5%b is related to series resistance in the device. Thus, bulk TCO properties are not always good indicators of device performance.

Behavior from ZnO:6%, the APCVD ZnO, is much worse for reasons which are not clear but are consistent with previous results [311]. Comparing the best devices on ZnO to the best devices on SnO_2, the gain in current generation (integrated QE) with ZnO is about 0.6 mA/cm^2, as expected based on calculations [306]. The lower V_{OC} and FF for ZnO are also consistent with reports of higher contact resistance at the ZnO/p interface [307].

3.3.1.3.1 Impact of improved generation with ZnO on multijunction solar cells

It is well known that multijunction a-Si solar cells are required to meet performance and stability goals [313]. To investigate the potential benefits of ZnO in a multijunction device, we have calculated the i-layer thicknesses needed to give 8 mA/cm^2 current generation (AM1.5 global) in each cell of a triple junction device for SnO_2 or ZnO front TCO window layers. Calculations used absorption data from USSC [314] for 1.80 eV top cell, 1.60 middle cell, and 1.42 bottom cell. Absorption losses in doped p and n-layers as well as front reflection loss of 8% were included. The bottom cell was assumed to have the benefits of mild optical enhancement due to the back reflector, represented by a doubling of optical pathlength and a rear reflectivity of 0.9. The transmission of SnO_2:7% was used for SnO_2 and ZnO:5%a for ZnO.

Figure 3-7 shows the QE and TCO transmission. The i-layer thicknesses for the devices with SnO_2 or ZnO are shown in Table 3-8. The primary advantage of ZnO in such a triple junction device is a 27% reduction in the low bandgap a-SiGe i-layer thickness, from 3400 Å to 2500 Å. The middle bandgap cell can be thinner as well. Together, this will improve stability, reduce costs (GeH_4 is very expensive) and reduce deposition time. Thus, the greatest benefit of the increased generation possible with ZnO compared to SnO_2 is related to the stability and manufacturing costs, not the higher J_{SC}.

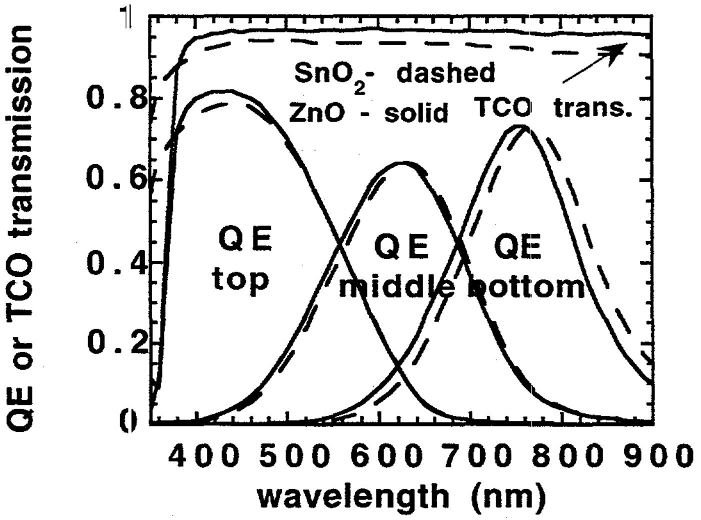

Figure 3-7 Calculated QE for triple junction devices having i-layer bandgaps of 1.8, 1.6, and 1.42 eV with SnO2 or ZnO TCO windows. Thicknesses needed to provide 8 mA/cm^2 each junction given in Table 3-8. TCO transmission corrected for reflection as T/(1-R).

Table 3-8 Thickness of top, middle and botom cell i-layers to give 8 mA/cm^2 with SnO_2 and ZnO (Figure 3-7)

TCO matl.	top cell	middle cell	bottom cell
SnO_2:7%	1400 A	3600 A	3400 A
ZnO:5%a	1300 A	3300 A	2500 A

3.3.1.4 Conclusions

Our results show that in presently available textured ZnO, current generation is about 0.6 mA/cm^2 greater than in textured SnO_2 for single junction devices. The advantage of using ZnO as a front TCO to obtain higher J_{SC} must be balanced with the apparent difficulty in maintaining V_{OC} and FF. There may be other advantages to using ZnO in multijunction devices since thinner i-layers will give the same J_{SC} leading to improved stability and reduced costs.

3.3.2 TCO Contacts for n-i-p and p-i-n Devices

3.3.2.1 Introduction

Transparent conducting oxide (TCO) materials are critical in fabricating thin film solar cells. They provide low sheet resistance contacts for lateral current flow while maintaining high transparency. TCO materials are used to provide a window layer for the incident illumination at the front of a device. In this configuration, they may also serve as an antireflection coating since $n_{Air}<n_{TCO}<n_{SC}$ where the index of refraction of the TCO is between that of air (or glass) and that of the semiconductor [315]. They are also used in a-Si solar cells at the back contact as a dielectric buffer layer between the a-Si or µc-Si doped contact and the metal contact [316-319]. Additionally, TCO's can be textured to provide scattering which increases the optical absorption of weakly absorbed light. The two most commonly used TCO materials are indium tin oxide (ITO), and zinc oxide (ZnO). Both are degenerate n-type semiconductors which can be optimized to have bandgaps greater than 3.3 eV, with absorption less than 10% over the visible spectrum and resistivities less than 10^{-3} W-cm [320, 321]. The most common deposition techniques for ITO and ZnO for solar cell applications are chemical vapor deposition, evaporation and sputtering. In this paper, the solar cell performance of single junction a-Si devices having sputtered ITO and ZnO contacts are compared. The effect of O_2 in the sputter discharge is investigated. Both ITO and ZnO are applied as contacts to substrate type n-i-p devices and superstrate p-i-n devices. The impact of the TCO on the optical and electrical performance of both types of devices is presented.

3.3.2.2 TCO deposition and Device Fabrication

TCO materials were r.f. sputtered in Ar or Ar/O_2 onto unheated substrates of 7059 glass, for optical and electrical characterization, or onto a-Si devices. The ITO target was In_2O_3 mixed with 9% SnO_2. The ZnO target was ZnO mixed with 1% Al_2O_3. Nearly optimum film properties were found by sputtering the ITO at 700W and the ZnO at 900W. Deposition rates were approximately 0.1 µm/min. Sputtering in an Ar/O_2 mixture improved the transparency of the TCO films with a slight loss in resistivity. ITO and ZnO films were sputtered with and without O_2 in the Ar. O_2 had a negative effect on devices in some cases as discussed below. TCO and Ag contacts were deposited through masks onto devices.

Two different a-Si device structures were investigated. Substrate type devices with stainless steel/n-i-p/TCO configuration were deposited by ECD. The p-layer was μc-Si. These devices were intended to duplicate the top cell of a triple junction device. Therefore, they lacked any optical enhancement such as texture or a back reflector, and the i-layer was very thin (<0.1 μm). The J_{SC} from these cells was around 8 mA/cm^2 as required for a top cell [322]. Superstrate type devices with glass/SnO_2/p-i-n/TCO/Ag structure were deposited at IEC. The SnO_2 (Asahi type U) was textured. The i-layers were 0.5 μm thick. The p-i-n cells had a-SiC p-layers and C graded buffers between the p and i-layers. Otherwise identical devices with a-Si or μc-Si n-layers were deposited for this study. The μc-Si n-layer was deposited at high hydrogen dilution (H_2:SiH_4 of 100:1) and higher power and pressure than the a-Si layer. The high conductivity (1 S/cm) and low activation energy (0.05 eV) confirm the microcrystalline nature of the n-layer. After sputtering TCO on the p-i-n cells, a 0.6 μm Ag layer was evaporated through the same mask for a low resistance highly reflective TCO/Ag contact. Cells were 0.4 cm^2 in area. Current voltage measurements were made with AM1.5 global illumination from an Oriel simulator at 28° C.

3.3.2.3 TCO Material Properties

TCO layers were sputtered over a range of rf power and oxygen partial pressure. Optimum ITO and ZnO film properties were obtained at 700 W and 900 W with 0.9 and 0.1% O_2 in Ar, respectively. Table 3-9 shows the thickness D, sheet resistance R_{sq}, resistivity, and normalized transmission for ITO and ZnO films deposited with and without O_2. The normalized transmission $T_n = T/(1-R)$ was averaged over 400-900 nm.

The presence of O_2 during sputtering has a major impact on the ITO film properties [320]. The ITO film without O_2 was brownish and had high absorption, unsuitable for solar cell applications. O_2 has a much smaller effect on the ZnO films. Note that the ITO and ZnO films deposited with O_2 have the same optical transmission at the same R_{SH} (see Table 3-9), indicating equivalent thickness trade-off between the need for low lateral current carrying resistance losses (thicker TCO) and high window layer transparency (thinner TCO). The resistivity of optimized ZnO is 2.5 times higher than that of ITO.

Table 3-9 Sputtered TCO properties

TCO	O2 in Ar (%)	D (μm)	R_{SH} (Ω/sq)	$\rho \times 10^{-4}$ (Ω-cm)	averaged Tn 400-900nm
ITO	0	0.2	35	7	0.72
ITO	0.9	0.2	19	4	0.96
ZnO	0	0.4	15	6	0.94
ZnO	0.1	0.5	20	10	0.96

3.3.2.4 TCO Contacts on stainless steel/n-i-p/TCO Devices

ITO and ZnO were sputtered with and without O_2 in the Ar discharge onto the μc-Si p-layers of ss/n-i-p substrates. The a-Si devices were essentially identical since they had been cut out of a large area sheet. The TCO films were typically of the thickness range shown in Table 3-9. This relatively low sheet resistance allowed the cells to be fabricated without grids since the area was small. However, thinner TCO films (~70 nm) are typically used in this application primarily for their AR effect.

Results are shown in Table 3-10. The most important observation is that devices with ITO have higher FF than devices with ZnO. The decrease in FF is accompanied by an increase in resistance R_{OC} which is dV/dJ at V_{OC}. Figure 3-8 shows the reduced FF for devices with ZnO is due to curvature near V_{OC} (i.e. increasing R_{OC}), suggesting a second junction opposing the n-i-p cell. Table 3-10 shows that the effect of sputtering in an O_2 atmosphere is quite different between ITO and ZnO. Adding O_2 during ITO sputtering increases J_{SC}, as expected from the difference in Tn in Table 3-9, but has no effect on V_{OC} or FF. Adding O_2 during ZnO sputtering reduces V_{OC} and FF but has no effect on J_{SC}.

Table 3-10 Performance of stainless steel/n-i-p/TCO devices with ITO or ZnO contacts

TCO	TCO process	R_{SH} (Ω/sq)	V_{OC} (V)	J_{SC} (mA/cm^2)	FF (%)	R_{OC} (Ω-cm^2)	Eff. (%)
ITO	no O_2	35	0.844	7.3	66.0	14	4.1
ITO	O_2	19	0.860	8.3	65.1	13	4.6
ZnO	no O_2	15	0.840	8.4	60.0	26	4.4
ZnO	O_2	20	0.750	8.5	52.2	39	3.3

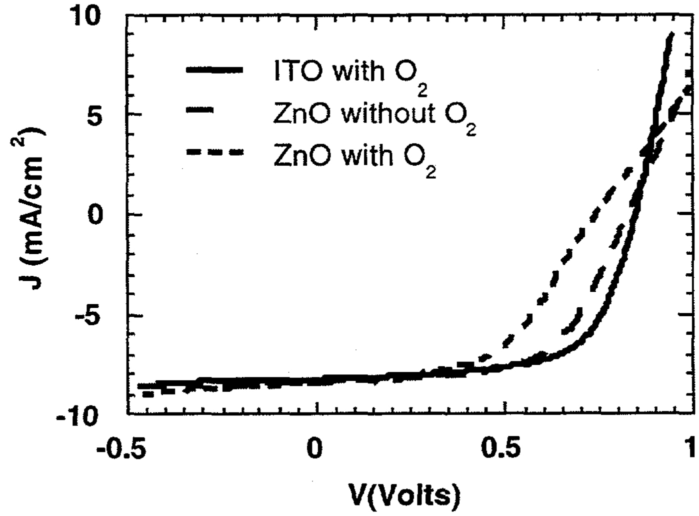

Figure 3-8 J-V curves for stainless steel/n-i-p/TCO devices with ITO or ZnO contacts. Cell performance is shown in Table 3-10

3.3.2.5 TCO Contacts on glass/SnO_2/p-i-n/TCO/Ag Devices

Superstrate devices were deposited on glass/textured SnO_2 substrates. Four devices were deposited with μc-Si n-layers in one run and four with a-Si n-layers the following run. ZnO was sputtered with or without O_2 and ITO was sputtered with O_2 on both types of devices through a mask. Ag was evaporated through a mask on all TCO layers. For comparison, Ti/Ag contacts were also evaporated on both types of devices.

Results with µc-Si and a-Si n-layers with all four types of contacts are shown in Table 3-11. Devices with the Ti/Ag metal contacts had FF~70% for both a-Si and µc-Si n-layers. However, for all three TCO/Ag contacts, the µc-Si n-layer had higher FF than the a-Si n-layer. The µc-Si n-layer also had higher V_{OC} and J_{SC}. The higher V_{OC} with the µc-Si n-layer suggests better pinning of the Fermi level which increases the built-in voltage. The µc-Si n-layer increases J_{SC} by ~ 0.5 mA/cm^2 for Ti/Ag contacts and by ~1 mA/cm^2 with TCO/Ag contacts. Both ITO and ZnO give comparable FF on µc-Si n-layers (FF~68-69%) with or without O_2, but ZnO gives higher V_{OC} and J_{SC}.

Table 3-11 Cell performance of glass/SnO_2/p-i-n/TCO/Ag devices with either a-Si or µc-Si n-layers.

back contact	TCO process	n-layer	V_{OC} (V)	J_{SC} (mA/ cm^2)	FF (%)	R_{OC} (Ω/cm^2)	Eff. (%)
Ti/Ag	none	a-Si	0.863	13.5	70.2	6.3	8.2
		µc-Si	0.875	14.0	69.8	6.0	8.5
ITO/Ag	w/ O_2	a-Si	0.853	13.8	60.0	23.1	7.0
		µc-Si	0.865	14.9	69.1	5.9	8.9
ZnO/Ag	w/ O_2	a-Si	0.864	14.9	52.0	55.7	6.7
		µc-Si	0.885	16.1	67.8	6.0	9.7
ZnO/Ag	w/o O_2	a-Si	0.872	15.0	62.6	14.5	8.2
	w/o O_2	µc-Si	0.881	16.2	67.7	5.8	9.7

Figure 3-9 shows that sputtering ITO or ZnO with O_2 on an a-Si n-layer gives curvature at V_{OC}, suggesting a second junction. This curvature is not present on the µc-Si n-layers as shown in Figure 3-9. Comparing Figure 3-9 with Table 3-11, the large values of R_{OC} on these devices are indicative of curvature around V_{OC} and the possible formation of a second junction.

The effect of sputtering ZnO with or without O_2 is shown in Figure 3-10. Sputtering ZnO with O_2 onto an a-Si n-layer gives strong curvature around V_{OC} and low FF (52.0%), where as sputtering without O_2 gives less curvature, and a higher FF (62.6%). Sputtering with O_2 onto a µc-Si n-layer gives no evidence of a second junction, with FF=67.8%.

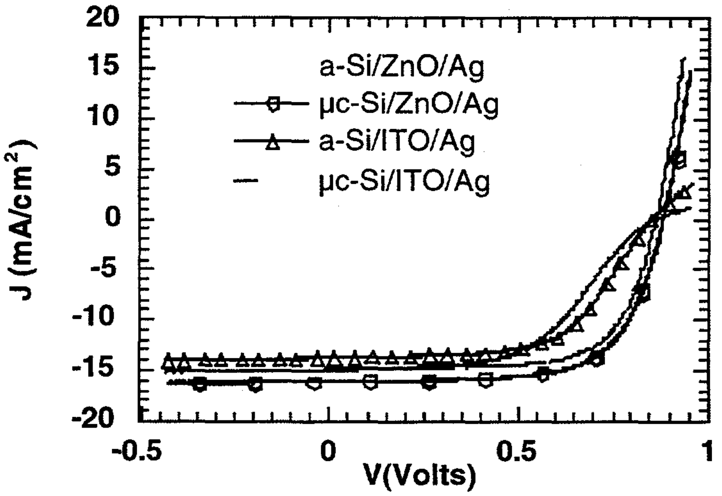

Figure 3-9 J-V curves for glass/SnO$_2$/p-i-n/TCO/Ag devices with a-Si or μc-Si n-layers. ITO and ZnO were sputtered with O$_2$. Cell performance is shown in Table 3-11.

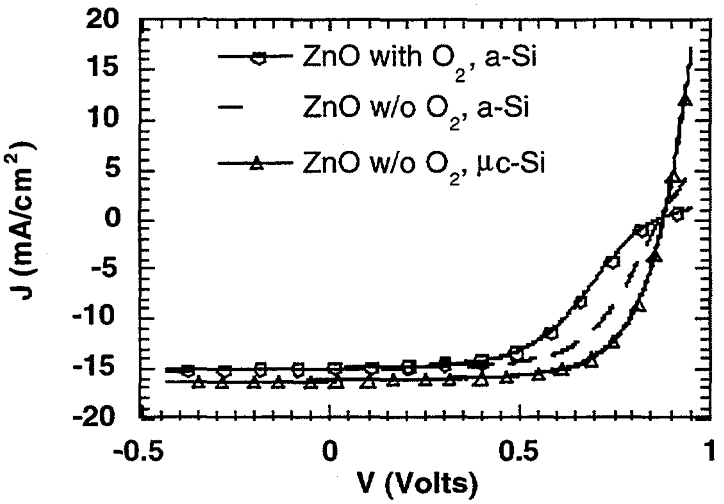

Figure 3-10 J-V curves for glass/SnO$_2$/p-i-n/ZnO/Ag devices showing the effect of sputtering with or without O$_2$ on a-Si or μc-Si n-layers. Solar cell performance is shown in Table 3-11.

3.3.2.6 Discussion and Conclusions

We found poor FF and evidence for a second junction with ZnO/p contacts on n-i-p devices. Although this is the first time such behavior has been reported for the n-i-p device structure, poor electrical contacts leading to low FF have been observed in glass/ZnO/p-i-n devices deposited on a glass/ZnO substrate [301, 323, 324]. In the p-i-n structure, the ZnO was typically deposited by APCVD or LPCVD, and the p-layer, typically a-SiC, is grown on the ZnO at 150-250°C. In our work, the ZnO is sputtered onto an unheated μc-Si p-layer, which has much higher conductivity than the a-SiC layer. Yet, the two device structures exhibit the same problem, despite the fact that the ZnO, the p-layer, and ZnO/p contact are formed from very different conditions. This strongly suggests that the ZnO/p contact is fundamentally a poor ohmic contact. We speculate that an oxide layer may contribute to this problem since sputtering ZnO in O_2 gave much poorer FF than with no O_2 yet the bulk resistivity of ZnO with O_2 is only a factor of 2 higher. There is no technical reason to switch from the standard ITO contact to ZnO for n-i-p devices in view of the poorer contact. However, re-optimization of the μc-Si p-layer with ZnO instead of ITO may improve the contact.

Regarding the p-i-n devices, we found significant differences between a-Si or μc-Si n-layers. The a-Si n-layer is more absorbing than the μc-Si layer. The larger improvement in J_{SC} for TCO/Ag with the less absorbing μc-Si n-layer is consistent with increased multiple reflections and higher back reflection for the TCO/Ag contact compared to Ti/Ag. As optical enhancement and light trapping in the device improves, it becomes more crucial to reduce parasitic absorption at contacts and interfaces.

Table 3-11 and Figure 3-9 also clearly show the improved electrical contact properties with a μc-Si n-layer compared to an a-Si n-layer when contacted with either ITO or ZnO. These results are consistent with those of Hayashi et al [319] who investigated ZnO/Al or Al contacts on a-Si or μc-Si n-layers and found poorest FF with ZnO/Al on an a-Si n-layer.

The effect of sputtering ZnO with or without O_2 is quite different between n-i-p and p-i-n cells. Sputtering ZnO onto μc-Si n-layers in p-i-n cells gave equivalent device results with or without O_2, whereas sputtering ZnO with O_2 was clearly detrimental in contacting μc-Si p-layers in n-i-p devices.

Barriers between TCO and doped [325, 326] or undoped [325, 327] a-Si layers have been previously reported. However, those interfaces were formed by depositing the a-Si onto the TCO in order to study the interaction between the plasma and the TCO, and subsequent metallic Schottky barrier formation. In our study, the TCO was sputtered onto the a-Si, which eliminates the question of TCO reduction and Schottky barrier formation. It is unclear that previous results for the TCO/a-Si interface [325-327] apply to our a-Si/TCO contacts. Computer modeling of p-i-n/ZnO devices [328] suggests that very thin n-layers (a few nanometers) will improve FF and V_{OC}. This is about 10 times thinner than typical n-layers, as we used in our devices. Among ZnO, ITO, and SnO_2, ZnO has the lowest work function difference with n-type a-Si [328]. Thus, ZnO should have a negligible barrier with the a-Si n-layer and effectively pin the Fermi energy. However, the model results find a very thin n-layer remains necessary to compensate for the negative interface space charge. In contrast to the modeling results [328], experimental results [318] showed a better FF with ZnO by increasing the n-layer thickness 3 times greater than their standard thickness for metal contacts. Clearly, the a-Si/sputtered TCO contact needs further study to understand the fundamental junction and contact properties.

Regarding sputtered TCO contacts for a-Si devices, we conclude: 1) ITO is a better top contact for μc-Si p-layers in stainless steel/n-i-p/TCO devices than ZnO; 2) ZnO sputtered with or without O_2 is a better back contact compared to ITO for μc-Si n-layers for p-i-n/TCO/Ag devices; 3) ZnO sputtered with O_2 is detrimental to obtaining a low resistance contact to μc-Si p-layers and a-Si n-layers but has little effect on contacting μc-Si n-layers.

3.3.3 Analysis of Optical Enhancement Using a Detachable Back Reflector

3.3.3.1 Introduction

Analyzing the optical enhancement in a-Si solar cells is a challenging problem for both superstrate (glass/TCO/p-i-n/BR) and substrate (SS/BR/n-i-p/TCO) device structures where BR is the back reflector, TCO is a transparent conductive oxide and SS is the stainless steel substrate. Typically, in a superstrate device the front TCO provides the texture and the rear BR provides reflectivity, while in the substrate device the BR provides both texture and reflectivity. The BR increases short circuit current (J_{SC}) and red response by reflecting and scattering (if textured) weakly absorbed photons. This increases their optical pathlength. The theoretical maximum for the enhancement in pathlength is m~60 [329] but this decreases rapidly with parasitic absorption in the device. Gains of m=2-5 in optical pathlength have been obtained experimentally [330, 331] suggesting parasitic absorption losses exceeding 25% [329]. Despite considerable analysis, BR enhancement and parasitic losses are not well understood [332, 333]. We have studied optical enhancement in a-Si n-i-p solar cells with detachable BRs by separating the effects of substrate texture, BR texture, and BR reflectivity. Detachable BRs have been previously used to study optical enhancements and were reported to have less parasitic losses than integral BRs [329].

3.3.3.2 Device Structures

Substrates were glass with TCO layers having haze at 700 nm of 0, 1, 5 and 14%. The smooth TCO (0% haze) was sputtered ZnO, the TCO with 5% haze was LPCVD ZnO, and the TCO with 1 and 14% haze were APCVD SnO_2 [332]. Single junction a-Si n-i-p devices with ~0.25 um i-layers were deposited by glow discharge at ECD having a device structure: ITO/p-i-n/TCO/glass. For comparison, devices were codeposited on SS and textured ZnO/Ag/SS [334], which are standard substrates for the n-i-p device configuration. Reflection (R), transmission (T), quantum efficiency (QE), and J_{SC} (AM1.5 global) were measured for illumination through the ITO (front) and the glass (rear) sides. QE was measured at -1V to minimize collection losses. Then, a smooth Ag BR (Ag film evaporated on glass) or textured Ag BR (Ag film evaporated on the 14% haze SnO_2) was optically coupled to the glass substrate with an index matching coupling liquid having n=1.5, giving a removable external Ag BR (Figure 3-11). This allowed measurements of three different BR (no Ag, smooth Ag, or textured Ag) on the same device sample, without changing the device structure or substrate texture.

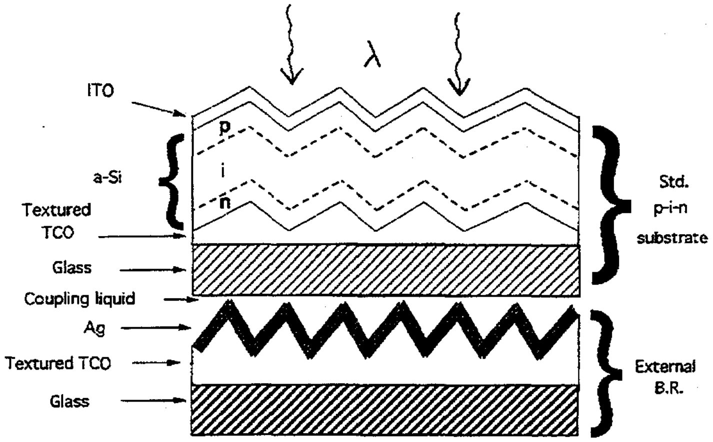

Figure 3-11 ITO/p-i-n/TCO/glass device on textured TCO substrate with external BR and coupling liquid.

3.3.3.3 Results

Figure 3-12 shows the QE for light through the ITO/p front contact for the four different TCO/glass substrates without any Ag BR. Note the large improvement in red QE as haze increases from 0 to 5%, but there was no further gain in red QE for haze above 5%. Table 3-12 lists J_{SC} and QE at 700 nm for the devices before and after applying the external smooth Ag BR, confirming the limited increase in J_{SC} for haze greater than 5%. Similar conclusions have been reached for superstrate p-i-n devices [303, 335]. Devices on ECD's ZnO/Ag BR had slightly higher J_{SC} than the 14% textured TCO with Ag BR. The J_{SC} and QE are very similar and low for the devices on smooth ZnO and on SS, indicating very little reflection or optical enhancement for either. Also note that the smooth Ag BR increases the QE at 700 nm by ~0.1 for all textured devices but has a much smaller effect on the smooth device (0% haze). Figure 3-12 and Table 3-12 indicate a significant increase in optical enhancement with even 1% haze over a smooth substrate. For example, with the smooth Ag BR, the substrate with 1% haze TCO provides over half of the gain in J_{SC} and QE achieved by the 14% haze substrate.

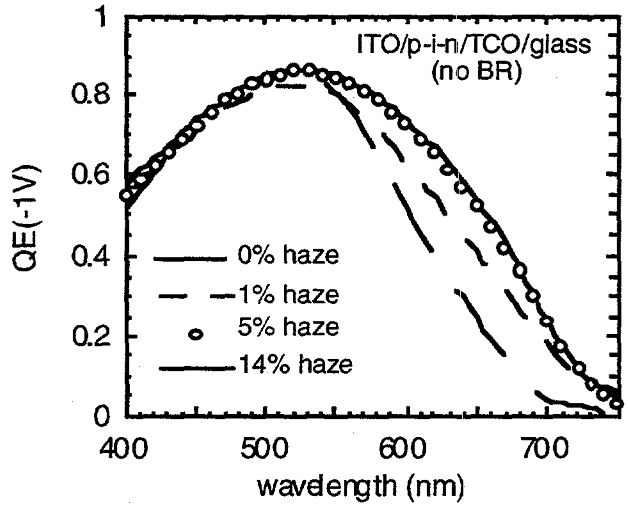

Figure 3-12 QE for devices on textured TCO substrates with different haze (no back reflector).

Table 3-12 J_{SC} and QE for devices of Figure 3-12 without and with a smooth external Ag BR. Devices deposited on ECD's standard n-i-p stainless steel substrates (no BR) and textured ZnO/Ag/stainless steel (BR) shown for comparison.

haze	J_{SC} (mA/ cm^2)	J_{SC} (mA/ cm^2)	QE@700 nm	QE@700 nm
	no Ag BR	smooth Ag BR	no Ag BR	smooth Ag BR
0%	11.6	13.0	0.05	0.07
1%	12.5	14.1	0.12	0.22
5%	13.7	14.7	0.22	0.32
14%	13.9	15.1	0.22	0.32
ECD	11.3 (SS)	15.5 (ZnO/Ag)	0.04	0.39

Figure 3-13 shows the QE at -1V with different external back reflectors for devices having the least (0%) and greatest (14%) haze. Since the BRs were externally coupled, they only increase reflection and/or scattering of weakly absorbed light but do not affect the a-Si surface texture, substrate or n/TCO reflectivity. This is a unique feature of these devices. Enhanced QE with the optically coupled smooth Ag BR was equivalent to that found by evaporating an Ag film directly on the back of the glass substrate, indicating no additional losses associated with the coupling of the external BR. Table 3-13 shows J_{SC}, both absolute and normalized to the smooth TCO without an Ag BR (11.6 mA/ cm^2), along with the QE, and total reflection and transmission all at 700 nm. The device with 0% haze shows that J_{SC} increases by 12% with the external smooth Ag BR and 15% with the external textured Ag BR. Thus, most of the increase occurs due to increased reflectivity of the smooth Ag. The texture of the BR has a smaller impact than the reflectivity of the BR. The reflection at 700 nm for the device with 0% haze increases substantially, by ~0.20, with either the smooth or textured Ag BR, yet the QE only increases by 0.02 or 0.06, respectively. Thus, at most one tenth of the light transmitted through the smooth device at 700 nm is captured when an Ag BR applied.

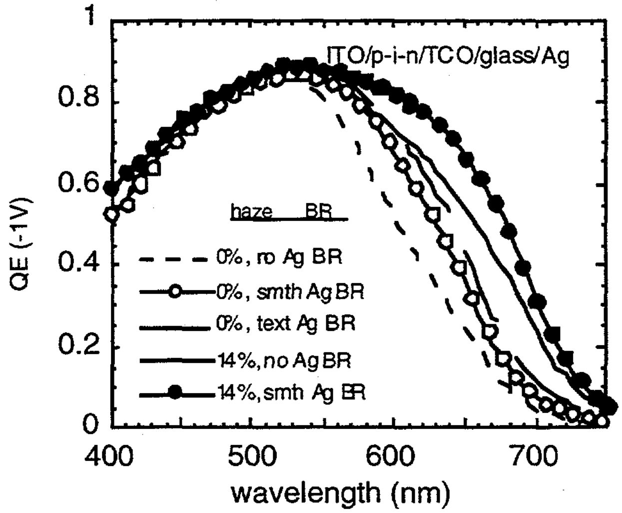

Figure 3-13 QE for devices on smooth and textured TCO with no BR, smooth Ag BR, and textured Ag BR. QE for device on textured TCO with textured BR was same as for smooth BR (solid circles), hence not shown.

Table 3-13 J_{SC} data for devices of Figure 3-13 with 0 and 14 % haze and different Ag BRs. Note: (the J_{SC} ratio is the ratio with and without a BR).

Haze	external BR	J_{SC} (mA/ cm^2)	J_{SC} ratio	QE @700nm	T @700 nm	R @700 nm
0%	none	11.6	1.00	0.05	0.52	0.27
	smooth Ag	13.0	1.12	0.07	0	0.46
	text. Ag	13.3	1.15	0.11	0	0.48
14%	none	13.9	1.20	0.22	0.20	0.15
	smooth Ag	15.0	1.30	0.32	0	0.18
	text. Ag	15.0	1.30	0.32	0	0.18

Instead, a much larger fraction of the previously transmitted light escapes the device by reflection from the front. Regarding the device on the textured substrate (14% haze), J_{SC} increases by 20% without any BR compared to the smooth substrate. Either the smooth or textured rear Ag BR gives an additional 10% increase in J_{SC} for the device on the textured substrate. With the BR, half of the light transmitted through the textured device at 700 nm without the BR is absorbed and contributes to increased QE (from 0.22 to 0.32). Thus, a textured substrate without a BR, even though transparent, is much more effective at light trapping than a textured Ag BR on a smooth device. This suggests that the replication of the substrate texture on the top a-Si surface is crucial to enhance multiple scattering from the underlying substrate.

Comparing the total and diffuse reflection, shown in Figure 3-14 and 5, can give further insight to the QE results of Figure 3-13. The total reflection for the device on the smooth TCO substrate with either no BR or the smooth Ag BR (Figure 3-14) shows strong interference beyond 600 nm, and negligible diffuse reflection (<0.04), as expected for a smooth device and smooth BR. Interference effects would be expected for a device deposited on a smooth integral Ag BR (p-i-n/Ag/glass). The smooth or textured Ag BR causes a significant increase in the red reflection, but little increase in red QE (Table 3-13). Figure 3-15 shows that a device on a textured substrate has identical total or diffuse reflection with either the smooth or textured Ag BR. There is no additional diffuse reflection with a textured substrate having a textured BR nor was there any increase in J_{SC} or QE (Table 3-13). Note that the reflection between 400-500 nm is lower for the device on the textured substrate (Figure 3-15) compared to the device on the smooth substrate. The QE in this region is higher for the device on the textured substrate as expected (Figure 3-13). The textured substrate produces a textured front surface, which has lower total reflection but much higher diffuse reflection compared to a smooth device. This has also been found for p-i-n devices in the superstrate configuration [336]. Thus, devices on textured substrates have higher QE in the blue due to lower front surface specular reflection, and higher QE in the red due to enhanced light trapping and lower rear specular reflection.

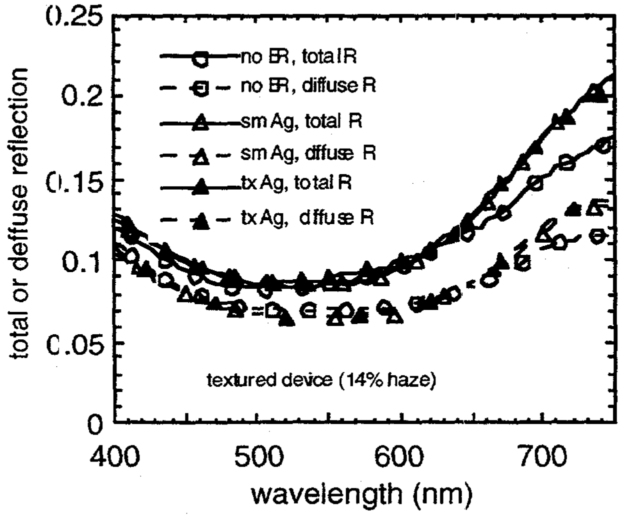

Figure 3-14 Total and diffuse reflection from front ITO/p surface for device on smooth TCO (0% haze) with no BR, smooth BR, and textured BR.

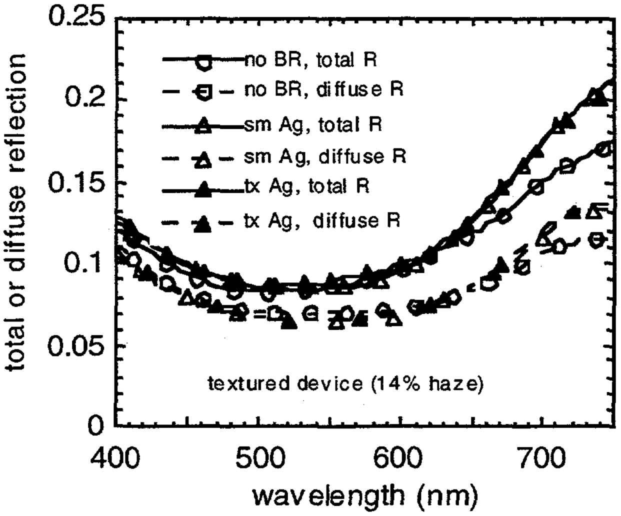

Figure 3-15 Total and diffuse reflection from front ITO/p surface for device on textured TCO (14% haze) with no BR, smooth BR, and textured BR.

3.3.3.3.1 Effect of Illumination Direction (n-i-p vs. p-i-n)

QE was also measured through the glass side on devices without any Ag BR. Figure 3-16 compares the QE through the front ITO/p contact and through the rear glass/textured TCO contact for the most textured (14% haze) device. The QE beyond 600 nm was the same through the glass side as through the ITO. This was true for devices with 1% and 5% haze as well. Thus, superstrate p-i-n and substrate n-i-p devices can achieve equivalent optical enhancement from a given textured substrate, before application of a Ag BR, in agreement with [337].

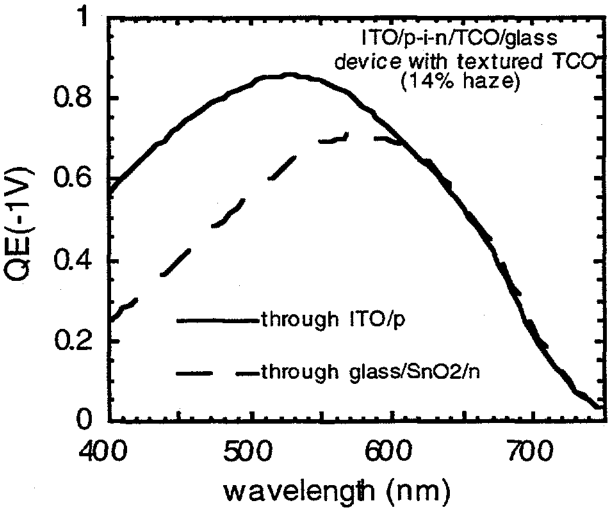

Figure 3-16 QE for device on textured (14% haze) TCO through ITO/p and glass/TCO/n sides, no BR.

3.3.3.4 Discussion and Conclusions

The effect of substrate and BR texture and BR reflectivity on optical enhancement has been analyzed and separated in ITO/p-i-n/textured TCO/glass devices with a range of substrate texture. There is negligible increase in J_{SC} and red response for haze greater than 5%, in agreement with studies on superstrate p-i-n devices. A textured substrate is significantly more effective at increasing red response than a smooth substrate with external textured Ag BR. Devices on smooth substrates with a textured Ag reflector have much higher specular reflection losses than devices on textured substrates with smooth Ag reflectors. Applying the external BR to a device on a smooth substrate increases the red QE only slightly. Instead, the reflection of red light escaping the front surface after being reflected at the BR increases due to incomplete internal reflection. Textured substrates have lower front reflection losses and hence higher blue response, thus having higher QE at all wavelengths. There appears to be no advantage to having a highly textured BR in addition to a separate highly textured substrate. These results have direct consequences for designs which propose to improve stability by depositing very thin devices on smooth substrates, to avoid shunting problems, and achieve optical enhancement with an external textured BR as studied here. Such devices will have inefficient light trapping and reduced J_{SC} compared to a device on a textured substrate, independent of whether they are a superstrate or substrate configuration.

3.4 J-V ANALYSIS OF SINGLE AND MULTIJUNCTION SOLAR CELLS

3.4.1 Introduction

To first order, the main difference between amorphous silicon (a-Si) p-i-n solar cells and crystalline silicon (c-Si) or other thin film polycrystalline p-n solar cells is that a-Si depends almost exclusively on field aided drift rather than diffusion of minority carriers to collect the photocurrent [338, 339]. Since the diffusion length is a thousand times smaller in a-Si compared to c-Si (~0.1 µm vs ~100 µm), a-Si solar cells are designed to establish a high field region in the i-layer to sweep photocarriers to the contacts before they recombine. The electric field in the i-layer is strongly dependent on the voltage bias across the device which makes the photocurrent collection dependent on the operating bias of the cell. This well-known effect complicates the J-V analysis since superposition is invalid and presents a limitation to performance of a-Si compared to other solar cell technologies [339]. Field dependent collection reduces photocurrent collection at forward bias, which primarily reduces the fill factor of the solar cell. The J-V curve will appear to have a voltage dependent shunt loss.

Numerical modeling and analysis of a-Si solar cells [340-343] typically requires a large number of material and physical parameters as input. Although such modeling provides detailed insight into the microscopic behavior of a-Si devices, many of the required material parameters are experimentally inaccessible or imperfectly known. There is not a unique relation between input parameters and solar cell performance. Thus, it is difficult to link the numerical model results to measurable device performance due the complexity of the models and uncertainty in the input parameters. While progress in refining these numerical models continues, a simple but accurate model with a few parameters closely connected to measurable data would be useful for practical device analysis and for giving physical insight.

We have previously shown [344] a method to analyze experimental a-Si J-V curves in light and dark to obtain six parameters completely characterizing the illuminated junction. The parameter $\frac{L_C}{D}$, the ratio of field driven collection length (L_C) to i-layer thickness (D) at zero volts bias, and the flat band voltage (V_{fb}) have the dominant influence on the illuminated cell performance. $\frac{L_C}{D}$ represents the i-layer quality related to the field dependent collection. In this paper, we show that this simple model is in excellent agreement with measured J-V curves for a wide range of single junction devices and conditions, including p-i-n and n-i-p cells on smooth and textured substrates, cells with a-Si and a-SiGe i-layers, in initial and stabilized states, and under AM1.5 or red or blue filtered light. After establishing the validity of the model, the influence of the device parameters on solar cell performance and limitations in existing devices are explored.

3.4.2 Device samples and J-V measurements

The single junction a-Si and a-SiGe devices which were analyzed were deposited by plasma CVD at five different laboratories. Since there was no distinctive behavior between any devices based on their source, they will not be identified. Devices had either superstrate (glass/textured SnO_2/p-i-n/back contact) or substrate (stainless steel/back contact/n-i-p/ITO) configurations. Back contacts were either Al, Ag, ZnO/Ag, or Ti/Ag. The i-layers ranged from 0.08 to 0.60 μm thick. The superstrate devices had a-SiC p-layers while the substrate devices had mc-Si p-layers. All cells were measured at room temperature (25-28°C) with illumination from an Oriel simulator at 1 sun (AM1.5, 100 mW/cm^2). Select devices were measured at lower intensity with either neutral density filters or color filters having blue (Corning #5-56, $\lambda<550$ nm) or red (Corning #2-62, $\lambda>610$ nm) transmission. Some devices were exposed to prolonged illumination (100-600 hrs) to study the effect of light soaking. a-Si devices were light soaked under white light at 1 sun intensity while a-SiGe devices were light soaked under red filtered light ($\lambda>610$ nm) to represent their light exposure in a multijunction cell structure. The red filter reduced the intensity and generation to about one third of the unfiltered values.

3.4.2.1 Analysis: the model

The analysis is based on applying established models of a-Si material and device behavior. Applicability of these models will be tested by comparison to experimental J-V data. The light-generated photocurrent is analyzed by applying a model [345] which assumes a spatially uniform field F(V). Under weakly absorbed (red) light leading to uniform carrier generation, the photocarrier transport occurs by field assisted drift since there is little diffusion. This model has been used to study transport in a-Si p-i-n devices using weakly absorbed light [345, 346]. It has also been applied to measurements under strongly absorbed (blue) light to analyze the effect of interface layers [347], and separating hole and electron transport using bifacial illumination in a-Si [348] and a-SiGe [349] p-i-n devices. In this work, we evaluate the applicability of this model to solar cells under AM1.5 illumination.

The net (measured) current through the device is:

$$J(V) = J_L(V) - J_D(V)$$

Equation 3-1

$J_D(V)$ is the forward bias diode current and $J_L(V)$ is the photocurrent, which opposes $J_D(V)$. We assume that $J_D(V)$ is independent of light intensity, i.e. values determined in the dark can be used to represent the forward diode current under illumination. This assumption will be verified in Section 3.4.2.3 by comparing J(V) and $J_L(V)$ curves measured at different intensities. The diode current is given by the standard expression:

$$J_D(V) = J_0\left(e^{\frac{qV_j}{AkT}} - 1\right)$$

Equation 3-2

where the junction voltage V_j is corrected for series resistance as:

$$V_j = V - R\,J$$

Equation 3-3

Experimental methods of determining series resistance R, diode factor A, and recombination current J_0 from dark J-V data will be shown in Section 3.4.2.2. The physical origin and temperature dependence of J_0 and A are discussed further in Section 3.4.2.3.

The photocurrent $J_L(V)$ in a-Si solar cells decreases with increasing bias because of the reduction in the internal electric field. The uniform field:

$$F(V) = \frac{\left(V_{fb} - V_j\right)}{D}$$

Equation 3-4

goes to 0 when the junction voltage V_j equals the flat band voltage V_{fb}. Experimentally, V_{fb} is obtained, after accounting for series resistance, from the voltage at which the J(V) and $J_D(V)$ curves cross, or are of equal magnitude, so that $J_L(V)=0$ at $V=V_{fb}$. In comparison, V_{OC} is the voltage at which J=0.

Crandall [345] derived an expression for $J_L(V)$ as:

$$J_L\left(V_j\right) = J_{L0}\,h\left(V_j\right)$$

Equation 3-5

where J_{L0} is the saturated (optically limited) photocurrent at far reverse bias, and the bias dependent collection efficiency $h(V_j)$ is:

$$h\left(V_j\right) = x\left(1 - e^{\frac{1}{x}}\right)$$

Equation 3-6

with:

$$x = \left(\frac{L_C}{D}\right)\left(1 - \frac{V_j}{V_{fb}}\right)$$

Equation 3-7

and:

$$\frac{L_C}{D} = \frac{\mu\tau F_0}{D} = \frac{\mu\tau V_{fb}}{D^2}$$

Equation 3-8

where $F_0 = \frac{V_{fb}}{D}$ is the field at zero applied bias. The collection length L_C is the mean distance a carrier drifts in the field before being trapped or collected. At low fields or low $\mu\tau$, the photocurrent is linear with field (i.e. ohmic), while at large fields or large μt, the photocurrent saturates at J_{L0}. Applying Equation 3-5 -> Equation 3-8 to measured J-V curves will be the focus of this work.

The effect of voltage dependent photocurrent collection is illustrated in Figure 3-17 for two cases: $\frac{L_C}{D} = 10$ corresponding to a typical a-Si device; and $\frac{L_C}{D} = \infty$ corresponding to an "ideal" solar cell, defined here as one with no bias dependent photocurrent collection. The other parameters used to calculate the J-V curves in Figure 3-17 were: $J_0=10^{-9}$ mA/ cm^2, A=1.8, R=0, J_{L0}=15 mA/cm^2, and V_{fb}=0.9 V. With $\frac{L_C}{D} = \infty$, the illuminated J-V curve is obtained by superposition of the dark forward diode current and the constant light generated current J_{L0} since h(V)=1 for all voltages. The FF is limited by the forward dark current. In contrast, with $\frac{L_C}{D} = 10$, h(V)<1 and decreases with forward bias and the J-V curve is governed largely by $J_L(V)$ as shown in the figure. The FF decreases from 82% to 68% as $\frac{L_C}{D}$ decreases from ∞ (e.g. ideal solar cell) to $\frac{L_C}{D} = 10$ (e.g. a-Si solar cell).

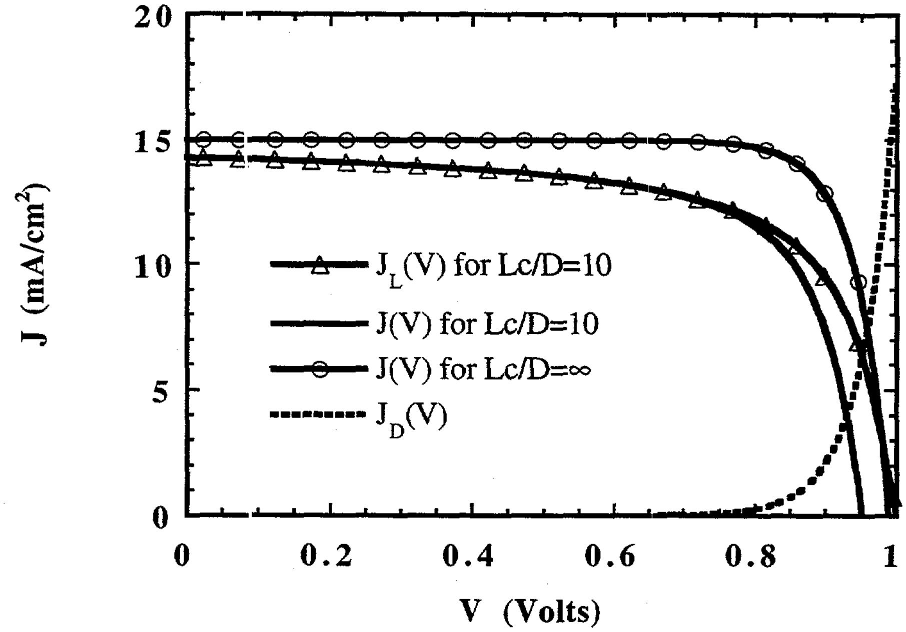

Figure 3-17 Calculated J-V curves showing model behavior for ideal ($\frac{L_C}{D}$=∞) and typical a-Si ($\frac{L_C}{D}$=10) devices. $J_L(V)$ for the a-Si is shown, and $J_D(V)$ for both devices. Other parameters given in the text.

3.4.2.2 Analysis: Applying The Model To Measured Data

From Equation 3-2 the derivative $\left(\frac{dV}{dJ}\right)$, providing $J_L(V) \ll J_D(V)$, is:

$$\frac{dV}{dJ} = R + \left(\frac{AkT}{q}\right)\left(\frac{1}{J_D(V)}\right)$$

Equation 3-9

When $\frac{dV}{dJ}$ is plotted against $\frac{1}{J_D(V)}$ the slope is $\frac{AkT}{q}$ and the intercept is R, the series resistance. Figure 3-18 shows $\frac{dV}{dJ}$ vs. $\frac{1}{J}$ for an a-Si device #4298 (D=0.5 μm) and an a-SiGe device #3342 (D=0.15 μm). Using the value of R from the intercepts in Figure 3-18, a graph of log $J_D(V)$ vs V_j yields a straight line with slope is $\frac{q}{AkT}$ and intercept J_0, as shown in Figure 3-19. Plotting the data against V_j corrects the measured voltage for the series resistance losses. Values of R, A and J_0 obtained from slopes and intercepts of the data in Figure 3-18 and Figure 3-19 are shown in Table 3-14 (a-Si device) and Table 3-15 (a-SiGe device). Typically, the parameter A from the two different methods agree within +/-5%. Analyzing $\frac{dV}{dJ}$ vs. $\frac{1}{J}$ and log J vs. V under illumination such that $J_L(V) >> J_D(V)$ leads to errors since the voltage dependence of $J_L(V)$ dominates the voltage dependence of J(V) instead of Equation 3-2 and Equation 3-9.

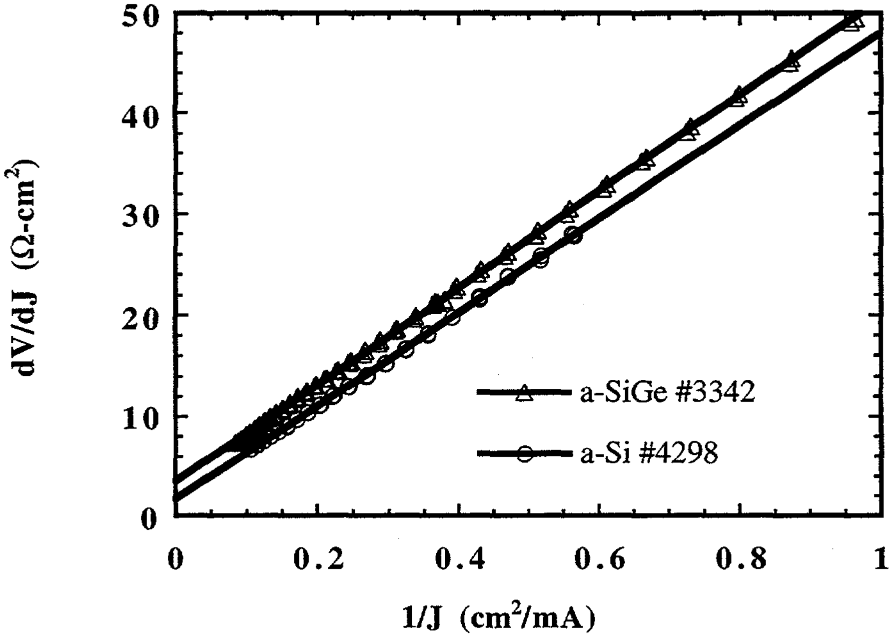

Figure 3-18 Plot of dV/dJ vs 1/J for a-Si and a-SiGe device, from analysis of measured dark J-V data. Slope is AkT/q and intercept is R.

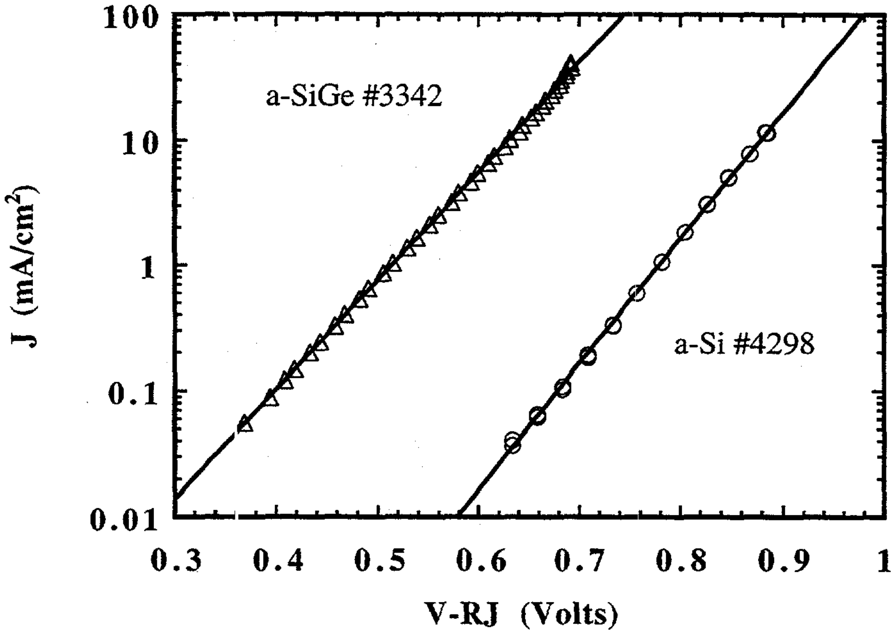

Figure 3-19 Plot of Log J vs (V-JR) from measured dark J-V data for same two devices as in Figure 3-18. Slope gives q/AkT and intercept is J_0.

Table 3-14 Parameters obtained from fitting measured JV curves of a-Si device #4298 under AM1.5 illumination light in initial and light soaked state (200 hrs.).

state	J_{L0} mA/cm^2	V_b Volts	L_C/D	J_0 x10^{-8} mA/cm^2	A	R Ω-cm^2
initial	13.6	0.92	20.7	2	1.7	1.6
soaked	13.6	0.90	7.0	20	1.9	1.2

state	J_{SC} mA/cm^2	V_{OC} Volts	FF %	Power mW/cm^2
initial	13.3	0.859	71.6	8.2
soaked	12.0	0.837	64.3	6.4

Table 3-15 Parameters obtained from fitting measured JV curves of a-SiGe device #3342 under AM1.5 illumination and red filtered light in initial and light soaked state (200 hrs. red light).

Illum.	state	J_{L0} mA/cm^2	V_b Volts	L_C/D	J_0 x10^{-5} mA/cm^2	A	R Ω-cm^2
AM1.5	initial	20.1	0.65	8.1	6	2.0	2.1
	soaked	20.1	0.63	5.6	20	2.1	2.3
red	initial	6.8	0.61	7.7	6	2.0	2.1
	soaked	6.8	0.61	5.1	20	2.1	2.3

Illum.	state	J_{SC} mA/cm^2	V_{OC} Volts	FF %	Power mW/cm^2
AM1.5	initial	20.1	0.622	59.7	7.0
red	soaked	20.1	0.585	55.7	6.0
	initial	6.8	0.577	61.1	2.2
	soaked	6.8	0.540	57.7	1.8

The photocurrent $J_L(V)$ is obtained by adding the measured diode current $J_D(V)$ in the dark to the measured current J-V under illumination as per Equation 3-1. J_{L0} was obtained from the current at far reverse bias. The primary fitting parameter, $\frac{L_C}{D}$, was varied until an optimum fit was obtained. In practice, V_{fb} was sometimes adjusted slightly (~10 mV) from the value determined experimentally from the intercept of the light and dark currents in order to improve the fit around V_{OC}. The fitting criteria was to minimize the sum, over all voltages, of the absolute value of the difference between the measured J-V and Equation 3-1 while forcing measured and calculated values to agree within ±0.5% at maximum power. Figure 3-20 shows the measured and calculated J-V data under AM1.5 illumination for the a-Si and a-SiGe devices whose dark J-V data were analyzed in Figure 3-18 and Figure 3-19. The parameters J_{L0}, V_{fb} and $\frac{L_C}{D}$ used to calculate $J_L(V)$ are in Table 3-14 Table 3-15 along with the solar cell performance parameters V_{OC}, J_{SC}, FF, and efficiency. Since measured and calculated performance typically agree within 0.5%, no distinction is made between them in the rest of the paper. The good agreement in Figure 3-20 from reverse bias to beyond V_{OC} indicates that the model can accurately represent all portions of the J-V characteristic for both a-Si and a-SiGe solar cells. The close agreement shown in Figure 3-20 was typical of most devices analyzed.

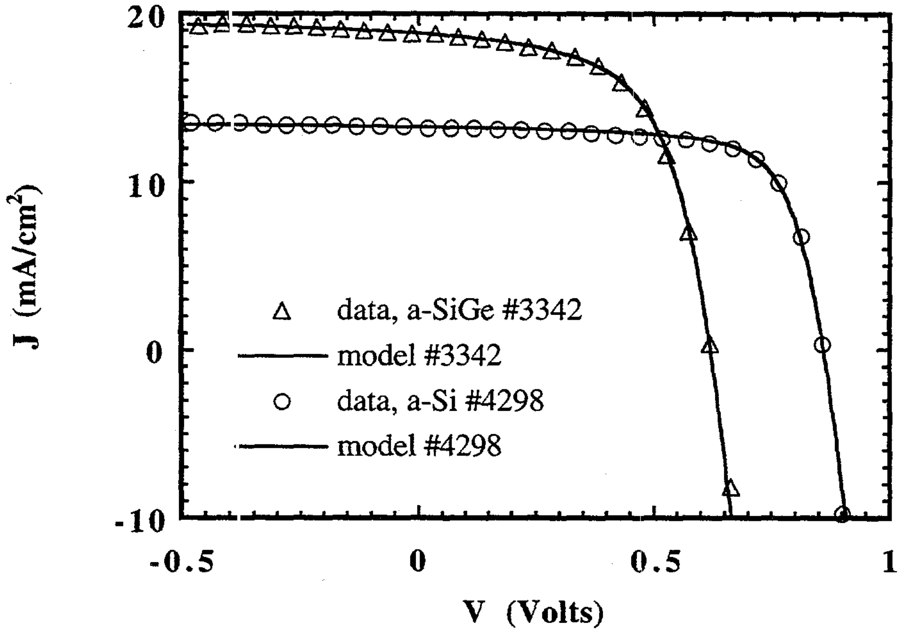

Figure 3-20 Measured (under AM1.5 light) and calculated J-V for same two devices. Calculated values obtained with parameters in Table 3-14 (#4298) and Table 3-15 (#3342). Agreement was within 0.2 mA/cm^2 from reverse bias to V_{OC}. V_{OC}, J_{SC} and FF are also shown in Table 3-14 and Table 3-15.

3.4.2.3 Assumptions, approximations and limitations of the model

It was assumed that the forward bias diode current $J_D(V)$ was independent of illumination so that J(V) can be separated algebraically into a $J_L(V)$ term and a $J_D(V)$ term. The assumption is necessary because $J_D(V)$ was obtained at different illumination than J(V). This assumption and the actual procedure used here of separating $J_L(V)$ from J(V) can be verified as follows. Applying Equation 3-1 and Equation 3-5 to data measured at two different intensities, and taking the difference of the measured currents $J_1(V)$ and $J_2(V)$ gives:

$$J_1(V) - J_2(V) = \left[J_{L01}\,h(V) - J_{D1}(V)\right] - \left[J_{L02}\,h(V) - J_{D2}(V)\right]$$

Equation 3-10

where $J_1(V)$ is at higher intensity than $J_2(V)$. This can be rearranged to give the collection function h(V) as follows:

$$h(V) = \frac{J_1(V) - J_2(V)}{J_{L01} - J_{L02}}$$

Equation 3-11

only if the forward current $J_D(V)$ is independent of intensity, i.e. $J_{D1}(V) = J_{D2}(V)$. This is how $\frac{L_C}{D}$ was fit in Figure 3-20, with $J_{L02} = 0$ since $J_2(V)$ was in the dark. Figure 3-21 shows measured data from a-Si p-i-n cell #4484 (Table 3-16) with D=0.45 μm where $J_1(V)$ was measured at 1 sun and $J_2(V)$ was measured at 0, 0.25, or 0.63 suns. The excellent agreement between the curves demonstrates that $J_L(V)$ and h(V) at a given intensity can be obtained with $J_D(V)$ measured in the dark as well as in the light at lower intensity. Figure 3-21 shows that it is not necessary to analyze the forward J-V data to determine A, J_0 and R_S in order to obtain $\frac{L_C}{D}$ and V_{fb}. Instead, J(V) at low intensity can be subtracted from J(V) at higher intensity and the resulting h(V) curve can be fit instead, eliminating the need for analyzing the dark diode. In the rest of this paper, we fit $\frac{L_C}{D}$ to $J_L(V)$ obtained with $J_2(V) = J_D(V)$ from the dark, and have analyzed the dark forward J-V to obtain A, J_0 and R_S.

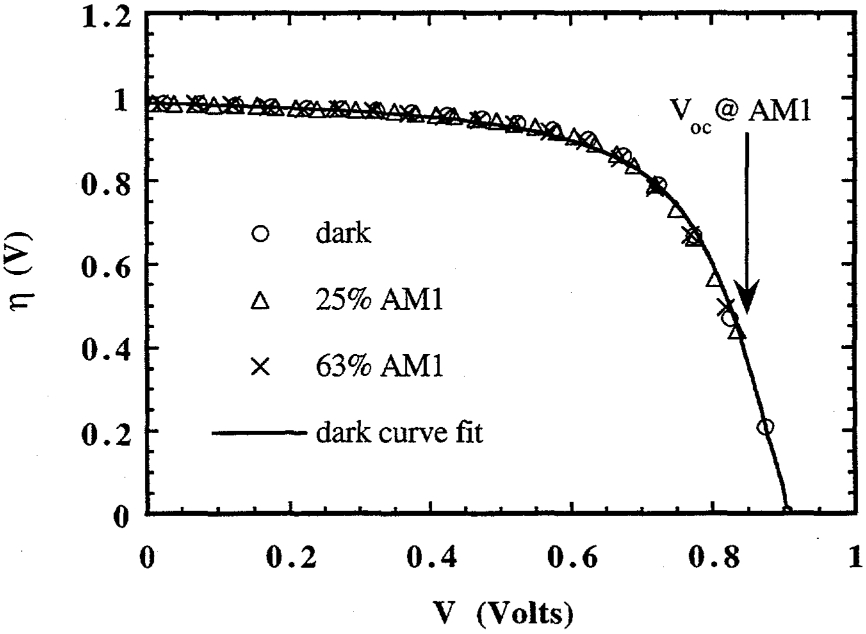

Figure 3-21 Experimental collection efficiency from Equation 3-11 for a-Si p-i-n #4484. $J_1(V)$ was measured at one sun, and $J_2(V)$ was obtained for three illumination intensities (dark, 0.25, and 0.63 suns).

Table 3-16 Parameters obtained from fitting measured JV curves of a-Si device #4484 under AM1.5 (100 mW/cm^2) light and low intensity white, red, and blue light.

Illum.	J_{L0} mA/cm^2	V_b Volts	L_C/D	J_0 x10^{-9} mA/cm^2	A	R Ω-cm^2
AM1.5	16.5	0.88	14.0	3	1.5	1.7
2% AM1.5	0.36	0.77	24.0	3	1.5	1.7
2% red	0.18	0.73	24.1	3	1.5	1.7
2% blue	0.15	0.79	15.3	3	1.5	1.7

Illum.	J_{SC} mA/cm^2	V_{OC} Volts	FF %	Power mW/cm^2
AM1.5	15.9	0.842	68.7	7.6
2% AM1.5	0.36	0.714	74.2	0.19
2% red	0.18	0.684	74.4	0.09
2% blue	0.15	0.679	73.1	0.07

The assumption of a uniform field is required to derive the simple closed form expression for h(V). This is a common approximation in the analysis of a-Si p-i-n solar cells [345-349]. In reality, the field varies across the i-layer depending on illumination and trapped space charge. However, numerical models [350, 351] have found that photocurrent collection was more sensitive to the limiting carrier $\mu\tau$ value than to the actual field profile. For example, reference [351] reports that the $\mu\tau$ value giving the best fit to data varies by less than a factor of two for a wide range of assumed field profiles. First order corrections to Equation 3-4 have been proposed which divide the field into a strong bias-independent "interface" field and weaker field in the bulk i-layer having the standard linear bias dependence [350, 352]. These corrections introduce two additional unmeasureable fitting parameters, the width and potential of this "interface" field region. Equation 3-6 has given very good agreement to the J-V data of all devices measured so far, including after light soaking. We speculate that the uniform field approximation accurately represents limiting carrier photocurrents in a wide variety of real a-Si p-i-n devices because it is the average field which determines the collection probability under white light illumination. Since we find an excellent fit with the simple uniform field approximation, we avoid *ad hoc* modifications which introduce unnecessary additional parameters.

The assumption of uniform generation is also required to simplify the analysis since carrier diffusion can then be ignored. The generation rate profile has been calculated [353] using an optical model developed elsewhere [354]. Figure 3-22 shows the generation profile for a p-i-n device with D=0.4 µm, a 1.72 eV bandgap, scattering due to front texture and a back contact with reflectivity R_b=0.9 for three illumination spectra. The blue and red filtered spectra were determined by reducing the AM1.5 spectrum by the transmission of the blue and red filters used in this study. The red generation profile is very uniform, as expected. The AM1.5 generation is nearly uniform beyond the first 0.1 µm, changing by less than a factor of two between 0.1 and 0.4 µm. The average generation obtained from averaging the total integrated photocurrent over the i-layer is $G_0 = \frac{J_{L0}}{qD}$ and is given in the caption for Figure 3-22 for all three profiles.

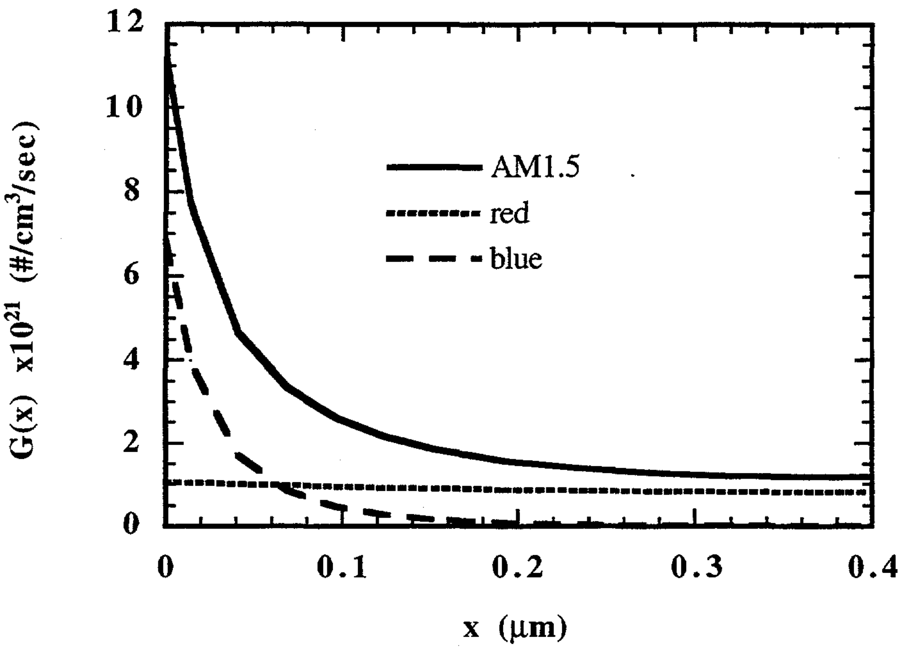

Figure 3-22 Calculated generation profiles for typical single junction a-Si p-i-n cell described in text, shown for the three illumination conditions used in this work. The volume averaged generation: $G_0 = \frac{J_{L0}}{qD}$ is; 2.1 for AM1.5, 0.9 for red and 0.7 for blue (x10^{21} #/cm^3/sec) respectively.

Equation 3-2 and Equation 3-9 show specific temperature dependencies which are not explored in this work since all measurements were at 25-28°C. The temperature dependence of J_0 and A have been extensively studied in a-Si p-i-n solar cells [355-359]. J_0 has been shown to have the form:

$$J_0 = J_{00} e^{\frac{-E_a}{kT}}$$

Equation 3-12

Experimental results indicate that both J_{00} and E_a are closely related to recombination at or near the p-i interface not the bulk [355-359]. Values of J_0 and A and their correlation to other properties presented here are valid at room temperature.

The collection model assumes all carrier collection occurs by drift and represents all photocarrier recombination losses with a single µt value, thus lumping together recombination at bulk i-layer defects or at interfaces. Whether this single µt value represents the carrier with the smaller µt (i.e. limiting carrier argument in references [340, 350]) or the longer µt (i.e. the sum of the electron and hole values in references [345, 348] will be discussed in Sections 3.4.3 and 3.4.4.

3.4.3 Results

3.4.3.1 Voltage dependence of quantum efficiency

The quantum efficiency (QE) is typically measured with a phase sensitive lock-in detector which senses only the photocurrent response due to the chopped ac monochromatic light. It rejects the dc component of the forward bias current. Thus, QE should measure $J_L(V)$ at each wavelength not J(V). Integration of the product of the QE with a given illumination spectrum gives the photocurrent that would be measured when the device was illuminated by that spectrum, independent of the forward diode current.

The QE of a-Si p-i-n device #4484 was measured from 350 to 750 nm with a variable voltage bias across the cell. The cell was illuminated with a dc bias light of about 1 sun intensity. At each bias voltage, the QE was integrated with the AM1.5 spectrum to obtain the expected photocurrent. Figure 3-23 shows the results of these QE measurements along with the measured and calculated J(V) and $J_L(V)$ characteristics. $J_L(V)$ was calculated with parameters in Table 3-16 for 1 sun illumination. The J(V) data decreases more rapidly than $J_L(V)$ or QE(V) beyond 0.6V because of the increasing forward bias current. The integrated QE values and independently calculated $J_L(V)$ values are in very good agreement at all voltage biases, going to zero at V_{fb}. This confirms that QE(V) and $J_L(V)$ have the same voltage dependence, given by Equation 3-6, and are independent of the forward diode current. This agreement further verifies application of the collection model to a-Si p-i-n solar cells under typical 1 sun illumination.

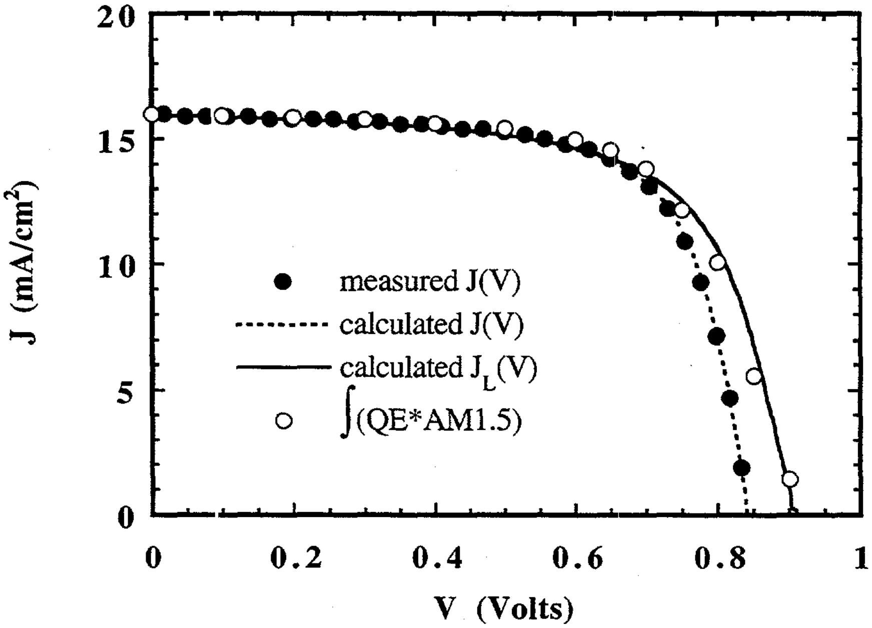

Figure 3-23 Measured and fitted J(V) and $J_L(V)$ for a-Si p-i-n #4484. Values of QE measured over a range of voltage bias and integrated with AM1.5 spectrum are shown.

It has been shown that the apparent decrease in QE with bias can be due to series resistance effects [360] in ideal Si devices without any voltage dependent collection. When $J_L(V)$ was recalculated without any resistance, the resulting curve differed negligibly from that shown in Figure 3-23, which was calculated with the actual value of $R=1.7\ \Omega\text{-cm}^2$. Thus, the voltage dependent QE in a-Si is due to field dependent collection h(V) in the i-layer not series resistance effects.

3.4.3.2 Effect of intensity and illumination spectra on $\frac{L_C}{D}$ and V_{fb}

J-V curves measured under color filtered and neutral density filtered illumination were analyzed because the intensity and spectral dependence of $\frac{L_C}{D}$, or μt, and V_{fb} are useful to interpret other measurements. For example, it is common to measure a-SiGe devices under long pass filtered red light to simulate their behavior in a multijunction device [361]. But filtering the spectrum also reduces the total illumination intensity. Transport properties in a-Si materials are known to be intensity dependent due to trapping of photocarriers and movement of the Fermi level under illumination [362, 363] and spectrally dependent as well [364, 365].

The collection length analysis has been applied previously to devices measured under non-uniformly absorbed light [347-349]. Depending which contact layer the device is illuminated through, the resulting μt value is identified with either the hole, electron, or their sum. It is generally acknowledged that photocarrier collection in a p-i-n cell is dominated by the "limiting carrier" [340, 350]. Under uniform illumination, the carrier with the shorter drift length limits current collection, typically holes. Under strongly absorbed (blue) illumination through the p-layer, the limiting carrier model predicts that $\frac{L_C}{D}$ is due to electron μt, assuming electron μt is much greater than hole μt. However, interface recombination [341] or back diffusion [345, 350] will reduce the current collection for strongly absorbed light which can be mistaken for spectral dependence of the apparent bulk μt. Thus, the value of μt resulting from measurements under strongly absorbed light will still be that of the electron, but whether it is due to bulk or interface-related recombination cannot be simply determined from these measurements.

The same a-Si device #4484 whose J-V data is shown in Figure 3-21 and Figure 3-23 was measured under a wide range of illumination conditions. The intensity was varied over two orders of magnitude with neutral density filters for three spectral distributions: no color filter (standard AM1.5 spectrum), a blue filter ($\lambda<550$ nm) and red filter ($\lambda>610$ nm). The same forward diode parameters J_0, A, and R (Table 3-16) were used for analyzing all filtered J-V tests since the forward diode was independent of intensity (Figure 3-21). J_{SC} was proportional to intensity and J_{L0} for all illumination conditions, and is used here to represent intensity.

Figure 3-24 shows the dependence of $\frac{L_C}{D}$ on J_{SC}, i.e. intensity. $\frac{L_C}{D}$ decreases steadily with intensity under red light but is independent of intensity under blue light. The power dependence m of $\frac{L_C}{D}$ on red light intensity I is I^{-m} with m=0.2. Under white light, $\frac{L_C}{D}$ decreases with intensity similar to the value under red light. Studies of the intensity dependence of hole transport on i-layers, using the steady state photocarrier grating (SSPG) or surface photovoltage (SPV) techniques, have found that hole μt also have $m\approx0.2$ [366-368]. The electron μt, from photoconductivity, can have a wide range of intensity dependence with $m\approx0.1\text{-}0.4$ Thus, the intensity dependence m=0.2 for red light in Figure 3-24 is consistent with either hole or electron collection . The intensity independence for blue light suggests that $\frac{L_C}{D}$ for strongly absorbed light may be determined by something other than bulk recombination, such as interface recombination [355, 356, 359, 369] and back diffusion [345, 350, 370]. Results for $\frac{L_C}{D}$, or any photocurrent measurement, at short wavelengths should be interpreted with great caution because Figure 3-24 indicates that they do not measure a bulk transport property.

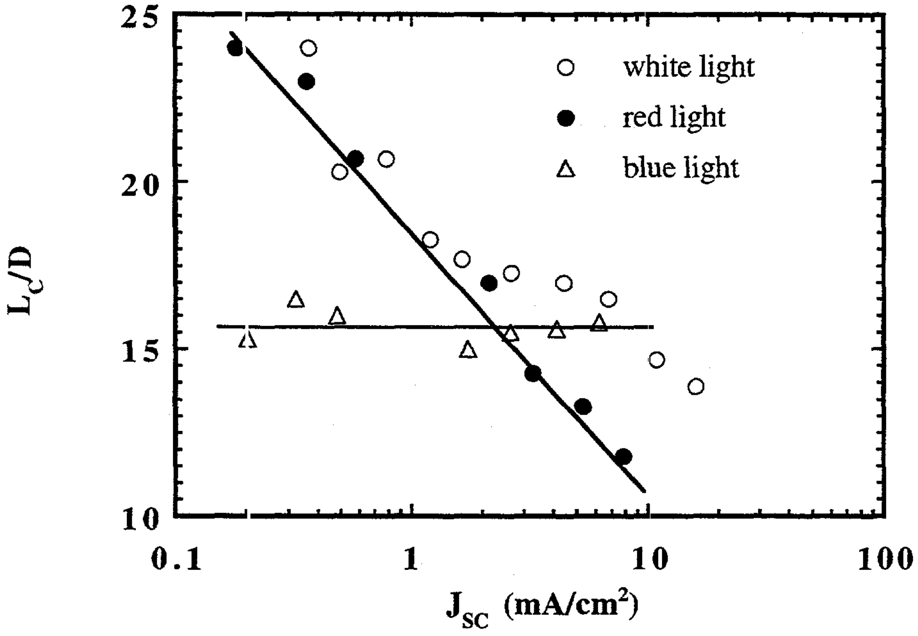

Figure 3-24 $\frac{L_C}{D}$ vs J_{SC} for a-Si device #4484 for unfiltered, red and blue filtered light at different intensities. Solid lines to guide the eye.

Figure 3-25 shows that V_{fb} depends on both intensity and spectrum. Figure 3-26 shows that V_{OC} changes linearly with V_{fb} as intensity varies but the slope depends on the spectrum. For a given value of V_{fb}, V_{OC} is lowest for blue light. This suggests that back diffusion and interface recombination losses, which predominate with blue light, reduce V_{OC} more than bulk recombination at an equivalent generation rate. Figure 3-25 and Figure 3-26 are critical to understanding the physical significance of V_{fb}, showing that it is not an intrinsic property of the device but depends on external variables. This is discussed further in section 3.4.4.3. Figure 3-24 and Figure 3-25 show that $\frac{L_C}{D}$ and V_{fb} for unfiltered white light, typically used for standard solar cell testing, behave more like values obtained under red light (uniformly absorbed) than blue light (strongly absorbed), confirming that the assumption of uniform generation applies to white light conditions.

Series resistance also has a major impact on intensity dependent measurements, especially FF. This is discussed in more detail in section 3.4.4.4.

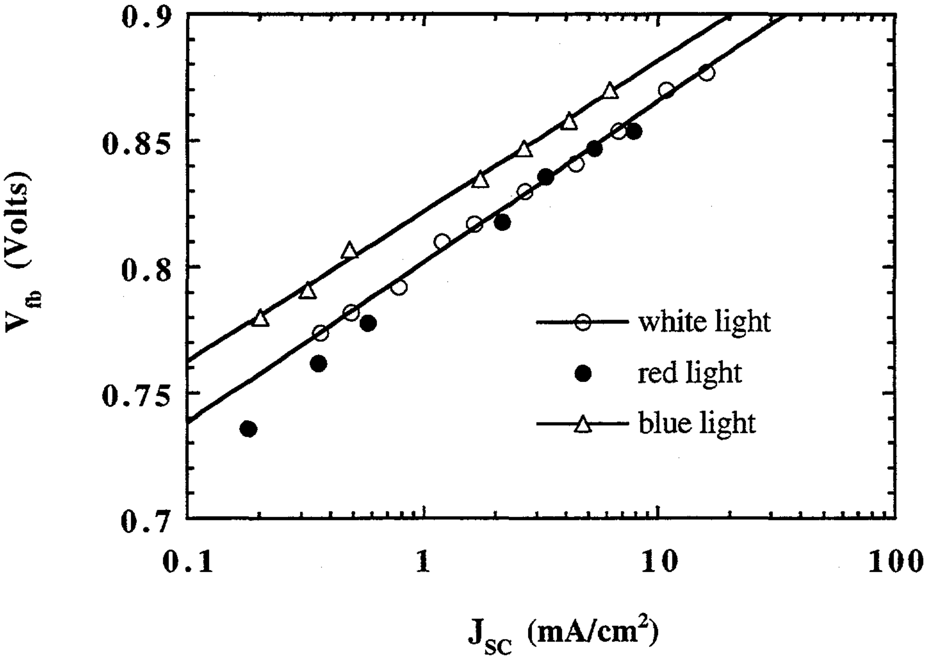

Figure 3-25 V_{fb} vs J_{SC} for a-Si device #4484 for unfiltered, red and blue filtered light at different intensities. Solid lines to guide the eye.

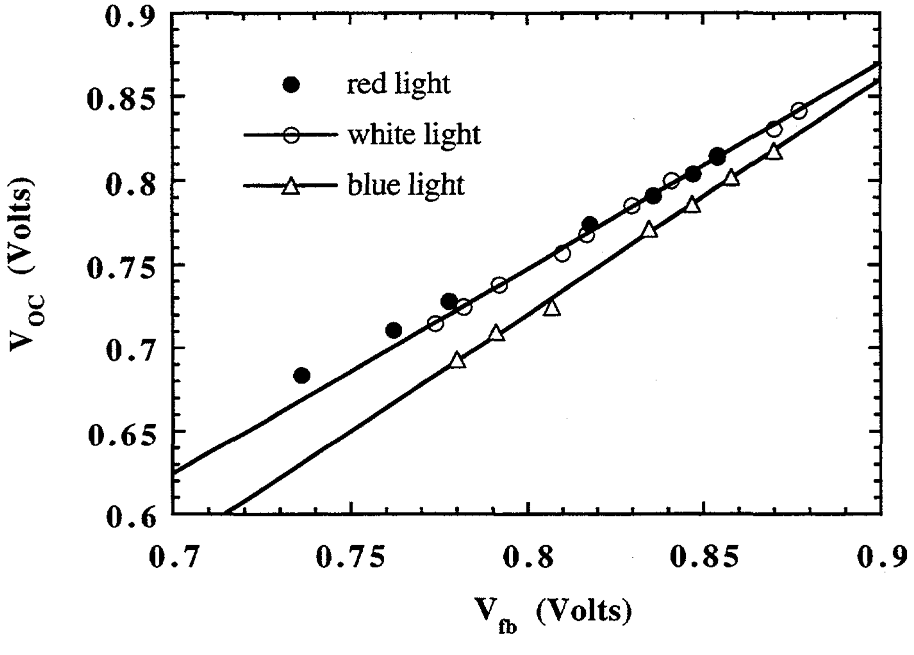

Figure 3-26 V_{OC} vs V_{fb} for a-Si device #4484 for unfiltered, red and blue filtered light at different intensities. Solid lines to guide the eye.

3.4.3.3 Stability and degradation due to light soaking

It is well known that light exposure increases the defect density in a-Si material and reduces the μt product of electrons and holes. Generally a logarithmic decrease in μt with light exposure time t is reported with $\mu\tau \propto t^{-b}$. Therefore, it is expected that $\frac{L_C}{D}$ should decrease with light soaking. Degradation studies of electron μt from photoconductivity [367, 371] have generally established that b~0.33 . Degradation studies of hole μt from SSPG in a-Si [372-374] have all found b~0.1, a much smaller degradation rate than found for electrons. We are unaware of any published degradation studies of hole μt in a-SiGe materials.

The two devices analyzed in Figure 3-18, Figure 3-19 and Figure 3-20 were exposed to 200 hours light soaking. The a-Si device #4298 was illuminated with unfiltered ELH lamps while the a-SiGe device was illuminated with red light (λ>610 nm) from filtered ELH lamps. Figure 3-27 shows the measured and calculated J-V curves under red test illumination of the a-SiGe device before and after light soaking. Parameters for each device after light soaking are shown in Table 3-14 and Table 3-15. These changes with light soaking are typical of what we have found for other devices in this study. The two parameters which show the largest change are J_0 and $\frac{L_C}{D}$. This is expected since they both represent recombination mechanisms, and light soaking increases the density of recombination centers. $\frac{L_C}{D}$ for the a-Si device decreased from 20.7 to 7.0, while that of the a-SiGe device decreased from 8.1 to 5.6. In general, we have found that J_0 increases by a factor of 5-15 and $\frac{L_C}{D}$ decreases by a factor of 2-3 for a-Si devices with D=0.4-0.5 µm after several hundred hours light soaking at 1 sun intensity. Other parameters show much smaller, less systematic changes.

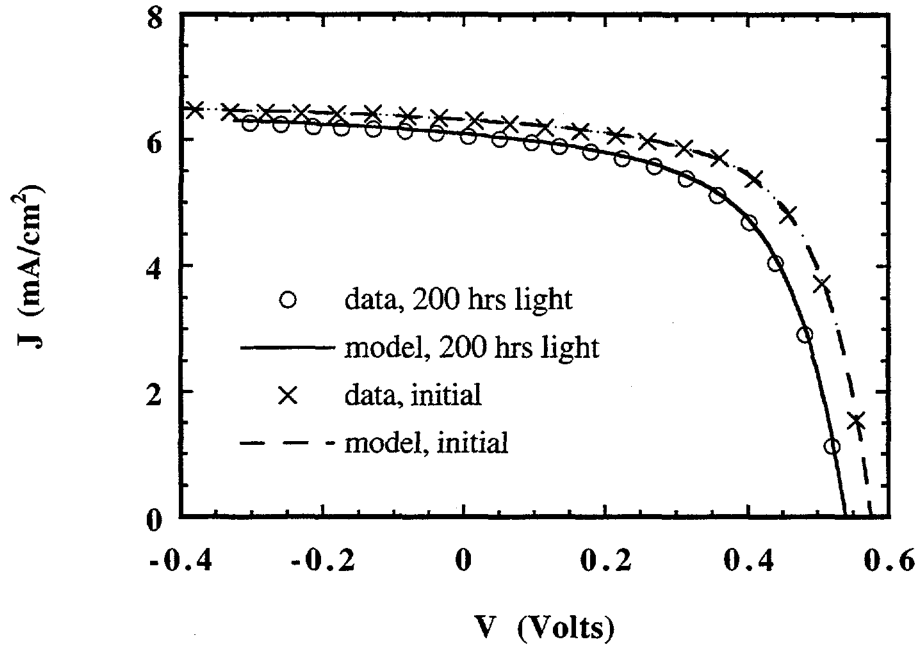

Figure 3-27 Measured (under red light) and calculated J-V for a-SiGe device #3342 in initial and light soaked states. Calculated with parameters in Table 3-15.

Figure 3-28 shows that the degradation of $\frac{L_C}{D}$ for both devices is nearly logarithmic with light soaking time. $\frac{L_C}{D}$ for a-Si device #4298 decreased at a greater rate than for the a-SiGe device. This is partially due to light soaking the a-Si device at a higher intensity. The degradation rate b=0.13 for the a-Si device is very comparable to values found for holes by SSPG on a-Si films.

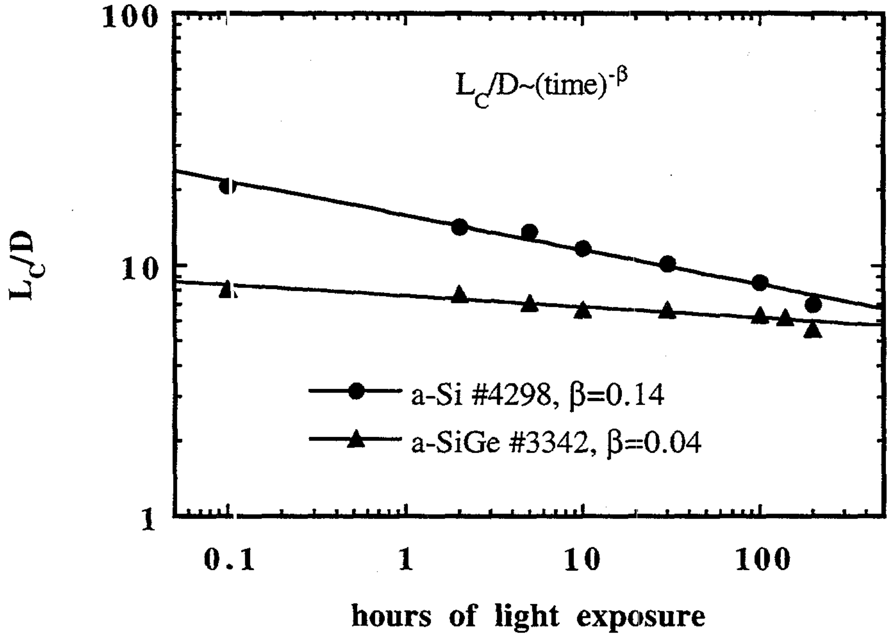

Figure 3-28 Change in $\frac{L_C}{D}$ over 200 hours of light soaking. #4298 was soaked under white light while #3342 was soaked under red light.

An a-Si device #4304, having a 0.50 µm thick i-layer deposited at low temperature (175°C) without any H_2 dilution, was light soaked. These deposition conditions were expected to yield large degradation with light soaking [375]. The J-V curves were analyzed in the initial state and after 100 hours of light soaking as shown in Figure 3-29. Table 3-17 shows the parameters and device performance in each state. The FF degraded from 69 to 49%. This corresponded to a decrease in $\frac{L_C}{D}$ from 14.2 to 3.1, obtained by fitting with the degraded values of J_0 and V_b from Table 3-17. To determine if the effect of light soaking could be described solely by changes in $\frac{L_C}{D}$, the J-V curve after light soaking was also fit with the same five parameters (A, J_0, R, J_{L0}, and V_{fb}) as determined for the *annealed* state, changing only $\frac{L_C}{D}$. Figure 3-29 shows that a good fit to the light soaked data is possible by changing *only* $\frac{L_C}{D}$, from 14.2 to 2.7. The J-V performance is nearly independent of the forward diode parameters for low values of $\frac{L_C}{D}$. We conclude that the effect of light soaking can be represented almost entirely by changes in $\frac{L_C}{D}$ even though V_{fb} and J_0 also degrade.

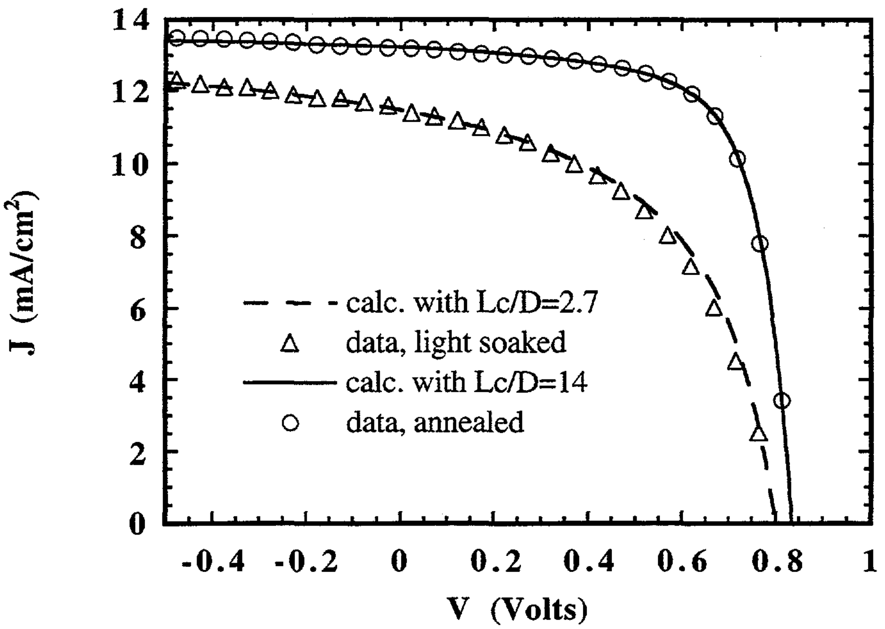

Figure 3-29 . Measured and calculated J-V for a-Si device #4304 in annealed and light soaked states. Calculations are shown using annealed parameters in Table 3-17 with $\frac{L_C}{D}$ =14.0 from the annealed state, and with $\frac{L_C}{D}$ =2.7 to represent the light soaked state.

Table 3-17 Parameters obtained from fitting measured JV curves of a-Si device #4304 under AM1.5 illumination in initial and light soaked state (100 hrs.). The last row (soaked*) shows results of calculating device performance with the same parameters as initial state except for $\frac{L_C}{D}$. Data from first and third rows are plotted in Figure 3-29.

state	J_{L0} mA/cm^2	V_b Volts	L_C/D	J_0 x10^{-8} mA/cm^2	A	R Ω-cm^2
initial	13.7	0.87	14.0	7	1.7	1.6
soaked	13.6	0.83	3.1	200	2.3	2.6
soaked*	13.7	0.87	2.7	7	1.7	1.6

state	J_{SC} mA/cm^2	V_{OC} Volts	FF %	Power mW/cm^2
initial	13.2	0.834	68.7	7.6
soaked	11.5	0.809	49.4	4.6
soaked*	11.3	0.811	50.1	4.6

3.4.3.4 Correlation of experimental results

Results of analysis of 23 cells, both a-Si and a-SiGe, are shown in Figure 3-30 -Figure 3-32. All devices were measured under AM1.5 illumination. Figure 3-30 shows the dependence of FF on $\frac{L_C}{D}$ in the initial and stabilized states. The solid line traces the degradation of a single a-Si device #4298 during a 200 hour light soaking. The dependence of FF on $\frac{L_C}{D}$ is similar whether cells degrade due to increasing Ge or light induced defects. Note that $\frac{L_C}{D}$ greater than 30 is required for FF to exceed 75% at 1 sun intensity.

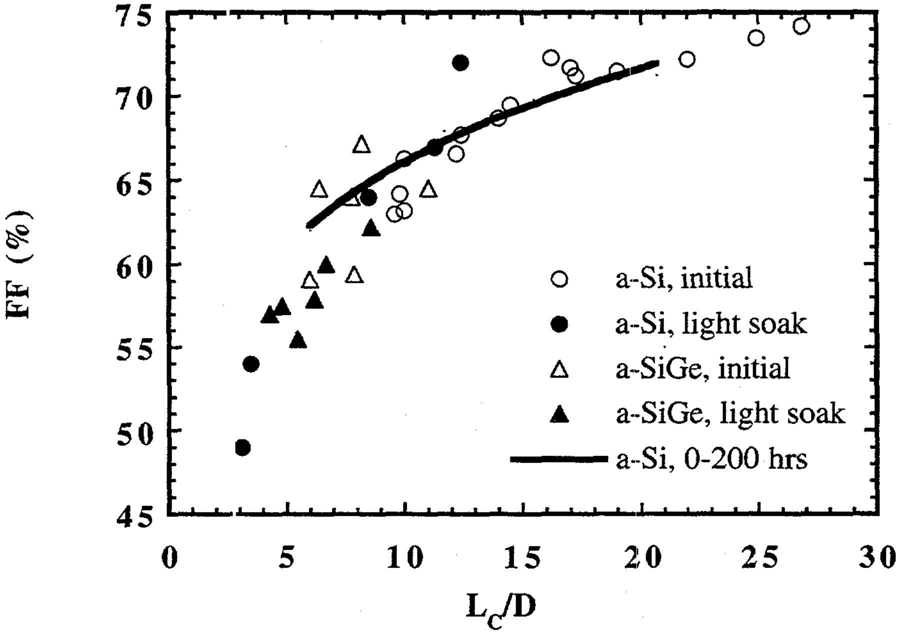

Figure 3-30 Correlation of FF with $\frac{L_C}{D}$ from 23 a-Si or a-SiGe solar cells. Both initial and light soaked values are shown for some devices. Solid line is a-Si device #4298 (Table 3-14) shown for various intervals during 200 hr. light soaking.

Figure 3-31 shows that V_{OC} is linearly proportional to flat band voltage V_{fb}, with a best fit of $V_{OC} = V_{fb} - 0.040$ V. Figure 3-32 shows that V_{OC} has a general inverse trend with log J_0, but with a large degree of scatter. J_0 can vary by over an order of magnitude without changing V_{OC}. This is not due to uncertainty on determining J_0; rather, it indicates V_{OC} is not limited by J_0. This is discussed further in section 3.4.4.4. Comparing Figure 3-31 and Figure 3-32, V_{OC} is more closely correlated with V_{fb} than J_0. The voltage dependent photocurrent $J_L(V)$ is a limitation to increasing V_{OC} which is usually not considered when analyzing V_{OC} losses.

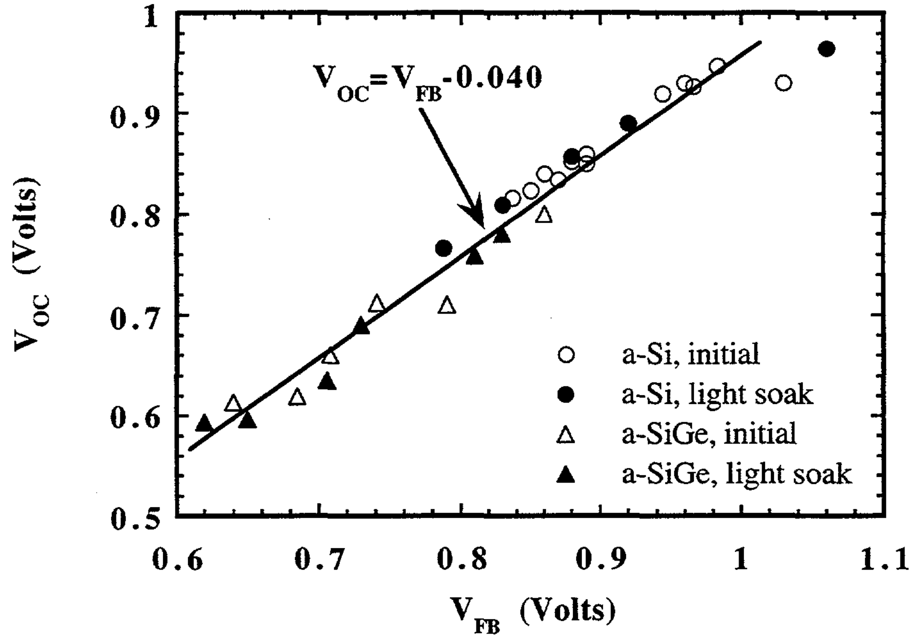

Figure 3-31 Correlation of V_{OC} with V_{fb} from 23 a-Si or a-SiGe solar cells. Both initial and light soaked values are shown for some devices.

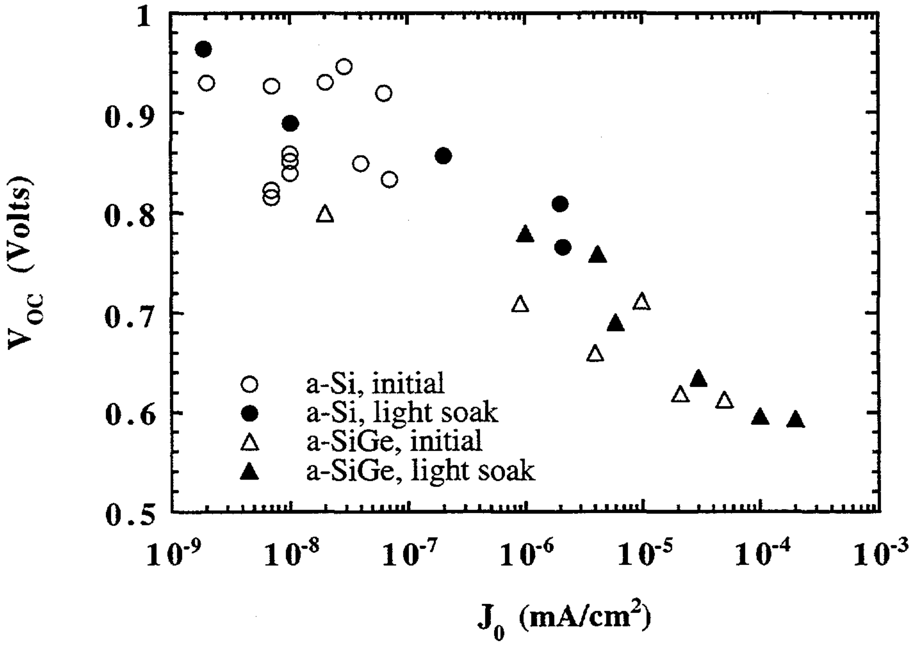

Figure 3-32 Correlation of V_{OC} with J_0 from 23 a-Si or a-SiGe solar cells. Both initial and light soaked values are shown for some devices

3.4.3.4.1.1 i-layer thickness dependence of $\frac{L_C}{D}$ and $\mu\tau$

From Equation 3-8, the $\mu\tau$ product for the carrier limiting the collection can be determined knowing $\frac{L_C}{D}$, D and V_{fb}. Figure 3-33 and Figure 3-34 show the thickness dependence of $\frac{L_C}{D}$ and μt for all of the devices analyzed in this study in the annealed (initial) state. $\frac{L_C}{D}$ for the a-Si devices with D>0.2 μm is consistent with a thickness independent drift length of L_C=5.5 μm as shown by the inverse relation between $\frac{L_C}{D}$ and D. The thinnest a-Si device has a much smaller $\frac{L_C}{D}$ (~16) than expected for its thickness (~0.08 μm) by extrapolating from the thicker devices yet it was a very high quality device (FF=72%) developed as a top cell of a high efficiency triple junction stack. Figure 3-34 shows that μt for a-Si i-layers becomes thickness independent with a value of 3-4x10^{-8} cm^2/V for D>0.2 μm.. The similar μt values between devices deposited in five different laboratories with different a-Si i-layer conditions and device structures is to be expected because these devices were produced under nearly optimized conditions by each group. The greater variation in μt for a-SiGe devices may be due to the greater variation and lack of optimization in deposition conditions. Note that the thinnest a-Si device has a very low μt, comparable to the thinnest a-SiGe device which had E_{gi}=1.4 eV. Thinner devices have a greater fraction of the total carriers generated closer to the p-i interface compared to thicker devices. Carriers generated near the p-i interface may have a different limiting recombination mechanism from bulk generated carriers as suggested by Figure 3-24 and Figure 3-26. Interface recombination [355, 356, 359, 369] or back-diffusion [340, 350, 370] of carriers generated near the interface may dominate bulk recombination losses in thin cells. This has a major impact on design and performance in multijunction cells where all layers will be thin for current matching and improved stability. More detailed numerical analysis of bulk and interface losses are needed.

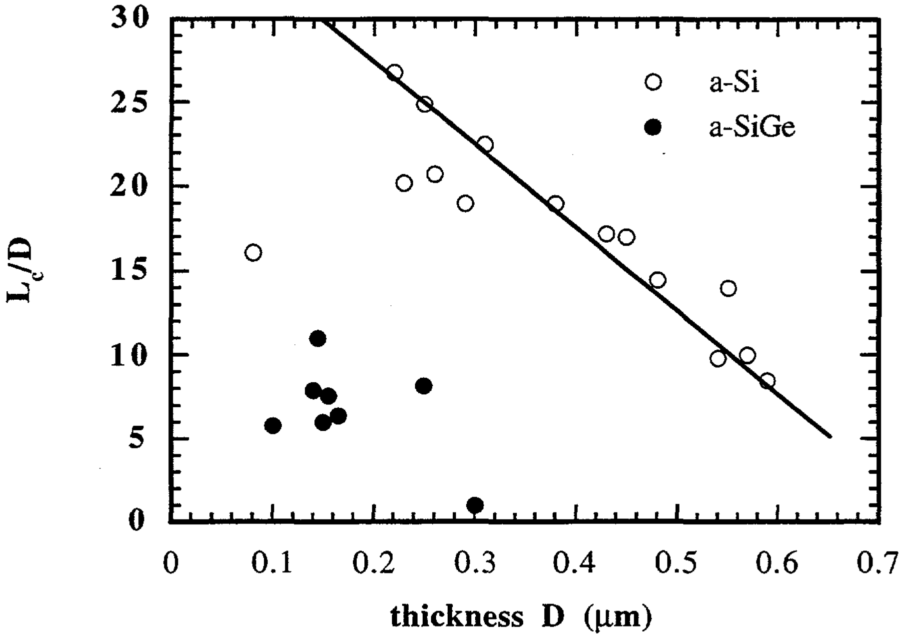

Figure 3-33 $\frac{L_C}{D}$ **vs D for 23 a-Si and a-SiGe devices in initial state. The straight line has a slope of -1.**

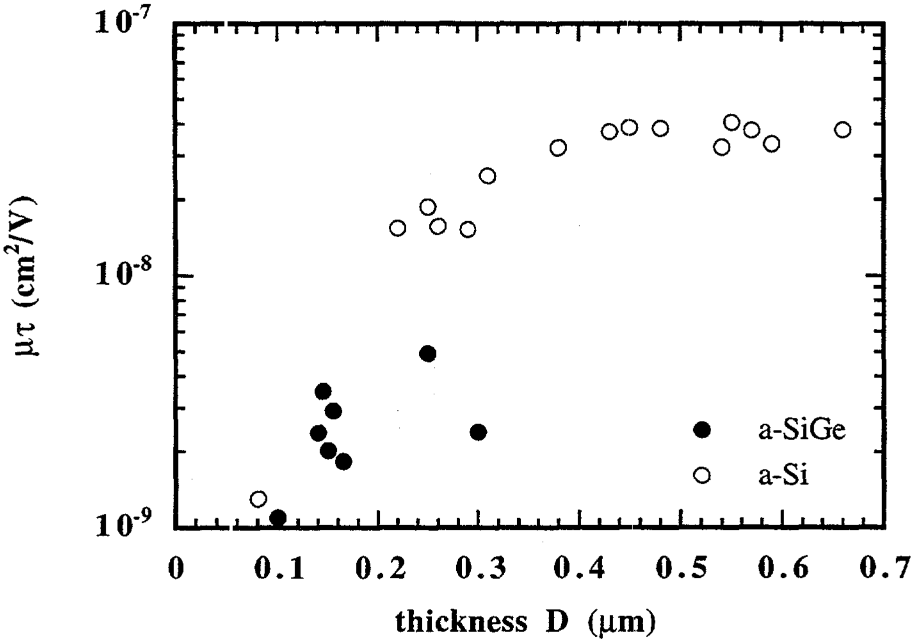

Figure 3-34 Mobility-lifetime product (from $\frac{L_C}{D}$) vs D for 23 a-Si and a-SiGe devices in initial state.

3.4.4 Applications of $J_L(V)$ model and discussion

3.4.4.1 Effect of $\frac{L_C}{D}$ on J_{sc} and V_{OC}

With the collection length model (Equation 3-5), each performance parameter is related to a model parameter: J_{SC} is proportional to J_{L0}; V_{OC} is proportional to V_{fb} (Figure 3-31); and FF is controlled by $\frac{L_C}{D}$ (Figure 3-30). However, J_{SC} and V_{OC} also depend on $\frac{L_C}{D}$ although to a much smaller extent (Figure 3-17 and Figure 3-29). From Equation 3-5, J_{SC} will be:

$$J_{SC} = J_L(V=0) = J_{L0}\left(\frac{L_C}{D}\right)\left(1 - e^{-1/\frac{L_C}{D}}\right) \approx J_{L0}\left(1 - \frac{1}{2\left(\frac{L_C}{D}\right)}\right)$$

Equation 3-13

where a second order expansion of the exponential was used assuming $\frac{L_C}{D} >> 1$. Thus, for $\frac{L_C}{D} = 10$, J_{SC} is reduced by 5% from J_{L0}.

From Equation 3-1, Equation 3-2 and Equation 3-5; V_{OC} will be:

$$V_{OC} = \left(\frac{AkT}{q}\right) \mathrm{Ln}\left(\frac{J_{L0}\, h(V_{OC})}{J_0}\right) = \left(\frac{AkT}{q}\right)\left\{ \mathrm{Ln}\left(\frac{J_{L0}}{J_0}\right) + \mathrm{Ln}\left(\frac{L_C}{D}\right) + \mathrm{Ln}(1-v) + \mathrm{Ln}\left(1 - e^{\frac{D}{L_C(1-v)}}\right)\right\}$$

Equation 3-14

where $v = \frac{V_{OC}}{V_{fb}}$. For typical values, the first two terms are positive while the last two negative. The first term is the only term needed in analyzing the ideal device where J_L is constant. Using Equation 3-14 with; $\frac{AkT}{q}$=0.047 V, J_{L0}=15 mA/cm^2, J_0=10^{-8} mA/cm^2, $\frac{L_C}{D}$=10, v=0.95; then V_{OC}=0.95 V. For the same parameters without voltage dependent collection losses, V_{OC} would be 0.99 V. Thus, the voltage dependent collection costs 0.04 V for these typical parameters.

3.4.4.2 Hole vs electron transport

From steady state photoconductivity and diffusion length measurements on thick a-Si films, it is found that electrons have μt ~10^{-6}-10^{-5} cm^2/V and holes have μt ~(0.5-4) x10^{-8} cm^2/V [348, 368, 376, 377]. It is well known that alloying with Ge reduces the electron and hole μt. For a-SiGe films with bandgaps in the same range as devices measured here, 1.4-1.6 eV, electrons have μt ~10^{-7}-10^{-6} cm^2/V and holes have μt ~1-5x10^{-9} cm^2/V [352, 377-380]. Values of μt in Figure 3-34 for a-Si and a-SiGe indicate hole-limited collection since they agree with reported hole values and are at least one order of magnitude less than typically reported electron values. Our data on μt from $\frac{L_C}{D}$ and its dependence on intensity and light exposure from a-Si p-i-n cells is summarized in Table 3-18, and compared to values from the literature obtained for holes by SSPG or SPV. Clearly, our μt properties from $\frac{L_C}{D}$ in typical p-i-n devices under standard solar illumination are in good agreement with hole μt properties in thicker films from other techniques. Previous measurements of $\frac{L_C}{D}$ obtained under chopped red light in thick Schottky barriers have been closely correlated with hole diffusion length obtained by SPV on the same devices [380]. From Figure 3-34, a μt of 4x10^{-8} cm^2/V gives a diffusion length of 0.15 μm, typical of values reported by SSPG for a-Si films.

Table 3-18 Comparison of published hole transport properties from SSPG on thick a-Si films with similar parameters obtained from Lc/D of a-Si p-i-n devices in this study.

parameter	this study	SSPG value	references for SSPG
μτ (cm^2 -V)	1-4 x10^{-8}	0.5-4x10^{-8}	[366-368, 374, 376, 377, 379]
intensity dependence m	0.20	0.20-0.27	[366-368]
degradation rate β	0.13	0.11- 0.14	[372-374]

Results presented here are in agreement with the limiting carrier model [301, 350] since they indicate hole limited transport for red or white light through the p-layer. An alternative model says that $\frac{L_C}{D}$ should represent the sum of the electron and hole collection lengths [345, 381], thus the sum of the $\mu\tau$ values. Since the electron $\mu\tau$ is typically 10-100 times greater than the hole $\mu\tau$ in a-Si, this implies $\frac{L_C}{D}$ values of 100-1000 which greatly exceed reported values of $\frac{L_C}{D}$.

3.4.4.3 Flat band voltage vs built-in voltage

Figure 3-31 and Figure 3-32 indicate that V_{OC} is strongly correlated with V_{fb} and somewhat correlated with J_0. In order to determine the limits to V_{OC} and under what conditions it depends primarily on V_{fb} or J_0, V_{OC} was calculated using Equation 3-1 with R=0, A=1.8, and J_{L0}=15 mA/ cm^2. Figure 3-35 shows the dependence of V_{OC} on V_{fb} for three values of J_0 and two values of $\frac{L_C}{D}$. V_{OC} is linearly proportional to V_{fb} for V_{fb} <0.8V, independent of J_0, and independent of V_{fb} for V_{fb} >1.1V. V_{OC} will vary as the inverse of log (J_0), as predicted by first term of Equation 3-11, only when V_{fb} is several tenths of a volt greater than V_{OC}. Reducing J_0 increases the range of V_{fb} where V_{OC} is proportional to V_{fb}. Figure 3-35 also shows that V_{OC} is nearly independent of $\frac{L_C}{D}$ for values expected for reasonable device performance ($\frac{L_C}{D}$>8). Calculated results in Figure 3-35 are very similar to measured data presented in reference [382] where V_{OC} begins to deviate from V_{fb} around V_{fb} ~0.9 V then saturate with V_{fb} >1.1 V. In general, Figure 3-35 indicates the importance of the voltage dependent photocurrent losses in the analysis of V_{OC} limitations.

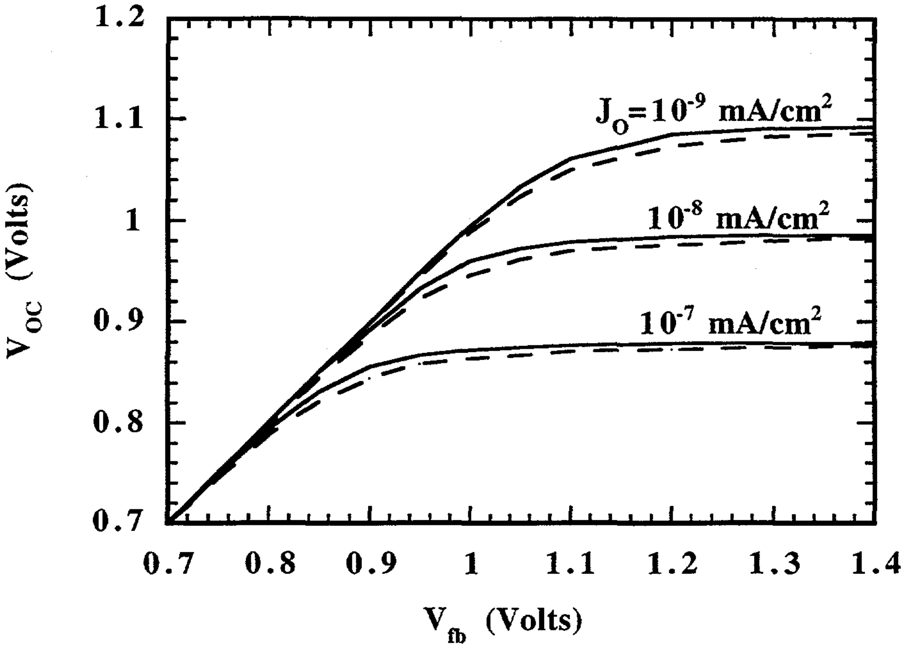

Figure 3-35 Calculated dependence of V_{OC} on V_{fb} for three values of J_O, and $\frac{L_C}{D}=16$ (solid lines) or $\frac{L_C}{D}=8$ (dashed lines).

V_{fb} is often assumed to be equivalent to the built-in voltage, V_{bi}, defined as $qV_{bi}=E_{gi}-E_n-E_p$ where E_{gi} is the i-layer bandgap and E_n and E_p are the Fermi level positions in the n and p-layers. For typical values of $E_{gi}=1.8$, $E_n=0.2$, and $E_p=0.4$ eV, V_{bi} would be 1.2V yet the largest V_{fb} we have measured is only 1.0 V. V_{bi} should be independent of intensity and spectrum, yet Figure 3-25 shows V_{fb} clearly depends on both. It has been estimated [383] that $V_{fb} \approx V_{bi} -0.35V \approx 0.85$ V which is very close to the majority of values we have found for a-Si devices. V_{fb}, the voltage at which field reversal occurs in the i-layer causing $J_L(V)$ to go to zero, is not a fundamental device property but depends on the i-layer defect distribution between deep states and band tails, and operating conditions. Further study is needed to understand the relation between V_{fb} obtained from this analysis and built-in potential from other methods such as temperature dependence of V_{OC} [357] and electroabsorption [384].

3.4.4.4 Effect of series resistance on FF

The maximum power, hence FF, of a solar cell decreases with increasing R due to (J^2R) power losses. Similarly, FF decreases with increasing intensity for the same reason. However, trapping and recombination at deep defects and bandtail states will also be intensity dependent [362, 363]. Recently, the reduction in FF with increasing intensity was attributed to trapping in band tails leading to field collapse in the i-layer using the AMPS model [385].

Figure 3-36 shows the dependence of FF on intensity. The experimental data are from the same a-Si device #4484 whose J-V behavior is presented in Figure 3-21 to Figure 3-24. The dependence of FF on intensity was calculated with Equation 3-1 using parameters for #4484 from Table 3-16 with J_{L0} varying to simulate the change in incident intensity with R=0 and 1.7 Ω- cm^2. Note the close agreement between data and the circuit model for the actual value of R=1.7 Ω- cm^2. Even closer agreement would have been obtained by letting $\frac{L_C}{D}$ vary with intensity as shown in Figure 3-24. The other calculated curve in Figure 3-36 is from the AMPS modeling program using parameters described in reference [385].

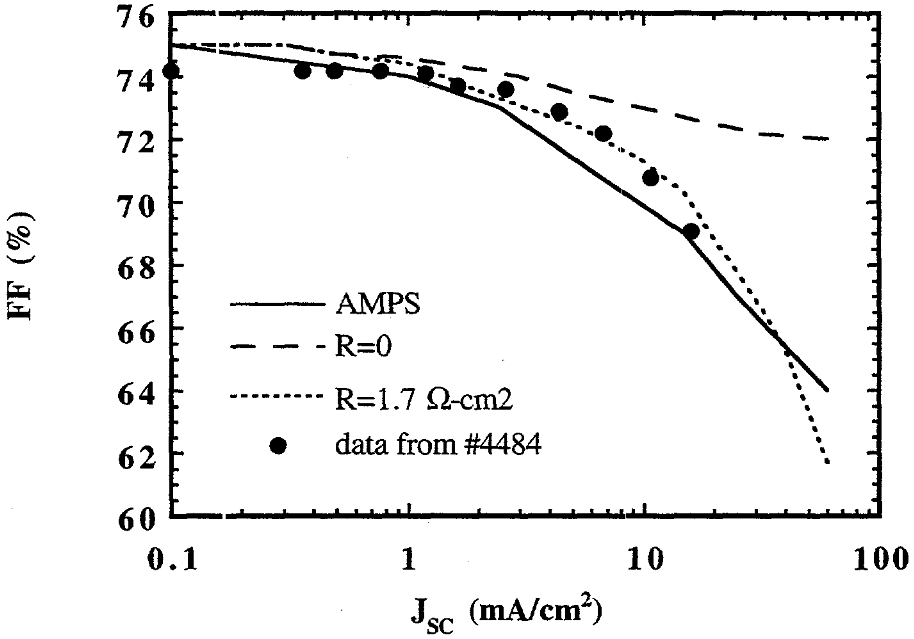

Figure 3-36 Measured and calculated dependence of FF on intensity (J_{SC}). Data points from a-Si device #4484, circuit model (Equation 3-1) with parameters from Table 3-16. The AMPS calculation is from reference [385].

Comparing results with R=0 to R=1.7 Ω- cm^2 shows that a major component of the decrease in FF with intensity is due to increased series resistance losses (J^2R). We conclude that the dependence of FF on intensity can be adequately explained with a simple series resistance circuit model.

3.4.4.5 Effect of device parameters on efficiency

The efficiency was calculated as a function of $\frac{L_C}{D}$ assuming 100 mW/cm^2 input power with the following parameters fixed: A=1.8, J_{L0}=15 mA/ cm^2, and R=0. These parameters represent a typical a-Si single junction device without series resistance. The values V_{fb} and J_0 were varied to determine the relative payback in improved performance. Figure 3-37 shows that for V_{fb} =1.0 V, there is little improvement seen by decreasing J_0 from 10^{-8} to 10^{-9} mA/ cm^2, while for V_{fb} =1.4 V there is a significant gain for decreasing J_0. Only after V_{OC} is no longer limited by low V_{fb} will decreases in J_0 give major improvements (Figure 3-35). All curves tend to approach saturation beyond $\frac{L_C}{D}$=20. The best stabilized value of $\frac{L_C}{D}$ we have found is 12.5, for a thin device (D≈0.1 μm) intended as a top cell of a multijunction device. There is little to be gained by improving on that value of $\frac{L_C}{D}$ by more than 50%. However, for low bandgap a-SiGe devices with stabilized $\frac{L_C}{D}$ values of around 5, there are major gains to be had by increasing $\frac{L_C}{D}$ or V_{fb}.

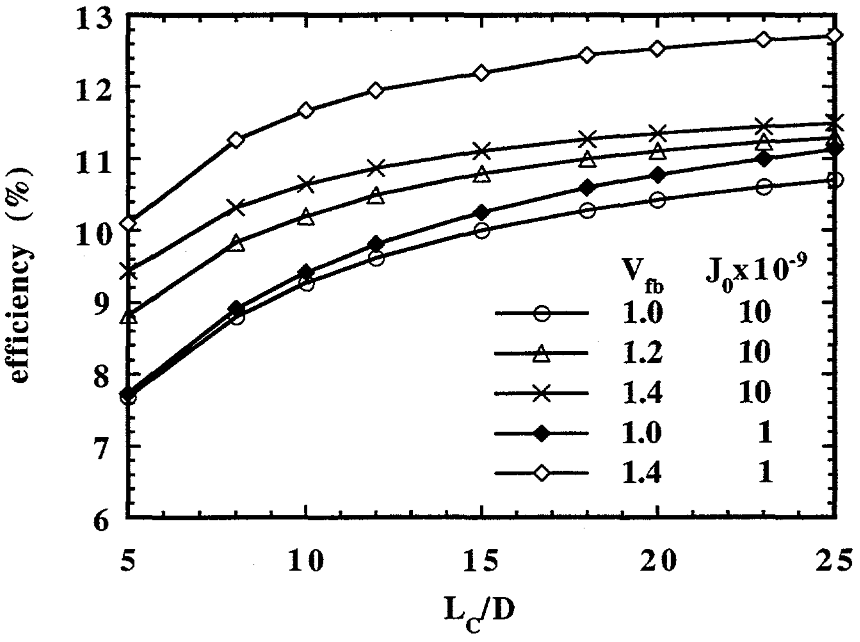

Figure 3-37 Efficiency calculated for various values of V_{fb} (Volts) and J_0 (mA/cm^2) as function of $\frac{L_C}{D}$. Other parameters were A=1.8, J_{L0}=15 mA/cm^2, and R=0.

3.4.5 Analysis Of Multijunction Devices

Much of the modeling and analysis of multijunction devices has been achieved with numerical models requiring a large number of material and physical parameters. Although such modeling provides detailed insight into the microscopic behavior, many of the required material parameters are experimentally inaccessible and the physics of some regions such as interfaces are imperfectly known. Thus, it is difficult to link the model to measurable device performance. Using the method of analysis presented in section 3.4.2, triple junction cells are analysed using a parameter set based on the stabilized high, middle and low bandgap cells from USSC.

Figure 3-38 shows the measured and calculated JV data under AM1.5 illumination for the a-Si top cell of a triple junction and Figure 3-39 the measured and calculated JV data under red filtered light for a low bandgap a-SiGe bottom cell of a triple junction both made by USSC.

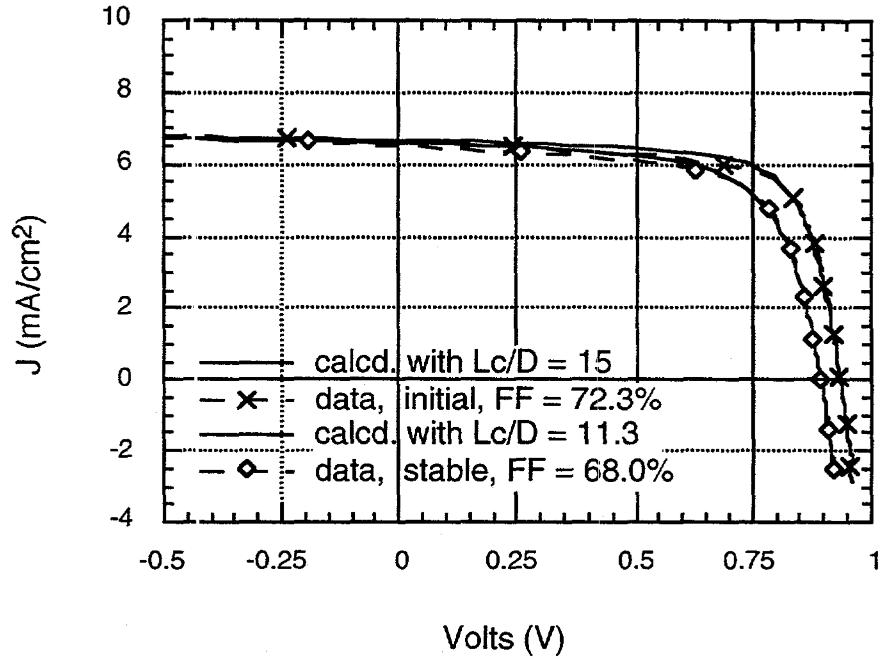

Figure 3-38 Measured (AM1.5) and calculated JV curve for USSC top cell (aSi) in initial and stabilized state. Calculated curves using parameters of Table 3-19, measured and calculated performance in Table 3-20.

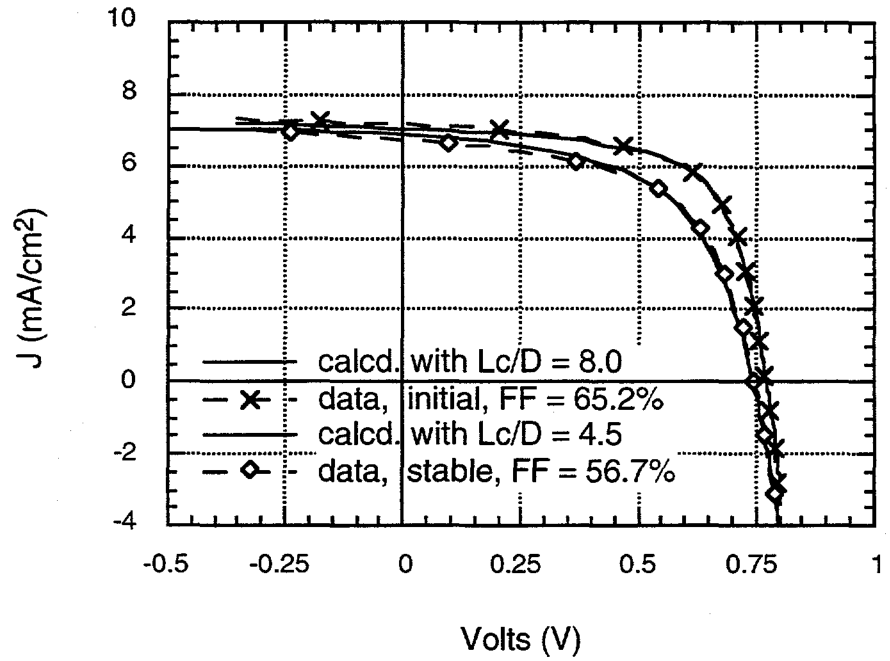

Figure 3-39 Measured (red filtered AM1.5) and calculated J-V curve for USSC middle cell (a-SiGe) in initial and stabilized state. Calculated curves using parameters of Table 3-19, measured and calculated performance in Table 3-20.

Both Figure 3-38 and Figure 3-39 show the initial and stabilized J-V curves. The good agreement of Figure 3-38 and Figure 3-39 from reverse bias to beyond V_{OC} indicate the model accurately represents all portions of the J-V characteristic. Agreement is typically within 0.4 mA/cm^2. Parameters obtained from analyzing the top, middle, and bottom cell JV curves provided by USSC are in Table 3-19.

Table 3-19 Parameters obtained from JV fitting and calculated and measured solar cell performance for initial and stabilized USSC component cells. Top cell degraded and measured under unfiltered light; middle, bottom cells degraded and measured under filtered light (see Ref. [386]).

cell	state	A	J_0 (mA/cm^2)	R (Ω·cm^2)	J_{L0} (mA/cm^2)	L_C/D	V_b (V)
top	initial	1.67	2x10^{-9}	2.5	6.9	15	1.03
	stable	1.75	1x10^{-8}	3.6	6.9	11.3	0.92
mid	initial	1.54	2x10^{-8}	3.4	7.5	8.2	0.86
	stable	1.93	1x10^{-6}	4.6	7.5	4.5	0.83
bot	initial	1.66	1x10^{-6}	3.3	9.2	5.3	0.89
	stable	1.88	6x10^{-6}	4.1	9.2	4.8	0.73

The parameters in Table 3-19 will form the basis for subsequent analysis of triple junction cells. Table 3-20 shows the illuminated J-V performance for each component cell calculated with parameters of Table 3-19 compared to the J-V performance measured by USSC under appropriate illumination. Very close agreement is found, demonstrating the applicability of this analysis to a-Si and a-SiGe devices under a range of conditions.

Table 3-20 Calculated and measured performance of USSC component cells. Calculated values obtained with the 6 parameters from Table 3-19.

cell	state	Calculated				Measured			
		V_{oc} (V)	J_{sc} (mA/cm^2)	FF (%)	Eff. (%)	V_{oc} (V)	J_{sc} (mA/cm^2)	FF (%)	Eff. (%)
top	initial	0.93	6.67	72.3	4.51	0.94	6.58	72.3	4.44
	stable	0.89	6.59	67.0	3.95	0.89	6.50	68.0	3.95
mid	initial	0.77	7.05	66.1	3.59	0.77	7.15	65.2	3.59
	stable	0.75	6.80	57.0	2.90	0.74	6.86	56.7	2.89
bot	initial	0.68	8.35	64.5	3.65	0.68	8.55	63.2	3.65
	stable	0.66	8.27	57.5	3.13	0.66	8.30	57.2	3.12

A triple junction device can be analyzed by solving Equation 3-1 for each junction with the requirement that the net currents are equal. Table 3-21 lists the performance of the triple junction devices consisting of the component cells of Table 3-19 in the initial and stabilized states. The efficiency decreases from 11.5 to 9.8% with light soaking (efficiency calculated assuming 100 mW/cm^2 input). Performance of USSC triple junctions [387] from this period are very comparable to the calculated values, with initial efficiencies of 11% and stabilized efficiencies of 9.5%.

Table 3-21 Calculated triple junction performance for different cases of input parameters.

case	conditions	V_{oc} (V)	J_{SC} (mA/cm^2)	FF (%)	Eff. (%)
1	initial cell parameters from Table 3-19	2.38	6.8	71.1	11.5
2	stabilized cell parameters from Table 3-19	2.28	6.7	63.6	9.8
3	same as case 2 except all $L_c/D=15$	2.34	6.8	71.8	11.4
4	same as case 2 except all V_b increased by 0.1V	2.35	6.7	66.4	10.4
5	same as case 2 except all J_0 decreased by 10X	2.43	6.7	62.0	10.1
6	combine improvements from cases 3, 4, and 5	2.65	6.8	72.5	13.1
7	same as case 6 except increase all J_{L0} to 8 mA/cm^2	2.65	7.7	69.3	14.2
8	same as case 6 with J_{L0} current imbalance top / mid / bot = 8 / 8.5 / 9 mA/cm^2	2.66	7.9	71.0	14.9

The model can be used to indicate the relative payback for improving a given device parameter. Figure 3-40 shows the triple junction efficiency as a function of the $\frac{L_c}{D}$ of the top, middle or bottom cell. All other cell parameters were the same as in the stabilized USSC component cells (see Table 3-19). Figure 3-40 shows that there is a significant improvement from increasing $\frac{L_c}{D}$ up to 15 in the middle or bottom cells, but improvement saturates beyond this point. The most important conclusion of Figure 3-40 is that there is little benefit to significantly improving i-layer collection in one cell in the stack, for example, by greatly reducing the defect density or increasing mobility or lifetime. Instead, as discussed below, all properties of all devices must be improved. It is known empirically that improved a-Si multijunction cell performance results from having a current mismatch between component cells [388, 389]. The cell with highest FF (the top cell) is designed to have the lowest J_{SC} (i.e., it becomes the current limiting cell) and cells with the lowest FF are designed to have higher J_{SC}. Current mismatch has the biggest impact on the FF of the triple junction device. However, there has been little effort to understand the details or provide a predictive model of this effect.

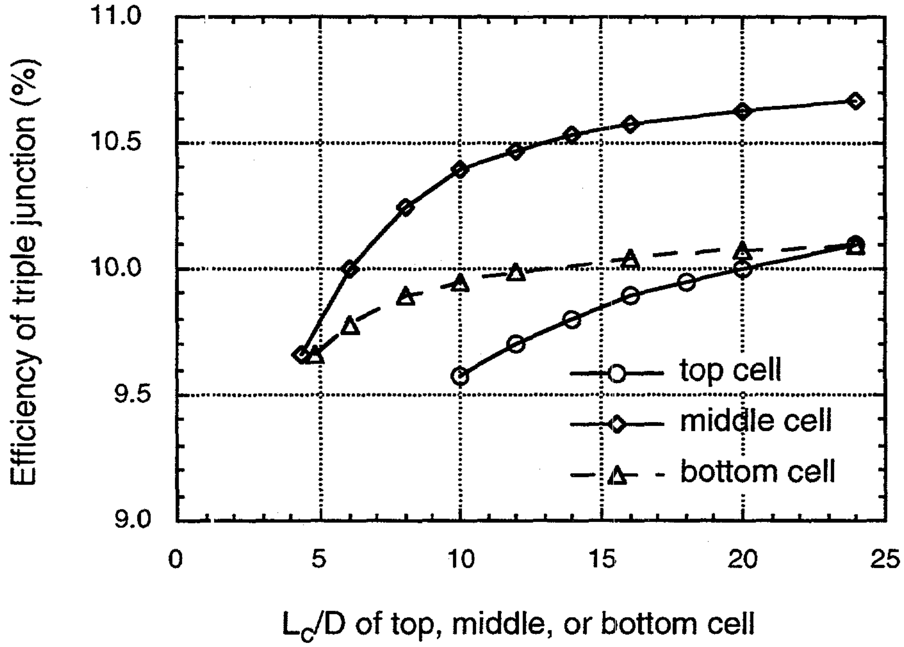

Figure 3-40 Efficiency of triple junction calculated for varying $\frac{L_C}{D}$ of each component cell. Default values of $\frac{L_C}{D}$ were 11.3, 4.5, and 4.8 for top, middle, and bottom cells. All other parameters from stabilized component cells of Table 3-19.

Figure 3-41 shows the effect of current limiting by varying the photocurrent J_{L0} of the middle and bottom cells, independently. Other parameters are from Table 3-19 for the stabilized component devices. The efficiency continues to increase as either cell is increasingly imbalanced. The magnitude of the effect is similar to that found by USSC in their present triple junctions. The analytical model can thus be used to quantify how much one needs to increase the bottom cell current to obtain an expected increase. The trade-off comes from the inevitable decrease in bottom cell stability if its i-layer is made thicker, and loss in V_{OC} and FF if the i-layer bandgap is decreased.

Table 3-21 also shows the impact of selected improvements needed to achieve 15% using stabilized device parameters from Table 3-19 as a starting point. By improving the i-layer collection $\frac{L_C}{D}$ to 15 (case 3) in all three cells, so that all three cells have i-layer quality comparable to the best initial a-Si device (Table 3-19), the triple junction FF only increases to 71.8% and efficiency increases to 12.6%. Note that V_{OC} increases by 0.06 V as the collection losses decrease because $J_L(V)$ remains larger at large forward bias. Case 4 shows that increasing the V_b of *each* cell by 0.1 V over the stabilized values increases the triple junction V_{OC} by only 0.07 V. Case 5 shows that reducing J_0 by an order of magnitude in each cell increases V_{OC} by 0.15 V, but efficiency increases by only 0.3 percentage points compared to case 2. Note that the FF actually decreases because V_{mp} is unaffected by J_0 while V_{OC} increases. This is proof that maximum power is almost unaffected by the dark diode, but rather is determined almost entirely by the bias dependent photocurrent collection. Case 6 combines all three major improvements of cases 3, 4, and 5, resulting in an improvement in V_{OC} of 0.37 V which is greater than the sum of gains in V_{OC} by changing each parameter individually. The FF increases only slightly (from 71.8% to 72.5%) compared with the value found by increasing only $\frac{L_C}{D}$ to 15 in case 3. This confirms that $\frac{L_C}{D}$ has the dominant effect on FF. Increasing the flat band voltage or reducing J_0 of each device has a greater impact as $\frac{L_C}{D}$ increases since the device becomes more ideal. It is well known that triple junction J_{SC} of 8 mA/cm^2 is needed to reach 15% efficiency [389]. Case 7 shows the performance when all improvements of case 6 are coupled with higher J_{L0} of 8 mA/cm^2 for all three devices. Although J_{SC} increases as expected, FF decreases since the benefits of *current mismatching* are lost. Case 8 shows the benefit of current limiting with the best cell (top cell). The J_{L0} values are 8, 8.5, and 9 mA/cm^2 in the three devices, resulting in no change in V_{OC}, small increase in J_{SC}, but a significant improvement in FF. This shows that current imbalance is an important technique to improve FF even when all three devices have identical and rather high values of $\frac{L_C}{D}$. Case 8 shows that to achieve 15% efficiency, it is necessary to increase $\frac{L_C}{D}$ significantly in the middle and bottom cells, to increase V_b in all three cells by 0.1 V, to reduce J_0 by an order of magnitude in all three cells, increase J_{SC} to nearly 8 mA/cm^2, and incorporate current limiting with the top cell.

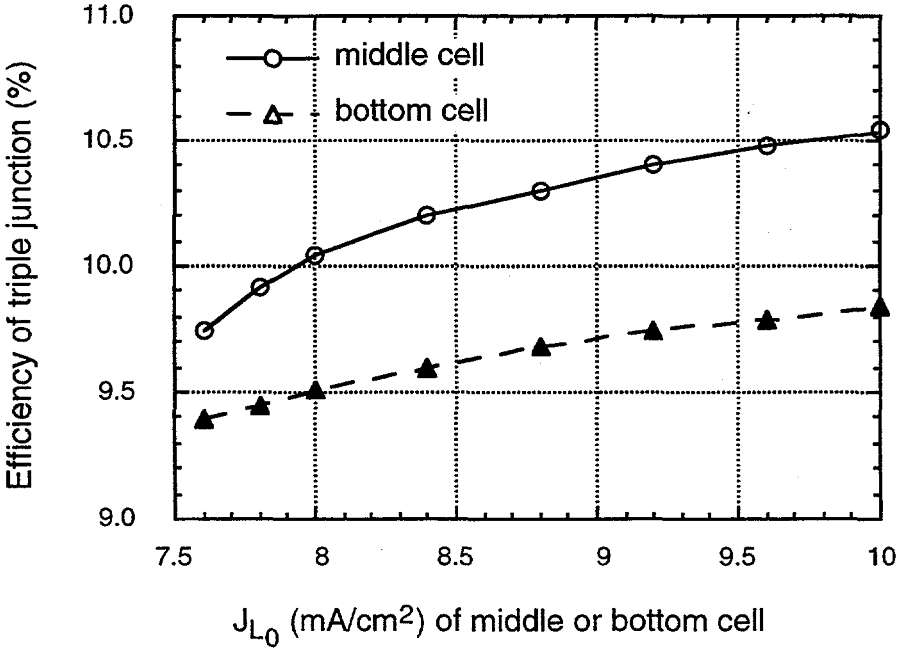

Figure 3-41 Effect of current mismatch on efficiency by varying J_{L0} of middle and bottom cells. All other parameters from stabilized component cells of Table 3-19.

3.4.6 Conclusions

A simple parametric model of current voltage behavior has been developed. Very close agreement between measured J-V data and the model has been found for over 20 solar cells from several laboratories. The model has been applied to a-Si and a-SiGe p-i-n solar cells in initial and light soaked states, under AM1.5, blue and red light. The strength of the present analysis is that it allows characterization of the device under typical operating illumination conditions of dc AM1.5 light, in terms of two basic parameters, $\frac{L_C}{D}$ and V_{fb}. Basic material properties such as hole $\mu\tau$ can be studied in an actual solar cell configuration. To first order, changes in FF can be represented with a single parameter $\frac{L_C}{D}$, which we have shown is proportional to the hole drift length for a-Si or a-SiGe devices. $\frac{L_C}{D}$ in devices thinner than ~0.2μm may be strongly influenced by non-bulk recombination (interface or back diffusion). The dependence of FF on $\frac{L_C}{D}$ is the same whether cells degrade due to increasing Ge or light induced defects. The voltage dependent current collection reduces V_{OC} by 40-100 mV, an effect which is typically ignored. V_{OC} in present devices is limited by V_{fb}, not J_0. Series resistance alone can explain the intensity dependence of the FF, even though $\frac{L_C}{D}$ is intensity dependent as well.

Since this analysis was begun, top cells with V_{OC} of 1.0 V have been reported and used in triple junctions. Also, the J_{SC} of the triple junctions has increased. Together, these improvements have lead to triple junction devices with stabilized efficiencies of 11.8% [390]. Single junction device parameters reflecting these improvements have been incorporated into the model in the current contract year, giving results typical of today's best triple junction devices. These will then be used to evaluate directions and device features needed to extrapolate to DOE's 15% efficiency goal.

4. CdTe/CdS RESEARCH

4.1 SUMMARY

4.1.1 CdTe/CdS Device Performance

In this reporting period vapor phase $CdCl_2$ treatments were developed, permitting the effects of reaction temperature and chloride concentration on materials and devices to be investigated. Vapor $CdCl_2$ treatment at 420°C was found to result in uniform modification of the film properties. Combined with the contacting process developed in the previous reporting period, the uniform and reproducible treatments have translated into greater consistency in device performance at an efficiency level of 12% [401] The J-V curve of such a cell is shown in Figure 4-1. The V_{OC} is approaching state-of-the-art values, but J_{sc} and FF are low. The resistance at V_{OC} in these devices is in the range of 6 to 10 $\Omega\text{-cm}^2$. Reducing this to 1–2 $\Omega\text{-cm}^2$ by optimizing the CdTe doping and contact are expected to increase FF to >72% and should enhance the V_{OC}. Control over S interdiffusion with vapor treatment and use of alloyed films is described in the sections below and offers several avenues for improving J_{SC}: 1) use thick CdS (~250 nm) and high S diffusion process to thin down the CdS, boosting J_{SC} contributions from 300–550 nm and 750–900 nm; 2) use ultrathin CdS (<50 nm) and low S diffusion process to minimize loss of CdS film; and 3) deposit $CdTe_{1-x}S_x$ films with x near the solubility limit on ultrathin CdS to minimize driving force for interdiffusion.

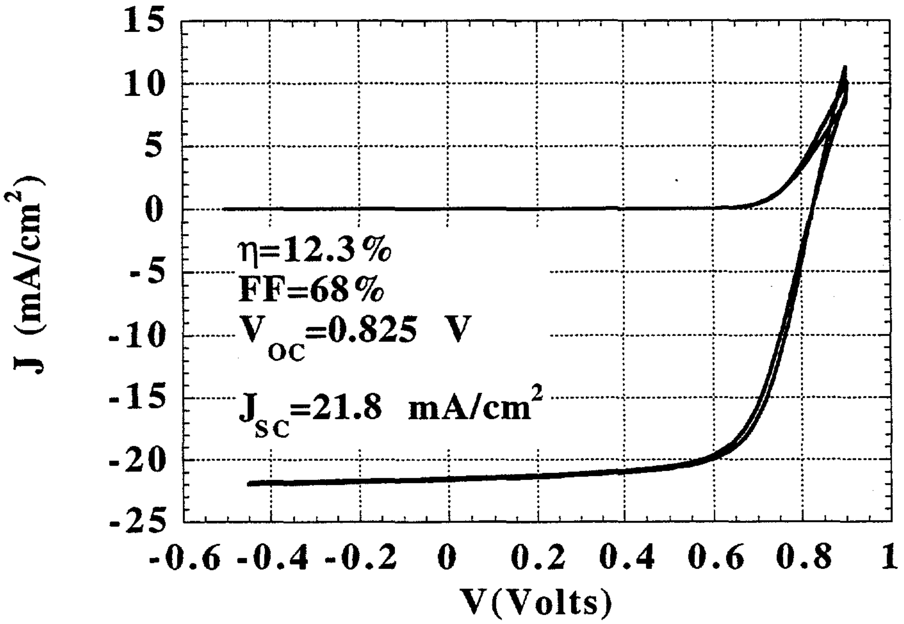

Figure 4-1. J-V curve of PVD CdTe/CdS device 40926.11-3 processed with $CdCl_2$ vapor (using a coated plate as the vapor source).

4.1.2 $CdCl_2$ Treatment

All-vapor post deposition processing holds many advantages the over conventional coat-and-rinse techniques that are employed for CdTe cells [402, 403]. For example, the thermal separation of CdTe/CdS films from the chloride source allows independent control of both the reaction temperature and species concentration. This facilitates temperature-time configurations that: can reduce the CdS loss via interdiffusion; increase the V_{OC}; reduce the treatment time; and produce a residue-free CdTe surface. Figure 4-2 shows the CdTe (511) XRD peak profile in 2.5 μm CdTe/0.2 μm CdS structures after $CdCl_2$ vapor treatment. The bimodal profile obtained for the sample in which the $CdCl_2$ and CdTe/CdS structure were heated together indicates extensive CdTe-CdS mixing and corresponds to an equivalent CdS thickness of approximately 65 nm. Delaying the delivery of $CdCl_2$ vapor by two minutes after reaching reaction temperature results in a diffusion tail that corresponds to an equivalent CdS thickness of less than 20 nm.

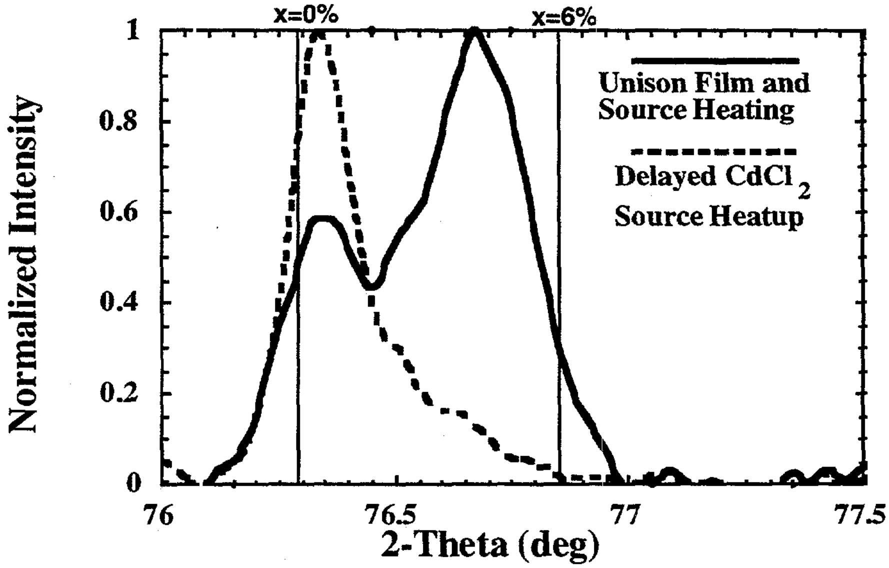

Figure 4-2 $CdTe_{1-x}S_x$ (511) XRD profile for CdTe/CdS structures heated in unison with (solid) and prior to (dotted) the $CdCl_2$ source.

The vapor chloride processing yields a spatially uniform grain size and a clean CdTe surface free of residual chlorides, oxides, and chlorates. This eliminates the necessity for rinsing or handling of rinsates prior to contact formation. From a device perspective, these benefits translate into spatially uniform properties and performance. Table 4-1 shows the current-voltage parameters for four 0.2 cm^2 area cells fabricated on a 1" x 1" sample processed with $CdCl_2$ vapor treatment.

Table 4-1. Current-voltage parameters for CdTe/CdS cells demonstrating spatial uniformity of device performance with vapor chloride processing.

Cell	V_{OC} (mV)	J_{SC} (mA/cm^2)	FF (%)	Eff (%)
1	786	21.4	67	11.2
2	795	21.8	64	11.1
3	779	21.0	66	10.8
4	790	21.5	66	11.2

The role of $CdCl_2$ in promoting recrystallization, grain growth and interdiffusion between CdS and CdTe layers in physical vapor deposited CdS/CdTe thin film solar cells is has been examined[404]. CdTe/CdS thin film samples prepared with different CdTe film thicknesses and treated in air at 415°C for different times with and without a surface coating of $CdCl_2$. The samples were characterized by scanning electron microscopy, transmission electron microscopy, energy dispersive x-ray spectroscopy, x-ray diffractometry, and optical absorption. The results show that $CdCl_2$ treatment enhances the recrystallization and diffusion processes, leading to a compositional variation within the CdTe layer due to diffusion of S from the CdS. The highest S concentrations observed, after 30 minute treatments with $CdCl_2$ at 415°C, are near the solubility limit for S in CdTe. The compositional distributions indicated by x-ray diffraction measurements of samples with different CdTe thickness show that the S-rich $CdTe_{1-x}S_x$ region lies near the CdTe-CdS interface. A multiple step mixing process must be inferred to account for the diffraction profiles obtained.

4.1.3 CdTe-CdS Alloys and Devices

The CdTe-CdS alloy system has been characterized at typical solar cell processing temperatures in order to elucidate the role of interdiffusion in CdTe/CdS-based solar cells [405, 406]. Predominately single phase $CdTe_{1-x}S_x$ thin films with $x\int[S]/([S]+[Te])$ ranging from 0 to 0.45, were grown by vacuum co-evaporation of CdS and CdTe. Phase segregation was promoted by heat treatment of the films at 415°C in the presence of $CdCl_2$. The solubility limits of S in CdTe and Te in CdS at 415°C were derived by measuring the compositions of the two phases in the films after the $CdCl_2$ treatment. The solubility limit of S in CdTe was determined to be 5.8%. Solar cells were fabricated with compositionally uniform absorber layers of $CdTe_{1-x}S_x$ with x near the solubility limit before heat treatment. An efficiency of 10.8% was achieved by a $CdTe_{1-x}S_x$/CdS device. The V_{OC}, J_{SC}, FF and spectral response of this device were all very similar to vacuum evaporated conventional CdTe/CdS cells where the alloy is formed by diffusion of S during cell processing.

4.1.4 HCl Vapor Treatment

Data on the structural and optical properties and cell performance of thermally evaporated CdTe/CdS films were determined as functions of the HCl concentration and temperature of a post-deposition heat treatment [407]. The degree of preferred (111) orientation decreased while the grain size of the CdTe films increased with increasing HCl concentration and temperature. The sulfur content of a $CdTe_{1-x}S_x$ layer also increased with HCl concentration and temperature to a maximum value of ~2%. Cell performance improved over as-deposited values to ~8% efficiency.

4.1.5 Stress Testing of CdTe/CdS Devices

CdTe/CdS solar cells have been known to exhibit various combinations of reversible and irreversible degradation of conversion efficiency after being subjected to temperature, voltage and illumination at levels which equal or surpass those expected in field conditions[408]. This paper describes a series of measurements designed to quantify these phenomena. The QE and light and dark J-V characteristics of a set of CdTe devices were measured, then devices were subjected to various combinations of stresses within the parameter space of 0-70 mW/ cm^2 illumination, -0.5 V to +5 mA/ cm^2 electrical bias, and temperatures from 72° to 112°C. The device characteristics were measured and changes are interpreted in the context of an equivalent circuit which includes the effects of both the main junction diode, series resistor and a rectifying back contact.

4.2 $CdCl_2$ TREATMENT

4.2.1 Vapor $CdCl_2$ Treatment

4.2.1.1 Introduction

Several approaches to fabricate high efficiency CdTe/CdS thin film solar cells rely on post deposition heat treatment of the CdTe/CdS structure by $CdCl_2$ in air to enhance the device performance [409-412]. The treatment usually consists of coating the CdTe surface with a saturated solution of $CdCl_2$ in methanol, drying, heat treating the $CdCl_2$/CdTe/CdS structure in air at ~400°C for 10 to 30 minutes, and rinsing or etching the structure prior to the contacting process. This approach is susceptible to spatial variability and irreproducibility depending on the uniformity of the $CdCl_2$ layer produced by the wet application technique [413](pp. 69-74). Module fabrication processes would have to contend with the application, recovery and recycling of the $CdCl_2$ containing solutions. Further, analytically quantifying the action of the $CdCl_2$ on the CdTe/CdS structure is limited by the coupling of the $CdCl_2$ concentration and the reaction temperature.

Previously, we have demonstrated that physical vapor deposited CdTe films could be recrystallized by $CdCl_2$ vapor at 25 torr with a CdTe and $CdCl_2$ separation of several centimeters [414] (pp. 42-46). The reaction uniformly recrystallized the CdTe films and produced devices having 9-10% efficiency. The experimental configuration, however, did not allow determination of the $CdCl_2$ vapor phase concentration at the CdTe surface. Zhou, et. al. [415] demonstrated >10% efficient devices using a vapor treatment with either $CdCl_2$ or HCl on CdTe/CdS deposited by a high temperature process. More recently we demonstrated that >10% efficient devices could be achieved by treatment at atmospheric pressure by placing the $CdCl_2$ in close proximity to the CdTe surface [416]. This configuration does not permit the variation of the parameters over a wide range because the $CdCl_2$ vapor phase concentration is fixed by the CdTe temperature. In the present work a new approach is described which overcomes these limitations and which allows the critical treatment parameters to be studied in detail.

4.2.1.2 Experimental

Thin films of CdTe and CdS were grown on In_2O_3:Sn (ITO) coated 7059 glass by thermal evaporation from CdTe source powder. Prior to CdTe deposition the 0.2 μm thick CdS films were heat treated with $CdCl_2$ vapor to reduce optical absorption and to minimize diffusion of Te into CdS during subsequent processing [417].

The treatments were performed by exposure of the CdTe/CdS films to vapor generated from a powder $CdCl_2$ source in a quartz reactor fitted with temperature controlled graphite susceptors heated externally by FCM lamps in linear housings. The $CdCl_2$ source powder was evenly distributed in a graphite susceptor supported on a quartz frame with a milled central cavity. A mica mask was used as both a separator and radiative/thermal insulator between the source susceptor and the thin film sample. A second graphite susceptor rested on top of the thin film sample to provide independent heating control. Using a CdTe/CdS/ITO/glass sample with an embedded microthermocouple, the time needed to heat the sample to 400°C was measured to be 40 seconds. The time to heat the $CdCl_2$ susceptor to 400°C was measured to be 20 seconds. Thus, the heatup rate of the susceptors, not the characteristic diffusion times (~2 sec), controls the time to reach equilbrium conditions in the reaction zone.

Evaluation of the effects of $CdCl_2$ vapor phase concentration and reaction temperature was made by independently controlling the temperatures of the thin film (T_f) and the $CdCl_2$ source (T_S): 1) $T_f > T_S$; 2) $T_f = T_S$; 3) $T_f < T_S$ (CSVT mode). Two types of heating profiles were employed: delayed heating to allow the CdTe/CdS sample to reach thermal equilibrium before the $CdCl_2$ and unison heating to simulate the conditions of $CdCl_2$-coated samples. To prevent $CdCl_2$ condensation on the CdTe/CdS in cases 1 and 2 due to mismatched heating rates, the CdTe/CdS was heated prior to and cooled after the $CdCl_2$. Atmospheric pressure treatments were conducted under flowing gas at a total flow rate of 0.94 l/m at one atmosphere total pressure. The system was pumped to < 50 mTorr prior to backfilling, which, for vacuum and argon treatments established a maximum oxygen partial pressure of <10 mTorr.

Film surface morphology and average grain size (AGS) were assessed by scanning electron microscopy (SEM). Energy dispersive spectroscopy (EDS) was used to examine the chemical composition of the CdTe surface after treatments. Optical transmission and reflection were measured in the wavelength region near the CdTe bandedge for evidence of S diffusion into CdTe. Scanning x-ray diffraction (XRD) patterns of the films were taken with Cu ka radiation using Bragg-Bretano focusing geometry to determine the normalized (111) orientation parameter, p(111) [418] and the precision lattice parameter [419]. High resolution x-ray diffraction scans of high order (hkl) reflections were made to assess alloying between CdTe and CdS. To maximize detection sensitivity of the thin layers at the CdS-CdTe interface, the absorptive loss of signal in the overlying CdTe was overcome by using films thinner than the penetration depth for that x-ray energy and Bragg angle. Either ~2.5μm thick CdTe films were employed, or thicker films (4-5 μm) were thinned after processing by a polishing etch with a buffered solution of $K_2Cr_2O_7$:H_2SO_4, such as Dichrol. Devices were completed by use of the diffused copper contacting process described elsewhere [420]. Light and dark current-voltage (J-V) traces and quantum efficiency measurements were used to determine conversion efficiency and spectral response changes within the devices.

4.2.1.3 Estimation of $CdCl_2$ Vapor Concentration

To understand the behavior of the gases in the reaction zone, the mass and thermal diffusion characteristics were determined for the reactor geometry in all thermal modes of operation. The results of this modelling show that the characteristic times to reach thermal equilibrium in air at 1 atm and mass transfer equilibrium are less than 2 seconds for isothermal reactions with a 2 mm separation between sample and $CdCl_2$ surface at 400°C, assuming no mass transport out of the reaction zone. Table 4-2 lists the $CdCl_2$ equilibrium vapor phase concentration, number of collisons with CdTe surface per unit area per second, and the saturation pressure [421] for the temperatures listed in the reaction zone.

Thermometric and gravimetric measurements of the source and substrates in isothermal mode verify the assumptions of the model. In CSVT mode at T_S=420°C and T_f=320°C the $CdCl_2$ deposition rate on glass agreed with the model prediction, providing a check on the assumption that the $CdCl_2$ powder reaches the susceptor set point temperature.

Table 4-2 $CdCl_2$ vapor phase heat treatment reactor equilibrium conditions for isothermal reactions.

T $CdCl_2$ (°C)	[$CdCl_2$] at CdTe $x10^{-10}$ (mol/cm^3)	Surface Collisions $x10^{17}$ (#/cm^2/s)	P_{sat} (mTorr)
380	0.325	1.35	1.3
410	1.33	5.62	5.7
420	2.06	8.79	9.0
430	3.16	1.36	14.0
450	7.15	31.1	32.7

4.2.1.4 Material Results

4.2.1.4.1 Thermal Effects

Table 4-3 presents the materials data for treatments conducted in bottled air under isothermal, $T_f = T_S$, and other thermal conditions. Isothermal treatments with delayed heating at 380°C, 410°C, 420°C and 430°C show increasing grain size with temperature as has been observed for the $CdCl_2$:methanol method [421]. The grain structure and morphology obtained after vapor treatment at 410°C and 430°C for 20 minutes are shown in Figure 4-3. EDS of the surfaces showed no evidence of residual Cl. The extent of S diffusion, even at 430°C, is substantially less than that obtained by the $CdCl_2$:methanol method at 410-420°C.

Fixing the $CdCl_2$ concentration at 1 mTorr and increasing the reaction temperature from 380°C to 450°C resulted in progressive grain growth at 380°C-420°C but produced a two layer structure with underlying grains that are of comparable dimension to those found with the isothermal case at 420°C. Fixing the reaction temperature at 420°C but increasing the $CdCl_2$ concentration produced similar grain size to that obtained under isothermal conditions at 420°C but, as expected, the surface was coated with dendritic clusters of $CdCl_2$ which rinsed away in methanol.

Table 4-3. Treatment conditions and materials results for 4.5 µm CdTe/0.2µm CdS films before and after processing by $CdCl_2$ vapor treatment. All samples were processed with delayed heating except the last.

T_f (°C)	T_S (°C)	t (m)	P_S (m Torr)	AGS (µm)	a_0 (Å) ±0.001	[S]/ [Te]+[S] (%)(±0.2)	p(111)
as dep	-	-	-	0.6	6.485	0	3.4
380	380	45	1.3	0.9	6.480	0.1	1.2
410	410	20	5.7	1.5	6.479	0.3	0.6
420	420	20	9.0	2.1	6.477	0.6	1.0
420	420	20	9.0	1.7	6.477	0.6	0.8
430	430	20	14.0	2.3	6.477	0.6	1.2
380	380	45	1.3	0.9	6.480	0.1	1.2
420	380	20	1.3	1.2	6.477	0.6	1.1
420	380	45	1.3	1.2	6.477	0.6	1.1
450	380	20	1.3	2.0	6.478	0.5	0.9
420	**380**	20	1.3	1.2	6.477	0.6	1.1
420	**420**	20	9.0	2.1	6.477	0.6	1.0
420	**450**	20	32.7	1.7	6.476	0.8	2.6
420	420	20	9.0	1.1	6.481	0.0	2.9
420	420	20	9.0	2.0	6.446	5.3	2.9

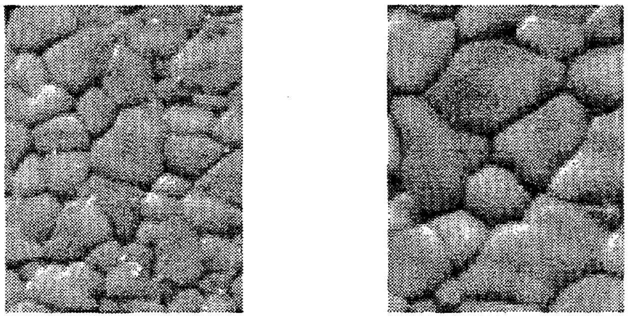

Figure 4-3 CdTe surface SEM photograph (5000X) after isothermal $CdCl_2$ vapor heat treatment at 410°C (left) and 430°C (right).

Decoupling the $CdCl_2$ temperature from the reaction temperature shows that reaction temperature has a strong effect in controlling the grain growth, and the two treatment times used for 420/380°C demonstrates that the grain growth is not kinetically limited in the time spans examined. Sulfur content in CdTe is constant for fixed $CdCl_2$ concentration at reaction temperatures above 380°C but increased to ~1% by increasing the $CdCl_2$ concentration with $T(CdCl_2)$=450°C. In general, the recrystallization reduced the (111) preferred orientation from the as-deposited condition.

Repeating the isothermal case at 420°C but varying the thermal heat-up history of the CdTe/CdS film and the $CdCl_2$ source produced distinct differences in the final structure. Unison heating of the CdTe/CdS and $CdCl_2$ promoted a flat morphology with uniform grain size. The x-ray diffraction results of these films shows extensive diffusion of S diffusion into the CdTe compared to all of the delayed heating reactions (Figure 4-4). The delayed heating method results in a sharp diffraction peak with a small tail extending towards the position of the solubility limit for S in $CdTe_{1-x}S_x$ [405] and is consistent with the low S incorporation shown in Table 4-3. The unison heating produced extended diffusion profiles with alloy layers out to the solubility limit for S in $CdTe_{1-x}S_x$.

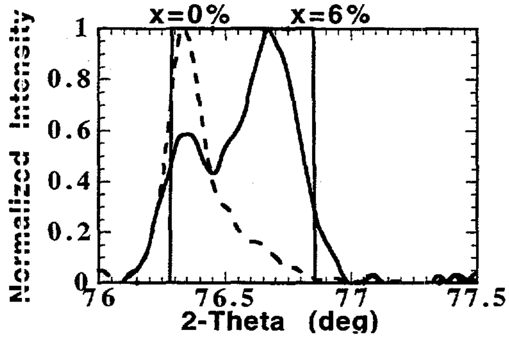

Figure 4-4 High resolution (511) XRD profiles of $CdCl_2$ vapor treated films exhibiting very different degrees of S diffusion.

4.2.1.4.2 Oxygen Effects

Treatment in Ar/O_2 mixtures and at reduced total pressure allowed investigation of the effects of oxygen on film properties and devices. Isothermal reactions at 420°C for 20 minutes with delayed heating were employed to permit evaluation of the influence of oxygen concentration on the S diffusion. Table 4-4 shows materials data for 2.5 μm CdTe/0.2 μm CdS films treated with $CdCl_2$ vapor under different O_2 concentrations at 420°C for 20 minutes. All cases were treated in $Ar:O_2$ except the reduced pressure case which was treated under dynamic roughing pump conditions with residual ambient air. Progressive grain growth was obtained with increasing O_2 concentration at 1 atm. total pressure. At very high O_2 concentration, S diffusion is greatly enhanced. The (511) XRD peak profiles for the highest O_2 case resembles the highly alloyed case of Figure 4-4. The optical transmission curves, normalized for reflection, show a progressive shift in location of the CdTe bandedge towards lower energy with increasing oxygen that is consistent with formation of alloy layers with increasing S content (Figure 4-5). The case treated at reduced pressure exhibited no measurable interdiffusion and retained a high degree of (111) preferred orientation. Similar results were obtained on structures with 4.5 μm thick CdTe, which were processed into devices.

Table 4-4. Grain size and x-ray diffraction results for films before and after treatment at 420°C for 20 min at different pressure and O_2 concentration.

Total P (torr)	$p(O_2)$ (torr)	p(Ar) (torr)	AGS (µm)	a_0 (A) ±0.001	[S]/ [Te]+[S] (%) (±0.2)	p (111)
as dep	-	-	0.4	6.486	0	4.0
0.04	0.01	0	1.1	6.481	0	3.1
760	0.01	760	1.1	6.477	0.7	0.9
760	190	570	1.4	6.475	0.8	2.4
760	380	380	2.1	6.477	0.7	1.9
760	570	220	2.5	6.462	2.9	1.1

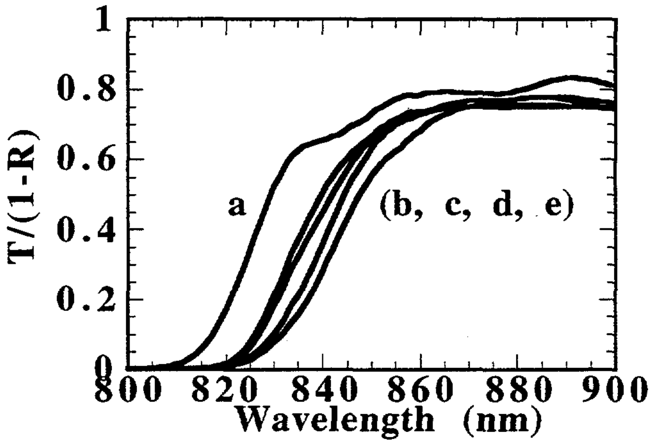

Figure 4-5 Normalized optical transmission curves for CdTe/CdS films of Table 4-4: a) as deposited, b) 0.01 , c) 190, d) 380, and e) 570 mTorr O_2.

4.2.1.5 Device Results

J-V data for samples treated with $CdCl_2$ vapor under various conditions of temperature and atmosphere are shown in Table 4-5. For the isothermal reactions, the device performance is comparable to that obtained by $CdCl_2$:methanol treatment and is optimal at treatment temperatures of 420°C to 430°C. We find that the fill factors of devices across each sample are uniform within ±5 rel %.

Table 4-5 Device results for samples treated with $CdCl_2$ vapor. $CdCl_2$ partial pressures are based on Table 4-2.

T_f (°C)	T_S (°C)	Atm	P_S (mTorr)	$P(O_2)$ (Torr)	V_{OC} (mV)	J_{SC} (mA/cm^2)	FF (%)	Eff (%)
380	380	Air	1.3	160	740	19.1	57.1	8.1
410	410	Air	5.7	160	763	21.8	58.1	9.7
420	420	Air	9.0	160	815	20.4	67.7	11.3
430	430	Air	14.0	160	786	20.2	71.0	11.3
380	**380**	Air	1.3	160	740	19.1	57.1	8.1
420	**380**	Air	1.3	160	722	20.4	62.9	9.3
450	**380**	Air	1.3	160	734	20.6	62.6	9.5
420	**450**	Air	32.7	160	793	20.9	51.7	8.6
420	420	Ar/O	9.0	**570**	791	23.5	61.8	11.5
420	420	Ar/O	9.0	**0.008**	737	21.9	56.7	9.1
420	420	**Vac**	9.0	0.008	809	21.8	66.5	11.7

At reduced $CdCl_2$ concentration (T=380°C) but spanning reaction temperature from 380°C to 450°C there was little difference in V_{OC}, J_{SC}, and FF with reaction temperature in spite of very different grain size. However, at a reaction temperature of 420°C, increasing the $CdCl_2$ concentration from 1 mtorr to 33 mtorr improved the V_{OC} to the range obtained in isothermal cases. Thus, for reactions at one atmosphere total pressure of air, isothermal reactions in the range of 420°C to 430°C yield comparable performance to the $CdCl_2$:methanol method, but with improved uniformity and reproducibility. This suggests that the beneficial modifications of the $CdCl_2$:air ambient mixture are optimal when the CdTe films are at the temperature required to maintain the $CdCl_2$ at equilibrium in the range from 5 to 10 mtorr.

Oxygen concentration, which was shown to affect interdiffusion and grain growth in the materials, does not appear to play an efficiency limiting or enhancing role in the range explored. The O_2 concentration influences the consumption of CdS and could be used to control that process, either by allowing ultrathin layers to survive processing (low O_2 concentration), or by deliberately promoting consumption (high O_2) to either produce an ultrathin layer from a thicker starting layer or to tailor the CdTe bandgap slightly.

The quantum efficiency spectra of vapor treated devices are similar to those treated by $CdCl_2$:methanol but exhibit reduced interdiffusion, evidenced by the long wavelength cutoff [406]. For devices treated at high O_2 concentration, the short wavelength response for 350-550 nm was higher due to reduction in CdS thickness by the S diffusion.

4.2.1.6 Conclusions

Treatment of CdTe/CdS thin films with $CdCl_2$ vapor can be used for processing of high efficiency devices. Reactions in isothermal mode replicate materials and device results obtained with the commonly used $CdCl_2$:methanol method. The vapor approach produces uniform modification of film properties and chemically clean surfaces resulting in uniform device performance. The materials and device uniformity are not contingent on uniform deposition of $CdCl_2$ on the CdTe surface. The absence of rinsing and drying steps makes the vapor processing a favorable approach for large area reactions. The extent of grain growth and interdiffusion can be controlled to some extent by the thermal history and oxygen content of the ambient. Greater than 11% conversion efficiency was achieved with films treated in wide range of oxygen partial pressures at 420°C to 430°C.

4.2.2 Materials Analysis of $CdCl_2$ treated Films

4.2.2.1 Introduction:

Post-deposition processing of polycrystalline CdS/CdTe solar cells with $CdCl_2$ has been demonstrated to improve cell efficiency by improving the electrical properties of the films for photovoltaic operation [409]. In many cases the treatment also produces significant structural changes which are coupled to the electronic properties of the semiconducting layers and which can impose limits on device performance. Treatment or exposure to $CdCl_2$ is a component of every process for fabricating high efficiency CdTe solar cells, regardless of CdTe film formation temperature. For example, films which are fabricated from sintered powder slurries are processed with $CdCl_2$ additives at temperatures of 600-700°C to encourage grain growth and film densification [422-425]. Other devices, such as those deposited by physical vapor deposition (PVD) and molecular beam epitaxy, receive a lower temperature treatment to achieve efficiencies in the 11 to 13% range [426, 427]. They are coated with a $CdCl_2$:CH_3OH solution, dried, then heat-treated at ~400°C. Cells formed by electrochemical deposition receive an analogous treatment where they are synthesized in a plating bath containing Cl ions to produce a Cl-doped CdTe layer and then heat-treated at 400°C for 30 minutes [428].

Many effects of the $CdCl_2$ processing on the CdTe/CdS layers have been observed but their significance to device operation have not been quantitatively explained. For example, grain growth in both the CdS and CdTe layers is greatly enhanced, while porosity is minimized [409, 422-428], but among the different high efficiency devices represented, a considerable range of grain size, porosity and film orientation is found. Previous work has also established that substantial S diffusion occurs in CdTe films over a wide range of thermal processing temperatures [422-426]. A significant degree of S diffusion has also been noted following 400°C treatments with $CdCl_2$ in which consistent shifts were observed in the CdTe x-ray diffraction spectra, CdTe optical absorption edge, and the CdTe spectral response cutoff in CdS/CdTe solar cells [406, 409, 426]. In addition, secondary ion mass spectroscopy (SIMS) has shown that the average S content of the CdTe film increases as the distance to the CdS/CdTe interface decreases [429]. During high temperature treatments, T > 500°C, S diffusion into CdTe is believed to have led to homojunction formation within the S-rich portion of the $CdTe_{1-x}S_x$ layer [424, 425]. These observations are all consistent with the diffusive transport of S into CdTe during $CdCl_2$ processing which reduces the CdS window layer and forms a $CdTe_{1-x}S_x$ layer. Likewise, Te diffusion into CdS produces $CdS_{1-y}Te_y$, which reduces the high energy portion of the device spectral response, resulting in lower current densities. Recrystallization treatments of the CdS layer have been developed which limit the extent of this process [430, 431]. The extent of the CdS consumption establishes a lower limit to the thickness of CdS that can be employed to achieve high efficiency. Control over the effective CdS thickness obtained after processing is thus critical to achieving high current densities while retaining the junction properties of the CdTe/CdS, which controls the open circuit voltage of the device. Loss of the CdS layer will result in formation of a $CdTe_{1-x}S_x$/TCO junction having inferior performance [430].

This paper examines recrystallization and S diffusion in CdTe at ~400°C through a detailed analysis of CdTe/CdS structures before and after the $CdCl_2$ treatment as a function of treatment time. The treatment temperature and time range used in this work were selected to be in the range used to make high efficiency devices. Macroscopic and microscopic materials analyses were performed to assess changes in structure and composition of the CdTe layer.

4.2.2.2 Experimental:

4.2.2.2.1 Film Deposition and $CdCl_2$ Treatment

The CdS/CdTe cells were prepared in a superstrate configuration, so that light enters the cell through the transparent conductive oxide (TCO) coated glass superstrate. First, 0.2-0.5 μm of CdS were deposited at 200°C by evaporation onto indium tin oxide (ITO) coated 7059 glass substrates. CdTe films of several thicknesses, 0.5, 1, 2, and 4 μm, were then evaporated at a growth rate of ~8 Å/s and a substrate temperature of 250°C on top of the CdS layers. These deposition conditions yielded uniform single phase CdTe films. For transmission electron microscopy (TEM), samples with 2 μm CdTe on 0.5 μm CdS were deposited on polished Si wafers coated with ITO. To ensure that the CdTe/CdS deposited on this substrate yielded comparable electrical performance to the standard cells, a semi-transparent Au layer was used as the contact to CdTe to allow backwall current-voltage measurements to be made. Comparable backwall performance was obtained from the two device structures.

The CdTe/CdS/ITO/7059 samples were coated with 0.8 μm of solid $CdCl_2$ by placing 1 drop per cm^2 of 1% (wt) $CdCl_2$:CH_3OH solution on the top surface of the CdTe film, then evaporating the CH_3OH in a drying oven at 85°C. During the subsequent air heat-treatment, the samples were held at 415°C for either 10 or 30 minutes. Thermal transients were minimized by rapid introduction and withdrawal of the samples from the hot zone of the furnace tube. The heat-treatment step was followed by a rinse in deionized water to remove most of the residual $CdCl_2$ coating.

4.2.2.2.2 Microscopy Measurements

The CdTe grain sizes were determined using the method of Heyn [432] from the top surface of the CdTe film and from polished 90 degree sample cross-sections using scanning electron microscopy (SEM). The CdTe grains were clearly distinguishable on the top surface of the samples once they had been rinsed. Polished and etched 90 degree cross-sections were prepared by vacuum impregnating in epoxy, polishing with 0.05 μm alumina grit, then rinsing in hot water.

The CdTe grain boundaries in the polished samples were revealed by first polishing in a 0.0125% (wt) Br_2:CH_3OH solution and then reacting in a 0.1M CuCl/deionized water solution (adjusted to pH=2.25 through addition of HCl) at 65°C for 30 to 60 seconds. The reaction, $CdTe + 2CuCl \rightarrow CdCl_2 + Cu_2Te$, occurs preferentially along grain boundaries. To reveal the grain boundaries, the $Cu_{2-x}Te$ was etched in a 0.2M KCN/water solution at 65°C for 30 seconds. After each step, the samples were rinsed with room temperature, deionized water and dried.

TEM and energy dispersive x-ray spectroscopy (EDS) was used to examine the cross-sectional grain structure and composition on a CdTe/CdS/ITO/Si sample before and after heat treatment with $CdCl_2$ [433].

4.2.2.2.3 X-ray Diffraction Measurements

The x-ray diffraction (XRD) patterns of the CdTe films were generated using a computer controlled Philips/Norelco diffractometer with Bragg-Bretano focusing geometry and CuK_a radiation. Wide angle 2q scans from 20 to 80 degrees taken at 0.05 degree steps were used to identify the phases present in the samples. The Rachinger correction [435] was used to remove a_2 components for lattice parameter determination and peak profile examination. Errors in peak centrum location lattice parameter determination and peak profile examination. Errors in peak centrum location associated with specimen placement and geometry were corrected using the function of Nelson, Riley, Sinclair, and Taylor (NRST), so that the CdTe film lattice parameters could be precisely determined [435-437]. The sulfur content, x, of the $CdTe_{1-x}S_x$ film was determined quantitatively from the lattice parameters by assuming a Vegard's relation:

$$x = 1.508(6.481-a)$$

Equation 4-1

where a is the lattice parameter of the sample.

The degree of preferred orientation in the films was calculated from the a_1 peak intensities of the broad scans using the method of Harris for polycrystalline fiber texture analysis [418]. For the {111} reflection, the orientation parameter, p(111), is defined:

$$p(111) = \frac{N[I(111)/I_0(111)]}{[\sum I(hkl)/I_0(hkl)]}$$

Equation 4-2

where N is the number of peaks in the region considered, I(hkl) is the measured intensity of peak (hkl), and I_0(hkl) is the relative intensity of the corresponding peak from a powder reference. For p(111) = N, all the grains of the films are oriented in the <111> direction normal to the substrate, while p(111) = 1 indicates random grain orientation, and p(111) < 1 indicates preferred orientation along an axis other than <111>.

Diffraction scans at 0.01 degree steps were acquired at constant counts per step to obtain constant signal to noise ratio from sample to sample for individual peak profile determination. The peak profiles were assumed to represent the entire sample alloy composition range resulting from diffusion of S into CdTe. To ensure the validity of this assumption, primary and diffracted beam attenuation, which increases surface selectivity, was minimized by using samples less than 3 µm thick. One film was mechanically separated from the TCO/glass and remeasured from the CdS side, yielding the same diffraction profile. To obtain adequate angular resolution, higher order peaks such as the (422), (511) and the (531) were measured. The extent of S diffusion into the grains was shown to be independent of the grain orientation with respect to the substrate surface by examining all (hkl) peak profiles on a single sample. Profiles exhibiting high symmetry, and therefore low diffusion tails, were fit to a Pearson VII function [438] to determine the full width at half maximum (FWHM) for comparison with the diffractometer instrument function. In cases of high asymmetry, Fourier deconvolution of the diffractometer instrument function was performed to establish the limits of compositional broadening.

4.2.2.2.4 Optical Absorption Measurements

Optical transmission, $T(\lambda)$, and reflection, $R(\lambda)$, of the CdTe/CdS/ITO/glass structures were measured on a Perkin-Elmer Lambda 9 spectrophotometer and were transformed to an effective absorption coefficient, $\alpha_{eff}(\lambda)$ to allow comparison of the absorption edge location after the various treatments. For this, the effective absorption coefficient of the structure was determined by:

$$\alpha_{eff}(\lambda)=\frac{\mathrm{Ln}\left[\frac{T(\lambda)}{1-R(\lambda)}\right]}{d}$$

Equation 4-3

where d is the thickness. Plots of a α^2_{eff} versus energy were used to determine relative shifts in the absorption edge due to the alloying of CdTe and CdS over a sufficient film thickness to influence the overall absorption. The S content of the absorbing layer was estimated by comparison of the shift of the absorption edge with that reported for kinetically limited or metastable $CdTe_{1-x}S_x$ thin films [405, 439] in which the CdTe bandgap, E_g, is reduced due to formation of $CdTe_{1-x}S_x$ alloys from x=0 to 1 according to:

$$E_g(x)=1.74x^2-1.01x+1.51\ [436].$$

Equation 4-4

Equilibration of alloy films at ~400°C leads to a miscibility gap from x=5.8% to x=97% but with similar E_g versus x dependence over the alloy existence region.

4.2.2.3 Results:

4.2.2.3.1 Microscopy

As-deposited films have lateral grain size of ~0.1-0.25 μm depending on film thickness. Films heat treated at 415°C without $CdCl_2$ for up to 30 minutes have similar structure to as-deposited films, with little observable change in grain size or morphology. However, substantial grain growth occurs for samples coated with $CdCl_2$ (Table 4-6). Figure 4-6 (a-i) shows SEM top surface micrographs of 0.5, 1, and 2 μm thick CdTe films for as-deposited (a-c) and $CdCl_2$ treated at 415°C for 10 minutes (d-f) and 30 minutes (g-i). For the different CdTe film thicknesses there is a trend toward larger final grain sizes with thicker CdTe films and with longer heat treatment times, although for the 2 μm thick films, the average grain size is the same after 10 and 30 minutes of treatment (Table 4-6). After 30 minutes of treatment there are no detectable sub-micron grains, and the grain boundaries meet at 120° angles, as expected for a film in equilibrium [440].

Table 4-6. Tabulated values of grain size, orientation parameter, lattice parameter, and (111) peak intensity for CdTe powder and for CdTe films in 2 μm CdTe/0.5 μm CdS/ITO/glass structures.

Sample	Condition	Average Grain Size (μm)	p(111)	I(111) (counts)	a_0 (Å)	(511) FWHM (deg)
Powder	-	NA	1.0	NA	6.481	NA
Film	As Deposited	0.2	4.0	8849	6.489	0.248
Film	10', 30' and 60' HT no $CdCl_2$	0.2	2.3	4908	6.480	0.140
Film	10' HT with $CdCl_2$	1.3	0.8	5823	6.481	0.140
Film	30' HT with $CdCl_2$	1.3	0.9	3004	6.460	>0.40

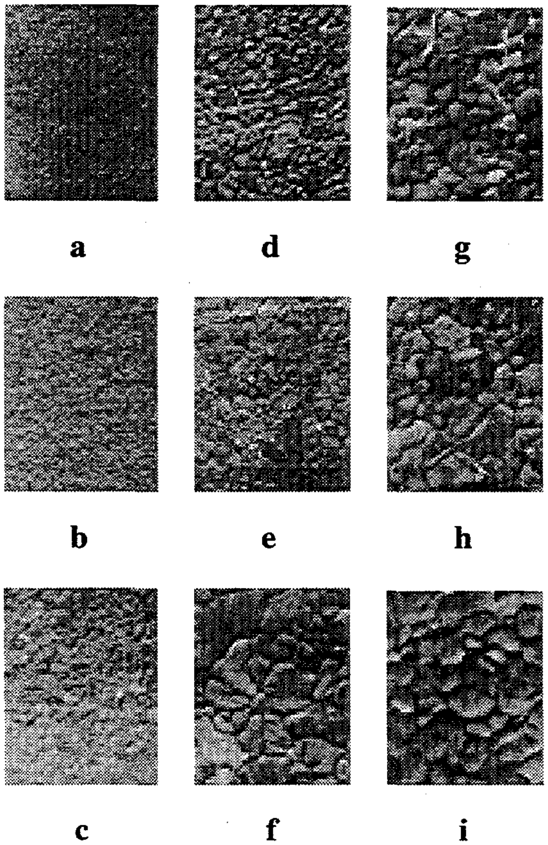
a d g
b e h
c f i

Figure 4-6 SEM top surface micrographs (x 5000) of 0.5, 1, and 2 μm CdTe/0.5 μm CdS/ITO/glass structure in as-deposited condition (a-c); after heat treatment at 415°C for 10 minutes with $CdCl_2$ (d-f); and after heat treatment at 415°C for 30 minutes with $CdCl_2$ (g-i).

Cross-section SEM micrographs in conjunction with top surface micrographs show that the increase in grain dimension extends down to the CdTe/CdS interface as shown in Figure 4-7 for 4.5 μm and 2.0 μm thick CdTe samples. The micrographs in Figure 4-7 demonstrate that the coalesced CdTe grains after $CdCl_2$ heat-treatment are at least as wide as they are deep. This is quite different from the as-deposited microstructures, which are difficult to analyze by SEM analysis, since the grain sizes are less than 250 nm.

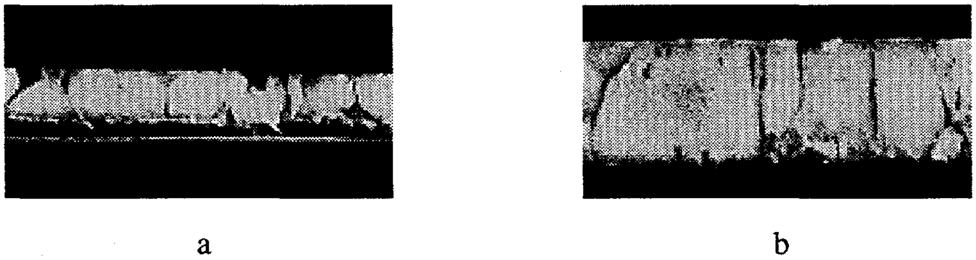
a b

Figure 4-7 SEM cross-section micrographs (x 5000) of 2 μm and 4 μm CdTe samples after heat treatment at 415°C for 30 minutes with $CdCl_2$.

Cross-section TEM analysis was carried out on as-deposited 2 μm CdTe/0.5 μm CdS samples and the same samples $CdCl_2$ treated at 415°C for 30 minutes. The micrographs of the CdTe/CdS/ITO/Si cross-sections suggest that the as-deposited CdTe grains are epitaxial with the underlying CdS grains and are highly faulted and columnar (Figure 4-8). Spot TEM/EDS analysis showed no evidence of S or Te interdiffusion in the as-deposited films. Selected area electron diffraction of the individual layers showed that the CdTe film is predominantly cubic, while the CdS film contains a mixture of cubic and hexagonal phases. High resolution lattice imaging confirmed that the CdTe grains are epitaxially related to the CdS grains[433]. Recrystallization of the as-deposited film is thus energetically favored, since it will reduce the strain energy within the CdTe layer arising from the ~10% lattice mismatch between the CdS (001) and the CdTe (111) planes. After heat treatment with $CdCl_2$, TEM imaging (Figure 4-9) shows substantial grain growth in both layers with little or no epitaxial coordination between the CdS and the CdTe. The TEM micrographs show thermal grooving at the surface of the CdTe near the grain boundaries and independent restructuring of the CdS and CdTe films, resulting from reduction in the interfacial energy. Selected area EDS measurements indicated S and Te interdiffusion across the interface after treatment.

Figure 4-8. TEM cross-section micrograph of 2 μm CdTe/0.5 μm CdS/ITO/Si in as-deposited condition.

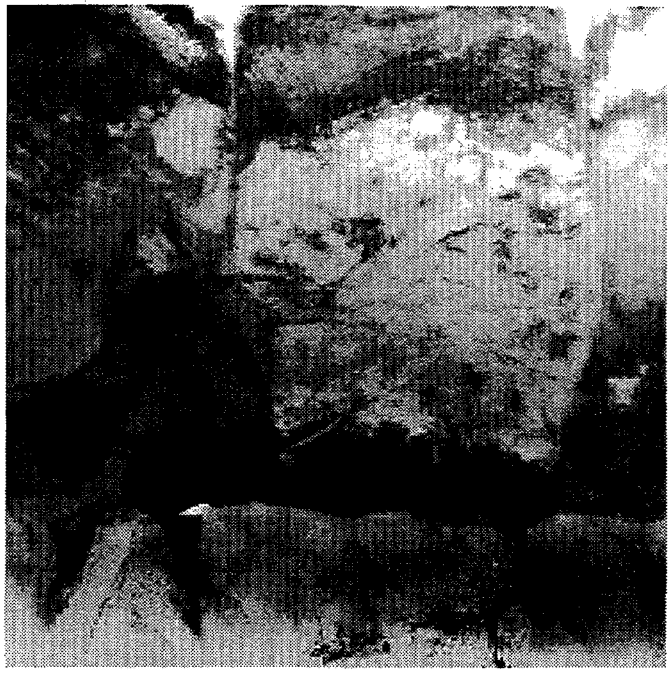

Figure 4-9 TEM cross-section micrograph of 2 μm CdTe/0.5 μm CdS/ITO/Si after heat treatment at 415°C for 30 minutes with $CdCl_2$.

4.2.2.3.2 Wide Angle X-Ray Diffraction Scans

Wide angle x-ray diffraction scans were made on all samples: as deposited, treated without $CdCl_2$, treated with $CdCl_2$ at 415°C for 10 and 30 minutes. The XRD scans show that recrystallization of the CdTe film occurs during heat treatment with or without $CdCl_2$. Figure 4-10 specifically compares wide angle scans of an as-deposited sample to two samples cut from the same piece and treated for 10 minutes at 415°C in air. One of the samples was coated with $CdCl_2$ prior to the heat treatment. The as-deposited film shows a very strong {111} texture with $p(111) = 4$. Heat-treatment at 415°C for 10, 30, or 60 minutes in the absence of $CdCl_2$ produces a modest degree of sharpening of the individual peaks, and a reduction of preferred orientation to $p(111) = 2.3$. Heat-treatment of $CdCl_2$-coated samples at 415°C for 10 minutes, however, produces near-random orientation of the grains, with $p(111) < 2$. The samples treated with $CdCl_2$ exhibit additional peaks in the patterns due to residual $CdCl_2$ phases on the CdTe surface after treatment.

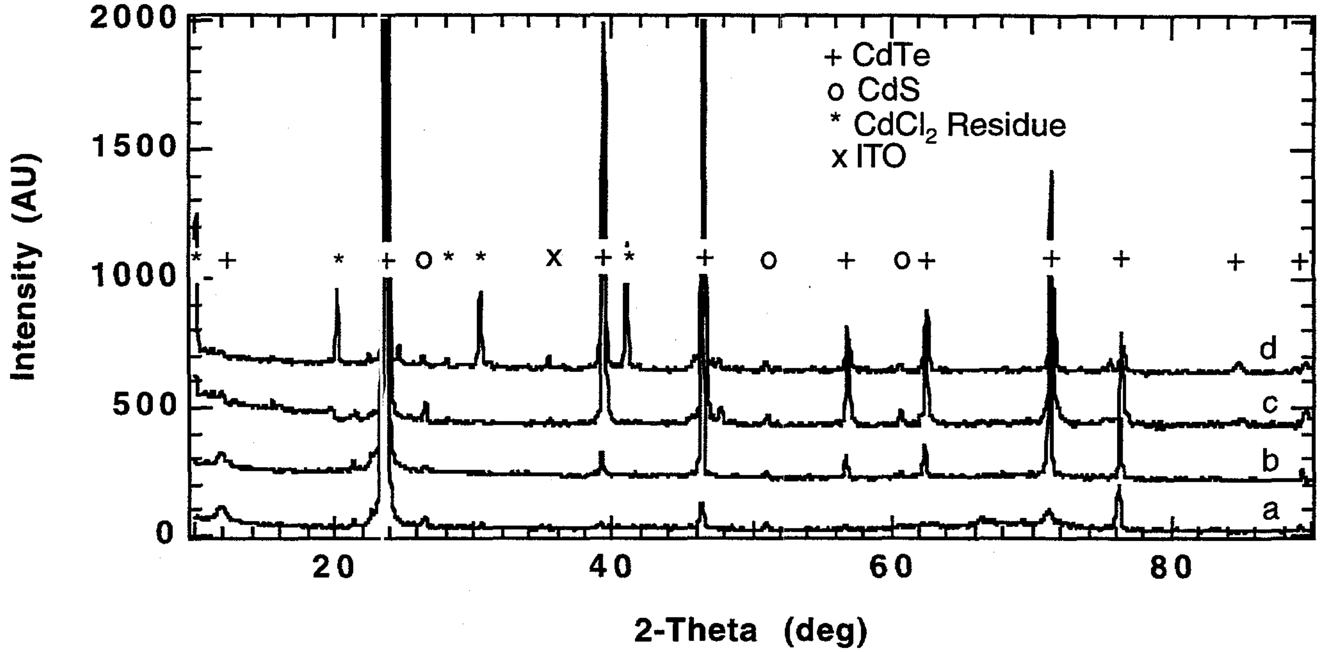

Figure 4-10 Wide angle XRD scans of 2 μm CdTe/0.5 μm CdS/ITO/glass structure in as-deposited condition (a), after heat treatment at 415°C for 10 minutes with no $CdCl_2$ (b), after heat treatment at 415°C for 10 minutes with $CdCl_2$ (c) and after heat treatment at 415°C for 30 minutes with $CdCl_2$.

Heat treatment without $CdCl_2$ shifted all the diffraction peaks slightly towards higher angle, while treatment with $CdCl_2$ shifted and broadened the diffraction peaks towards higher angle. Table 4-6 summarizes the changes in grain size, orientation parameter, precision lattice parameter, and FWHM obtained with and without $CdCl_2$ during heat treatment. The as-deposited films appear to be strained, with lattice parameter greater than expected for CdTe. The increase in a_0 along the <hkl> growth axis can be explained by a compressive stress perpendicular to the growth axis, i.e., in the growth plane. The TEM results described above suggest that the heteroepitaxial nature of the CdTe-CdS films can account for strain in the as-deposited films given the ~10% lattice mismatch between atoms in the CdS (001) and CdTe (111) planes. Heat treatment without $CdCl_2$ relieves the strain, which produces the observed reorientation and shift in a_0 to that expected for pure CdTe. Consistent with prior work, [425, 428] the heat treatment with $CdCl_2$ shifts the centrum of the CdTe peaks toward smaller lattice parameter. This is explained by the diffusion of sulfur into CdTe to form a $CdTe_{1-x}S_x$ solid solution, since S substitutes onto Te sites in the CdTe lattice and has a smaller atomic radius than Te which reduces the interatomic bond length in the molecule.

4.2.2.3.3 Narrow Angle X-ray Diffraction Scans

High resolution scans of all (hkl) diffraction lines show the same profile, indicating that the CdS-CdTe mixing process is independent of crystallographic direction. Analysis of the (511) CdTe diffraction peaks before and after $CdCl_2$ processing were made to illustrate the strain relief and compositional variations promoted by the $CdCl_2$ processing. Figure 4-11 shows the (511) peak profile of a 1 μm thick CdTe film in the as-deposited state and after 10 and 30 minute $CdCl_2$ heat-treatments at 415°C. The evolution of the profile indicates either a strain state or compositional inhomogeneity in the CdTe film. Our subsequent analysis is based on the latter assumption, given the supporting evidence of the TEM/EDS and SIMS measurements.

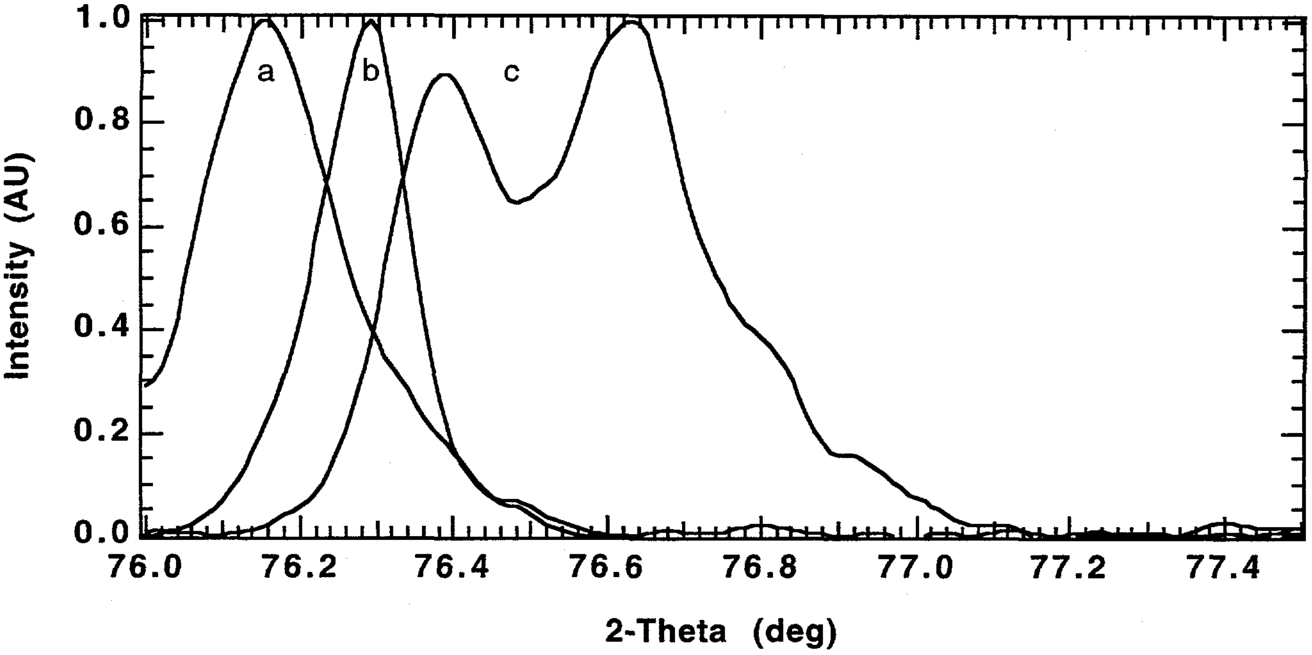

Figure 4-11 XRD (511) profile of 2 μm CdTe/0.5 μm CdS/ITO/glass structure in as-deposited condition (a), after heat treatment at 415°C for 10 minutes with $CdCl_2$ (b), after heat treatment at 415°C for 30 minutes with $CdCl_2$ (c).

In Figure 4-11, the centrum of the as-deposited (511) peak profile again has larger d-spacing than expected for pure, unstrained CdTe. The FWHM of the (511) peak is approximately twice that of the diffractometer instrument function. After 10, 30 and 60 minutes of treatment without $CdCl_2$ and 10 minutes with $CdCl_2$ the peak shifted to d-spacing expected for pure CdTe and sharpened to the value obtained for the diffractometer instrument function. Grain coalesence reduced small-particle scattering and relieved the strain which sharpened the peak and shifted the lattice parameter. After 30 minutes of treatment with $CdCl_2$ the peak profile is a doublet having a significant tail extending towards lower d-spacing and lattice parameter.

Fourier deconvolution of the diffractometer instrument function from this profile indicates two strong maxima centered at a_0 = 6.478 Å and a_0 = 6.459 Å, corresponding to compositions of x= 0.5% and x= 3.3%, respectively in $CdTe_{1-x}S_x$. The high angle tail extends to the solubility limit found for S in CdTe [405, 406]. Chemical removal of the top micron of film eliminated the high a_0 component of the diffraction profile so the low S portion of the film was removed. Thus, the S-enriched portion lies in the region of the structure closest to the CdS-CdTe interface. The resulting profile is similar to the profiles obtained from thinner CdTe samples treated under exactly the same conditions as in Figure 4-11. This implies that the compositional distribution with depth is obtained that is independent of the total CdTe thickness and suggests a rapid diffusion process near the CdS-CdTe interface. Thus, treatment with $CdCl_2$ results in CdS-CdTe mixing that cannot be accounted for by a simple single step diffusion process. In curves b and c of Figure 4-12, for 1.0 μm and 0.5 μm thick CdTe films, the primary peak has shifted to the lower lattice parameter, indicating conversion of most of the film to $CdTe_{1-x}S_x$ with x = ~5%. In a 1 μm CdTe film, this corresponds to an equivalent CdS film thickness of ~40 nm that is consumed during the processing.

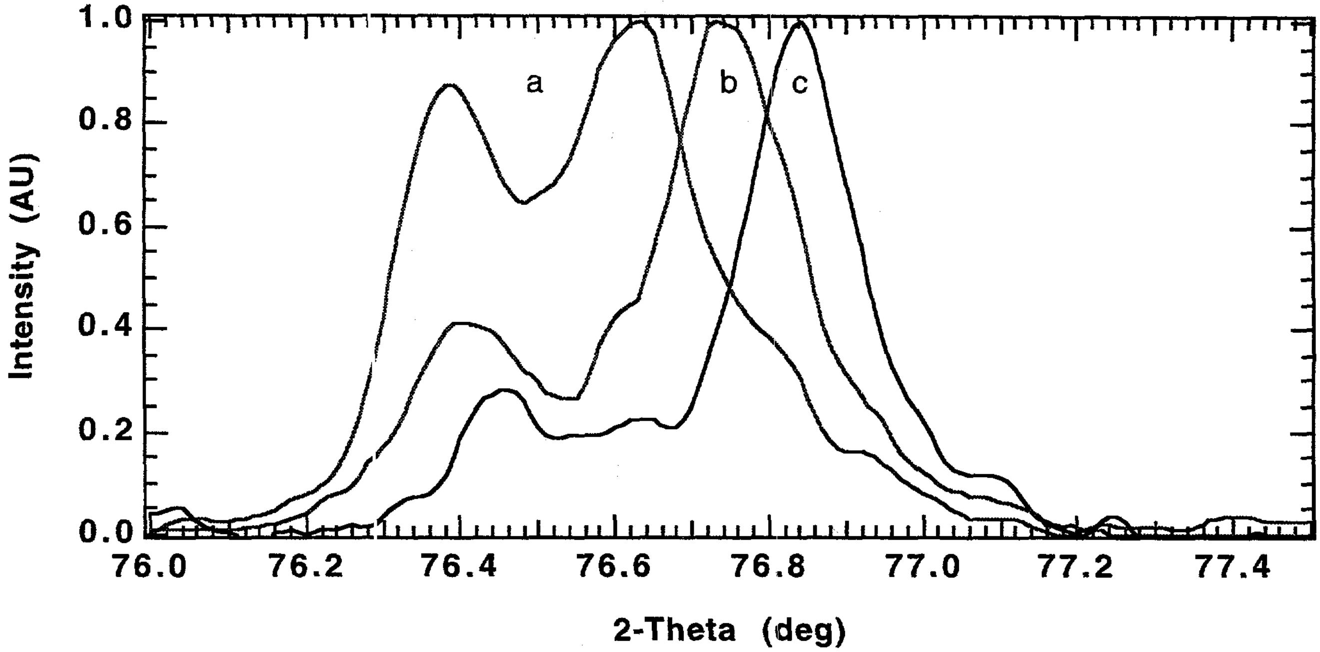

Figure 4-12 XRD (511) profile after heat treatment at 415°C for 30 minutes with $CdCl_2$ of 2 μm CdTe/0.5 μm CdS/ITO/glass structure (a), 1 μm CdTe/0.5 μm CdS/ITO/glass structure (b), and 0.5 μm CdTe/0.5 μm CdS/ITO/glass structure (c).

4.2.2.3.4 Optical Absorption Measurements

A plot of the square of the absorption coefficient versus photon energy is shown in Figure 4-13 for the 2 μm CdTe/0.5 μm CdS samples of Table 4-6. All samples exhibit similar absorption profiles and the energy shifts caused by the different treatments are listed in Table 4-7.

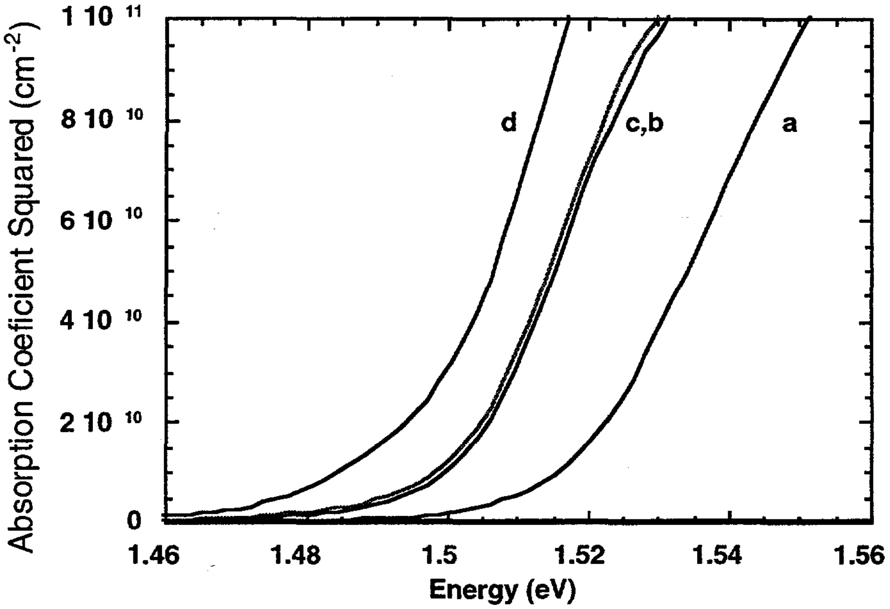

Figure 4-13 Absorption coefficient squared versus energy for 2 μm CdTe/0.5 μm CdS/ITO/glass structure in as-deposited condition (a), after heat treatment at 415°C for 10 minutes with no $CdCl_2$ (b), heat treatment at 415°C for 10 minutes with $CdCl_2$ (c), and heat treatment at 415°C for 30 minutes with $CdCl_2$ (d).

Table 4-7. Tabulated values of relative energy shifts from the as-deposited film at $a^2 = 5 \times 10^{10}$ cm^{-2} in Figure 4-13 and the corresponding S content.

Sample	Condition	ΔE (meV)	% S
a	As Deposited	0	0
b	10', 30' and 60' HT no $CdCl_2$	19	1.95
c	10' HT with $CdCl_2$	20	2.05
d	30' HT with $CdCl_2$	28	2.95

The samples treated for 10, 30 and 60 minutes without $CdCl_2$ and 10 minutes with $CdCl_2$ exhibited the same reductions in the energy of the absorption edge with formation of a $CdTe_{1-x}S_x$ layer containing ~2 % S. After treatment for 30 minutes with $CdCl_2$, however, the composition of the lowest bandgap absorbing layer corresponds to

$CdTe_{1-x}S_x$ containing ~3% S. At first glance, these compositions do not seem to be supported by the diffraction data, but the diffraction data is least sensitive to thin layers near the interface, while the optical data is most sensitive to highly absorbing layers of low bandgap, as expected near the interface. Thus, in the region of the interface, treatment at 400°C with or without $CdCl_2$ produces some intermixing of CdTe and CdS. This mixing is the primary mechanism for relieving elastic strain in as-deposited samples. For the sample treated with $CdCl_2$ for 30 minutes, the optical measurements indicate the presence of a layer with 3% S while the diffraction data consistently exhibits a maximum at ~3% but tails that extend to 5-6% S, at the solubility limit for S in CdTe [405, 406]. It is speculated that the higher S content regions do not form a continuous film of sufficient thickness to control the optical properties in the plane parallel to the interface. Thus, the higher S content regions (3-6% S) may exist along grain boundaries or other defects.

4.2.2.4 Conclusions:

As-deposited evaporated CdTe/CdS thin film structures consist of single phase columnar CdTe grains that are pseudo-epitaxially oriented on mixed cubic and hexagonal phase CdS films. The CdTe film is highly strained due to lattice mismatch and is free of sulfur.

Heat treatment of the structures at 415°C without $CdCl_2$ produces little or no detectable grain growth but relaxes interfacial strain due to a small amount of interfacial CdTe-CdS mixing. The treatment also induces some randomization of the CdTe film orientation with respect to the <111> axis.

Heat treatment with $CdCl_2$, needed to produce high efficiency devices from the evaporated materials, induces dramatic grain growth of both the CdTe and CdS layers, reduces surface and interfacial energy, promotes significant CdS-CdTe interdiffusion, and randomizes the CdTe film orientation. The recrystallization occurs in a time frame of ~10 minutes at 415°C, while interdiffusion is progressive up to 30 minutes and may involve more than one transport process to account for the doublet diffraction peak profiles observed. Further work is necessary to identify the mixing processes and their dependence on $CdCl_2$ concentration, reaction temperature and treatment time. The region near the original CdS-CdTe interface consists of a $CdTe_{1-x}S_x$ alloy with x^a 5%, which is the equilibrium solubility limit for S in CdTe. The extensive alloying forms a non-uniform $CdTe_{1-x}S_x$ layer and consumes a significant quantity of CdS from the device. This establishes a lower limit to the CdS film thickness that can be employed while still retaining a discreet CdS coating on the TCO.

4.3 CdTe-CdS ALLOYS AND DEVICES

4.3.1 INTRODUCTION

Interdiffusion between the window and absorber layer materials occurring during the processing of CdS/CdTe-based solar cells has been widely reported [409, 441-444]. The diffusion of Te into CdS results in the alloy, $CdS_{1-y}Te_y$, which features a wurtzite structure and a lower band gap than CdS. Thus, the diffusion of Te into the window layer has been observed to decrease the J_{SC} of the device [430, 442]. Similarly, the diffusion of S into CdTe results in the zincblende structured alloy, $CdTe_{1-x}S_x$, which features a lower band gap than CdTe. The effect of the formation of this alloy on device performance is difficult to estimate. A correlation between higher V_{OC} and enhanced interdiffusion has been claimed by at least one group [444]. The lower band gap could, conceivably, result in a lower V_{OC} and higher J_{SC}, but the better lattice match and corresponding reduction of interface states could also raise V_{OC} by lowering J_0. The possible effects of a difference in the native defect density between CdTe and the $CdTe_{1-x}S_x$ is also open for speculation.

As a further complication, sulfur diffuses into the CdTe during processing more quickly along grain boundaries than into the bulk of the grains [413]. This process results in a spatially non-uniform composition in the absorber layer conceivably resulting in two or three dimensional effects, and in a non-uniform consumption of the CdS window layer possibly resulting in pinholes.

The significance of the interdiffusion process will clearly depend on the composition of the alloys formed . If the diffusion process were allowed to continue long enough, the window layer would eventually contain the solubility limit of Te in CdS, and, provided that the CdS layer was sufficiently thick, the absorber layer would contain the solubility limited amount of S in CdTe.

These solubility limits have previously been measured only at temperatures no lower than 650°C [445].

In the work presented here, the solubility limits of S in CdTe and Te in CdS at typical temperatures used for device processing are derived by growing alloyed thin films with compositions within the miscibility gap and heat treating them in the presence of $CdCl_2$. Conventional CdTe/CdS devices are then compared to devices where the alloy composition of the absorber layer is uniformly at the solubility limit of S in CdTe, and to CdTe/ITO devices which contain no sulfur in the absorber layer.

4.3.2 EXPERIMENT

4.3.2.1 Alloyed Film Fabrication and Characterization

Thin films of $CdTe_{1-x}S_x$ were grown on glass, In_2O_3:Sn (ITO)/glass, and CdS/ITO/glass substrates by co-evaporation of CdS and CdTe at substrate temperatures of 200 and 250°C. Energy dispersive spectroscopy (EDS) was used to measure the overall atomic composition of the films. X-ray diffraction (XRD) analysis was used to determine the structures of the phases within the films. The atomic compositions of each phase within the films were estimated by using a Nelson-Riley-Sinclair-Taylor plot to extract a lattice parameter from the XRD peak positions, and then applying Vegard's law.

The optical transmission and reflection of the films were measured and used to estimate the absorption constant, a. The linear portion of $(ahn)^2$ verses hn was extrapolated to obtain an optical band gap.

4.3.2.2 Film Treatment

The alloyed films were subjected to one of two $CdCl_2$ heat treatment methods. In the traditional surface method, $CdCl_2$ was deposited directly on the film [409]. In the vapor method, $CdCl_2$ was kept at distance ≈0.1 mm away from the film surface 416]. In both cases, the $CdCl_2$ and film were heated in air at 415 to 420°C.

4.3.2.3 Device Processing

Conventional CdTe/CdS solar cells were made by vacuum evaporation of ~200 nm CdS and then ~5 μm of CdTe onto ITO/glass substrates. These structures were given a $CdCl_2$ vapor treatment in dry air at 420°C for 20 minutes. Back contacts were made to the devices by the deposition of 100 Å of copper, diffusion of copper into the film by heating at 180°C for 30 minutes in an argon atmosphere, etching away the copper remaining on the surface with a solution of bromine in methanol and then applying graphite paste [446]. Indium solder applied to the ITO served as the front contact.

$CdTe_{1-x}S_x$ /CdS/ITO, $CdTe_{1-x}S_x$/ITO, and CdTe/ITO solar cells were produced in a manor very similar to the conventional CdTe/CdS cells. The $CdTe_{1-x}S_x$ layers were deposited with a sulfur content of x=5 to 6%. The processing conditions used for each of the four device structures compared in this work are given in Table 4-8. The 200°C copper diffusion temperature was found to be critical to obtaining satisfactory $CdTe_{1-x}S_x$/CdS devices. The $CdTe_{1-x}S_x$/CdS devices treated at 180°C typically suffered from low J_{SC}, voltage dependent collection, and blocking contact behavior. For the CdTe/ITO device, a 500 Å thin insulating layer of ITO was deposited on the 20Ω/square ITO substrate prior to CdTe deposition. The use of this layer improved the J_{SC} and consistency of these devices. The use of an insulating ITO layer with $CdTe_{1-x}S_x$/CdS devices has not yet been explored.

Table 4-8 Device Processing Conditions (CdS thickness, substrate temperature during absorber layer deposition, as-deposited sulfur content, and copper diffusion temperature) and Performance Characteristics.

Device Structure	CdS thick. (Å)	substr. temp. (°C)	x (%)	Cu diff. temp. (°C)	V_{oc} (mV)	J_{sc} (mA/ cm^2)	FF (%)	h (%)	Label in Figs. 4, 5 & 6
CdTe/CdS/ITO	2600	275	0	180	769	20.4	67.6	10.6	(1)
CdTe/i-ITO/ITO	0	275	0	180	482	24.5	55.7	6.6	(2)
$CdTe_{1-x}S_x$/CdS/ITO	1800	250	5	200	787	21.1	64.8	10.8	(3)
$CdTe_{1-x}S_x$/ITO	0	250	5.5	200	336	22.7	36.2	2.8	(4)

4.3.3 RESULTS AND DISCUSSION

4.3.3.1 Properties of As Deposited Films

As-deposited $CdTe_{1-x}S_x$ films grown on ITO/glass and glass substrates were produced with overall atomic compositions ranging from $x= 0$ to 0.45. XRD analysis revealed that films with $x < 0.3$ were predominately single phase having a zincblende structure. Films with $0.35 < x < 0.45$ contained the wurtzite modification. The composition of the dominant phase in each as-deposited film closely matches the overall composition of the film (see Figure 4-14), even when the overall composition is well within the miscibility gap shown on published pseudo-binary phase diagrams for the CdTe-CdS system. The miscibility gap on these phase diagrams extends from $x=0.16$ to 0.86 at 650°C [416] and should be even wider at lower temperatures due to the smaller influence of the entropy on the free energy of the system. Therefore, these films demonstrate that single phase material of either structure may be created with compositions within the miscibility gap. The variation of optical band gap with composition was found to agree well with the data of [439].

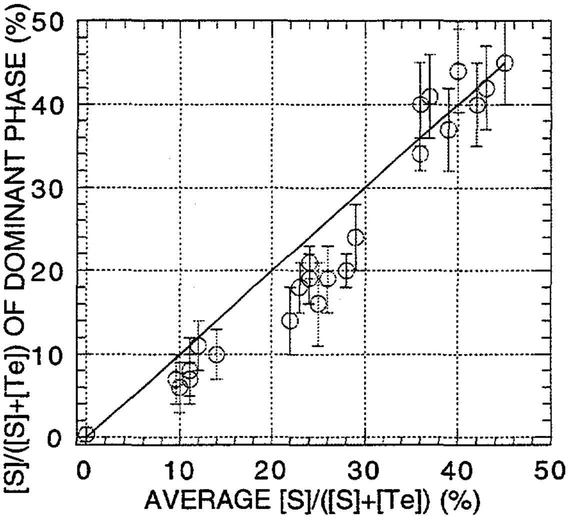

Figure 4-14 For each as-deposited film grown on ITO/glass substrates, the composition of the dominant phase, as determined by XRD analysis, is plotted against the average composition of the film, as measured by EDS. The solid line indicates where the two compositions are equal.

4.3.3.2 Response to $CdCl_2$ Treatment

XRD analysis revealed that heat treatment in the presence of $CdCl_2$ at 415°C caused the films with x>6% to segregate into two phases. The phase segregation process for one film is shown in Figure 4-15. It is felt that the phase distributions of the as-deposited films were either metastable or kinetically controlled, and that heat treatment drove the films towards equilibrium. The rate of phase segregation was affected by the sulfur content of the films and the $CdCl_2$ treatment method, but the end-point composition was not. If the $CdCl_2$ is assumed to only promote the phase segregation process, then the compositions of the two phases after heat treatment may be taken as measurements of the solubility limits of S in CdTe and Te in CdS, respectively. The 415°C solubility limit of S in CdTe is, thus, $x'=0.058\pm0.003$, and the solubility limit of Te in CdS is $y'=[Te]/([S]+[Te])=0.03\pm0.01$.

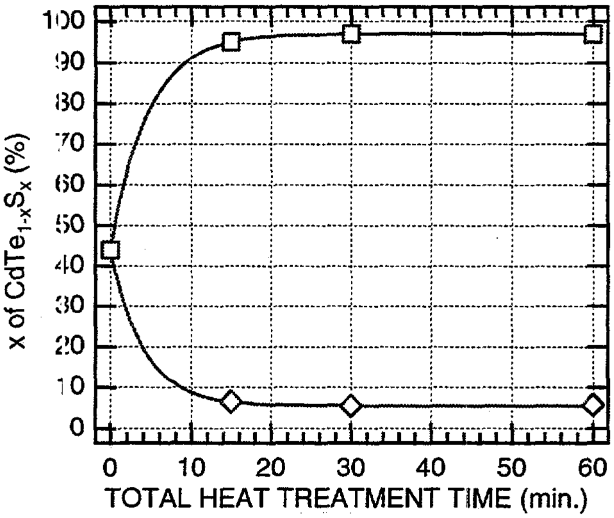

Figure 4-15 Composition of the zincblende structured (diamonds) and wurtzite structured (squares) phases in a film with an average composition of 40.3% as a function of $CdCl_2$ treatment time.

The grain structure of the $CdTe_{1-x}S_x$ films after $CdCl_2$ treatment was found to be quite different than the structure of CdTe films, even when x was less than the solubility limit. A surface layer is suggested by the cross-sectional view shown in Figure 4-16. A preliminary EDS analysis indicates that the surface layer may be richer in sulfur than the bulk. Clearly, the grain restructuring that occurs during $CdCl_2$ treatment is significantly influenced by the presence of sulfur in the film.

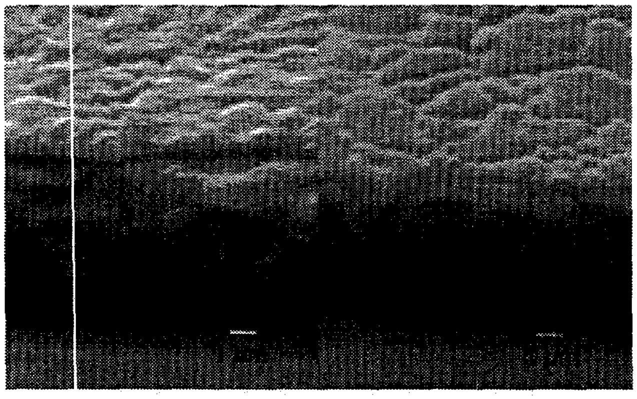

(a) **(b)**

Figure 4-16 Cross-sectional Scanning Electron Micrograph of (a) an alloyed film with a sulfur content [S]/([S]+[Te])=0.05, and (b) a CdTe film. The ~ 5 μm thick films received identical $CdCl_2$ heat treatments.

4.3.3.3 Device Results

As shown in Table 4-8, a $CdTe_{1-x}S_x$/CdS device with efficiency near 11% was obtained. The current-voltage characteristics of this device are comparable to those of the conventional CdTe/CdS device (see Figure 4-17). In comparison, the CdTe/ITO device features a high J_{SC} due to the absence of absorption from CdS (see Figure 4-18), but suffers from low V_{OC}. The best of the CdTe$_{1-x}$S$_x$/ITO devices made so far, suffer from even lower V_{OC} and voltage depend collection. It is not yet known whether these problems can be improved by adjusting the processing conditions.

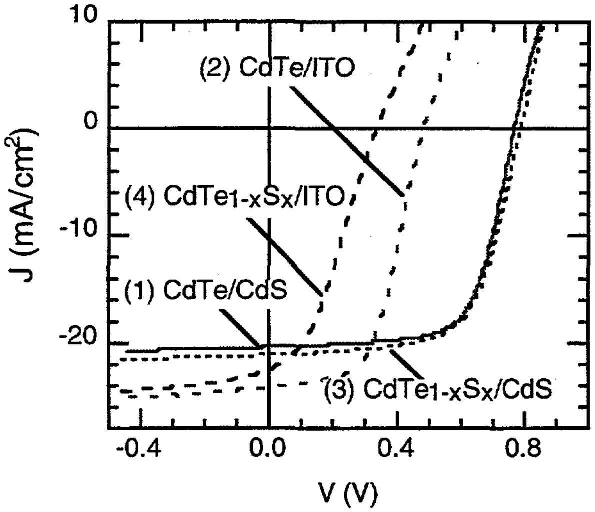

Figure 4-17 Current-voltage characterstics under standard AM1.5 global illumination conditions of the four devices listed in Table 4-8.

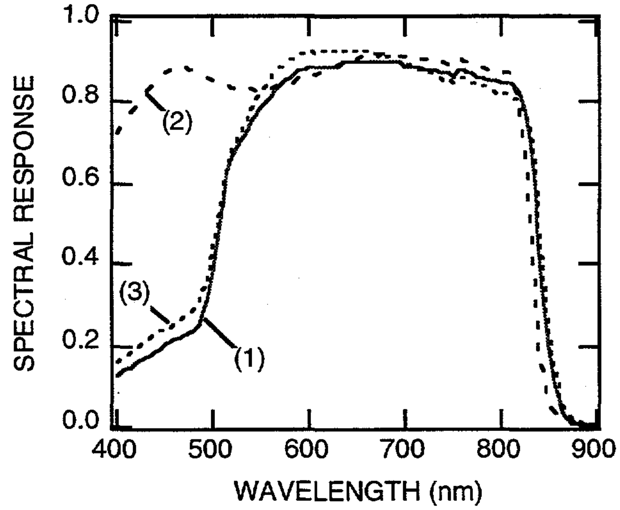

Figure 4-18 The spectral response under light bias of three of the devices listed in Table 4-8: (1) a conventional CdTe/CdS solar cell, (2) a CdTe/ITO solar cell, and (3) a CdTe$_{1-x}$S$_x$/CdS solar cell.

The similarity of the CdTe$_{1-x}$S$_x$/CdS device and the conventional CdTe/CdS device is further emphasized by the region of the spectral response near 850 nm where collection drops due to the band edge of the absorber material. That the drop in collection at the band edge of the conventional CdTe/CdS device closely matches the CdTe$_{1-x}$S$_x$/CdS device rather than the CdTe/ITO device indicates that sulfur content of the conventional device must be near the solubility limit in the region close to the junction where the majority of photons are absorbed. The band edge of the CdTe/ITO device stands apart from the others because, of the devices studied, it is the only device with a non-alloyed absorber layer after processing.

The physical difference between the $CdTe_{1-x}S_x/CdS$ and CdTe/CdS device structures is primarilly the uniformity of the alloy composition in the absorber. The absorber of the $CdTe_{1-x}S_x/CdS$ device was deposited with a sulfur content of x=5%. Since this is close to the solubility limit of S in CdTe, little to no increase in the sulfur content due to diffusion of S from the CdS layer was expected to occur during the cell processing. We believe, therefore, that the composition of the absorber layer of these cells is uniformly 5 to 6%. This is in contrast to the sulfur content in the absorber of conventional CdTe/CdS devices which has been found, after processing, to approach 6% near the CdS interface, and be less than 1% throughout the bulk of the material [405].

The difference between the uniformity of the absorber layers is evident only in the long wavelength tail of the spectral response where light penetrates more deeply into photon energy, it is seen that the band edge of the $CdTe_{1-x}S_x/CdS$ device is uniformly ~25 mV lower than that of the CdTe/ITO device (see Figure 4-19) which is consistent with the lower band gap of the alloy. While the spectral response of the conventional device matches that of the $CdTe_{1-x}S_x/CdS$ device in the high absorption region, at lower energies, where light is absorbed more uniformly though the absorber, the response tends towards that of the CdTe/ITO device. These results indicate that the bulk of absorber contains much less sulfur than the interface region.

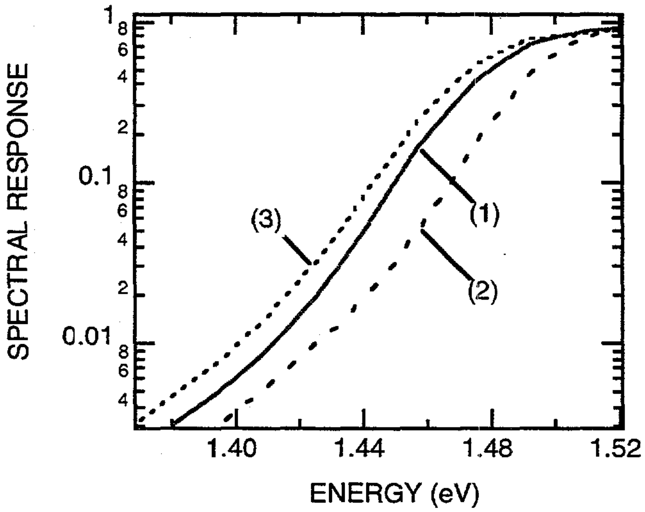

Figure 4-19 Long wavelength edge of the dark spectral response plotted against photon energy of (1) a conventional CdTe/CdS solar cell, (2) a CdTe/ITO solar cell, and (3) a $CdTe_{1-x}S_x/CdS$ solar cell.

4.3.4 CONCLUSIONS

Predominately single phase thin films of $CdTe_{1-x}S_x$ have been deposited by vacuum co-evaporation with compositions within the miscibility gap of the CdTe-CdS alloy system. These films phase segregated upon $CdCl_2$ heat treatment allowing a determination of the solubility limits of S in CdTe and Te in CdS. $CdTe_{1-x}S_x$ films with a uniform composition near the solubility limit of S in CdTe were grown on CdS/ITO substrates and processed into devices. The J-V characteristics and spectral response of these devices are very similar to conventional CdTe/CdS devices processed in a similar manner. In other words, the alloy formation due to the diffusion of S that takes place during processing of conventional CdTe/CdS devices results in device behavior very similar to that of devices with alloy composition at the solubility limit of S in CdTe uniformly throughout the absorber. These results suggest that two or three dimensional effects due to the spatial non-uniformity of alloy composition do not play a significant role in conventional devices with efficiencies up to 11%.

4.4 HCl VAPOR TREATMENT

4.4.1 Introduction

Fabrication of high efficiency CdTe/CdS thin film solar cells using CdTe deposited by non-screenprint or spray methods relies on a post-deposition treatment of the CdTe/CdS structure with $CdCl_2$ to improve the junction properties [410, 411, 447]. The most widely used treatment technique involves coating the CdTe surface with a $CdCl_2$:methanol solution, evaporating the methanol, heating at temperatures near 400°C, and rinsing the surface. However, this treatment is not amenable to high-throughput large scale processing due to problems associated with uniform application of the $CdCl_2$ coating, removal of post-treatment residues, and safe management of large quantities of the Cd salt. Alternative techniques such as evaporating $CdCl_2$ onto the CdTe [448], or reacting the CdTe/CdS in either $CdCl_2$ vapor [402, 414, 415] or Cl_2 vapor [415] have been shown to be suitable substitutes and are more amenable to large scale processing. Of these, the Cl_2 offers advantages with respect to vapor generation and Cd toxicity. Dilute mixtures of HCl offer another possibility. In this paper we report on the effects of treatment of physical vapor deposited CdTe/CdS structures in HCl vapor as a function of HCl concentration and treatment temperature. The effects on both materials properties and device performance are considered.

4.4.2 Experimental Considerations

There are several practical concerns that must be considered when performing the heat treatment (HT) in HCl. These issues not only played a role in developing the procedures reported herein, but may also be important in evaluating the commercial potential of this process step.

4.4.2.1 Source Gas

Initially the experiments were conducted using HCl gas generated by bubbling Ar through concentrated (25 Mol%) hydrochloric acid and the HCl concentration in the anneal ambient was determined from the integrated gas flow and the amount of HCl measured by titration in an exhaust bubbler. Bubbling Ar through hydrochloric acid led to experimental difficulties related to excessive H_2O vapor and poor control of HCl concentration. The origin of these difficulties is attributed to the fact that the HCl-H_2O system has an azeotrope such that liquid condenses (as on tubing or reactor walls or even the inside of the acid beaker) at a concentration of about 11 Mol%. The vapor in equilibrium with this condensed liquid is approximately 97 Mol% H_2O [449, 450]. In practice, the system displayed considerable hysteresis with respect to the measured HCl concentration. Once HCl had been introduced into the system its was difficult to remove it, and conversely, in freshly cleaned apparatus the HCl concentration was less than expected.

Another concern is the effect of humidity on the HT. From the literature we know that dry HCl is not very reactive and that reactions with dry HCl often take place only in the presence of catalysts whereas hydrogen chloride in water (hydrochloric acid) is an aggressive reagent [449, 450]. For both of these reasons it was decided to change the source gas from Ar bubbled through concentrated hydrochloric acid to dry HCl mixed with Ar. As condensation is to be avoided, at no time should the humidity of the source gas reach a level at which condensation occurs.

4.4.2.2 Oxygen

The effect of O_2 in the ambient HT gas could not be investigated because at T ~400 °C, heating in mixed HCl and O_2 produces coatings of solid $CdCl_2$ and Te layers on top of the CdTe surface. Earlier work has shown that Cl_2 reacts with CdTe to form $CdCl_2$ and Te [413]. In practice this reaction appears to dominate any other effect, such as oxygen doping, that might occur during the HT.

4.4.3 Experimental Techniques

4.4.3.1 Sample Preparation

The samples have the superstrate structure of 7059 glass/ITO/CdS/CdTe. ITO was deposited by sputtering to a thickness of ~2000 Å and sheet resistance of ~20 Ω/sq. Both CdS and CdTe were deposited by thermal evaporation with substrate temperatures of 200°C and 275°C and film thicknesses of 2200 Å and 5 μm, respectively.

4.4.3.2 Experimental Apparatus

The HCl post-deposition treatment was conducted in an evacuatable tube furnace system. Before each run the furnace was evacuated with a mechanical pump to ~0.1 torr and backfilled with high purity Ar. Two thermocouples were installed in the system, one was used for furnace temperature control and the other for measuring sample temperature. Commercial 5% HCl in Ar from Matheson was used as the HCl source. The concentration of HCl in the reaction chamber was reduced by adding additional Ar.

4.4.3.3 Experimental Parameters

Samples were divided into two groups. One group was used to study the effect of HCl concentrations of 0, 0.5%, 1.6%, 3.0% and 5% during a HT at a temperature of 400°C for 30 minutes. The second group was used to study the effect of temperatures of 380, 400, 420 and 440°C with a fixed 5% HCl concentration for 30 minutes.

After the film properties had been measured, back contacts were applied using the "diffused Cu" method [446] and applying carbon paste electrodes. The irregular shape of these electrodes led to ~10% uncertainty in the determination of device area and therefore of the current density.

4.4.4 Characterization

4.4.4.1 Film Morphology and Grain Size

The effects of treatment on the surface morphology and chemical composition were measured by scanning electron microscopy (SEM) and energy dispersive spectroscopy (EDS). The average grain size (AGS) was calculated by dividing the length of a line drawn across the SEM micrograph by the number of intersections with grain boundaries and then dividing by the magnification.

4.4.4.2 Preferred Crystal Orientation

The degree of preferred (111) orientation, p(111), was quantified from x-ray diffraction scans using the method of Harris for polycrystalline fiber texture analysis [418]. For the (111) peak this quantity is:

$$p(111)=\frac{I(111)/I_0(111)}{\frac{1}{N}\sum_{hkl} I(hkl)/I_0(hkl)}$$

Equation 4-5

where N is the number of peaks in the region considered, I(hkl) is the measured intensity of peak hkl, and I_0(hkl) is the relative intensity of the corresponding peak from a powder sample. In this case p(111) = 9 means that the film is completely (111) oriented while p(111) = 1 implies perfectly random distribution.

4.4.4.3 Optical Measurements

Transmission and reflection were measured to determine the absorption edge location, which allows shifts in the bandgap, ΔE_g, to be observed. The bandedge is expected to shift due to the formation of the $CdTe_{1-x}S_x$ as a result of interdiffusion near the CdTe/CdS interface. The shift was measured with respect to the absorption of as-deposited CdTe which has been confirmed by XRD measurements of lattice constant to have $x \approx 0$. The value of x was estimated assuming linear variation of E_g over the range 0 to 6% [451]. The shift in bandgap was determined from a plot of the absorption coefficient squared versus energy.

4.4.5 Results And Discussion

Results of the above measurements for films heated at 400 °C in various HCl:Ar concentrations are listed in Table 4-9; results for films heated at various temperatures at 5 vol% HCl:Ar are listed in Table 4-10.

Table 4-9 Film parameters vs HCl:Ar concentration (vol%) during a 30 min. HT at 400°C.

[HCl] (vol%)	AGS ±0.1 (µm)	p(111)	d(111)±0.01 (Å)	ΔE_g (meV)	[S], x (%)
as-dep	0.7	4 - 7	3.76	0	0
0	0.7	2.8	3.76	~5	~0.5
0.5	0.9	1.3	3.75	~10	~1.0
1.6	1.0	1.7	3.74	~15	~1.5
3.0	1.2	2.7	3.73	~15	~1.5
5.0	1.1	1.2	3.74	~15	~1.5

Table 4-10. Film parameters vs temperature during a 30 min. HT in 5 vol% HCl:Ar

Temp (°C)	AGS ± 0.1 (μm)	p(111)	d(111) ±0.01 (Å)	ΔE_g (meV)	[S], x (%)
380	1.0	1.9	3.76	~10	~1.0
400	1.0	3.2	3.77	~15	~1.5
420	1.2	1.8	3.75	~15	~1.5
440	1.4	0.8	3.75	~20	~2.0

4.4.5.1 **Film Properties**

SEM and EDS analysis pictures show that the surfaces of samples treated in HCl+Ar are clean and without residue.

Thermally evaporated as-deposited CdTe films have an average grain size of ~0.7 μm for 5 μm thick films. Figure 4-20 and Figure 4-21 show the surface structure for films heated in various HCl:Ar concentrations and temperatures. The measured average grain sizes are listed in Table 4-9. HCl in the anneal ambient clearly promotes grain growth; heating without HCl produced no change in average grain size. This confirms that HCl (as $CdCl_2$ does) may work as a flux which breaks down atomic diffusion barriers at grain boundaries and thereby promotes grain growth. The average grain size increases with increasing temperature over the range of 380 to 440°C, but only in the presence of HCl.

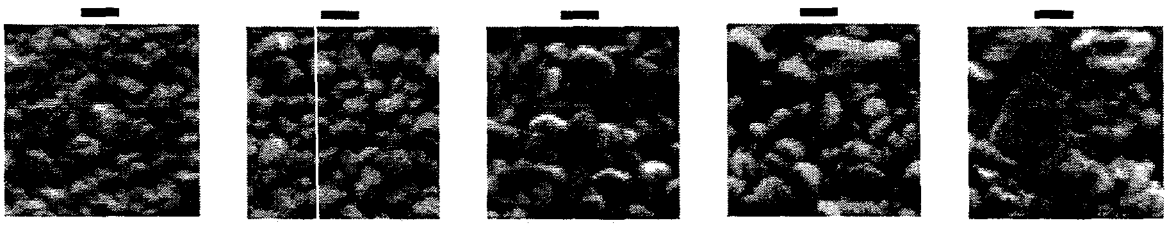
0.0 % 0.5 % 1.6 % 3.0 % 5.0 %

Figure 4-20. SEM photos of the surface of CdTe films heated at 400°C for 30 minutes at the HCl:Ar concentrations indicated. The scale bar is one micron.

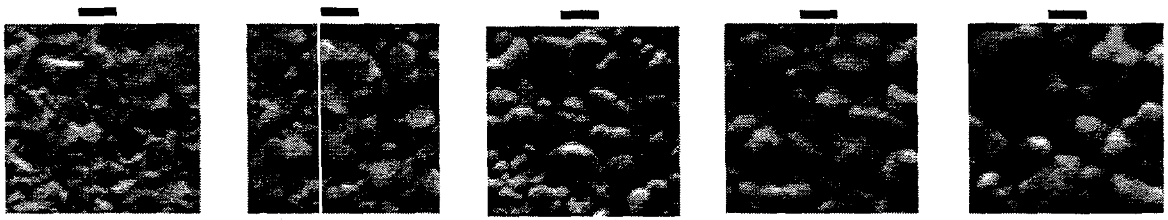
none 380 °C 400 °C 420 °C 440 °C

Figure 4-21 SEM photos of the surface of CdTe films heated in 5% HCl for 30 min. at the indicated temperatures. The scale bar is one micron.

It was found that for thermally evaporated as-deposited CdTe films, p(111) is usually in the range of 4 - 7. After post-deposition heat treatment in HCl+Ar for 30 minutes p(111) usually decreases to the range of 1-3. In addition, the data listed in Table 4-9 suggest that for these samples there is also a decrease in the lattice constant.

Plots of the square of the absorption coefficient versus energy are shown in 4-22 and Figure 4-23 for the CdTe/CdS structures treated at 400°C for 30 minutes at varying HCl:Ar concentration and at various temperatures in 5% HCl:Ar.. With increasing HCl concentration the optical absorption curves indicate a decrease in bandgap. The bandgap shift with HCl concentration suggests that the effect of the HCl reaches the CdTe/CdS interface, perhaps through grain boundaries, and enhances interdiffusion.

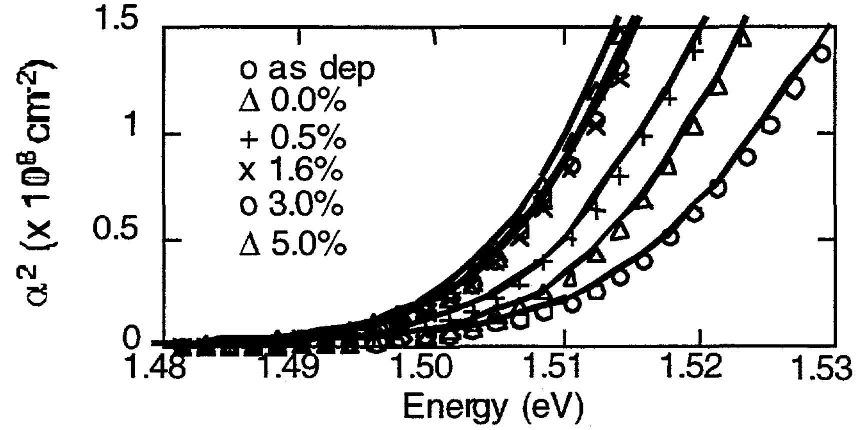

Figure 4-22 Plot of absorption coefficient squared versus energy for CdTe/CdS films treated at 400°C for 30 minutes at the HCl:Ar concentrations shown.

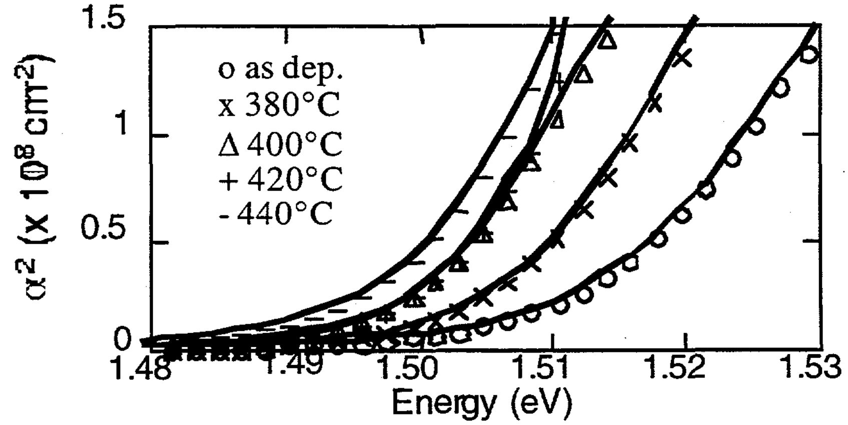

Figure 4-23 Plot of absorption coefficient squared versus energy for CdTe/CdS films treated in 5% HCl:Ar for 30 minutes at the temperatures indicated.

4.4.5.2 Cell Results

The effect of HCl concentration on the dark and light J-V behavior of devices is shown in Figure 4-24, for increasing HCl concentration from 0 to 5%. From the light data we note that carrier collection, as determined from the magnitude and slope of the curve near J_{SC}, improves with HCl concentration. It is not clear whether increasing concentration above the range included in this study would produce results similar to those obtained using $CdCl_2$ treatments. Figure 4-24 also shows that the light-dark crossover is less severe at the higher HCl concentrations suggesting that conductivity increases with HCl concentration. The mechanism for this is not apparent. In addition, it was noted that hysteresis between forward and reverse voltage sweeps was reduced at higher concentrations as well.

The effects of process temperature variations are summarized qualitatively in Figure 4-25. Changing the temperature of the heat treatment in 5% HCl over the range 380 to 440 °C had minimal effect on light or dark J-V behavior. The scatter in data is such that no trends are evident in either the light or dark J-V data. In addition, all of the HCl heat treated devices are characterized by strong light-dark crossover in the first quadrant and poor collection efficiency.

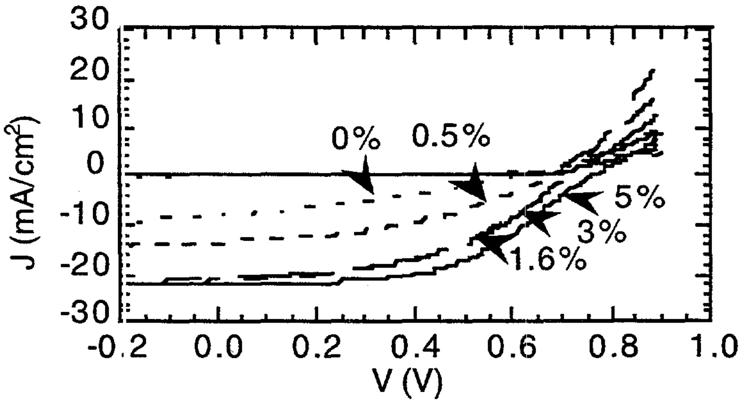

Figure 4-24. Dark and light J-V data for devices made from films heat treated for 30 min. at 400C in various HCl:Ar concentrations.

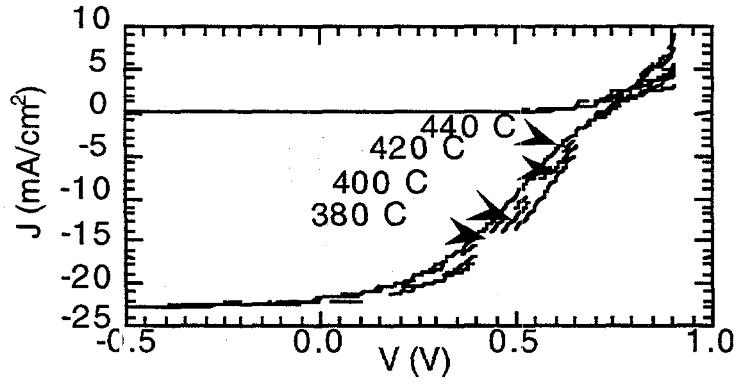

Figure 4-25 Dark and light J-V data for devices made from films heat treated for 30 min. in 5 % HCl at various temperatures.

4.4.6 Conclusions

Treatment of CdTe/CdS thin film structures in dilute mixtures of HCl vapor at 380°C to 440°C promotes similar microstructural changes in the structure to treatment with $CdCl_2$. While not yet optimized for high conversion efficiency, this shows promise as an alternative to treatments with $CdCl_2$. The structural properties are sensitive to both HCl concentration and treatment temperature. However, the device performance, particularly the short circuit current and fill factor, are highly sensitive to HCl concentration but only slightly sensitive to treatment temperature. Achieving higher efficiency than demonstrated here will require exploration of a wider parameter space, including higher HCl concentration and multiple step treatments, such as HCl treatment followed by air treatment. Some of the difficulties associated with the use of hydrochloric acid as the vapor source and with using $HCl:O_2$ mixtures have been identified.

4.5 STRESS TESTING OF CdTe/CdS DEVICES

4.5.1 Introduction

The most delicate feature of the CdTe/CdS device is believed to be the low loss back contact. Low resistance contacting methods typically involve use of Te-rich interfaces or p-type semiconductors such as HgTe or ZnTe, or thin layers including small amounts of Cu [452-454]. Some devices subjected to stress testing or life testing display high series resistance and/or evidence of a reverse diode - both characteristics which could be attributed to the back contact. It has been reported [455] that reverse voltage bias at elevated temperature causes rapid degradation of device parameters and that this effect can be, at least, partially reversed by the application of a forward bias. Similar effects have been observed with devices produced in our lab. Analysis of the IEC light J-V curves indicated that there were at least two mechanisms responsible. Reversible effects included increases in series resistance and decreases in J_0 of the reverse diode upon application of reverse bias (with opposite changes upon forward bias); permanent effects included an additional increase in series resistance and a reduction in collected photocurrent [456, 457]. At this point it is not clear whether all CdTe devices display these effects or have the same sensitivity to these stresses.

4.5.2 Experimental Procedure

Devices evaluated in this study had the standard superstrate structure of glass/TCO/CdTe/CdS/contact. The sodalime glass/ SnO_2:F/CdS/CdTe supplied by Solar Cells Inc. was cut into 2.5 x 2.5 cm pieces from a 7200 cm^2 superstrate which had been coated and processed using SCI's normal procedures up to the point of completion of the post-deposition heat treatment [415]. The devices were completed using the "diffused Cu" back contact processing [446], sputter deposition of Mo contacts through a mask, mechanical scribing, application of a room temperature curing urethane insulator. Electrical contact was made using Ag epoxy (Acheson Electrodag MB80021) which was cured in Ar at 140 °C for ~10 minutes. In order to facilitate the subsequent depth profiling, in selected devices the Ag epoxy was applied only to the perimeter of the cell. Wire leads were soldered to the exposed SnO_2 pads using Indalloy solder #204. The leads were necessary to apply and maintain voltage bias on the devices during stressing and were used for making all J-V measurements.

Devices were not encapsulated, but all stressing was done inside a glove box with flowing N_2. Inside the glove box relative humidity was less than 2% at 50° C; oxygen content was not determined.

Prior to beginning the stress testing, devices have been screened to select those whose J-V data are analyzable. Devices exhibiting excessive series resistance (>10 Ω cm^2), shunting conductance (>1 mS/ cm^2), or hysteresis were rejected as were devices whose dark J-V characteristics could not be described with a simple diode (apparent diode quality factor ≤ 2.0). Minimum acceptable V_{OC} and FF were 0.75 V and 60%, respectively. A total of 16 devices meeting these criteria were selected for testing. The active area of these devices was estimated and set to 0.6 cm^2. Of these devices, four were stressed only with temperature (no electrical or light stress), two were stressed with temperature and electrical bias (-0.5 Volts and +5 mA/ cm^2) and the remaining 10 were stressed with temperature, illumination (~70 mW/ cm^2) and electrical bias (see Table 4-11and Table 4-12).

Illumination was provided by tungsten filament spot lamps and was, therefore, quite "red" compared with the AM1.5 Global spectrum. The intensity was estimated from the short circuit current of the CdTe cells mounted in the stress test station.

Table 4-11 Electrical bias and temperature stress conditions for illuminated devices (~70 mW/ cm^2)

	82°C	92°C	112°C
-0.5 V		√	
J_{SC}	√	√	√
$R_L = 70\ \Omega$	√		√
V_{OC}	√	√	√
+5 mA/ cm^2		√	

Table 4-12 Electrical bias and temperature stress conditions for devices stressed in dark

	72°C	88°C	104°C
none	√	2	√
-0.5 V		√	
+5 mA/ cm^2		√	

J-V data were recorded at various intervals during the stress testing. In addition, devices were removed and room temperature J-V (at AM1.5 Global illumination and dark) and spectral response were also recorded prior to and at various times during stress testing . Total time under stress was 720 hrs.

4.5.3 Analysis

The most striking differences between the initial and final (720 hrs.) measurements occured in the J-V characteristics. These are examined in the context of a simple equivalent circuit containing a diode, a constant resistance (R_S) and a non-linear contact resistance (R_C).

$$V = \left(R_S + R_C\right)J + \left(\frac{AkT}{q}\right)\mathrm{Ln}\left(\frac{J}{J_0}\right)$$

Equation 4-6

Hence the the effects of series resistance (R_S) and that of contact resistance (R_C) can be separated by examining the slope or derivative of the J-V characteristic.

$$\frac{dV}{dJ} = R_S + \left(\frac{AkT}{q}\right)\left(\frac{1}{J}\right) + \frac{d(R_C J)}{dV}$$

Equation 4-7

Equation 4-7 shows that contact resistance can be separated from simple series by examining a graph of dV/dJ vs. 1/J in forward bias or small 1/J (see Figure 4-27, Figure 4-29, Figure 4-31 and Figure 4-33).

4.5.4 Results

All of the devices held under stress conditions exhibited a reduction in V_{OC} and FF. These reductions could not be due to either shunting effects or a loss in light generated current.

4.5.4.1 Electrical Bias

There were major differences in the J-V characteristics of devices stressed with reverse bias (-0.5 V and J_{SC}) compared to those stressed at forward bias (+5mA/cm^2 and V_{OC}). Those held in reverse bias exhibited larger reductions in J_{SC}, V_{OC} and FF compared to those held in forward bias. Examination of the J-V curves (Figure 4-26 to Figure 4-29) help explain why. The increase in series resistance is larger for devices held at reverse bias. This can be seen in both the J-V and dV/dJ graphs and can account for at least some of the differences seen in V_{OC}, FF and J_{SC}.

In addition, there is another qualitative difference between devices stressed with forward or reverse bias; this is the appearance of a blocking contact resistance for devices held at forward bias. It can be seen most clearly in the dV/dJ graph of Figure 4-29. This is probably due to the development of a rectifying contact at the back of the CdTe.

4.5.4.2 Illumination

There were no obvious or consistent differences in the J-V characteristics of illuminated devices compared to those stressed in the dark.

4.5.4.3 Temperature

All of the changes noted previously were either accelerated or increased in magnitude when the temperature was increased (Figure 4-30 to Figure 4-33). This suggests that all of the mechanisms noted are thermally activated.

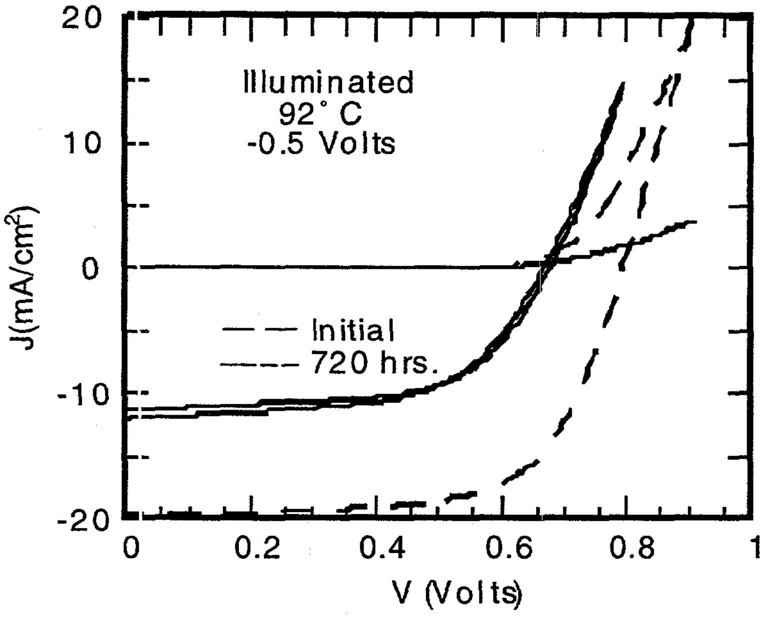

Figure 4-26 Light and Dark J-V characteristics before and after 720 hours stress at 92° C under illumination and -0.5V bias.

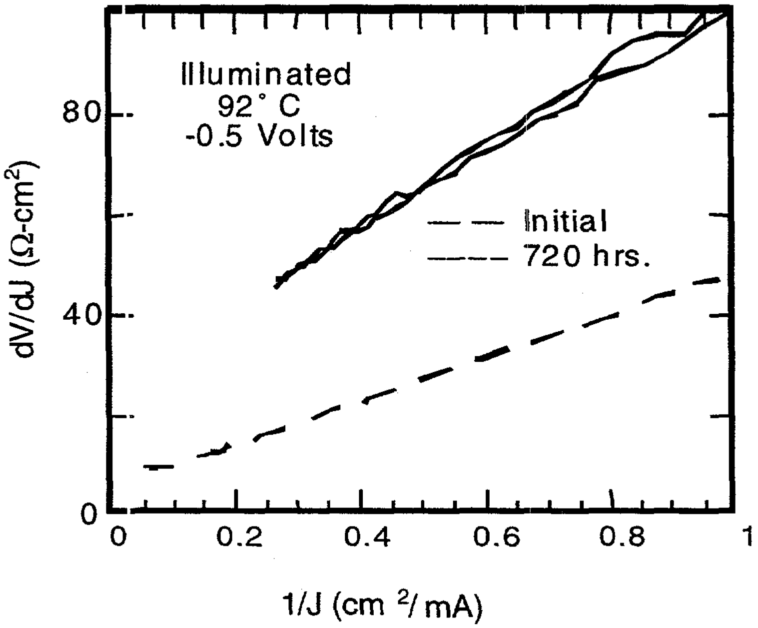

Figure 4-27 Dark dV/dJ vs. 1/J before and after 720 hours stress at 92° C under illumination and -0.5V bias.

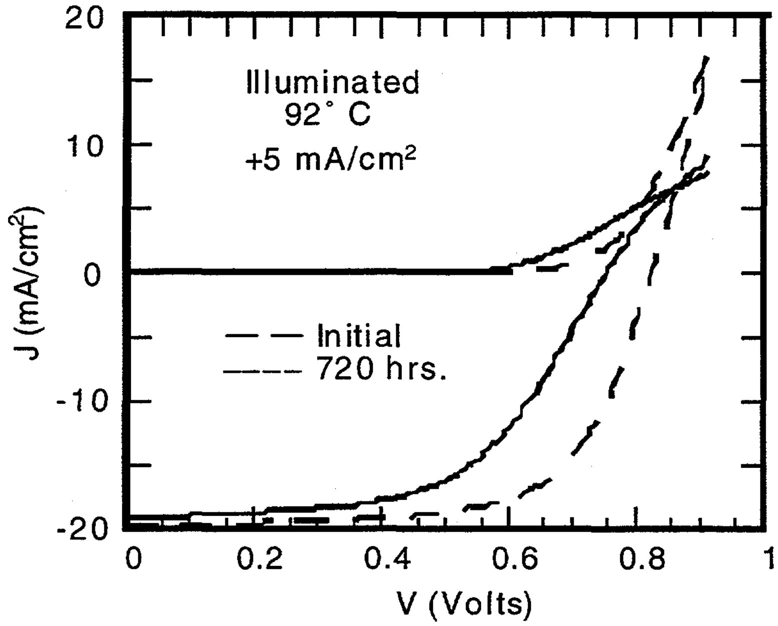

Figure 4-28 Light and Dark J-V characteristics before and after 720 hours stress at 92° C under illumination and +5mA/ cm² bias.

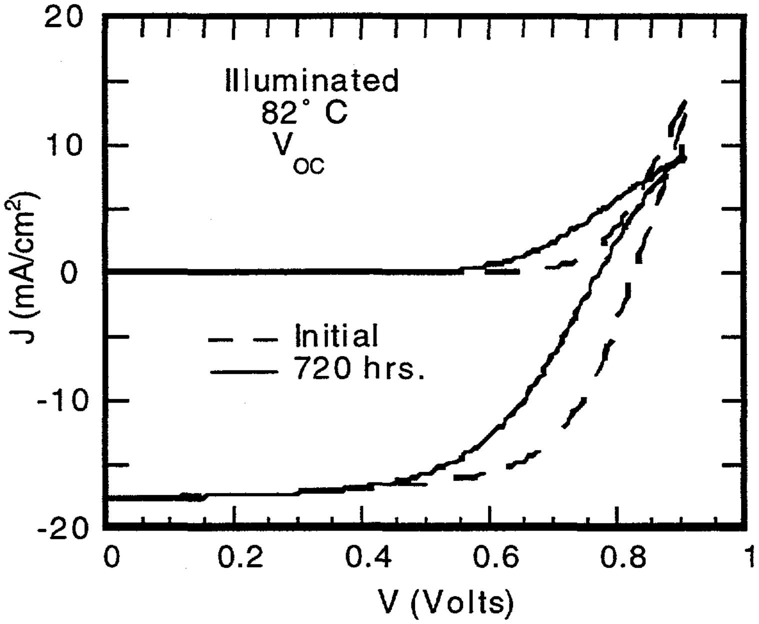

Figure 4-29 Dark dV/dJ vs. 1/J before and after 720 hours stress at 92° C under illumination and +5 mA/ cm² bias.

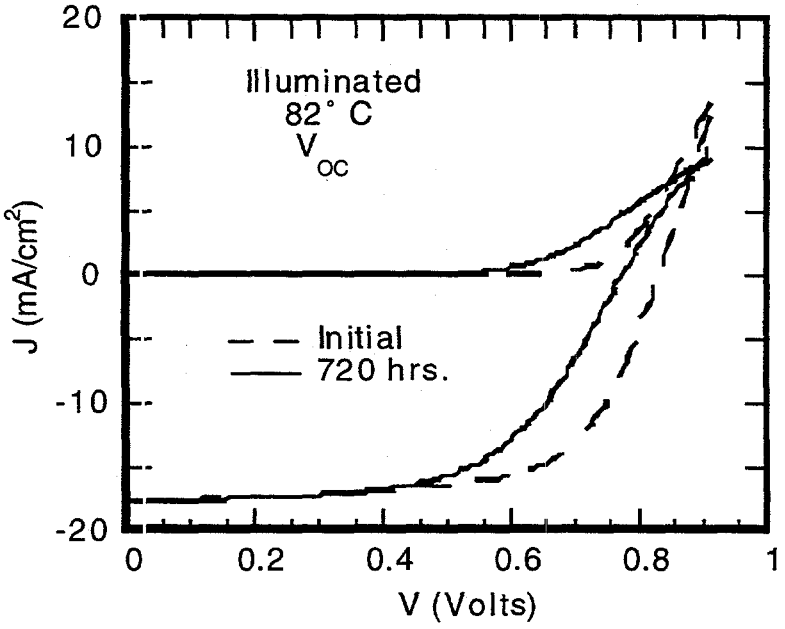

Figure 4-30 Light and Dark J-V characteristics before and after 720 hours stress at 82° C under illumination and held at V_{OC}.

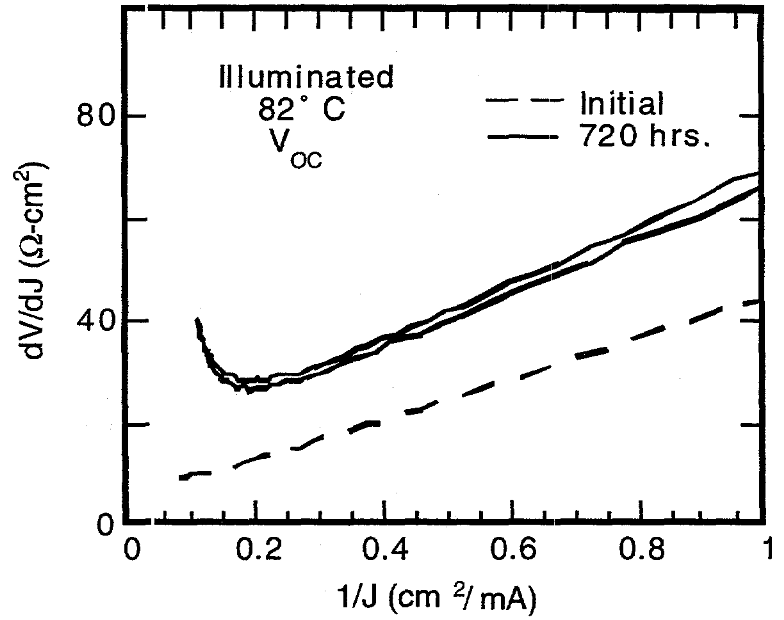

Figure 4-31 Dark dV/dJ vs. 1/J before and after 720 hours stress at 82° C under illumination and held at V_{OC}

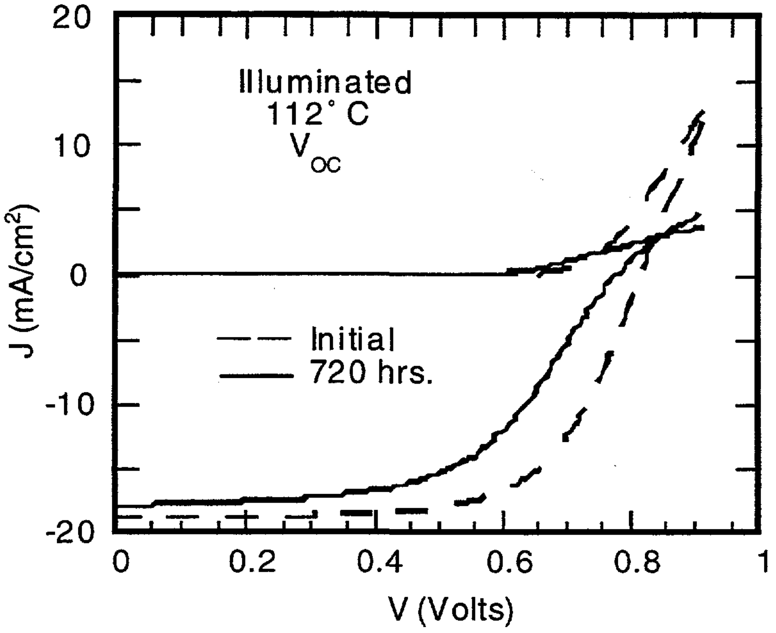

Figure 4-32 Light and Dark J-V characteristics before and after 720 hours stress at 112° C under illumination and held at V_{OC}

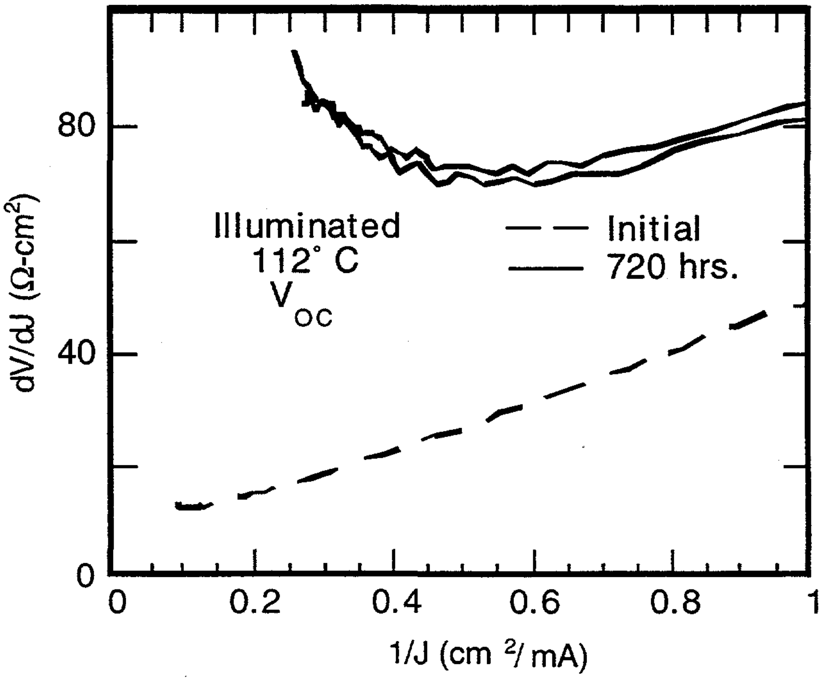

Figure 4-33 Dark dV/dJ vs. 1/J before and after 720 hours stress at 112° C under illumination and and held at V_{OC}.

4.5.5 Conclusions

In the specially prepared CdTe devices that have been subjected to stresses beyond normal operating conditions there appears to be changes that are associated with stress temperature and electrical bias. It is not clear whether there is a dependence on illumination level. One effect is promoted by reverse bias and affects primarily the bulk CdTe properties as indicated by the severity of the light-dark crossover of the J-V curves. Another effect is promoted by forward bias and results in the strengthening of a reverse diode. Finally there are changes in both the light generated current and J_0 whose magnitudes are also bias and light dependent. The data were recorded on a limited data set, 16 samples, and using a single method of device preparation. Additional experiments as well as other samples prepared by various groups are necessary to confirm or refute these results.

5. REFERENCES

5.1 SECTION 2 [Cu(In,Ga)Se_2]

201 R. W. Birkmire, J. E. Phillips, W. A. Buchanan, *et al.*, Annual Subcontract Report, National Renewable Energy Laboratory, Golden, CO, (1996).

202 W. N. Shafarman, R. Klenk, and B. E. McCandless, J. Appl. Phys **79**, 7324 (1996).

203 W. N. Shafarman, R. Klenk, and B. E. McCandless, in *25th IEEE Photovoltaic Specialists Conference*, 1996), p. 763.

204 W. N. Shafarman, R. W. Birkmire, M. Marudachalam, *et al.*, in *AIP Conference*, edited by C. E. Witt, M. Al-Jassim and J. M. Gee (AIP Press, Lakewood, CO, 1996), Vol. 394, p. 123-131.

205 M. Marudachalam, H. Hichri, R. W. Birkmire, *et al.*, Appl. Phys. Lett. **67**, 3978-3980 (1995).

206 M. Marudachalam, H. Hichri, R. W. Birkmire, *et al.*, in *25th IEEE Photovoltaic Specialists Conference*, 1996), p. 805.

207 W. N. Shafarman and J. E. Phillips, in *25th IEEE Photovoltaic Specialists Conference*, 1996), p. 917.

208 J. Hedstrom, H. Ohlsen, M. Bodegard, *et al.*, in *23rd IEEE Photovoltaic Specialists Conference* (Institute of Electrical and Electronics Engineers, Louisville KY, 1993), p. 364.

209 J. R. Tuttle, M. A. Contreras, T. J. Gillespie, *et al.*, Progress in Photovoltaics **3**, 235 (1995).

210 M. A. Contreras, J. Tuttle, A. Gabor, *et al.*, in *24th IEEE Photovoltaic Spcialists Conference* (Institute of Electrical and Electronics Engineers, Waikoloa, HI, 1995), p. 68.

211 J. M. Stewart, W. S. Chen, W. E. Devaney, *et al.*, in *7th Internatational Conference on Ternary and Multinary Compounds*, edited by S. K. Deb and A. Zunger (Materials Research Society, Pittsburgh, PA, 1987), p. 59.

212 K. Kushiya, Y. Ohtake, A. Yamada, *et al.*, Jpn. J. Appl. Phys. **33**, 6599 (1994).

213 H. W. Schock, in *12th European Photovoltaic Solar Energy Conference* (H S Stephens & Assoc. UK, Amsterdam, The Netherlands, 1994), p. 944.

214 J. Kessler, S. Wiedeman, L. Russell, *et al.*, in *25th IEEE Photovoltaic Specialists Conference*, 1996), p. 885.

215 J. Kessler, K. Velthaus, M. Ruckh, *et al.*, in *6th Int. Photovoltaic Science and Engineering Conference* (Oxford and IBH, New Delhi, New Delhi, India, 1992), p. 1005.

216 W. E. Devaney, W. S. Chen, J. M. Stewart, *et al.*, IEEE Trans. on Electron Devices **37**, 428 (1990).

217 B. Dimmler, H. Dittrich, R. Menner, *et al.*, in *19th IUEEE Photovoltaic Specialists Conference* (IEEE, New York, New Orleans, LA, 1987), p. 1454.

218 B. Grzeta-Plenkovic, A. Popovic, B. Celustka, *et al.*, J. Appl. Cryst. **13**, 311 (1980).

219 R. W. Birkmire, J. E. Phillips, W. A. Buchanan, *et al.*, Annual Subcontract Report, National Renewable Energy Laboratory, Golden, CO, (1995).

220 D. Schmid, M. Ruckh, F. Grunwald, *et al.*, J. Appl. Phys. **73**, 2902 (1993).

221 M. Roy, S. Damaskinos, and J. E. Phillips, in *20th IEEE Photovoltaic Specialists Conference* (IEEE, New York, Las Vegas, NV, 1988), p. 1618.

222 W. N. Shafarman and J. E. Phillips, in *22nd IEEE Photovoltaic Specialists Conference* (IEEE, New York, Las Vegas, NV, 1991), p. 934.

223 T. Walter, R. Menner, C. Koble, *et al.*, in *12th European Photovoltaic Solar Energy Conference* (H. S. Stephens & Assoc., UK, Amsterdam, The Netherlands, 1994), p. 1755.

224 X. Liu and J. Sites, J. Appl. Phys. **74**, 1 (1993).

225 T. Negami, N. Kohara, M. Nishitani, *et al.*, Appl. Phys. Lett. **67**, 825-827 (1995).

226 M. Eron and A. Rothwarf, Appl. Phys. Lett. **44**, 131 (1984).

227 M. Marudachalam, R. W. Birkmire, J. M. Schultz, *et al.*, in *24th IEEE Photovoltaic Specialists Conference* (IEEE, Hawaii, Waikoloa, HI, 1994), p. 234.

228 S. Verma, T. W. F. Russell, and R. W. Birkmire, in *23rd IEEE Photovoltaic Specialists Conference* (IEEE, New York, Louisville, KY, 1993), p. 431.

229 R. Klenk and H. W. Schock, in *12th European Photovoltaic Solar Energy Conference* (H. S. Stephens & Assoc., UK, Amsterdam, The Nethelands, 1994), p. 1588.

230 T. Walter and H. W. Schock, Thin Solid Films **224**, 74 (1993).

231 R. J. Borg and G. J. Dienes, in *An Introduction to Solid State Diffusion* (Academic Press, Inc., 1988), p. 317-319.

232 W. Miller and L. C. Olsen, IEEE Trans. Elec. Dev. **ED-31**, 654 (1984).

233 W. N. Shafarman and J. E. Phillips, in *23rd IEEE Photovoltaic Specialists Conference*, 1993), p. 453.

234 F. Abou-Elfotouh, L. Kazmerski, T. Coutts, *et al.*, J. Vac. Sci. Techn. **7**, 837 (1989).

235 J. Tuttle, J. Sites, A. Delahoy, *et al.*, Progress in Photovoltaics **3**, 89 (1995).

236 Y. J. Lee and J. L. Gray, in *12th European Photovoltaic Solar Energy Conference* (H. S. Stephens & Assoc., UK, Amsterdam, The Netherlands, 1994), p. 1561.

237 H. Schade and Z. E. Smith, J. Appl. Phys. **59**, 1682 (1986).

238 M. Roy and J. E. Phillips, in *21st IEEE Photovoltaic Specialists Conference*, 1990), p. 743.

5.2 SECTION 3 [a-Si]

301 S. S. Hegedus, W. A. Buchanan, X. Liu, *et al.*, in *25th IEEE Photovoltaic Specialists Conference* (IEEE, Washington, DC, 1996), Vol. 1, p. 1129.

302 S. S. Hegedus, W. A. Buchanan, E. Eser, *et al.*, in *AIP Conference*, edited by C. E. Witt, M. Al-Jassim and J. M. Gee (AIP Press, Lakewood, CO, 1996), Vol. 394, p. 547-555.

303 S. S. Hegedus and X. Deng, in *25th IEEE Photovoltaic Specialists Conference* (IEEE, Washington, DC, 1996), Vol. 1, p. 1061.

304 R. W. Birkmire, J. E. Phillips, W. A. Buchanan, *et al.*, Annual Subcontract Report, (National Renewable Energy Laboratory, Golden, CO, 1995).

305 R. W. Birkmire, J. E. Phillips, W. A. Buchanan, *et al.*, Annual Subcontract Report, (National Renewable Energy Laboratory, Golden, CO, 1996).

306 S. S. Hegedus, H. Liang, and R. Gordon, in *AIP Conference*, edited by H. S. Ullal and C. E. Witt (AIP Press, Lakewood, CO, 1995), Vol. 353, p. 465.

307 M. Kubon, E. Boehmer, M. Gastel, *et al.*, in *1st World Conference on Photovoltaic Energy Conversion*, 1994), p. 500.

308 R. R. Arya, R. S. Oswald, Y. M. Li, *et al.*, in *1st World Conference on Photovoltaic Energy Conversion*, 1994), p. 394.

309 J. Hu and R. Gordon, Solar Cells **30**, 43 (1991).

310 H. Sakai, T. Yoshida, T. Hama, *et al.*, Japan. J. Appl. Phys. **29**, 630 (1990).

311 J. Hu and R. Gordon, J. Electrochem. Soc. **139**, 2014 (1992).

312 M. Komakine, in *MRS Symposium*, 1990), Vol. 192, p. 69.

313 W. Luft, H. Branz, V. Dalal, *et al.*, in *AIP Conference*, edited by H. S. Ullal and C. E. Witt (AIP Press, Lakewood, CO, 1995), Vol. 353, p. 81.

314 U. K Hoffman, , 1994).

315 A. Banerjee and S. Guha, in *Materials Research Society Symposium*, 1990), p. 57-62.

316 J. Morris, R. R. Arya, J. G. O'Dowd, *et al.*, J. Appl. Phys. **67**, 1079-1087 (1990).

317 G. Tao, B. S. Girwar, G. E. N. Landweer, *et al.*, in *Materials Research Society Symposium*, 1993), Vol. 297, p. 845-849.

318 E. Terzini, A. Rubino, R. DeRosa, *et al.*, in *Materials Research Society Symposium*, 1995), Vol. 377, p. 681-686.

319 K. Hayashi, K. Masataka, A. Ishikawa, *et al.*, in *IEEE First World Conference on Photovoltaic Energy Conversion* (IEEE, Waikoloa, HI, 1994), Vol. 1, p. 674.

320 M. Buchanan, J. B. Webb, and D. F. Williams, Appl. Phys. Lett. **37**, 213-215 (1980).

321 R. E. I. Schropp and A. Madan, J. Appl. Phys. **66**, 2027-2031 (1989).

322 W. Luft, H. M. Branz, V. L. Dalal, *et al.*, in *AIP Conference* (AIP Press, 1994), p. 31-45.

323 M. Kubon, E. Boehmer, M. Gastel, *et al.*, in *IEEE First World Conference on Photovoltaic Energy Conversion* (IEEE, Waikoloa, HI, 1994), p. 500.

324 J. Hu and R. Gordon, Solar Cells **30**, 437-450 (1991).

325 R. S. Sanchez and R. Williams, J. Appl. Phys. **54**, 2757-2760 (1983).

326 K. Itoh, H. Matsumoto, T. Kobata, *et al.*, Appl. Phys. Lett. **51**, 1695 (1987).

327 B. Drevillon, S. Kumar, P. R. i. Cabarrocas, *et al.*, Appl. Phys. Lett. **54**, 2088-2090 (1989).

328 F. Smole, M. Topic, and J. Furlan, in *IEEE First World Conference on Photovoltaic Energy Conversion* (IEEE, Waikoloa, HI, 1994), Vol. 1, p. 496.

329 H. Deckman, C. Wronski, H. Witzke, *et al.*, Appl. Phys. Lett. **42**, 968 (1983).

330 G. Walker, R. Hollingsworth, and A. Madan, in *MRS Symposium*, 1987), Vol. 95, p. 527.

331 F. Leblanc, J. Perrin, and J. Schmitt, J. Appl. Phys. , 1074 (1994).

332 A. Banerjee and S. Guha, J. Appl. Phys. **69**, 1030 (1990).

333 A. Banarjee, K. Hoffman, X. Xu, *et al.*, in *1st World Conference on Photovoltaic Energy Conversion* (IEEE, Waikoloa, HI, 1994), p. 539.

334 X. Deng, M. Izu, K. Narasimhan, *et al.*, in *MRS Symposium*, 1994), Vol. 336.

335 R. E. I. Schropp, H. Meiling, W. G. J. H. M. v. Sark, *et al.*, in *10th E.C. Photovoltaic Solar Energy Conference* (Kluwer Academic Publishers, Dordrecht, The Netherlands, Lisbon, Spain, 1991), p. 1087-1090.

336 H. Stiebig, A. Kreisel, K. Winz, *et al.*, in *IEEE First World Conference on Photovoltaic Energy Conversion* (IEEE, Waikoloa, HI, 1994), Vol. 1, p. 603-606.

337 G. Tao, M. Zeman, and J. Metzalaar, in *First World Conference on Photovoltaic Energy Conversion* (IEEE, Waikoloa, HI, 1994), Vol. 1, p. 666-669.

338 V. Dalal, IEEE Trans. Electron Devices **ED-27**, 662 (1980).

339 S. Sze, *Physics of semiconductor devices* (John Wiley and Sons, New York, 1980).

340 M. Hack and M. Shur, J. Appl. Phys. **58**, 997 (1985).

341 H. Tasaki, W. Y. Kim, M. Hallerdt, *et al.*, J. Appl. Phys. **63**, 550 (1988).

342 J. K. Arch, F. A. Rubinelli, J. Y. Hou, *et al.*, J. Appl. Phys. **69**, 7057 (1991).

343 F. Smole and J. Furlan, J. Appl. Phys. **72**, 5964 (1992).

344 S. S. Hegedus and J. E. Phillips, in *First World Conference on Photovoltaic Solar Energy Conversion* (IEEE, Waikoloa, HI, 1994), Vol. 1, p. 654-657.

345 R. S. Crandall, J. Appl. Phys. **54**, 7176 (1983).

346 B. W. Faughnan and R. S. Crandall, Appl. Phys. Lett. **44**, 537 (1984).

347 R. R. Arya, A. Catalano, and R. S. Oswald, Appl. Phys. Lett. **49**, 1089 (1986).

348 R. S. Crandall and K. Sadlon, in *Materials Research Society Symposium*, 1989), Vol. 149, p. 423.

349 Y. Higaki, M. Aiga, S. Terazono, *et al.*, Technical Digest of the International PVSEC **1**, 209 (1984).

350 K. Misiakos and F. A. Lindholm, J. Appl. Phys. **64**, 383 (1988).

351 R. Rocheleau, submitted to Progress in Photovoltaics (1997).

352 V. Chu, J. P. Conde, D. S. Shen, *et al.*, Appl. Phys. Lett. **55**, 262 (1989).

353 R. Rocheleau, personal communication.

354 S. Wiedeman, J. Morris, and L. Yang, in *21st IEEE Photovoltaic Specialists Conference* (IEEE, Kissimmee, FL, 1990), Vol. 2, p. 1529.

355 H. Matsuura, A. Matsuda, H. Okushi, *et al.*, J. Appl. Phys. **58**, 1578 (1985).

356 Y. Yamamoto, K. Nomoto, T. Okuno, *et al.*, in *19th IEEE Photovoltaic Specialists Conference* (IEEE, New Orleans, LA, 1987), p. 901.

357 S. S. Hegedus, N. Salzman, and E. Fagen, J. Appl. Phys. **63**, 5126 (1988).

358 A. Mittiga, P. Fiorini, M. Falconieri, *et al.*, J. Appl. Phys. **66**, 2667 (1989).

359 H. Sakai, T. Yoshida, S. Fujikake, *et al.*, J. Appl. Phys. **67**, 3494 (1990).

360 J. R. Sites, H. Tavakolian, and R. A. Sasala, Solar Cells **29**, 39 (1990).

361 T. Glatfelter and J. Burdick, in *19th IEEE Photovoltaic Specialists Conference* (IEEE, New Orleans, LA, 1987), p. 1187.

362 C. R. Wronski and R. E. Daniel, Phys. Rev. **B-23**, 794 (1981).

363 M. Hack, S. Guha, and M. Shur, Phys. Rev. B **30**, 6991 (1984).

364 C.-D. Abel, H. R. Paes, and G. H. Bauer, in *10th European Conference of Photovoltaic Solar Energy Conversion*, Lisbon, Portugal, 1991), p. 161.

365 S. S. Hegedus and J. M. Cebulka, J. Appl. Phys. **67**, 3885 (1990).

366 L. Yang, A. Catalano, R. R. Arya, *et al.*, Appl. Phys. Lett. **57**, 908 (1990).

367 E. Sauvain, J. Hubin, A. Shah, *et al.*, Philosophical Magazine Letters **63**, 327 (1991).

368 I. Balberg, K. A. Epstein, and D. Ritter, Appl. Phys. Lett. **54**, 2461 (1989).

369 H. Pfleiderer, W. Kusian, E. Gunzel, *et al.*, in *20th IEEE Photovoltaic Specialists Conference* (IEEE, Las Vegas, NV, 1988), p. 180.

370 J. Reichman, Appl. Phys. Lett. **38**, 251 (1981).

371 M. Stutzmann, W. Jackson, and C. C. Tsai, Phys. Rev. **B32**, 23 (1985).

372 D. Ritter, K. Weiser, and E. Zeldov, J. Appl. Phys. **62**, 4563 (1987).

373 E. Sauvain, P. Pipoz, A. Shah, *et al.*, J Appl Phys **75**, 1722 (1994).

374 F. Wang and R. Schwarz, J. of Non-Crystalline Solids **198-200**, 423 (1996).

375 J. Yang, X. Xu, and S. Guha, in *1994 MRS Symposium*, 1994), Vol. 336, p. 687.

376 P. Chaudhuri, A. R. Middya, and S. Ray, in *6th International Conference on Photovoltaic Solar Energy Conversion*, 1992), p. 631.

377 J. Z. Liu, X. Li, P. R. i. Cabarrocas, *et al.*, in *21st IEEE Photovoltaic Specialists Conference* (IEEE, Kissimmee, FL, 1990), p. 1606.

378 G. Conte, D. D. Sala, F. Galluzzi, *et al.*, Semicond. Sci. Technol. **5**, 890 (1990).

379 G. H. Bauer, C. E. Nebel, and N.-D. Mohring, in *MRS Symposium*, 1988), Vol. 118, p. 679.

380 B. Faughnan, A. Moore, and R. Crandall, Appl. Phys. Lett. **44**, 613 (1984).

381 H. Okamoto, H. Kida, S. Nonomura, *et al.*, J. Appl. Phys. **54**, 3236 (1983).

382 M. Isomura, T. Takahama, S. Tsuda, *et al.*, Jpn. J. Appl. Phys. **32**, 1902 (1993).

383 R. Crandall and E. Schiff, in *AIP Conference*, edited by H. S. Ullal and C. E. Witt (AIP Press, Lakewood, CO, 1996), Vol. 353, p. 101.

384 Q. Wang, E. A. Schiff, and S. S. Hegedus, in *Materials Research Society Symposium*, 1994), Vol. 336, p. 365.

385 Q. Wang, R. Crandall, and E. Schiff, in *25th IEEE Photovoltaic Specialists Conference* (IEEE, Washington, DC, 1996), Vol. 1, p. 1113.

386 X. Xu, J. Yang, and S. Guha, in *23rd IEEE Photovoltaic Specialists Conference* (IEEE, Louisville, KY, 1993), Vol. 1, p. 971.

387 S. Guha, J. Yang, A. Banerjee, *et al.*, in *AIP Conference*, edited by R. Noufi (AIP Press, Denver, CO, 1993), Vol. 306, p. 127.

388 R. Arya, *et al.*, Final Report for Subcontract ZM-0-19003-1, (National Renewable Energy Laboratory, Golden, CO, 1994).

389 W. Luft, H. M. Branz, V. L. Dalal, *et al.*, in *AIP Conference*, edited by R. Noufi and H. S. Ullal (AIP Press, Denver, CO, 1993), Vol. 306, p. 31.

390 J. Yang, X. Xu, A. Banerjee, *et al.*, in *25th IEEE Photovoltaic Specialists Conference* (IEEE, Washington, DC, 1996), Vol. 1, p. 1041.

5.3 SECTION 4 [CdTe]

401 R. W. Birkmire, J. E. Phillips, W. A. Buchanan, *et al.*, Annual Subcontract Report, (National Renewable Energy Laboratory, Golden, CO, 1996).

402 B. E. McCandless, H. Hichri, G. Hanket, *et al.*, in *25th IEEE Photovoltaic Specialists Conference*, 1996), p. 781.

403 B. E. McCandless, R. W. Birkmire, D. G. Jensen, *et al.*, in *14th NREL/SNL Photovoltaics Program Review* (AIP Press, Lakewood, CO, 1996), p. 647-654.

404 B. E. McCandless, L. V. Moulton, and R. W. Birkmire, Prog. Photovolt. Res. Appl. **5**, 249-260 (1997).

405 D. G. Jensen, B. E. McCandless, and R. W. Birkmire, in *MRS Meeting*, San Francisco, CA, 1996).

406 D. G. Jensen, B. E. McCandless, and R. W. Birkmire, in *25th IEEE Photovolaic Specialists Conference* (IEEE, Washington, DC, 1996), p. 773-776.

407 Y. Qu, P. V. Meyers, and B. E. McCandless, in *25th IEEE Photovoltaic Specialists Conference* (IEEE, Washgton, DC, 1996), Vol. 1, p. 1013-1016.

408 P. V. Meyers and J. E. Phillips, in *25th IEEE Photovoltaic Specialists Conference* (IEEE, Washington, DC, 1996), Vol. 1, p. 789-792.

409 B. E. McCandless and R. W. Birkmire, Solar Cells **31**, 527-535 (1991).

410 R. W. Birkmire, B. E. McCandless, and S. S. Hegedus, Int. J. Solar Energy **12**, 145-154 (1992).

411 J. Britt and C. Ferekides, Appl. Phys. Lett. **62**, 2851-2852 (1993).

412 J. Skarp, E. Anttila, A. Rautiainen, *et al.*, Int. J. Solar Energy **12**, 137-142 (1992).

413 R. W. Birkmire, J. E. Phillips, W. A. Buchanan, *et al.*, Annual Subcontract Report, (National Renewable Energy Laboratory, Golden, CO, 1994).

414 R. W. Birkmire, J. E. Phillips, W. A. Buchanan, *et al.*, (National Renewable Energy Laboratory, Golden, CO, 1993).

415 T. X. Zhou, N. Reiter, R. C. Powell, *et al.*, in *First World Conference on Photovolaic Energy Conversion* (IEEE, Waikoloa, HI, 1994), Vol. 1, p. 103-106.

416 R. W. Birkmire, H. Hichri, R. Klenk, *et al.*, in *13th NREL Photovoltaics Program Review* (AIP Press, Lakewood, CO, 1995), p. 420-427.

417 B. E. McCandless and S. S. Hegedus, in *22nd IEEE Photovoltaic Specialists Conference* (IEEE, 1991), p. 967-972.

418 G. B. Harris, in *Phil. Mag.*, 1952), Vol. 43, p. 113.

419 H. P. Klug and L. E. Alexander, *X-Ray Diffraction Procedures* (John Wiley & Sons, New York, 1974).

420 B. E. McCandless, Y. Qu, and R. W. Birkmire, in *First World Conference on Photovoltaic Energy Conversion* (IEEE, 1994), Vol. 1, p. 107-110.

421 O. Knacke, O. Kubaschewski, and K. Hesselmann, (Springer-Verlag, Dusseldorf, 1991), p. 411.

422 I. Clemminck, M. Burgelman, M. Casteleyn, *et al.*, in *22nd IEEE Photovoltaic Specialists Conference* (IEEE, Las Vegas, NV, 1991), p. 1114.

423 H. Matsumoto, A. Nakano, H. Uda, *et al.*, Jpn. J. Appl. Phys. **21**, 800 (1982).

424 J. S. Lee, H. B. Kim, A. L. Fahrenbruch, *et al.*, J. Electrochem. Soc. **134**, 1790 (1987).

425 J. S. Roh and H. B. Kim, J. Mat. Sci. **23**, 2267 (1988).

426 R. W. Birkmire, B. E. McCandless, and S. S. Hegedus, Int. J. Solar Energy **12**, 145 (1992).

427 S. A. Ringel, A. W. Smith, M. H. MacDougal, *et al.*, J. Appl. Phys. **70**, 881 (1991).

428 S. K. Das and G. C. Morris, Solar Energy Materials and Solar Cells **28**, 305 (1993).

429 A. Nelson and S. Asher, (NREL.

430 B. E. McCandless and S. S. Hegedus, in *22nd EIII Photovoltaic Specialists Conference* (IEEE, Las Vegas, NV, 1991), p. 967-972.

431 R. W. Birkmire, S. S. Hegedus, B. E. McCandless, *et al.*, in *AIP Conference*, edited by R. Noufi (AIP Press, Denver, CO, 1992), Vol. 268, p. 212-217.

432 S. H. Avner, *Introduction to Physical Metallurgy* (McGraw-Hill, New York, 1974).

433 M. M. Al-Jassim, F. S. Hasoon, K. M. Jones, *et al.*, in *23rd IEEE Photovoltaic Specialists Conference* (IEEE, Louisville, KY, 1993), Vol. 1, p. 459.

434 W. A. Rachinger, Jour. Sci. Inst. **25**, 254 (1948).

435 C. Barrett and T. B. Massalski, *Structures of Metals* (Pergamon Press, London, 1980).

436 J. B. Nelson and D. P. Riley, Proc. Phys. Soc. **57**, 160 (1945).

437 A. Taylor and H. Sinclair, Proc. Phys. Soc. **57**, 126 (1945).

438 R. A. Young and D. B. Wiles, J. Appl. Cryst. **15**, 430-438 (1982).

439 K. Ohata, J. Saraie, and T. Tanaka, Jpn. J. Appl. Phys. **12**, 1641 (1973).

440 J. H. Brophy, R. M. Rose, and J. Wulff, *Thermodynamics of Structure* (Wiley and Sons, New York, 1966).

441 N. Nakayama, H. Matsomoto, A. Nakano, *et al.*, Jpn. J. Appl. Phys. **19**, 703-712 (1980).

442 I. Clemminck, M. Burgelman, M. Casteleyn, *et al.*, in *22nd IEEE Photovoltaic Specialists Conference* (IEEE, Las Vegas, NV, 1991), p. 114-119.

443 M. E. Ozsan, D. R. Johnson, D. W. Lane, *et al.*, in *12th EC Photovoltaic Solar Energy Conversion Conference* (H. S. Stephens & Assoc., Bedford, UK, Amsterdam, The Netherlands, 1994), p. 1600-1603.

444 D. M. Oman, K. M. Dugan, J. L. Killian, *et al.*, Appl. Phys. Lett. **67**, 1896-1899 (1995).

445 S. Nunoue, T. Hemmi, and E. Kato, J. Electrochem. Soc. **137**, 1248-1251 (1990).

446 B. E. McCandless, Y. Qu, and R. W. Birkmire, in *1st World Conf. on Photovoltaic Energy Conversion* (IEEE, Waikoloa, HI, 1994), Vol. 1, p. 107-110.

447 P. V. Meyers, C. H. Liu, and M. Doty, , US, 1989).

448 A. Compaan and A. Bhat, Int. J. Solar Energy **12**, 155-169 (1992).

449 F. Ullmann, *Ullmann's Encyclopedia of Industrial Chemistry* (VSJ Publishers, Deerfield Beach, FL, Weinheim, Fed. Rep. Germany, 1985).

450 (Wiley and Sons, New York, 1978), Vol. 12, p. 983-1011.

451 J. Saraie, H. Kato, N. Yamada, *et al.*, Phys. Stat. Sol. **39**, 331-336 (1977).

452 A. F. Fahrenbruch, Solar Cells **21**, 399-412 (1987).

453 Y. S. Tyan, US patent (1980).

454 H. Uda, S. Ikegami, and H. Sonomura, Solar Energy Mater. **35**, 293-298 (1994).

455 T. X. Zhou, Final Technical Report, (National Renewable Energy Laboratory, Golden, CO, 1995).

456 A. Fahrenbruch and J. Sites, personal communications.

457 G. Stollwerk and J. R. Sites, in *13th European Photovoltaic Solar Energy Conference* (H. S. Stephens & Assoc., Bedford, UK, Nice, France, 1995).

6. ABSTRACT

This report describes results achieved during the a four year subcontract to develop and understand thin film solar cell technology related to $CuIn_{1-x}Ga_xSe_2$, a-Si and its alloys and CdTe. Accomplishments during this phase include:

- Fabrication of 15% efficient $CuIn_{1-x}Ga_xSe_2$ cells over a wide range of Ga compositions ($x \leq 0.5$).
- Fabrication of uniform single phase $Cu(Ga_xIn_{1-x})Se_2$ films and solar cells from the selenization of Cu-In-Ga precursors with the optical bandgap and device results expected for the precursor composition.
- Development of µc n-layers which have allowed fabrication of a-Si devices with efficiencies as high as 10%.
- Completion of the analysis and measurements that quantify the improvement in performance of a-Si solar cells due to optical enhancements from a wide range of TCO texture substrates and back reflectors.
- Development of uniform and reproducible vapor phase $CdCl_2$ treatments for CdTe/CdS films that have translated into greater consistency in device performance.
- Characterization of the CdTe-CdS alloy system at typical solar cell processing temperatures in order to elucidate the role of interdiffusion in CdTe/CdS-based solar cells.
- Development of a HCl vapor treatment of CdTe/CdS films that promote changes in the structure of the films similar to those treated with $CdCl_2$.

In addition to these in-house activities, IEC has maintained an active role in the collaboration with over ten different PV and thin film research and development organizations.

REPORT DOCUMENTATION PAGE

Form Approved
OMB NO. 0704-0188

1. AGENCY USE ONLY (Leave blank)	2. REPORT DATE November 1997	3. REPORT TYPE AND DATES COVERED Final Report

4. TITLE AND SUBTITLE Processing and Modeling Issues for Thin-Film Solar Cell Devices; Final Report	5. FUNDING NUMBERS C: XAV-3-13170-01 TA: PV804401
6. AUTHOR(S) R.W. Birkmire and J.E. Phillips	
7. PERFORMING ORGANIZATION NAME(S) AND ADDRESS(ES) Institute of Energy Conversion University of Delaware Newark, Delaware	8. PERFORMING ORGANIZATION REPORT NUMBER
9. SPONSORING/MONITORING AGENCY NAME(S) AND ADDRESS(ES) National Renewable Energy Laboratory 1617 Cole Blvd. Golden, CO 80401-3393	10. SPONSORING/MONITORING AGENCY REPORT NUMBER SR-520-23835

11. SUPPLEMENTARY NOTES

NREL Technical Monitor: B. von Roedern

12a. DISTRIBUTION/AVAILABILITY STATEMENT	12b. DISTRIBUTION CODE UC-1263

13. ABSTRACT *(Maximum 200 words)*

During the three phases of the subcontract, the Institute of Energy Conversion researchers continued to provide the thin-film photovoltaic (PV) community with greater depth of understanding and insight into a wide variety of issues including: the deposition and characterization of CuIn$_{1-x}$Ga$_x$Se$_2$, a-Si, CdTe, CdS, and TCO thin films; the relationships between film and device properties; and the processing and analysis of thin-film PV devices. This has been achieved through the systematic investigation of all aspects of film and device production and through the analysis and quantification of the reaction chemistries involved in thin-film deposition. This methodology has led to controlled fabrications of 15%-efficient CuIn$_{1-x}$Ga$_x$Se$_2$ solar cells over a wide range of Ga compositions, improved process control of the fabrication of 10%-efficient a-Si solar cells, and reliable and generally applicable procedures for both contacting and doping CdTe films.

14. SUBJECT TERMS photovoltaics ; processing ; modeling ; thin-film solar cells ; copper indium gallium diselenide ; amorphous silicon ; cadmium telluride ; cadmium sulfide ; transparent conducting oxides	15. NUMBER OF PAGES 167
	16. PRICE CODE

17. SECURITY CLASSIFICATION OF REPORT Unclassified	18. SECURITY CLASSIFICATION OF THIS PAGE Unclassified	19. SECURITY CLASSIFICATION OF ABSTRACT Unclassified	20. LIMITATION OF ABSTRACT UL

NSN 7540-01-280-5500

Standard Form 298 (Rev. 2-89)
Prescribed by ANSI Std. Z39-18
298-102